Gravitational Waves and Dynamical Processes in Hot Newborn Compact Stars

LAU, Hoi Kwan

A Thesis Submitted in Partial Fulfillment
of the Requirements for the Degree of
Master of Philosophy
in
Physics

The Chinese University of Hong Kong
February 2010

Thesis/Assessment Committee

Professor CHU, Ming Chung (Chair)
Professor LEUNG, Pui Tang (Thesis Supervisor)
Professor LIU, Renbao (Committee Member)
Professor COMER, Gregory L. (External Examiner)

In the memorial of my beloved grandparents

Mr. Shing-Ming Leung (1931-2009)

and

Ms. Mo-Ching Chan (1931-2009)

～ ～ ～ ～ ～ ～ ～ ～ ～

謹此懷念親愛的公公和婆婆

梁成銘先生 (1931-2009)

及

陳慕貞女仕 (1931-2009)

Abstract

Gravitational wave driven by oscillations of hot compact stars is studied within the framework of the linearized general relativity.

While most previous works are conducted on mature compact stars that temperature is negligible, we try to extend the investigation to compact stars with surface temperature as high as 5 MeV, which is the temperature range of a supernova remnant one minute after the explosion. GW quasi-normal mode (QNM) is computed for both neutron stars (NS) and quark stars (QS), as two possible forms of hot remnant. We find that gravity mode (g mode) frequencies vary significantly as temperature decreases, while spacetime modes and the fundamental mode (f mode) are insensitive to temperature variations. We propose that g mode is the most noticeable GW signal that can identify the cooling process during the compact star evolution, while changes of f mode and spacetime mode frequencies are recognizable if extensive transition of stellar composition occurs.

Behavior of each QNM is analyzed separately. We find that the temperature insensitivity of f mode and spacetime modes frequencies can be explained by the fact that, these mode spectra are mainly determined by the stellar mass and geometry but not the composition. We find a new set of universalities to describe the mode distributions, based on functions of mass and the moment of inertia. Our proposal is not only more accurate than other empirical relationships proposed before, but also applicable for both NS and QS. By this discovery, we suggest that the values of mass, radius, and the moment of inertia

of compact stars can be deduced to high precision from GW signals detected.

On the other hand, pulsation mechanism of g mode is mainly determined by the local properties of composed matter. Mode frequency of QS is calculated under various physical conditions. We find that its value is mostly influenced by the properties of matter during pulsation, whereas the value of strange quark mass and the stellar temperature profile are also important factors.

Finally, we discuss the GW excitation caused by astronomical dynamical processes. Power spectrum and waveform of GW induced by a collapsing dust shell are computed. We find that the features of GW emitted are dominated by the f mode oscillation, which occupies about half of the wave energy, while g mode and w mode are hardly excited. Validity of the results obtained by the linearized relativistic formalism is verified by comparing with that of full general relativity simulation. We find that although f mode signal is still significant, contribution of g mode is much larger than the linearized result, which is a finding worth attention in the future.

摘要

在本篇論文中，我們利用了線性化的廣義相對論，探討由高温致密星震動所激發的重力波現象。

關於由星體發出的重力波現象早已被廣泛討論，但大部分的研究都只考慮低温的成熟致密星。 本文的目標是把過往的探討推廣至熱致密星。因為超新星爆炸後一分鐘，其遺跡的表面温度約五百萬電子伏特，所以我們的討論將集中在此温度範圍，並同時考慮超新星遺跡會以中子星或夸克星的形式存在。 首先，我們計算了重力波的類標準震動模式 (Quasi-normal mode)，觀察其頻譜在不同星體表面温度下的差異。我們發現引力震動模式 (g mode) 的頻率會隨温度顯著改變，相反温度不會明顯影響基本模式 (f mode) 和時空模式的頻率。因此只有引力震動模式的重力波能揭示致密星的演化過程中的冷卻效應。除非演化過程中星體成份急劇改變，否則基本模式和時空模式的頻率不會有太大轉變。

在本文的下半部分，我們分析了上述温度對重力波的效應。我們發現引力震動模式的頻率，主要受星體構成物在震動時的特性影響。另一方面，我們認為基本模式和時空模式的頻率不隨温度改變，是因為致密星的幾何特性才是主要決定這兩種震動頻率的因素。我們發現，如果以星體的轉動慣量來表達這兩種震動模式的普適性，就能夠統一描述中子星和夸克星的基本模式和時空模式重力波頻譜，並且能提升普適性的準確度，有助利用實驗觀測到的重力波波頻，來推斷致密星的幾何特性。

論文的最後部分，將研究因物質崩塌所激發重力波的特性。我們發現引力模式和時空模式較難被激發，oam amyo 基本震動模式會主導重力波的波形和功率分佈。可是，全相對論模擬的結果卻顯示，引力模式所包含的能量

遠高於線性化相對論的推測。我們認為這項發現會是往後值得探討的方向。

Acknowledgments

May I express my greatest gratitude to my supervisors Prof. P.T. Leung and Dr. L.M. Lin for their patience, inspiring guidance, and sincere help in all aspects. My attitude towards physics and living are greatly influenced. I also thank Miss Y.C. Zhang for fruitful discussion on the radius of neutron stars, Mr. P.O. Chan for his data of the moment of inertia, and Mr. K.C. Woo for his kindly support. Special thank is given to colleagues of Information Technology Services Centre in the Chinese University of Hong Kong, for their technical support in implementing the full GR simulations.

I am pleased with my friends, especially Mr. Tony C. Kwok, Mr. K.T. Ho, and Mr. Y.H. Tam, for their mental support during the toughest time in my MPhil period. Finally, I sincerely thank my parents, Mr. W.H. Lau and Ms. K.L. Leung, for their unlimited tolerance and care.

Contents

List of Figures

List of Tables

Chapter 1

Introduction

1.1 Gravitational wave astronomy

Humans have been looking at stars in the sky since for at least as long as the historical record. Through observing those seemingly tiny shining objects, we have learnt much about the nature of our living place. For example, from motions of celestial objects, Kepler and Newton have found laws of motion and gravity; from the light spectrum of solar radiation, we learn more about the ingredients of sun and the mechanism of nuclear fusion.

However, the signals which we have received from the sky is more or less the same for thousands of years, the only way of detection is to use 'eyes', either human or electronic, to receive electromagnetic radiation, no matter if it is visible, $\gamma-$ray or infra-red (IR). It is efficient to obtain information from star by collecting light, especially for heat generating stars during stellar evolution. However this kind of detection has shortcomings, there are astronomical objects and events which are not bright enough to detect easily, and light is easily screened or scattered by dust and matter on the pathway to the earth. To fully utilize the sky as a big natural laboratory, new kinds of detection have been proposed in recent years, among which gravitational radiation is believed to be a viable form of signal.

Gravitational radiation arises naturally in Einstein's general relativity (GR)

in 1916. After linearization of the generically nonlinear Einstein equations in free space, a Klein-Gordon-like equation emerges, revealing that perturbation of spacetime will propagate in the form of wave. As gravity originates from the curvature of space-time, the disturbance is recognized as a gravitational wave (GW).

Since GW is only weakly coupled to matter, it is not easily screened by obstacles in the pathway of traveling towards the Earth, which would provide fruitful information in supplement to traditional observation. Despite rich theoretical support of presence of GW, there has not been any direct observation on the signal till present years. The closest indirect proof is the measurement made by Hulse and Taylor on the binary pulsar system PSR B1913+16 [6]. By analyzing the pulses received, they found that the orbiting period of the binary star is continuously shrinking, and the rate of power loss matches the prediction of gravitational radiation by general relativity.

In the new millennium, direct detection of gravitational waves has become one of the major goals of physicists, several ground-based detectors (LIGO, VIRGO, GEO600, etc) and space-based detectors (LISA) are already running or will be operating in the coming years [7]. To fully utilize their potential, tons of theoretical work must be carried to coordinate with experimental measurements. For example, numerical simulations are done to deduce possible waveform emitted from various astronomical events. From their results, an appropriate wave extraction method is set up to facilitate recognition of GW signals, so as to extract more accurate results from detection. Besides, the wave amplitude and frequency can also be estimated, providing guidelines for configuring GW detectors for most meaningful operation. My thesis adds a little piece into the pool, we compute GW frequency emitted from hot compact stars, so as to obtain information about temperature of compact stars from future GW data.

1.2 Stellar pulsation and gravitational radiation

As perturbations of spacetime are caused by motion of masses, massive objects are usually strong sources of gravitational radiation, such as blackholes and compact stars. In particular, polar GW of compact stars attracts attention of astrophysicists and nuclear physicists. It is because of the pioneer theoretical work of Thorne and Campolattaro, under the framework of linearized general relativity theory, that we know fluid motion will be coupled to polar metric perturbations [8], therefore gravitational wave signals could reveal properties of nuclear matter in return.

Since then, theoretical work was focused on obtaining the relationship between typical frequencies of GW, called quasi-normal mode (QNM) frequencies, and different stellar properties. For example, Lindblom and Detweiler refined the formalism of Thorne *et al.*, and surveyed the dependence of QNM frequencies on the gravitational redshift of compact stars [9]. By similar methods, Andersson and Kokkotas [5] attempted to obtain universal pattern of QNM distribution against compactness (ratio of mass to radius) of stars, from which an inversion scheme was proposed to infer stellar mass and radius. Further investigation suggests that QNM frequencies also contains information about stellar structure [10], as well as density discontinuities inside the stars possibly due to phase transitions of nuclear matter [11].

These findings best describe mature compact stars, where temperature is well below the Fermi temperature of nuclear matter, because most of them employed theoretical equation of states (EOS) calculated by nuclear physicists at zero temperature. Most existing compact stars observed are cold, because of effective cooling mechanisms which remove thermal energy within a short period comparing to the astronomical timescale. Ferrari *et al.* [12], however, showed that the pattern of QNM emitted from hot new born compact stars

deviate significantly from the trend of their mature counterparts. In view of numerous drastic astronomical events happening at early stage of compact stars, such as asymmetric accretion of matter and phase transition of the nuclear state, excitation of gravitational waves is likely, thus mode frequencies of new born compact stars deserve much attention.

As described by Ferrari *et al.*, the structure of proto-neutron stars experience drastic changes in the first minute of evolution, before forming stable neutron stars (NS). These changes include rapid contraction of radius due to reduction of lepton pressure by neutrino losses, heating of nuclear matter by diffusion of high energy neutrinos, and an expeditious decrease of average temperature because of effective cooling mechanism. It is hence expected that such a re-distribution of the matter state would shift the QNM spectrum. After the first minute, the supernova remnant will become a compact star with geometrical properties close to mature ones.

This does not, however, mean that the behavior of QNM frequencies is well understood hereafter, because a compact star at this stage is still hot enough ($T \sim$ MeV range), to impose non-trivial effect. As a simple illustration of thermal effects, buoyancy oscillation of fluid element is closely related to convective stability of the stars, which definitely depends on the temperature profile. Besides, the electron pressure could also be magnified by thermal effect, whose contribution becomes significant in the low density region. Deviation of stellar structure would alter the geometry and spacetime curvature of compact stars, and characteristics frequency is obviously affected.

Another interesting phenomena is the existence of quark matter. Since Witten [13] proposed that quark matter can stably exist as a mixture of deconfined quarks, it is believed to be a possible ground state of nuclear matter in high temperature and density regions. As such conditions could be found near the centre of compact stars, it is widely anticipated that nuclear matter can undergo phase transition and form a quark core (c.f. [14, 15, 16] and their

references). Some authors even proposed strong interaction binding energy per particle is lower for quark matter than nuclear matter, a neutron star would finally transform to a quark star (QS), which is a compact star composed entirely of quark matter, during stellar evolution [17].

On the other hand, temperature and density of a supernova remnant is hot and dense throughout the whole star, which is a favorable condition for QS formation [18, 19]. Investigation suggests the structure of QS is significantly altered from ordinary neutron stars [16], and so their GW spectra should be affected [4]. Similar to NS, we consider in this thesis that a QS is formed after a supernova explosion and cools continuously. If the temperature of QS drops below phase transition temperature T_p, macroscopic phase transition would be induced, and QS is transformed to ordinary neutron star [18]. The drastic change in stellar structure and hence cause a sudden shift of QNM spectrum. In other words, if such a jump of mode frequencies is detected, it would put constraints on T_p, which the value is not yet confirmed yet.

1.3 Outline

In the context of the interesting uncertainties presented above, this thesis will focus on how compact star temperature will influence gravitational radiation. The outline of the thesis is as follow:

In the first three chapters, we will discuss the technical background of the calculations. An outline of our scenario is shown schematically in Fig. 1.1.

A hydrostatic star has first to be constructed using the relativistic structural equation, usually referred to as the Tolman-Oppenheimer-Volkoff [20] [21] equation. The idea and mathematical form is presented in Chapter 2. We will show that the stellar structure is very dependent on the properties of nuclear matter, which is described by EOS. In this thesis, we mainly employ the EOS of hot nuclear matter and quark matter, a brief introduction to be

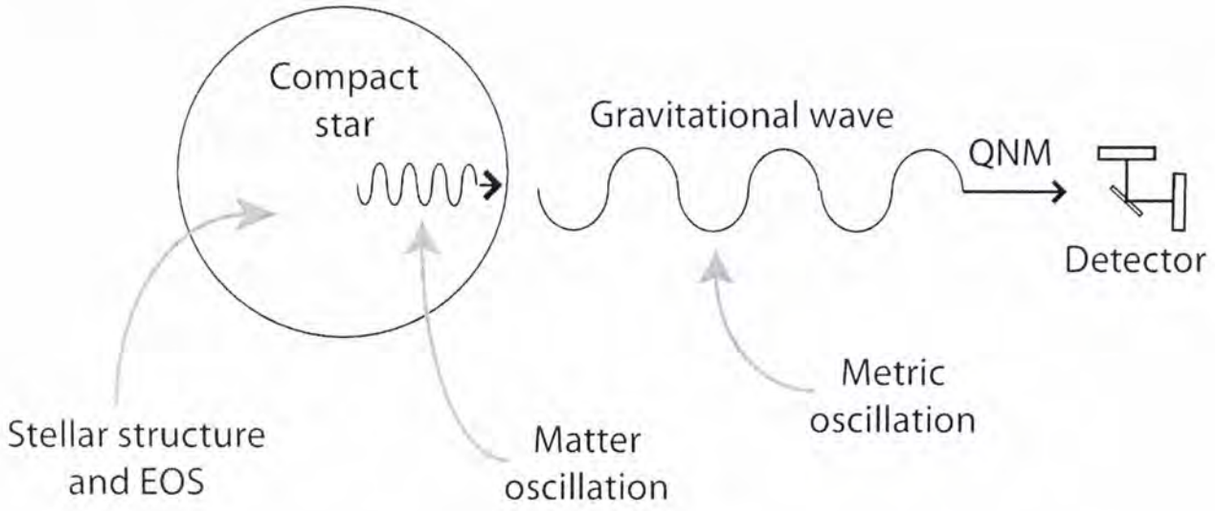

Figure 1.1: Outline of the scenario.

given in Chapter 3.

Next, we set the system to oscillate, and all the oscillations are governed by the equations of linearized general relativity. Since oscillations of stellar matter would induce disturbances of spacetime which would propagate in vacuum space as GW, the system is naturally divided into two parts for consideration. Inside the star, we use the equations developed by Lindblom and Detweiler in 1985 [22] to describe coupled matter and spacetime oscillation. For the vacuum region outside the star, spacetime oscillation is described by the metric perturbation equation derived by Zerilli in 1970 [23]. The above mathematics is presented in Chapter 4.

After gathering all the necessary technical ingredients, the QNM spectrum of hot compact stars is computed in Chapter 5. We consider hydrostatic neutron stars and quark stars with surface temperature from 0 - 5 MeV, which is the temperature range of a compact star born 1 minute after a supernova explosion. In addition, the percentage change of mode frequencies caused by phase transition from quark star to neutron star is also estimated.

To understand how temperature affects the QNM spectrum, analysis is done in two following chapters. In Chapter 6, universal trends are obtained

empirically to describe the pattern of mode frequency against geometric parameters of compact stars. On the other hand, influence of local properties of nuclear matter on QNM is investigated in Chapter 7.

We discuss the detectability of GW in Chapter 8, by considering GW induced by a collapsing dust shell as an example. The GW power spectrum and waveform are computed by linearized theory of general relativity, and features are analyzed on characteristics of compact stars and QNM. Validity of these linearized results are then compared with full general relativity simulations. In addition, we account for influence of non-adiabatic effect on oscillation by adding thermal dissipation effect of superconductivity to QS.

Finally, all the results above is summarized in Chapter 9, with some final comments on prospects for gravitational wave astronomy.

Unless otherwise stated, we choose $G = c = 1$ such that all astronomical data is presented in unit of km, where G is the gravitational constant, c is the speed of light; while we also choose $h = k_B = 1$ such that all data of particle physics is presented in MeV, where h is Planck's constant and k_B is the Boltzmann constant.

Chapter 2

Hydrostatic stellar structure

After the collapse of a main sequence star, the remnant forms a compact stellar object, either a black hole, a neutron star or a white dwarf. If the core mass is higher than the Chandrasekhar limit (about 1.4 solar mass), a white dwarf cannot be formed and stellar matter condenses to form a blackhole or a neutron star. The maximum mass limit for neutron stars maybe as high as 3 solar masses (hereafter denoted as $M_{\odot}$) [16], however the exact value is still under debate. According to the no hair theorem, a blackhole is merely an event horizon with 3 characteristic parameters (mass, angular momentum, charge) only, whose internal structure (if any) can be neglected. On the other hand, if gravity is not strong enough to overcome the degenerate pressure of particles, masses would sustain to occupy a finite volume in space and form a compact star.

Unlike white dwarfs which are supported by the electron degenerate pressure of closely packed atoms, the compact star pressure is so high that atoms are compressed to form closely packed nuclei. Such kind of matter is called nuclear matter. Historically speaking, compact stars were first proposed in the form of a neutron star [24], which is solely composed of neutron. With this idea, Oppenheimer and Volkoff [21] employed the work of Tolman [20] and found the degenerate pressure of a Fermi neutron gas cannot sustain mass more than 0.7 $M_{\odot}$. This value was later found to be too low, according to the

observational data of possible neutron star candidates. It is because nuclear matter is not an ideal Fermi fluid, nuclear interactions between species are strong to affect its properties. Furthermore, the composition of nuclear matter is not only neutron, but other particles such as protons, quarks, hyperons and leptons. Details of the EOS will be discussed in the next chapter.

In spite of predicting too small a maximum mass, the equations derived by Tolman, Oppenheimer and Volkoff, conventionally cited as Tolman-Oppenheimer-Volkoff (TOV) equations in literature, correctly describe the structure of a spherical hydrostatic compact star. In our situation, we consider hydrostatic compact stars formed by nuclear matter existing as degenerate particles, which can be regarded as a perfect fluid (since anisotropic behavior would only be expected in the outer crust according to most theoretical EOS models). We also assume the compact star is isolated and non-rotating for simplicity, such that the whole system is spherically symmetric, and hence well described by the Schwarzschild metric,

$$ds^2 = -e^{\nu(r)}dt^2 + e^{\lambda(r)}dr^2 + r^2(d\theta^2 + \sin^2\theta d\phi^2) \ . \tag{2.1}$$

All the non-rotating compact star equilibria we are going to consider in this thesis are solutions of TOV equations. In this chapter, we will briefly illustrate the idea of the TOV equation with the aid of Newtonian hydrostatic equation as an analog.

2.1 Structural equation

Hydrostatic equilibrium of a Newtonian star is similar to that of gases in the Earth atmosphere. Because the fluid is in equilibrium, the pressure gradient and gravity balance each other; there is no net force throughout the star. Consider an arbitrary position inside the star, the relationship of forces per

unit volume can be expressed as

$$\nabla p(r) = \bar{\rho}(r)\vec{g}(r) \ , \tag{2.2}$$

where r is the distance from the star centre, and $p(r)$, $\bar{\rho}(r)$, $g(r)$ are pressure, mass density and gravity at distance r respectively. According to Newton's theory of gravitation,

$$\vec{g} = -\frac{Gm(r)}{r^2}\hat{e}_r \ , \tag{2.3}$$

where G is the gravitational constant, $\hat{e_r}$ is the radial unit vector, $m(r)$ is the total mass interior to distance r satisfying

$$m(r) = \int \bar{\rho}(\vec{r})d^3\vec{r} \ . \tag{2.4}$$

By the assumption of spherical symmetry, the gradient of any quantity consists of the radial component only, thus Eq. 2.2 is transformed to

$$\frac{dp(r)}{dr} = \bar{\rho}(r)g(r) \ , \tag{2.5}$$

also known as the momentum equation for a static fluid. As long as density and mass are functions of r only, Eq. 2.4 can be simplified and rewritten in differential form as

$$\frac{dm(r)}{dr} = 4\pi r^2 \bar{\rho}(r) \ . \tag{2.6}$$

In general relativity, the hydrostatic equation is derived by simplifying Einstein equation, and the result is

$$\frac{dm}{dr} = 4\pi r^2 \rho \ , \tag{2.7}$$

$$\frac{d\nu}{dr} = \frac{2m + 8\pi r^3 p}{r(r-2m)} \ , \tag{2.8}$$

$$\frac{dp}{dr} = -\frac{1}{2}(p+\rho)\frac{d\nu}{dr} \ , \tag{2.9}$$

where p is pressure as in the Newtonian case; m is the gravitational mass including both rest mass and energy of particles, and gravitational energy of the field; ν is the tt metric component of the line element in Schwarzchild

coordinates; ρ is total energy density instead of rest mass density as in the Newtonian case. It is easily checked that the three TOV equations correspond to Eq.s 2.6, 2.3 and 2.5 respectively. The major difference is the generalization of Eq. 2.3 to Eq. 2.8, from which gravity originates as spacetime curvature and described by variation of metric components.

TOV equations describe profiles of 4 variables: p, ρ, ν and m, meaning the structure of a compact star is basically determined by these 4 physical quantities. But the TOV equation is a 3-rd order differential equation system; the extra condition is properties of matter given by the EOS, which is usually a relationship between pressure p and total energy density ρ.

Every compact stars has to be regular at the origin; in other words there is no mass singularity at centre, i.e.

$$m(r = 0) = 0 \ . \tag{2.10}$$

Besides, the metric component ν is required to connect smoothly with the Schwarzschild solution in vacuum outside the star,

$$e^{-\nu(R)} = e^{\lambda(R)} = 1 - \frac{2M}{R} \tag{2.11}$$

where M is the total gravitational mass of the star; R is radius defined as the position where pressure vanishes,

$$p(r = R) = 0 \ . \tag{2.12}$$

Mathematically speaking, the physical requirements of Eq. 2.10 and 2.11 are two boundary conditions on the TOV equations. We need one more specification to determine a unique compact star, which is to fix the value of the central pressure p_0 or the total mass of the star (other choices of quantity, such as the central energy density ρ_0, or total mass M, is technically equivalent).

As a summary to the above discussion, stellar structure is governed by both TOV equations, which is the same for all compact stars in our investigation,

and the nuclear properties are described by EOS, which is the feature of stars we are going to investigate. We end this chapter by illustrating how EOS and stellar structure would affect GW emission. Firstly, different EOS would give notably deviated matter profile. For a static and spherically symmetric configuration, the distribution of mass determines spacetime curvature at any position inside the star, perturbation of spacetime is hence altered by EOS. More importantly, spacetime oscillation would couple with fluid motion. Recalling the case of non-rotating blackhole, it is merely an event horizon without internal structure, therefore GW only consists of spacetime oscillation. However, compact stars are sustained by nuclear pressure to occupy a finite volume in space, therefore a class of characteristic frequencies is associated to the star.

Chapter 3

Finite temperature equations of state of nuclear matter

In the previous chapter, we showed how the matter distribution inside compact stars is closely related to the nuclear matter state; hence gravitational wave spectra are sensitive to EOS. The effect has been well surveyed by various authors before (e.g. [5, 25]), but most of them have assumed the EOS to be for zero temperature. This is the case for mature neutron stars, with temperatures far below the Fermi temperature ($T_F \sim 100$ MeV) of nuclear matter. However, the temperature of remnants of supernovae can be as high at 10 MeV range, and temperature effects are non-trivial. In this chapter, we present two possible kinds of hot compact star as supernova remnants, which are ordinary neutron stars constructed by finite temperature nuclear matter EOS, and quark stars constructed by the finite temperature MIT bag model.

3.1 Finite temperature ordinary nuclear matter

Even in the zero temperature case, the exact behavior of nuclear matter at high density is still not known. Theoretical works are in abundance, based on different models of nuclear interactions and compositions, resulting in a zoo of

zero temperature EOS. The case is obviously more complicated if temperature is included. To date, there are two most commonly employed finite temperature nuclear matter EOS: the Lattimer and Swesty EOS [26], and Shen EOS [27, 28]. Since the latter one is given in tabulated form, for simplicity, we use the Shen EOS here to construct hot NS.

The Shen EOS is constructed for investigating mechanisms and phenomena of supernova explosion through full GR numerical simulation [27, 28]. Since the EOS covers a wide range of density and temperature, it is also appropriate to be employed for constructing high temperature neutron stars. The Shen EOS is roughly divided into 3 regions, which is the nuclear matter region in the high density range, a packed nuclei region in the low density range, and the mixture of both in a phase transition region. The high density nuclear matter is solved by relativistic mean field (RMF) theory with inclusion of non-linear meson coupling terms. Characteristics parameters used in RMF calculations are the values that can yield results comparable with experimental data. The low density region is assumed to be non-uniform, in which heavy nuclei are formed and packed in BCC lattice structure, and surrounded by free lepton gases. In the intermediate region, a nucleon gas may co-exist with packed heavy nuclei. Shen *et al.* applied the Thomas-Fermi method to seek the lowest free energy state for each density, composition and temperature.

The Shen EOS table only provides thermodynamic properties of nuclear matter, without contribution of leptons and photons. It is because Shen *et al.* chose proton fraction Y_p, temperature T, and baryon number density n_B, as primary variables. For a state with fixed proton fraction, leptons can be treated as independent particles. It is because the minimization of the nuclear matter free energy is not affected if the contribution electromagnetic interaction to total free energy is low. As usual practice we include the contribution of leptons by adding electrons and positrons as ideal Fermi gases, whose energy

density and pressure are given by

$$p_l = \frac{g_l}{6\pi^2}\int_0^\infty k^3 \frac{\partial \epsilon_l(k)}{\partial k}\frac{1}{e^{(\epsilon_l(k)-\mu_l)/T}}dk \ , \tag{3.1}$$

$$\rho_l = \frac{g_l}{2\pi^2}\int_0^\infty k^3 \frac{1}{e^{(\epsilon_l(k)-\mu_l)/T}}dk \ , \tag{3.2}$$

where $g_l = 2$ is the spin degeneracy of electron and positron, μ_l is the chemical potential of the leptons; $\epsilon_l(k) = k$ because the electron mass is too small when compared with the Fermi momentum. Other thermodynamic properties are generated by the same formalism (see details in [16]). It is noted we consider electrons and positrons as the only leptons, because we have checked muons are far less abundant.

3.2 Strange Quark Matter

Under high temperature and density, quarks are deconfined and there is no definite region of a nucleon. As a result, quarks behave almost as an ideal Fermi gas within the quark matter. A proposal of a quark matter EOS may include gluon interactions, color-flavor-locked (CFL) phenomena, and other physical effects that are not precisely verified up to date, so for simplicity, we use the finite temperature MIT bag model as the EOS of quark matter [16]:

$$p_f = \frac{g_f}{6\pi^2}\int_0^\infty \frac{\partial \epsilon_f(k)}{\partial k}\frac{k^3}{e^{(\epsilon_f(k)-\mu_f)/T}}dk - B \ , \tag{3.3}$$

$$\rho_f = \frac{g_f}{2\pi^2}\int_0^\infty \epsilon_f(k)\frac{k^2}{e^{(\epsilon_f(k)-\mu_f)/T}}dk + B \ , \tag{3.4}$$

$$n_f = \frac{g_f}{2\pi^2}\int_0^\infty k^2 \frac{1}{e^{(\epsilon_f(k)-\mu_f)/T}}dk \ , \tag{3.5}$$

where B is the bag constant mimicking long distance interaction for quark confinement; the subscript f denotes the flavor of quarks, which consist of up, down, and strange (u, d, and s) quark for strange quark matter; g_f is the degeneracy of each flavor, where $g_f = 2_{\text{spin}} \times 3_{\text{colour}}$ for the 3 quarks; $\epsilon_f(k) = \sqrt{m_f^2 + k^2}$ is the dispersion relation for quarks. Because the up and

down quarks are negligibly light (MeV range), leaving only the non-vanishing strange quark mass m_s. Leptons are also added to the composition of quark matter, and their expressions are the same as the ordinary case. The exact mathematical form of the thermodynamic quantities are given in [16], but in practice, we expand the integral in Eq. 3.3-3.5 by the Sommerfield expansion. For quantities of the up and down quarks, their masses are zero and the Fermi integral can be exactly expressed by a quadratic series in T/μ. But the integral of strange quarks cannot be expressed analytically, so we expand the series up to the forth order correction in (m_s/μ_s) and (T/μ_s) (c.f. Appendix B).

For this simple kind of quark matter EOS, only two parameters are involved in specifying a model, which are the strange quark mass and the bag constant. We choose $B^{1/4} = 154.5$ MeV and $m_s = 150$ MeV unless otherwise stated, as these values can yield physical parameters that matches results of terrestrial experiments [19].

3.3 Equilibrium and Dynamic EOS

In the zero temperature case, pressure is a function of energy density only due to lacking dependence on other thermodynamic properties. But a hot EOS naturally depend on temperature and other physical quantities. For the Shen EOS, pressure and energy density are functions of number density, proton fraction, temperature and electron chemical potential; the local properties of strange quark matter are determined by 5 quantities, which are temperature and the chemical potentials of 3 species of quarks and electrons. Additional information is therefore required to construct a stellar profile. The first assumption is charge neutrality, i.e.

$$\sum_f q_f n_f = 0 \tag{3.6}$$

where f is the species of particles; q_f and n_f are the charge and the number density of that species. We also assume the background is in beta equilibrium, which imposes the relationship

$$\mu_n = \mu_p + \mu_e \tag{3.7}$$

for ordinary neutron stars, and

$$\begin{cases} \mu_d &= \mu_u + \mu_e \\ \mu_d &= \mu_s \end{cases} \tag{3.8}$$

for quark stars. Only one degree of freedom is left, which can either be fixed by the temperature or entropy profile. In fact, determination of the temperature profile involves consideration of various physics, including cooling mechanisms, neutrino transport, supernova mechanism [29], and stars with different composition. These can yield significantly different profiles. Due to the lack of any consensus on temperature inside early stage compact stars, we will specify the temperature profile dedicated for the investigations in each chapter.

The above conditions only determine the properties of an unperturbed stellar configuration. The physical condition, however, can be different during a perturbation. It is because the equilibrium restoring time could be longer than the oscillation period, depending on the nature of each physical process. We hereafter denote the EOS for perturbation as the dynamic EOS to distinguish it from the EOS of the stellar background. In our calculations, we assume charge neutrality always holds during oscillations as a common practice [12]. However, preservation of beta equilibrium is debatable [19]. In the literature, some authors assume beta equilibrium is violated and the chemical composition is instead preserved [30], i.e.

$$d\frac{n_i}{N} = 0 \ , \tag{3.9}$$

where i denotes the particle species, and N is the total particle density of a

fluid element, defined by

$$N = \sum_i n_i \ . \tag{3.10}$$

On the other hand, recent investigations suggest beta equilibrium can be faster than a typical GW period when ordinary nuclear matter is hotter than 3 MeV [19]. Since we are going to consider stars with a wide range of temperature, we will calculate results for both conditions. It is worth noting that the choice of the dynamic EOS will not alter the background, i.e. quantities p, ρ, ν, m are unchanged, but only the adiabatic speed of sound c_s is affected. Recalling its definition,

$$c_s = \sqrt{\left(\frac{dp}{d\rho}\right)_F} \ , \tag{3.11}$$

where F is the set of constraints required by dynamic EOS. It does not only include the preservation of entropy per particle in the adiabatic case, because one constraint is not enough to eliminate extra degree of freedom in the EOS. Additional constraints are supplied by either beta equilibrium or composition preservation. Methods of practical calculations of the sound speed are presented in Appendix F.

Chapter 4

Stellar pulsation and gravitational radiation

Similar to radiation in electromagnetic theory, the relativity theory of gravitation predicts a disturbance of spacetime will propagate in free space as a waveform. It is believed that violent astronomical events will be strong GW sources, such as collisions of stellar objects, asymmetric accretion of masses, and the orbiting in binary systems. While conventional investigation of gravitational waves with full consideration of GR is currently a tough challenge for computational physics, linearization permits a simple analysis of the characteristic GW spectrum emitted by compact stars. In this chapter, the procedure of linearizing Einstein's equation is briefly outlined. We wish to give a simple insight on how gravitational waves are theoretically predicted, as well as their relationship with compact star oscillations.

4.1 Linearized theory of general relativity

For every phenomenon related to gravitational interaction, Einstein's equation $\mathbf{G} = 8\pi\mathbf{T}$ is the master equation governing the dynamics of mass-energy and spacetime. Unfortunately, the Einstein equation is a second order nonlinear 4×4-tensor differential equation, where the inter-dependence of tensor

components impose great difficulties in obtaining solutions, even with the aid of a state-of-the-art numerical facility. In order to get physical insight into particular simplified scenarios, a standard approach is to conduct a perturbative analysis on the equations, which is to consider physical consequence of a slight disburbance on a static background. The perturbed Einstein's equation is obviously

$$\delta\mathbf{G} = 8\pi\delta\mathbf{T} \ , \tag{4.1}$$

where $\delta\mathbf{G}$ is the perturbation of Einstein's tensor, describing first order changes of the spacetime curvature (metric components); $\delta\mathbf{T}$ is the perturbation of the stress-energy tensor which only contains the matter contribution.

Eq. 4.1 is merely an abstract equation as the gauge and coordinates is not fixed yet. For a static, spherically symmetric, asymptotically flat background, the spacetime can be described by the Schwarzschild metric, Eq. 2.1, and the first order perturbation is expressed as

$$ds^2 = (\bar{g}_{\mu\nu} + h_{\mu\nu})dx^\mu dx^\nu = ds_0^2 + h_{\mu\nu}dx^\mu dx^\nu \ , \tag{4.2}$$

where $\bar{g}_{\mu\nu}dx^\mu dx^\nu = ds_0^2$ is the background metric stated in Eq. 2.1; $h_{\mu\nu}$ is the first order metric perturbation. It is noted that although the background is spherically symmetric, the perturbation may involve all sorts of angular dependence.

The metric factor $\bar{g}_{\mu\nu}$, $h_{\mu\nu}$ and their derivatives span the left hand side of Eq. 4.1, while the right hand side contains the perturbations due to matter. We have already assumed the background is vacuum except a compact object with mass M centered on the origin, in order to employ the Schwarzschild metric. This is physically equivalent to assume the mass of other matter sources m_0 is small, i.e. $m_0 \ll M$, and all the influence is a first order correction to the background solution. The general form of the stress tensor of a perfect fluid is given by [31]

$$T^{\mu\nu} = (p + \rho)u^\mu u^\nu + pg^{\mu\nu} \ , \tag{4.3}$$

where $u^\mu = \frac{dx^\mu}{d\tau}$ is the 4-velocity of a fluid element. For complicated matter distributions with intrinsic hydrodynamic properties, the stress tensor is highly non-trivial and has to be obtained numerically even in the linear approximation. But if a shell is assumed to be constructed by dust, as a weakly interacting sparse matter source, pressure is absent and the tensor can be simplified. In this thesis, we only consider shell formed by dust, which can be expressed as a collection of falling dust particle. Mathematically, the accounting of the particle collection is simply a sum over single particle sources $T_i^{\mu\nu}$:

$$\delta T^{\mu\nu} = \sum_i T_i^{\mu\nu} = \sum_i m_i \int \delta^4(\vec{x} - \vec{x}_i(\tau)) \frac{dx^\mu}{d\tau} \frac{dx^\nu}{d\tau} d\tau \ , \tag{4.4}$$

where $\vec{x}_i(\tau)$ is the geodesic of the i-th test mass, where m_i is small so that the whole expression is a first order perturbation.

Regardless of the kind of matter source, linerization can be conducted if we can get the first order perturbation of the stess tensor, and put it into Eq. 4.1. But each tensor involves ten independent entries, which means that the system of linearized equations consist of ten coupled differential equations. Luckily the system can be further simplified by two concepts, parity and gauge transformation. Parity is a symmetry describing the change of behavior under spatial inversion, i.e. upon the transformation $r \to r$, $\theta \to \pi - \theta$, $\phi \to \pi + \phi$ in spherical coordinates. The parity change can be viewed as an operator, which consists of two eigenvalues, $(-1)^l$ and $(-1)^{l+1}$, where l is the azimuthal 'quantum' number. For a function which changes as $(-1)^l$, it is called even parity, or electric, or polar; whereas that changes as $(-1)^{l+1}$ is called odd parity, or magnetic, or axial. In the spherically symmetric system we are considering, components with different parity decouple naturally. The 10-th order linearized equations are separated into 3 odd elements and 7 even elements.

Because the system has spherical symmetry, it is natural to expand all

tensors with the complete set of tensor spherical harmonics, and each harmonic having a definite parity. We follow the notation of Zerilli [23] of the ten tensor harmonics, $\mathbf{a}^{(0)}_{lm}, \mathbf{a}^{(1)}_{lm}, \mathbf{a}_{lm}, \mathbf{b}^{(0)}_{lm}, \mathbf{b}_{lm}, \mathbf{c}^{(0)}_{lm}, \mathbf{c}_{lm}, \mathbf{d}_{lm}, \mathbf{f}_{lm}, \mathbf{g}_{lm}$, where the $\mathbf{a}$'s, $\mathbf{b}$'s, $\mathbf{f}, \mathbf{g}$ are polar and $\mathbf{c}$'s, $\mathbf{d}$ are axial. Details of each tensor are not shown here, their expressions are referred to Eq. A2a-A2j in [23] or Eq. A7-A16 in [32]. Zerilli expands the metric tensor by these components; a typo-corrected equation is given as Eq. A5 in [32]. Similarly, the stress tensor is expressed in tensor harmonics as

$$\begin{aligned} \delta\mathbf{T} &= \sum_{lm} \left[A^{(0)}_{lm}\mathbf{a}^{(0)}_{lm} + A^{(1)}_{lm}\mathbf{a}^{(1)}_{lm} + A_{lm}\mathbf{a}_{lm} \right. \\ &+ B^{(0)}_{lm}\mathbf{b}^{(0)}_{lm} + B_{lm}\mathbf{b}_{lm} + Q^{(0)}_{lm}\mathbf{c}^{(0)}_{lm} + Q_{lm}\mathbf{c}_{lm} \\ &+ \left. D_{lm}\mathbf{d}_{lm} + G^{(0)}_{lm}\mathbf{g}^{(0)}_{lm} + F_{lm}\mathbf{f}_{lm} \right] . \end{aligned} \tag{4.5}$$

As usual, the employment of spherical harmonics aims to separate the angular dependence of functions in order to concentrate on temporal and radial variations. All of our investigation will focus on $l = 2$ polar components, which are believed to contain the most energetic gravitational waves [33], although our code and formalism can be easily extended to other modes.

Further simplification is conducted by fixing the gauge of the system. Although we have specified the Schwarzschild coordinates for the background, the perturbed quantities are allowed to follow another gauge, by performing a first order gauge transformation [34]. Since there is freedom to choose four linearly independent vectors to describe the perturbed system, ten dependent equations will be reduced to six linearly independent ones. Zerilli employed the Regge-Wheeler (RW) gauge proposed in [35]. The gauge can eliminate 4 out of 10 tensor harmonics, hence the degree of freedom for axial component is reduced from 3 to 2, and the polar components are reduced from 7 to 4. The choice of RW gauge tunes the relative contribution of harmonics such that the expansion coefficients of $\mathbf{b}^{(0)}_{lm}, \mathbf{b}_{lm}, \mathbf{d}_{lm}, \mathbf{f}_{lm}$ are zero for the metric tensor. These components are removed such that polar and axial metric tensors

only depend on Y_{lm} and first derivatives of Y_{lm} respectively. This operation facilitates differential operation and separation of the Einstein tensor, however it does not eliminate any component of the stress tensor. The stress tensor generally includes all components of tensor harmonics, depending on motion and distribution of extended matter source.

Since Einstein's equation is a dynamic equation, it describes time variation of quantities that experiences gravitational interactions. In order to conduct spectral analysis of gravitational radiation, Regge and Wheeler [35], and Zerilli [23] performed Fourier transforms to obtain linearized equations in the frequency domain. The convention of Regge, Wheeler and Zerilli is

$$X(\vec{r},t) = \int \tilde{X}(\vec{r},\omega)e^{-i\omega t}d\omega \ , \tag{4.6}$$

which the time dependence of all Fourier components are $e^{-i\omega t}$ for any time-dependent function $X(\vec{r},t)$. It is noted that some authors, such as Lindblom and Detweiler [9], use $e^{i\omega t}$ for the Fourier transform.

Now the angular derivatives of metric tensors are resolved by introducing spherical harmonics as eigenfunctions in RW gauge, and the time derivatives are removed by Fourier transform, leaving aside derivatives with respect to radial position r only. Among the three equations in axial parity, Regge and Wheeler [35] found one of them is redundant and the two remaining ones can be combined to become a second order differential equation, known as the RW equation [36]. Since RW equation is a Klein-Gordon-like equation (e.g. Eq. 2.6 in [23]), it suggests that perturbations of odd parity spacetime will propagate as axial gravitational waves. We do not investigate axial waves in this thesis, because axial waves do not couple with axial fluid motions [8] (we refer interested readers to the original paper of Regge and Wheeler [35] or section 2 in Nollert's review article [34] for further details).

Similar to the axial case, Zerilli obtained 7 equations relating the metric and stress perturbations but only two are linearly independent [36]. Zerilli

constructed a new metric function by combining linearly the expansion coefficients of the metric tensor (c.f. Eq. A5 in [32]), conventionally referred to as the Zerilli function $Z_{lm}(r,\omega)$. It satisfies a second order differential equation

$$\frac{d^2}{dr_*^2}Z_{lm} + (\omega^2 - V_l(r))Z_{lm} = S_{lm} \ , \tag{4.7}$$

where r_* is the tortoise coordinate related to r by

$$dr_* = \frac{dr}{1-\frac{2M}{r}} \ ; \tag{4.8}$$

the effective potential V_l is usually referred to as the Zerilli potential,

$$V_l = \left(1-\frac{2M}{r}\right)\frac{2\lambda^2(\lambda+1)r^3 + 6\lambda^2 M r^2 + 18\lambda M^2 r + 18M^3}{r^3(\lambda r + 3M)^2} \ ,$$

where $\lambda = l(l+1)/2$ is a constant (and not the exponent of rr metric $\lambda(r)$); S_{lm} is the source term obtained by contracting corresponding expansion coefficients of the stress tensor in Eq. 4.5 (some detail is provided in Section 8.2). The Klein-Gordon-like Eq. 4.7 describes a polar spacetime disturbance will propagate as wave in the tortoise coordinate. At a position very far away from the origin, i.e. $r \to \infty$, the tortoise coordinate r_* will be effectively the same as the conventional r.

In the sourceless case, the Zerilli equation is a homogeneous differential equation

$$\frac{d^2}{dr_*^2}Z_{lm} + (\omega^2 - V_l(r))Z_{lm} = 0 \ . \tag{4.9}$$

So the Zerilli function behaves asymptotically as plane wave, i.e.

$$Z \sim e^{i\omega r} \text{ or } e^{-i\omega r} \ . \tag{4.10}$$

For each given ω, the solution of the sourceless Zerilli equation will in general give a linear combination of both plane wave solutions, where the ratio of the respective amplitude depend on the boundary conditions of the central compact object. However, it is physical to anticipate that a gravitational wave is traveling radially outward when produced by the excitation mechanism of

the compact object. We expect the natural frequency of a stellar pulsation only yields a gravitational wave with only outgoing component at spatial infinity, i.e. $e^{i\omega r}$ ($e^{-i\omega r}$) in Zerilli (LD) notation, which is the definition of QNM. In general the requirement of an outgoing wave and the physics of the Zerilli equation does not restrict ω to be real, therefore QNM will have a real part ω_r, which is the oscillation frequency; and an imaginary part ω_i, corresponding to damping of the wave amplitude caused by radiation energy dissipation.

4.2 Stellar oscillation

Because the QNM frequency varies with the properties of the compact object, detection of gravitational wave QNM is a plausible source providing information of compact stars or blackholes. Frequency of QNM mainly depends on boundary condition provided by intrinsic dynamics of compact objects. In the case of blackhole, there is only one simple boundary condition, which requires gravitational wave to be purely ingoing to the blackhole on the event horizon. Its mathematical expression in Zerilli's notation is $Z \sim e^{-i\omega r_*}$ at $r_* \to -\infty$ or equivalently $r \to 2M$.

On the other hand, the boundary condition of compact stars is more complicated, which require analyzing the details of the stellar oscillation. Linearizing the Einstein equation for a spherically symmetric hydrostatic ideal fluid star was first conducted by Thorne *et al.* [8], which coupling between spacetime perturbation and matter displacement is considered. However the 5 equations that Thorne *et al* wrote down are linearly dependent. In 1985, Lindblom and Detweiler re-formulate the 5 equations to a set of 4 linearly independent ones [22]. (It is noted that they have another publication in 1983 [9], employing similar set of equations but different definition of variables, which is easily mixed up with the 1985 one.) The set of equations, usually referred to as LD

equation, is quoted as follow

$$
\begin{aligned}
H_1' &= -\frac{1}{r}\left[l+1+\frac{2Me^{\lambda}}{r}+4\pi r^2 e^{\lambda}(p-\rho)\right]H_1 \\
&\quad +\frac{1}{r}e^{\lambda}\left[H_0+K-16\pi(p+\rho)V\right] , \qquad (4.11)\\
K' &= \frac{1}{r}H_0+\frac{1}{2r}l(l+1)H_1-\left[\frac{l+1}{r}-\frac{\nu'}{2}\right]K-\frac{8\pi(p+\rho)e^{\lambda/2}}{r}W , \qquad (4.12)\\
W' &= -\frac{l+1}{r}W+re^{\lambda/2}\Big[\frac{e^{-\nu/2}}{(p+\rho)c_s^2}X-\frac{l(l+1)}{r^2}V+\frac{1}{2}H_0+K\Big] , \qquad (4.13)\\
X' &= -\frac{l}{r}X+(\rho+p)e^{\nu/2}\Big\{\frac{1}{2}(\frac{1}{r}-\frac{\nu'}{2})H_0 \\
&\quad +\frac{1}{2}\left[r\omega^2e^{-\nu}+\frac{l(l+1)}{2r}\right]H_1+\frac{1}{2}(\frac{3}{2}\nu'-\frac{1}{r})K-\frac{l(l+1)}{2r^2}\nu'V \\
&\quad -\frac{1}{r}\Big[4\pi(p+\rho)e^{\lambda/2}+\omega^2e^{\lambda/2-\nu}-\frac{1}{2}r^2\frac{d}{dr}(\frac{e^{-\lambda/2}\nu'}{r^2})\Big]W\Big\} , \qquad (4.14)
\end{aligned}
$$

where a prime denotes the derivative with respect to r. In the above equations, all capital letters represent expansion coefficients of perturbed quantities. H_0, H_1, K are coefficients of even parity metric tensor

$$
h_{\mu\nu} = -Y_{lm}e^{i\omega t}r^l\begin{pmatrix} e^{\nu}H_0 & i\omega r H_1 & 0 & 0 \\ i\omega r H_1 & e^{\lambda}H_0 & 0 & 0 \\ 0 & 0 & r^2K & 0 \\ 0 & 0 & 0 & r^2K\sin^2\theta \end{pmatrix} ; \qquad (4.15)
$$

W and V are related to Lagrangian displacement vector $\vec{\xi}$ of fluid as

$$
\begin{aligned}
\xi^r &= r^{l-1}e^{-\lambda/2}WY_{lm}e^{i\omega t} ; \qquad (4.16)\\
\xi^{\theta} &= -r^{l-2}V\partial_{\theta}Y_{lm}e^{i\omega t} ; \qquad (4.17)\\
\xi^{\phi} &= -r^{l}(rsin\theta)^{-2}V\partial_{\phi}Y_{lm}e^{i\omega t} ; \qquad (4.18)
\end{aligned}
$$

and X is the Lagrangian perturbation of pressure, related to other quantities by

$$
X=\omega^2(p+\rho)e^{-\nu/2}V-r^{-1}p'e^{(\nu-\lambda)/2}W+\frac{1}{2}(p+\rho)e^{\nu/2}H_0 . \qquad (4.19)
$$

My abbreviation on LD equation follow strictly their 1985 paper [22], except the γp in the original X' equation is replaced by $(\rho+p)c_s^2$ for better numerical convergence and further extension. c_s is the speed of sound at position r inside the star (defined in Eq. 3.11), which depends on dynamic EOS only. The subscript s conventionally denotes the oscillation is adiabatic (preservation of entropy per particle). If superconductivity does not present, it is good approximation even in the high temperature case.

Eq. 4.11-4.14 are differential equations of two metric perturbations, H_1, K, and two matter perturbations, W, X. In the original equations of Thorne *et al*, there is an additional equation regarding dynamics of H_0, but the equation is redundant because H_0 is an algebraic combination of other quantities

$$\begin{aligned} H_0 &= [3M+\frac{1}{2}(l+2)(l-1)r+4\pi r^3 p]^{-1}\times \\ &\quad \Big\{8\pi r^3 e^{-\nu/2}X-[\frac{1}{2}l(l+1)(M+4\pi r^3 p)-\omega^2 r^3 e^{-(\lambda+\nu)}]H_1+ \\ &\quad [\frac{1}{2}(l+2)(l-1)r-\omega^2 r^3 e^{-\nu}-r^{-1}e^{\lambda}(M+4\pi r^3 p)(3M-r4\pi r^3 p)]K\Big\}\ . \end{aligned} \tag{4.20}$$

LD equation is a system of 4-th order differential equations, 4 boundary conditions have to be specified for a unique solution. Two of them are required by the regularity at the stellar center,

$$\begin{aligned} X(0) &= (\rho_0+p_0)e^{\nu_0/2}\Big\{\Big[\frac{4\pi}{3}(\rho_0+3p_0)-\omega^2 e^{-\nu_0}/l\Big]W(0)+\frac{1}{2}K(0)\Big\}\ , \\ H_1(0) &= \frac{1}{l(l+1)}\{2lK(0)+16\pi(\rho_0+p_0)W(0)\}\ , \end{aligned} \tag{4.21}$$

and one condition presumes both pressure and its Lagrangian perturbation vanish at the star surface,

$$X(R)=0\ . \tag{4.22}$$

These three boundary conditions are the same in both source and sourceless situation, because they are imposed by the physical properties of a hydrostatic compact star.

4.3 Quasi-normal Mode

As mentioned before, GW QNM are frequencies at which spacetime perturbation propagate outward from a compact stellar object, thus it is expected GW observed on earth can be analyzed in terms of QNM. Gravitational radiation is driven by pulsation of compact stars, which the details of oscillation highly depend on matter distribution and local behavior of fluid elements. In other words, GW actually contains information about EOS and stellar profile, which is the incentive to investigate QNM spectrum.

As discussed in the previous section, three boundary conditions are imposed by physical requirement on LD equation. The forth one is imposed by definition of QNM, which requires that the surface value of LD variables produce a purely outgoing Zerilli function at spatial infinity. Lindblom and Detweiler connect LD variables and Zerilli function as [9]

$$\begin{pmatrix} 0 & 1 \\ a(r) & b(r) \end{pmatrix} \begin{pmatrix} H_0(r) \\ K(r) \end{pmatrix} = \begin{pmatrix} g(r) & 1 \\ h(r) & k(r) \end{pmatrix} \begin{pmatrix} Z(r) \\ dZ(r)/dr_* \end{pmatrix} \tag{4.23}$$

on the radius of the star, i.e. $r = R$. The coefficients are defined by

$$a(r) = -\frac{(\lambda r + 3m}{\omega^2 r^2 - (\lambda+1)m/r} , \tag{4.24}$$

$$b(r) = \frac{\lambda r(r-2m) - \omega^2 r^4 + m(r-3m)}{(r-2m)(\omega^2 r^2 - (\lambda+1)m/r)} , \tag{4.25}$$

$$g(r) = \frac{\lambda(\lambda+1)r^2 + 3\lambda m r + 6m^2}{r^2(\lambda r + 3m)} , \tag{4.26}$$

$$h(r) = \frac{-\lambda r^2 + 3\lambda m r + 3m^2}{(r-2m)(\lambda r + 3m)} , \tag{4.27}$$

$$k(r) = -\frac{r^2}{(r-2m)} . \tag{4.28}$$

In the quest of QNM frequencies, homogeneous Zerilli equation Eq. 4.9 is employed. Since the right hand side is zero, there is no restriction on the magnitude of perturbations, hence provides a freedom of normalization in addition to the four boundary conditions. This is an extra constraint to set up a Sturm-Liouville type problem for the QNM frequencies.

QNMs are characterized by nature of the restoring force and magnitudes of real and imaginary frequencies. To the best of our knowledge, there are 4 kinds of polar oscillations contributing to GW pulsation of a non-rotating star, denoted as the fundamental mode (f mode), the spacetime mode (w and wII mode), the gravity mode (g mode), and the pressure mode (p mode). Among which f, p, and g mode are relativistic analog of Newtonian normal mode of oscillation, these three modes are categorized as 'fluid mode'. On the other hand, w mode is a purely relativistic effect, it is hence coined as 'spacetime mode'. Since their physical origins are different, the distribution of each kind of mode reveal physics in different aspects. Characteristics of QNMs are introduced as below [37, 38]:

4.3.1 f mode

Regarding as the fundamental oscillation mode, f mode exists in all compact stars even if the star is incompressible. Just as the fundamental mode of a vibrating string, each star possess only one f mode, and the eigenfunction of f mode does not contain vibrating node inside the compact star. The maximum amplitude of oscillation locates at the stellar surface [37]. Although it is a fluid mode, f mode frequency is not sensitive to dynamic EOS. It mainly depends on the stellar mean density (M/R^3) [5]. This originates from a characteristic of f mode that the magnitude of pressure perturbation is far lower than metric and fluid motion [39]. Typical oscillation frequency is about $\sim 1-3$ kHz and damping time is same order as 0.1 s.

4.3.2 p mode

According to the best of our knowledge, pressure mode is the only fluid mode oscillating at frequency higher than that of f mode. In contrast to f mode, perturbation of pressure is significant among all quantities, because this kind

of oscillation is restored by pressure gradient [38]. Pressure mode is sensitive to dynamic EOS, as well as the properties of matter at low density region near the stellar surface. There is no limit on the number of p mode, the one with the lowest frequency is denoted as the 'first p mode'. Typical oscillation frequency of the first p mode is $\sim 4 - 8$ kHz, and its damping time is roughly 1 order longer than that of f mode.

4.3.3 g mode

The restoring force of g mode oscillation is the buoyancy of the fluid element. The magnitude of the buoyancy force can be accounted for by the Schwarzschild discriminant $S(r)$, defined as

$$S(r) = \frac{dp}{dr}\left(1 - \frac{c_s^2}{c_0^2}\right) \tag{4.29}$$

where $c_0^2 = dp/d\rho$ is the speed of sound determined by the static EOS. Stable g mode exists only if $S(r) > 0$ at some region inside the star, while unstable g mode exists if the Schwarzschild discriminant is negative somewhere. Stability of g mode is characterized by the sign of its imaginary part, such that stable g mode will damp as time but unstable g mode grows exponentially. It is noted that a star can exhibit both stable and unstable g mode, if there is a sign change of Schwarzschild discriminant.

Gravity mode can be induced by various mechanisms, including density discontinuity [11], temperature and chemical gradient [12], and other difference between dynamic and static EOS. However, g mode is absent for cold compact star if density profile is smooth, because pressure is a function of density only and the Schwarzschild discriminant vanishes everywhere. The frequency of g mode highly depends on its origin of induction. Typically, the real frequency of a g mode does not exceed 1 kHz, and the damping time is several orders longer than a minute. There is no limit on the number of g mode. Naming

starts from the highest frequency one, which is called the 'first g mode' or 'g-1 mode'.

4.3.4 w mode

To date, there are 3 types of spacetime mode discovered, which are the trapped mode, the interface mode, and the curvature mode [37]. The trapped mode is excited only by a star with very high compactness ration (i.e. $M/R > 1/3$) [38], such star is rare in reality and out of the range of stars we are going to consider. The curvature mode is usually referred to as w mode, and the interface mode is cited as wII mode. Both modes are characterized by relatively very short damping time, $\tau \sim \mu$s, which the damping rate is comparable to the oscillation frequency. There is no clear physical difference between wII and w mode, but wII is convenctionally classified as spacetime mode with larger imaginary part than the real part. Ordering of w(wII) mode starts from the one with lowest(highest) frequency. Typical real frequency of the first w mode is about $5 - 15$ kHz.

Chapter 5

Gravitational wave spectrum of hot compact stars

In this chapter, we aim to investigate how temperature affects gravitational wave frequencies. We compute QNM spectra of hot NS and QS, and use the result to simulate two physical scenarios. Firstly, we consider a situation which a compact star is observed. We want to see if information about its temperature can be obtained from the QNM. We compare compact stars with the same gravitational mass but different temperatures, in order to verify the thermal effect on GW signals. Secondly, we simulate the cooling of a compact star during evolution, by considering stars with the same total baryon number but different temperatures. Mode frequencies are computed to estimate qualitative change of signals due to heat loss. In addition, effect of phase transition is examined by comparing QNM frequencies of QS and NS with the same baryon number.

5.1 Numerical results

It is shown on Chapter 3 that the properties of nuclear matter are determined by thermodynamic variables as well as a set of physical constraints. In this section, we presume charge neutrality is always required, and beta equilibrium

is imposed on the background by assuming the star is in quasi-equilibrium. Temperature profile is another information to specify a stellar profile, but there is no consensus on its detail to date. Because our main consideration in this chapter is the thermal effect, we impose the simplest but non-trivial temperature profile: the star is assumed to be relativistic isothermal, i.e.

$$T(r) = T_0 e^{-\nu(r)/2} \ , \tag{5.1}$$

where T_0 is a free parameter to be fixed by either surface or central temperature. The above expression is a constant temperature profile with an additional redshift factor, therefore the parameter T_0 can also be viewed as redshifted temperature observed at spatial infinity.

Using the methods described in previous chapters, we compute the both real and imaginary part of f mode and w mode, and the real part of g mode. We decide not to present the damping time of g mode because it is very long ($\gtrsim$ 100s for NS; $\gtrsim$ a day for QS) that the oscillation is believed to be damped by other dissipation mechanism (e.g. viscous) other than the intrinsic energy loss in QNM [12], hence the imaginary part possesses little physical significance. In addition, the surface behavior of hot NS is not well understood, we do not consider p mode whose frequency highly depends on properties of matter in the low density region.

5.1.1 Temperature effect on QNM

We choose 0.5 MeV as the lowest surface temperature because the behavior of QNM would not alter much for even lower. The highest surface temperature is set at 5 MeV because it is roughly the highest surface temperature value in various proto-neutron star simulations [29]. Another reason is that the pressure of electron becomes large for $T > 5$ MeV, it will leave a thick atmosphere ($\sim$ 100 km) composed of low density matter (6 order smaller than than central temperature, but non-vanishing due to thermal pressure), which its existence

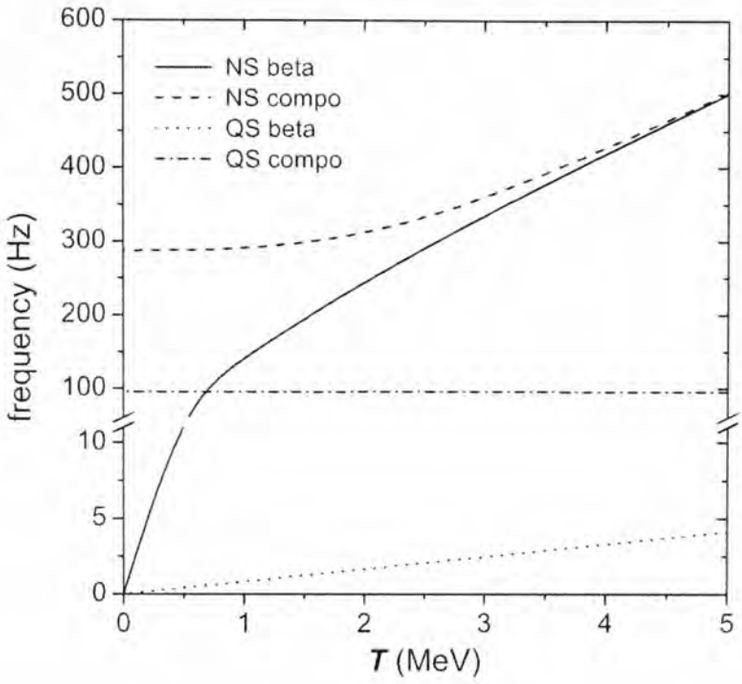

Figure 5.1: Gravity mode frequencies of NS and QS with the same mass ($M = 1.4\ \mathrm{M}_{\odot}$) at different temperatures. The lines noted as 'beta' and 'compo' show trend of β mode and Y_p mode respectively.

is doubtful in reality. For simplicity, we assume the QS are 'bare', i.e. there is no ordinary nuclear matter layer enclosing the QS, as the nuclear matter are evaporated at such a high temperature [18].

We first compute mode frequencies of NS and QS with the same gravitational mass ($M = 1.0,\ 1.4\ \mathrm{M}_{\odot}$) to account for effect of surface temperature. As shown in Fig.s 5.1 and 5.2, g mode frequency of NS decreases remarkably as temperature drops, and the behaviors differ significantly under two different dynamic EOS: (i) beta equilibrium is maintained and (ii) chemical composition is preserved. For convenience, we define the g mode oscillates under beta equilibrium (preserved chemical composition) as 'β mode (Y_p mode)'. At temperature $T \gtrsim 3$ MeV, both kinds of g mode roughly follow the same trend as frequencies decreases from $f \approx 500$ Hz at temperature $T \approx 5$ MeV. The β mode follows the same trend until $T \approx 1$ MeV and then decreases drastically

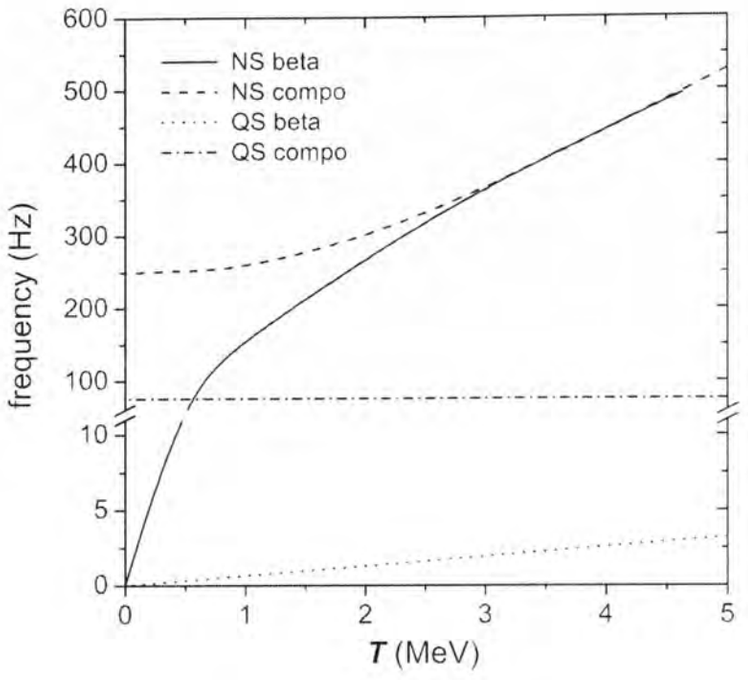

Figure 5.2: Same as Fig. 5.1 for NS and QS with mass $M = 1.0\ \mathrm{M}_{\odot}$.

to zero, while Y_p mode converges to a finite value at $T = 0$ MeV. This phenomena suggests that temperature gradient is a major source of buoyancy in NS at high temperature, but chemical gradient dominates at low temperature.

Behavior of g mode of QS is different from NS. For β mode, frequency lies at 1 Hz range and increases linearly with temperature. However, Y_p mode is about 100 Hz and nearly stays unchanged with temperature. From this observation, we believe adiabatic effect is not the dominant mechanism of g mode oscillation for QS in the temperature range $T \lesssim 5$ MeV.

Next, we compare g mode of stars composed of different matter. At high temperature, β mode frequency of QS is about 5 Hz, which is two order smaller than that of NS oscillates at 500 Hz. For Y_p mode, its frequency is about 100 Hz for QS, which is about one-third of the NS Y_p mode. Although the dynamic EOS of nuclear matter and quark matter in high density region is more complicated in reality than our current consideration, our calculations provide some evidence to support the analysis of Fu *et al.* [19], who suggest that g mode of hot QS is roughly 1 order less than that of hot NS. The deviation

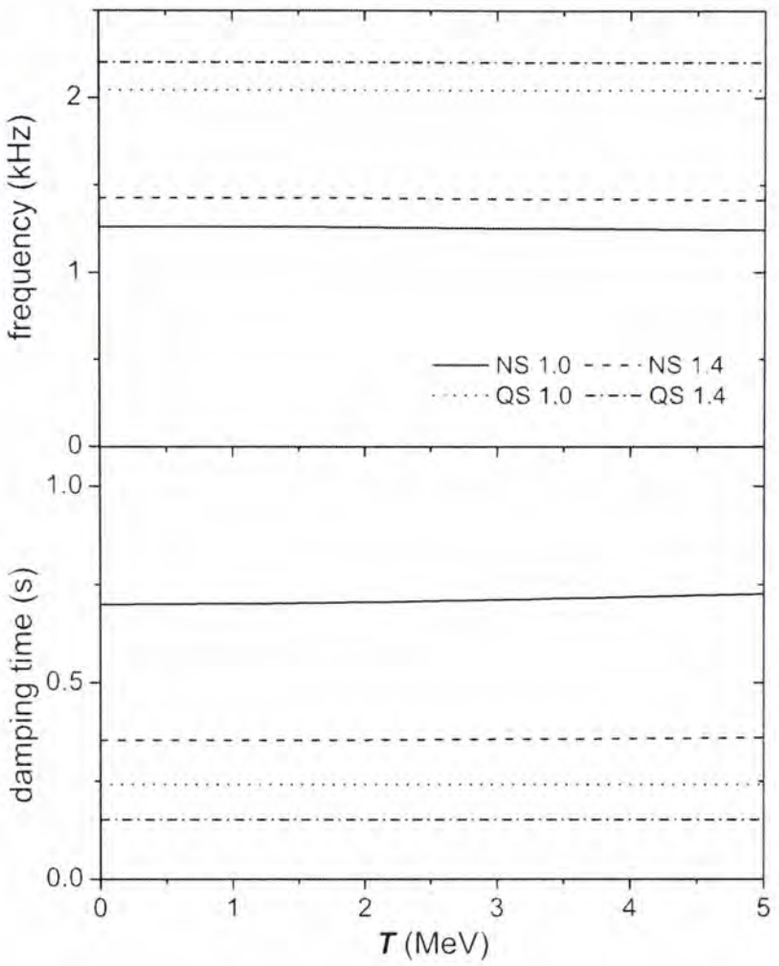

Figure 5.3: Fundamental mode frequencies of NS and QS with mass $M = 1.0, 1.4\ \mathrm{M}_{\odot}$ at different temperatures. Effect of dynamic EOS is not shown as the difference in mode frequencies is not noticeable, so we only show results of oscillation following beta equilibrium.

is however reduced when temperature drops. At temperature $T \lesssim 1$ MeV, beta decay timescale is far longer than period of g mode [40], composition is hence believed to be preserved for both stars. g mode frequency for NS is around 300 Hz, only 2-3 times larger than that of QS which is about 100 Hz. Our results suggest that the temperature of compact star is high, at where g mode excitation is facilitated [41], the distinction between g mode of QS and NS is large, hence QS and NS could be distinguished by the signal.

In the contrary to the significant effects of temperature on g mode, either oscillation frequency or damping time of f mode is nearly unchanged with temperature for both NS and QS, as demonstrated in Fig.s 5.3 and 5.4. Real

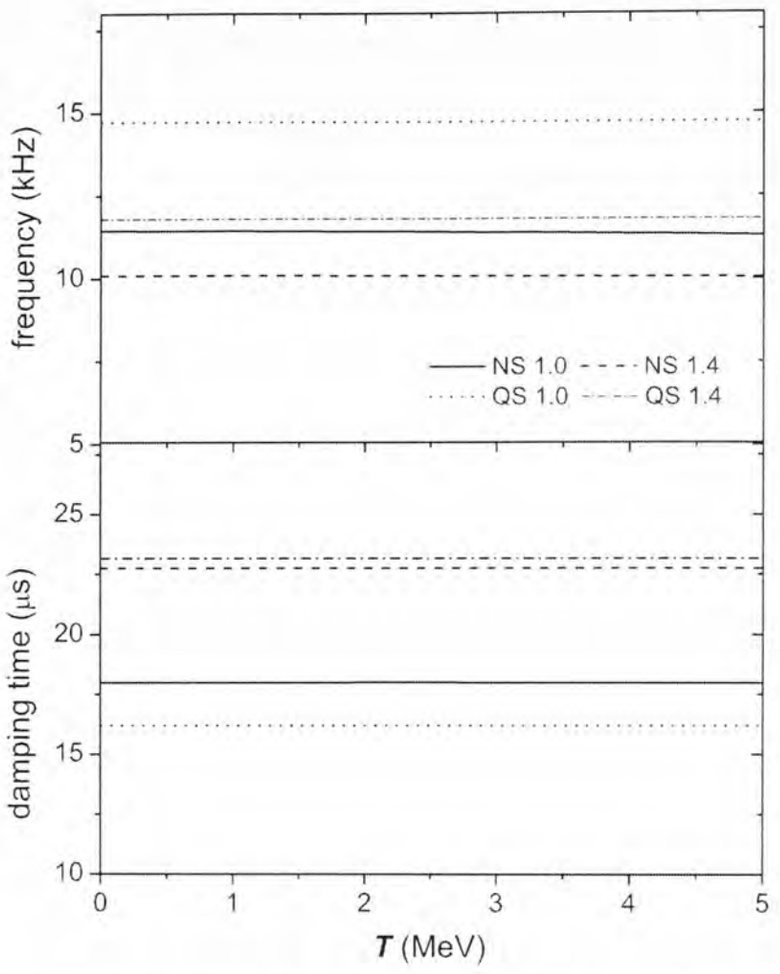

Figure 5.4: Same as Fig. 5.3 for w mode. Effect of dynamic EOS is not shown as the difference in mode frequencies is not noticeable, so we only show results of oscillation following beta equilibrium.

frequency of f mode of NS with 5 MeV temperature is only 1% less than the zero temperature NS, while the corresponding change of a QS is less than 0.1%. The imaginary part of f mode is slightly more sensitive to temperature than the real part. The f mode of the hottest NS damps 4% faster than its zero temperature counterpart, but the damping time of a QS is as robust as its real frequency.

Behavior of w mode is similar to that of f mode. The real part changes for less than 2% from the hottest to the coolest NS. The real part of QS and the imaginary part of both stars are insensitive to temperature, their changes are less than 0.1%.

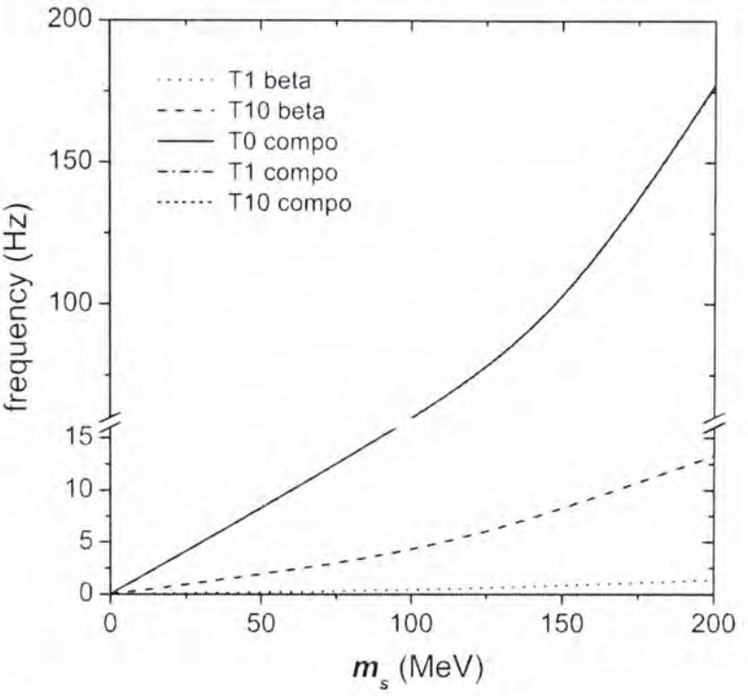

Figure 5.5: Effect of strange quark mass (m_s) in MIT bag model on g mode frequencies of a QS with mass $M = 1.4$ $M_\odot$. Temperature effect is also added into EOS, with $T = 0,\ 1,\ 10$ MeV (shown as T0, T1, T10 respectively). It is noted β mode frequency is exactly zero when $T = 0$.

We also checked how dynamic EOS would change f mode and w mode, but the difference is so small ($\lesssim 0.01\%$) to be shown in Fig. 5.3 and 5.4.

5.1.2 Temperature effect and QS model

We observe from the previous subsection that QNM frequencies of QS are nearly inert to temperature except the β mode. It is curious to see if this robustness depends on the quark matter model employed, so we consider different quark matter EOS by tuning the strange quark mass m_s in the MIT bag model. We consider m_s ranges from 0 to 200 MeV, which covers most values proposed by different theoretical calculations. We consider QS with temperature ranging from 0 to 10 MeV.

Our calculated values of g mode, f mode and w mode of QS are plotted in Fig.s 5.5, 5.6 and 5.7 respectively. For the Y_p mode, f mode, and w mode,

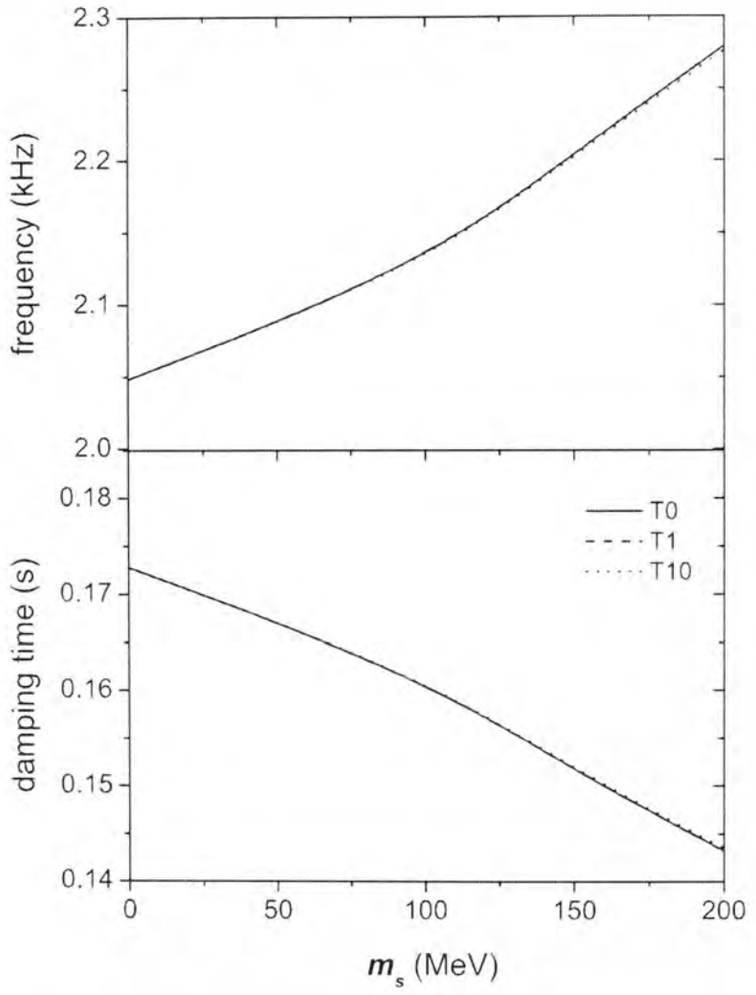

Figure 5.6: Effect of strange quark mass (m_s) in MIT bag model on f mode frequencies of a QS with mass $M = 1.4$ $M_\odot$. Temperature effect is also added into EOS, for $T = 0,\ 1,\ 10$ MeV (shown as T0, T1, T10 respectively). Only results following composition preservation is shown as the effect of dynamic EOS is insignificant.

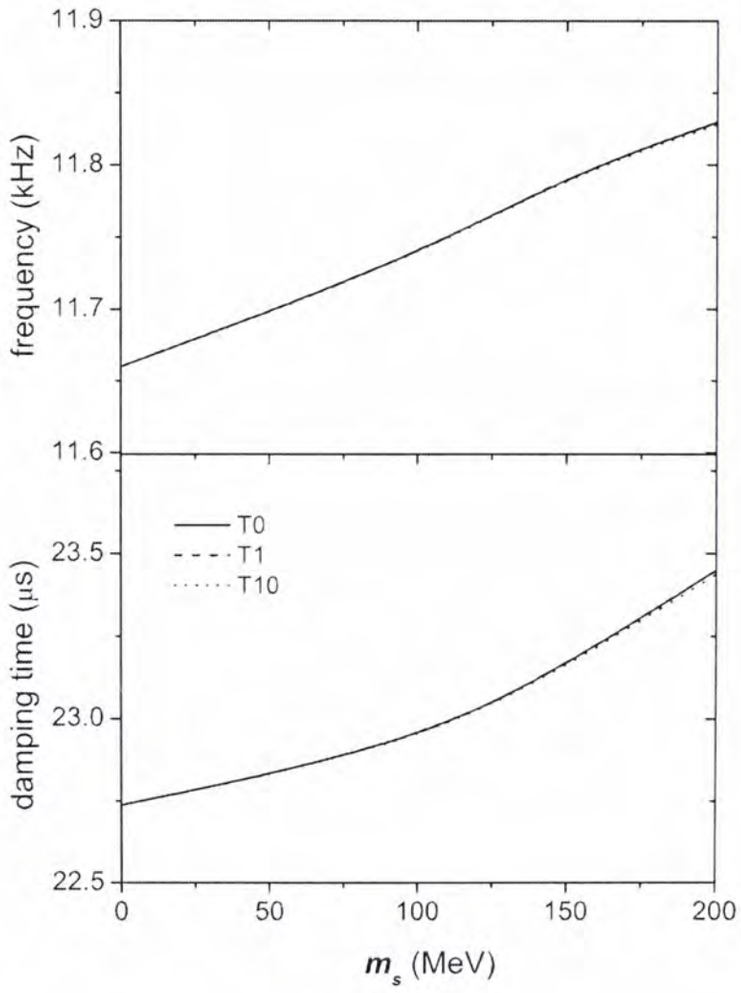

Figure 5.7: Same as Fig 5.6 for w mode.

temperature effect is nearly invisible regardless of value of m_s. These mode frequencies are inert to temperature for $m_s = 0$, and most deviated at $m_s = 200$ MeV for not more than 0.2%. Absence of temperature effect at $m_s = 0$ is not too surprising, because the MIT bag model can be exactly written as

$$\rho = 3p + 4B \ , \tag{5.2}$$

in zero quark mass limit. Therefore the magnitude of temperature does not alter the $p - \rho$ relationship, thus the stellar structure does not change. Furthermore, Eq. 5.2 leads to an exactly zero Schwarzschild discriminant, hence there is no restoring force for the g mode oscillation.

As seen from results in the last subsection, temperature effect only emerges in β mode. This phenomenon is observed for any non-zero m_s, but the deviation is greater for larger strange quark mass. For both kinds of g mode, frequencies rise as m_s, which agrees with the argument of Fu *et al.* that g mode of QS is induced by non-zero strange quark mass [19].

5.1.3 QNM shift due to phase transition

In this subsection, we consider mode frequencies shift of a compact star during the cooling process. Compact stars with constant baryon mass (i.e. baryon number $\times$ a.m.u.) but different surface temperature are considered. The total baryon number N_{baryon} of a star is calculated by [16]

$$N_{\text{baryon}} = \int_0^R \left(1 - \frac{2M}{R}\right)^{-1/2} r^2 n_{\text{baryon}} dr \ , \tag{5.3}$$

where the baryon number density n_{baryon} is: the sum of number density of proton and neutron in NS; $\frac{1}{3}$ of the total number density of the three species (u, d, s) of quarks in QS. This scenario is constructed in attempt to simulate cooling of proto-NS after vigorous evolution in the first minute. The change of stellar structure becomes steady; the evolution time scale is about 10 s which

is well longer than GW pulsation timescale [29]. We again assume the stars are relativistic isothermal within the whole period.

In addition, it is widely anticipated that nuclear matter would phase-transit to become strange quark matter under extraordinary high density and temperature, which is expected to happen near the core region of NS (c.f. [14, 15]). On the other hand, the remnant of supernova explosion exists as a hot proto-neutron star with high density and high temperature. There seems no reason to rule out that a hot remnant can be a pure QS. During the cooling of a proto-neutron star, temperature would eventually drops below a critical value T_p, quark matter will undergo phase transition such that QS would transform to a NS [18]. While the exact value of T_p is still unknown to date, it is commonly perceived that transition will happen at temperature higher than 1 MeV. Here we pick $T_p = 2$ MeV, and we assume the temperature profile of NS is same as that of QS before the transition. Since we want to investigate the order of magnitude of mode frequencies shifted by the change, choice of configuration would not qualitatively affect the conclusion of our investigation.

As shown in Fig. 5.8, g mode frequency of NS significantly reduces during cooling. For $T \gtrsim 3$ MeV, both β mode and Y_p mode frequency decrease with a similar trend. Dependence on the dynamic EOS enlarges for further cooling. Y_p mode frequency will converge to a finite value, while β mode frequency decreases continuously to zero. Fu *et al.* suggested that the restoration timescale of beta equilibrium is considerably longer than g mode pulsation period at temperature $T \lesssim 2$ MeV [40], therefore we believe that the actual variation of g mode frequency is better described by 'NS compo' curve in Fig. 5.8.

Gravity mode oscillation of QS highly depends on the dynamic EOS within the whole range of temperature. The Y_p mode of QS is only 0.3% smaller after the cooling, but β mode decreases linearly with temperature. If phase transition happens, mode frequency will increase for 2 order from 1 Hz range to about 300 Hz in the most abrupt case, which the g mode is β mode of QS

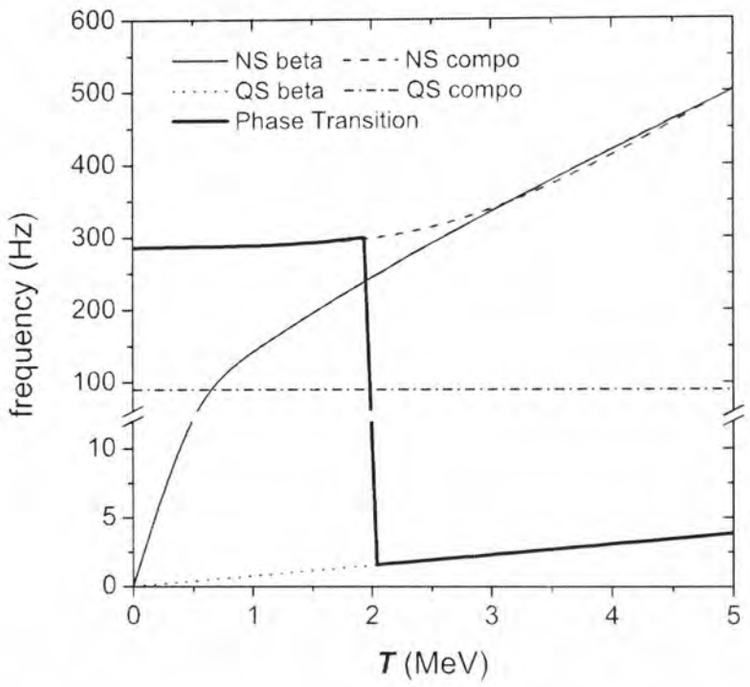

Figure 5.8: Gravity mode frequencies of cooling compact stars with the same baryon number $N_{\rm baryon} = 1.8 \times 10^{57}$ (baryon mass $M_{\rm baryon} \approx 1.5\ {\rm M}_{\odot}$). Abbreviation 'compo' and 'beta' denotes β mode and Y_p mode respectively. Thickened line shows a possible variation of frequencies during cooling. We assume the phase transition from beta equilibrium state of QS to composition preservation state of NS happens at $T = 2$ MeV.

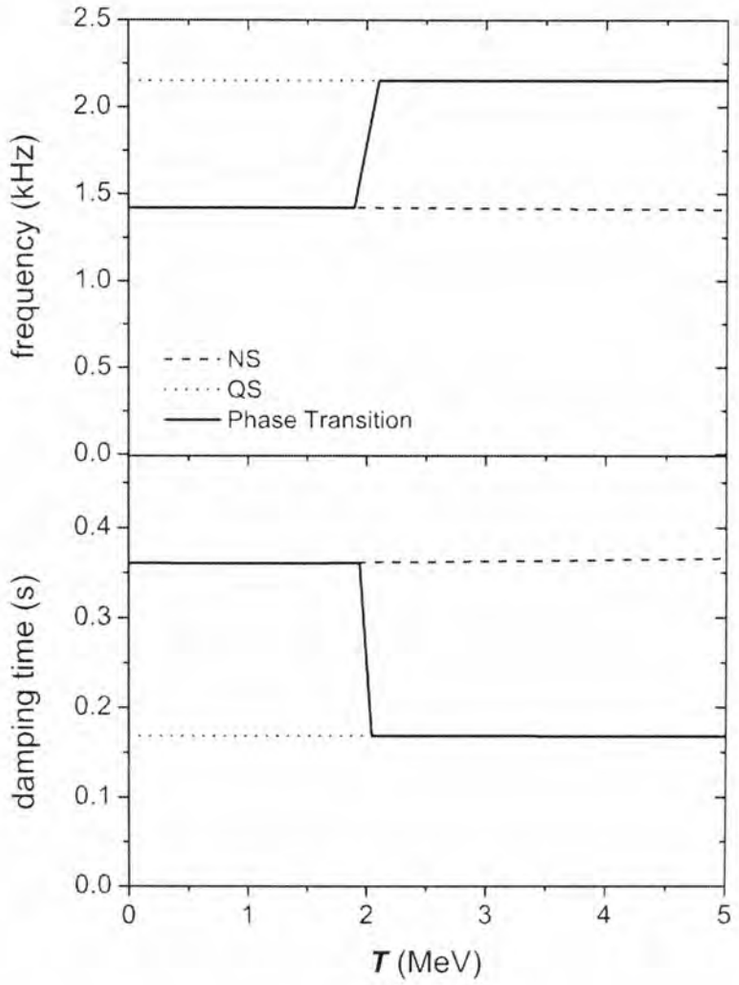

Figure 5.9: f mode of cooling compact stars with the same baryon number $N_{\text{baryon}} = 1.8 \times 10^{57}$ (baryon mass $M_{\text{baryon}} \approx 1.5\ \text{M}_{\odot}$). Thickened line shows a possible variation of frequencies during cooling. We assume the phase transition from QS to NS happens at $T = 2$ MeV. Only results following composition preservation is shown as the effect of dynamic EOS is insignificant.

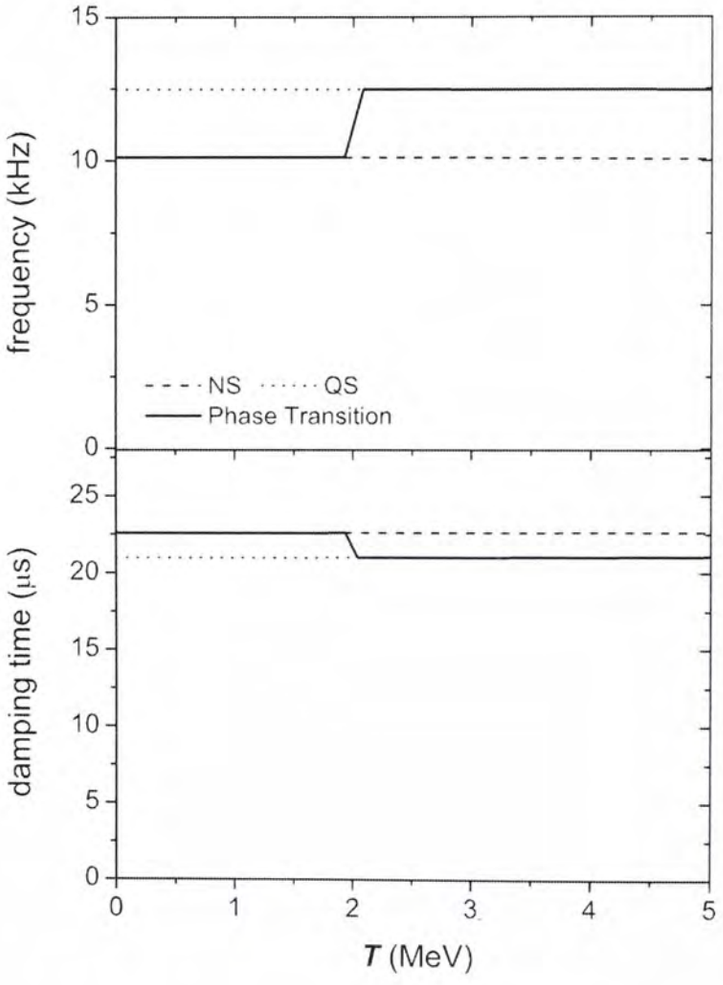

Figure 5.10: Same as Fig. 5.9 for w mode.

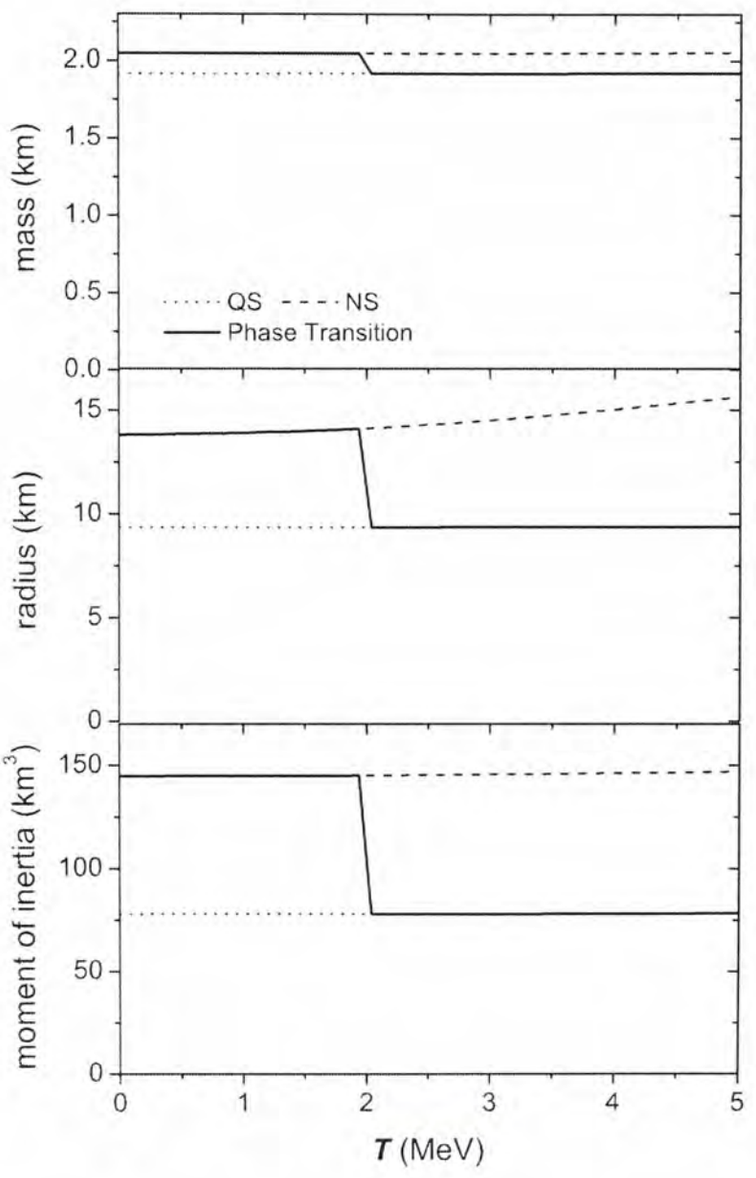

Figure 5.11: Change of mass, radius, and the moment of inertia of cooling compact stars with the same baryon number $N_{\rm baryon} = 1.8 \times 10^{57}$ (baryon mass $M_{\rm baryon} \approx 1.5$ $M_\odot$). Thickened line shows a possible variation of quantities during cooling. We assume the phase transition from QS to NS happens at $T = 2$ MeV.

before, but Y_p mode of NS after the transition. The change is less drastic if composition is preserved in both stars, but g mode still increase 3 times. It is noted the mode frequencies can also shift if dynamic EOS changes due to temperature difference or other physical phenomena, detailed mechanism is however too complicated which is outside scope of this thesis.

Changes in f and w modes are in general less dramatic than g mode, as demonstrated in Fig.s 5.9 and 5.10. If there is no phase transition, f mode and w mode of QS are shifted for not more than 0.5%. For NS, imaginary part of f mode is increased by 1.4% after the cooling, while other frequencies are changed for less than 1%. Phase transition causes a drop of f mode frequency for 30%, and doubles the damping time. For w mode, the real frequency is reduced by 20% and the damping time is increased by 10%.

In short, cooling effect is the most significant on g mode frequencies, whereas f mode and w mode are not much affected. As shown in Fig. 5.11, less than 0.3% of the gravitational mass is lost during cooling process, because the contribution of thermal energy is far less than the rest mass and kinetic energy of particles. It is hence difficult to perceive that variation of QNM spectrum actually corresponds to results obtained in Subsection 5.1.1. For the shift due to phase transition, the most obvious explanation is that stellar structure of NS is fundamentally different from that of QS. We also compare the percentage difference of QNM and geometric parameter of the compact stars. From Fig. 5.11, the total gravitational mass is increased by 5% after transition. This change is small because the baryon mass of both stars are the same, thus the change of gravitational mass is merely attribute of gravitational energy during structural modification. The radius is enlarged by 50% during the transition and drops for 3% as a NS cools from 2 MeV to zero temperature, and the moment of inertia is roughly doubled by the phase transition. The general trend of quantities M, R, I are steady if there is no change in EOS,

while drastic change only happens at phase transition. This pattern looks similar to the case of f mode and w mode, it suggests that the spectra of these two QNM are closely related to stellar structure instead of properties of nuclear matter, in the contrary to gravity mode which the frequency is very sensitive to temperature and the dynamic EOS.

5.2 Summary and prospective

In this chapter, temperature effect on QNM spectrum of finite temperature compact stars is investigated. We found g mode frequency of NS decreases as the star cools, but the actual behavior highly depends on the dynamic EOS. For Y_p mode of NS, its frequency decreases with temperature and eventually converges to a finite value, while β mode frequency reduces to zero. On the other hand, Y_p mode frequency of QS is rarely affected by temperature, but the β mode frequency varies linearly with temperature and it is about 1 order lower than Y_p mode frequency. However, f mode and w mode of both NS and QS are nearly insensitive to temperature.

We argue that the robustness of the f and w modes is related to the persistence of stellar structure against thermal change. This claim agrees with the investigation that both f and w modes follow universal trends on the mean density and compactness of compact stars, which the trend is EOS independent [5]. However, conventional universality are inadequate to account for the stability of QNM against temperature change due to two reasons. Firstly, current proposal of universality is obtained without considering bare quark stars. Secondly, those universal trends are not very accurate even in the zero temperature case. Aiming to reduce these shortcomings, we provide an alternative proposal of QNM universality in Chapter 6.

On the other hand, understanding the sensitivity of g mode requires detailed analysis on EOS. Analyzing nuclear matter is however mathematically

hopeless due to the complicated nature of Shen EOS. Nevertheless, quark matter EOS is computed by analytical expression of thermodynamic variables. Therefore, we will examine the relationship between quark matter EOS and g mode frequency in Chapter 7, in order to investigate the pulsation mechanism of g mode.

According to our results, cooling of compact stars with fixed EOS can only be revealed by the g mode signals. Phase transition is however believed to happen if the temperature drops below the critical temperature between nuclear and quark matter phase. Such conversion abruptly shifts all QNM frequencies, which g mode oscillation can be two order faster, f and w modes are changed for more than 10%. Although sudden jump of GW mode frequency seems to be a plausible signal of phase transition, recognizing such phenomena involves further consideration of the detectability of each QNM. Kokkotas *et al.* calculated the amount of threshold energies contained in QNM to be identified by current and future gravitational wave detectors [42]. According to their results, the minimum detectable energy of a w mode is enormous ($\sim 0.1\ M_{\odot}c^2$), due to its extremely short damping time, and hence the role of w mode is unimportant in practice. Detection of f mode is the most likely, the oscillation frequency can be accurately extracted even if only $10^{-5}\ M_{\odot}c^2$ is contained in the mode. Though they did not provide detectability of g mode, it is generally believed that QNM is more readily recognized if the energy content is higher. We want to estimate how much energy can be channeled into GW in common astronomical events, we consider the asymmetric accretion of a shell onto compact star as a sample GW excitation mechanism in Chapter 8.

Chapter 6

Universality of fundamental mode and spacetime mode

In the previous chapter, we showed that f and w modes are insensitive to temperature variation. This result agrees with common belief that frequencies of these modes are mainly determined by the geometric parameters of a star, which the parameters do not vary much as shown in Fig. 5.11. However, although the proposed universal curves fairly demonstrate QNM distribution of ordinary NS, they fail to describe results of QS. Furthermore, we found that the radius of a hot neutron star is reduced by 10% during cooling, which is much greater than the corresponding changes in mode frequencies. Meanwhile, the moment of inertia, another geometric factor of compact star, varies less than 2%. This simple comparison suggests that the moment of inertia is more appropriate to describe the universal trends of f mode and w mode spectra. This encourages us to construct a new of universality base on the moment of inertia.

6.1 Review

Since the highest pressure and density in the world are found inside compact stars, it is a hot research field of extracting useful data about nuclear physics

from astronomical observations. Since we do not know the details of the nuclear matter, astrophysicists usually employ results obtained by nuclear physicists to construct stars for comparison. One of the works was conducted by Lattimer and Prakash [43], who compared structure of compact stars constructed by nuclear EOS best at their time. In their paper, they demonstrated empirical relationships between EOS and some geometrical parameters, such as mass, radius, the moment of inertia, as well as some structural characteristics, such as matter distribution and central density. Their results can be applied to identify a compact star if it is observed with certain attributes. Lattimer and Schutz [1] further investigated the correspondence between EOS and the moment of inertia, in which they found a universality describing most of the numerical results. The universality of the moment of inertia provides bounds of choices of EOS, hence probes the composition of the compact star.

On the other hand, several GW detectors (VIRGO, LIGO, LISA, etc) are expected to conduct meaningful scientific run within 20 years, theoretical works are concurrently done to infer useful information from GW signals. One of which is the survey conducted by Andersson and Kokkotas [5]. They construct hydrostatic stars with a collection of EOS and subject the stars to oscillate. QNM are tabulated against geometric parameters of the stars. From their data, they found that f mode exhibits simple relationship with mean density of the stars, while the w mode show approximately universal dependence on the compactness ratio (M/R). If GW is detected, the mass and radius can hence be inferred by the frequency spectrum and universalities [5].

Although the generic universality of GW QNM is proposed according to certain physical argument, the fitting actually permits a wide range of error. The deviation from universality is the consequence of the difference in EOS and hence the internal structure. Kokkotas *et al.* [42] suggest that the individuality can be employed to distinguish stars with different EOS and obtain information of nuclear physics as a consequence.

Consider there are geometric parameters other than M and R, we instead want to ask if the individuality indeed represents a genuine difference of a stellar structure, or it is merely an artifact induced by wrong choice of independent variables? Undoubtedly, different EOS form stars with significantly different matter profile, and we do expect this difference would contribute to individual behavior. But different structural parameters describe geometry in different contexts. For example, mass M measures the overall disturbance to the spacetime; radius R briefly describes the volume of a compact object in space; compactness ratio M/R is related to the degree of spacetime curvature; and the moment of inertia, from its classical definition, is a weighted integration of mass with distance from origin, in other words, a measurement of distribution of matter. In case we changed the variable of universality and get a better or worse universality, we can get more insight into the geometric dependence of pulsation dynamics, conversely we can gain more information if GW signal is detected.

In this chapter, we propose to replace the role of radius R with the moment of inertia I as an independent variable in universality. The outline of this chapter is as follows: we first review the technical procedure in computing moment of inertia, and then reproduce the generic proposals of universality on compactness M/R. In the next section, we present our new universality of mode frequencies as a function of the moment of inertia. More explicitly, we replace the dimensionless compactness ratio M/R by the quantity $\sqrt{M^3/I}$. For most of the QNM we calculated, our new formulae show significant improvement in accuracy. In Section 6.4, we give conjectures on the accuracy of our proposal. By extending argument of the importance of Tolman VII (TVII) model on generic universality, to a more general and physical model of polytropic EOS, we are able to empirically understand the improved fitness by considering stars of various stiffness. After obtained a set of more precise universal formulae, in Section 6.5 we give a practical example to apply our findings, which is to

infer mass, radius, and the moment of inertia if gravitational wave signal is detected. Our extraction method does not only give more precise values, but it is also applicable to QS, which is excluded in previous schemes. We summarize this chapter at Section 6.6 with a brief discussion.

6.2 Generic proposal of universalities

Obviously, universality represents similar behavior of physical phenomena for objects with different fundamental attributes. In the branch of compact star astrophysics, stars can be characterized by the properties of composition, which is described by the EOS. Nuclear matter EOS are obtained through various theoretical models or empirical findings in earth laboratory, which may display greatly different behaviors. The deviation is conventionally described by the stiffness, or effective adiabatic index γ in analogy to the classical polytropic model

$$p = k\rho^{\gamma} \ . \tag{6.1}$$

In spite of the deviation, magnitude of pressure and energy density of nuclear matter EOS are roughly the same order.

Assuming that the compact stars are hydrostatic, their structure follows the TOV equation. Since the stars obey the same structural equation and magnitude of EOS are about the same, it is not so surprising that matter profile are similar for most compact stars up to some normalization. Therefore, we expect properties which are sensitive to the matter profile, such as f mode, w mode [3], and the moment of inertia, would follow similar pattern among EOSs. It is our crudest interpretation of universality found in compact stars.

6.2.1 Moment of Inertia

In the scope of astronomical observation, mass is relatively easier and more precisely obtained, through, for example, measuring orbiting period of companion. However, methods for estimating stellar radii are not always accurate and feasible. A typical way is to measure the redshift effect of the radiation emitted. It is practical if the emission spectrum contains notable features, but it is not always the case. Furthermore, ambiguities due to, e.g. atmospheric conditions and interstellar absorptions, also increase the difficulties for precise radius determination [1].

Instead of relying on the detection of radiation, Bejger and Haensel propose the moment of inertia can be applied to fix the physical parameters of the Crab pulsar [2]. Lattimer *et al.* also suggest that the moment of inertia can provide useful bounds on the values of radius and other properties of compact stars [1]. According to their paper, the moment of inertia can be determined by measuring the precession of the angular momentum if the compact star belongs to a binary system. Since rotation of a compact star is closely related to X-ray emission, precession will lead to a periodic shift of radiating direction. Moreover, spin angular momentum is coupled to the orbital angular momentum of the system, precession hence changes inclination of orbital plane.

Theoretical investigation of the moment of inertia I starts from the slowly rotating model of hydrostatic stars [16]. For stars rotating rigidly with uniform angular velocity Ω, I is calculated by

$$I = \frac{8\pi}{3}\int_0^R r^4(\rho + p)e^{-(\nu+\lambda)/2}(\bar{\omega}(r)/\Omega)dr \ , \tag{6.2}$$

where $\bar{\omega}(r)$ is a rotational parameter satisfying

$$\frac{1}{r^4}\frac{d}{dr}\left(r^4 e^{-(\nu+\lambda)/2}\frac{d\bar{\omega}(r)}{dr}\right) + \frac{4}{r}\bar{\omega}(r)\frac{d}{dr}e^{-(\nu+\lambda)/2} = 0 \tag{6.3}$$

with boundary condition $\bar{\omega}(R) = \Omega(1 - 2I/R^3)$. Procedures of computing the moment of inertia is presented in Appendix D.

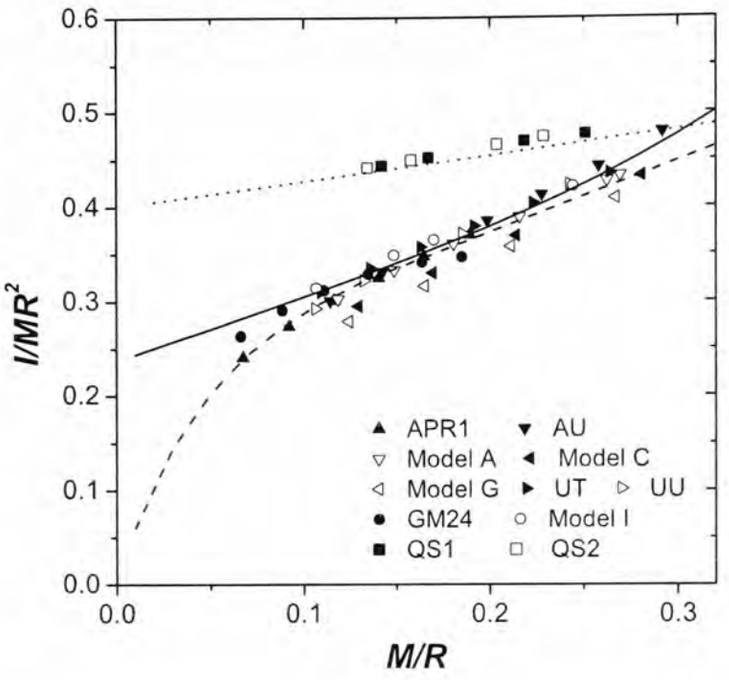

Figure 6.1: Specific moment of inertia (I/MR^2) is plotted against the compactness ratio (M/R) for various types of compact stars, resembling Fig.2 in [1] and Fig.1 in [2]. Solid and dashed lines are universality suggested by Lattimer *et al.* [1] and Haensel *et al.* [2] respectively. The triangles and dots denote NS constructed by ordinary EOS, following notations in [3]. Squares represent QS with different bag constant and temperature, which both lie on the universality for QS suggested by Haensel *et al.* [2], presented as dotted line in the figure.

Lattimer *et al.* constructed hydrostatic stars by standard ordinary EOS, and calculated their moment of inertia within the slowly rotating limit [1]. When plotting the specific moment of inertia I/MR^2 against the compactness ratio, there appear to be a unified relationship between the two quantities. We reproduce their plot as Fig. 6.1.

In the figure, we show results of compact stars constructed by the following EOS:

1. ten ordinary matter EOS (Model A, Model C, Model G, Model I, APR 1, APR 2, AU, UU, UT, GM24, our notation follows [3]), which cover a

wide range of stiffness ($\gamma \sim 1.6 - 4$ in dense region);

2. two QS models QS1 and QS2 are finite temperature MIT bag models with non-zero strange quark mass (c.f. Chapter 3). Characteristic parameters of QS1 (QS2) are bag constant $B^{1/4} = 154.5$ MeV (150 MeV), strange quark mass $m_s = 150$ MeV (100 MeV), and temperature $T = 0$ MeV (10 MeV).

We also present three curves of universality between the specific moment of inertia and the compactness. Bejger and Haensel [2] first explicitly write down a formula for the empirical universal dependence, after analyzing data from 30 realistic EOS and exploring numerous combination of M and R. They conclude that the relationship between specific moment of inertia and compactness of ordinary stars can be well approximated by

$$\tilde{I} \simeq \begin{cases} x/(0.1+2x) & \text{if } x < 0.1 \ , \\ \frac{2}{9}(1+5x) & \text{if } x > 0.1 \ , \end{cases} \tag{6.4}$$

where $\tilde{I} = I/MR^2$ and $x = 0.677M/R$. They also fit another dedicated line for results of QS,

$$\tilde{I} = \frac{2}{5}(1+x) \ , \tag{6.5}$$

which deviates significantly from the curve of NS due to the considerable difference in their density profiles. These curves well demonstrate the universal behavior, particularly for the stars with low compactness ratio ($M/R \lesssim 0.25$). Lattimer and Schutz modified the fitting to provide better description on ordinary stars with higher compactness [1],

$$\tilde{I} \simeq 0.237(1 + 4.2x + 90x^4) \ . \tag{6.6}$$

The compact stars we generate have mass $M \sim 1 - 2\ M_\odot$, corresponding to stars with middle to high compactness ratio $M/R \sim 0.05 - 0.3$. Within this range, the universality of both authors lie between our data points in Fig. 6.1 with a mild range of error.

In fact, the fitness is sensitive to radius R, which consists of ambiguities in both numerical and physical aspects. Conventional definition of radius follows the fact that pressure is zero at stellar surface (c.f. Eq. 2.12). However, vanishing pressure will cause instability during numerical calculation, various treatments are employed to deal with the low density region, such as truncating the integration at a very small pressure p_b, and fitting the density profile with that of polytropic model. The difference in definition imposes technical uncertainty on value of radius. In physical sense, solid crust may exist near the surface of compact stars, it violates the assumption of hydrostatic star of the TOV equation. Therefore, the physics of stellar surface is beyond our understanding based on current ordinary EOS proposals, hence reduce the significance of using radius R as an independent variable to represent universality. In addition, we found that pressure of thermal electron would extend the low density region deep into space and hence radius is very sensitive to low density treatment, whereas value of moment of inertia converges. As a result, it deserves a trial to replace R with appropriate combination of M and I.

6.2.2 Gravitational wave spectrum

Similar to a vibrating string on a violin, a compact star oscillates at QNM frequencies, as described in Section 4.3. Universality is proposed in attempt to connect QNMs with certain combinations of mass and radius, but it does not work properly for g mode and p mode. It is because g mode and p mode are driven by adiabatic density gradient and pressure gradient respectively, which are sensitive to local properties of matter. On the other hand, f mode and spacetime modes are mainly determined by matter distribution, their spectra are expected to be independent of EOS.

Gravitational wave spectra of isolated neutron stars are studied extensively by Andersson and Kokkotas [5]. They analyzed f mode, w mode and p mode

QNM	frequency	a	b	c
f mode	real	0.15	0.56	-0.020
f mode	imaginary	-5.8 $\times 10^{-4}$	6.7 $\times 10^{-4}$	-6.2 $\times 10^{-5}$
w mode	real	-8.2	3.9	0.055
w mode	imaginary	-10	3.3	0.043
w-II mode	real	2.3	1.2	-0.033
w-II mode	imaginary	-3.6	2.0	0.092

Table 6.1: Parameters of quadratic fitting curves of universality of polar QNM frequencies against compactness. Values of f mode and w mode are copied from reference [4], and w-II mode are fitted according to our data computed.

of stars composed with twelve different EOS. Empirical universalities are formulated in attempt to infer radius and mass from the mode spectra. According to their argument, f mode oscillation is related to dynamical timescale of fluid motion, which is roughly scaled as the square root of mean density, i.e. $\omega_r \sim \sqrt{M/R^3}$. Besides, the damping time of f mode is caused by energy lost by gravitational radiation, hence the imaginary part is related to quadrupole radiation formula, $\omega_i \sim M^3/R^4$. Apart from f mode, they found that w mode frequencies give robust universality when plotted against the compactness ratio.

On the other hand, in quest of a dimensionless universal dependence between mode frequencies and stellar structure, Leung and Tsui expressed all universality in a power series of compactness using perturbative approach [4]. QNM frequencies are normalized by stellar mass, and fitted by a quadratic formula,

$$M\omega = a\left(\frac{M}{R}\right)^2 + b\left(\frac{M}{R}\right) + c \ , \tag{6.7}$$

where a, b, c are dimensionless parameters. Their values for f mode and w mode are shown in Table 6.1

Mode frequencies of the ten EOS mentioned above are calculated and plotted against compactness in Fig.s 6.2, 6.3 and 6.4. For the purpose of systematic

analysis in future section, we employ a 2-nd order polynomial Eq. 6.7 as the functional form of universality, following the approach of Leung and Tsui [4] regardless of the physical origin. Universality for w-II mode is newly found according to our data.

In general, the six QNM frequencies follows a trend as the compactness changes, although the difference in EOS contributes notable deviation from the universality. From Fig.s 6.2 and 6.4, real frequencies of f mode and w-II mode vary roughly linearly with compactness, therefore the universalities are well described by low order polynomials. The imaginary part of f mode seemingly varies with compactness as a cubic function, which Eq. 6.7 is no longer an appropriate model. The 3-rd to 4-th order dependence on compactness originates from the functional form of the quadrupole radiation formula, as claimed by Andersson and Kokkotas [5]. The pattern of w-II mode imaginary part is approximately a quadratic function, but the data points are seriously scattered. As shown in Fig. 6.3, real and imaginary part of w mode exhibit distinct behaviors. Pattern of real frequencies are nicely demonstrated by a quadratic curve, but the trend of damping frequencies diverges when $M/R \gtrsim 0.15$.

We also present the results of two models of QS for comparison. It is generally believed QS possess different behavior from NS, because their density profiles are nearly uniform until a sudden drop near the surface. Therefore a QS with a particular mass is more compact than a NS with the same mass. The effect can be observed in Fig.s 6.2 and 6.4, both real and imaginary part of normalized f mode, w mode, and w-II mode of QS shift away from the ordinary universality towards region with higher compactness.

We end this section by a comment. Although Andersson and Kokkotas [5] construct the universality of f mode by some physical arguments, whereas the fitting of Leung and Tsui [4] is merely a mathematical trick, both formalism appear to describe the universal trends fairly. Considering both proposals

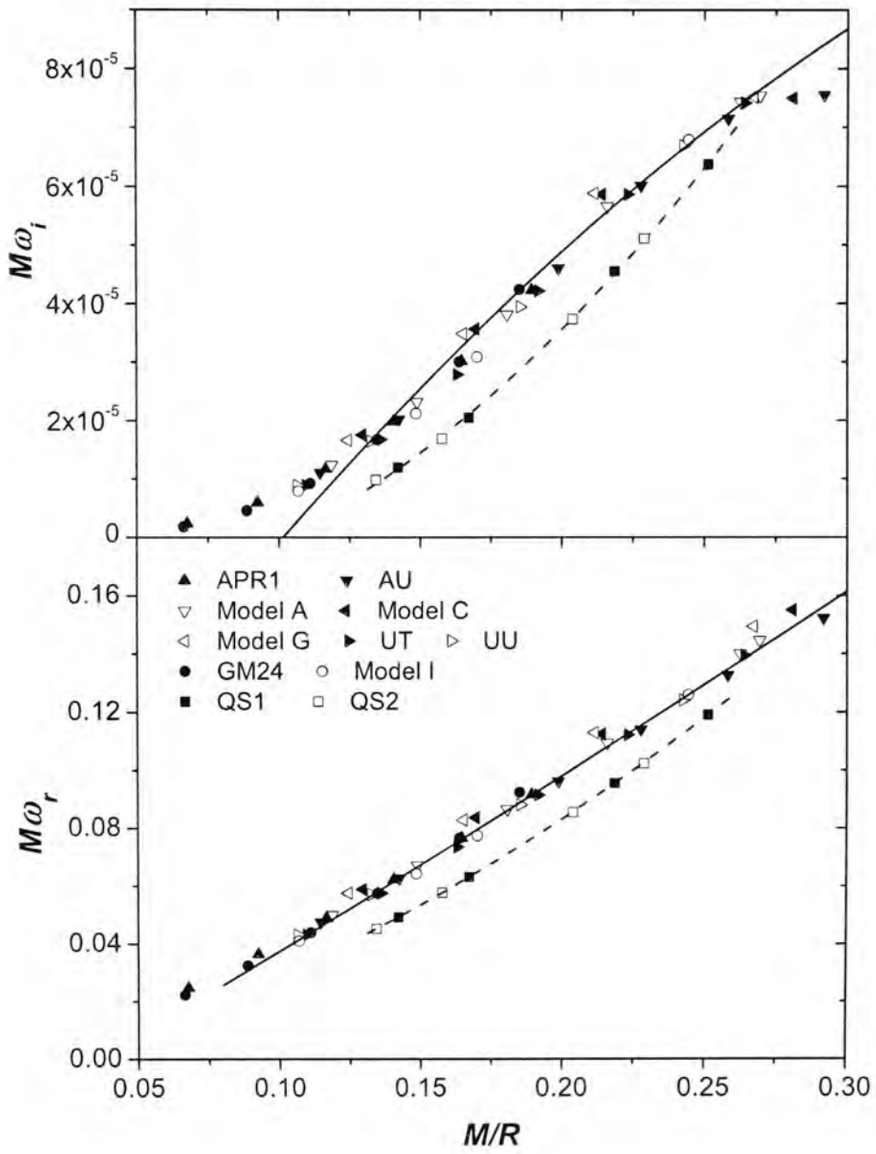

Figure 6.2: Normalized f mode is plotted against the compactness ratio. The lower panel shows the result of real frequency ω_r, and the upper panel shows the imaginary frequency ω_i. Solid line shows the universality suggested by Leung *et al.* [4], described by Eq. 6.7 with parameters shown in Table 6.1. Fitting of the 8 QS data points is also shown as a dashed line.

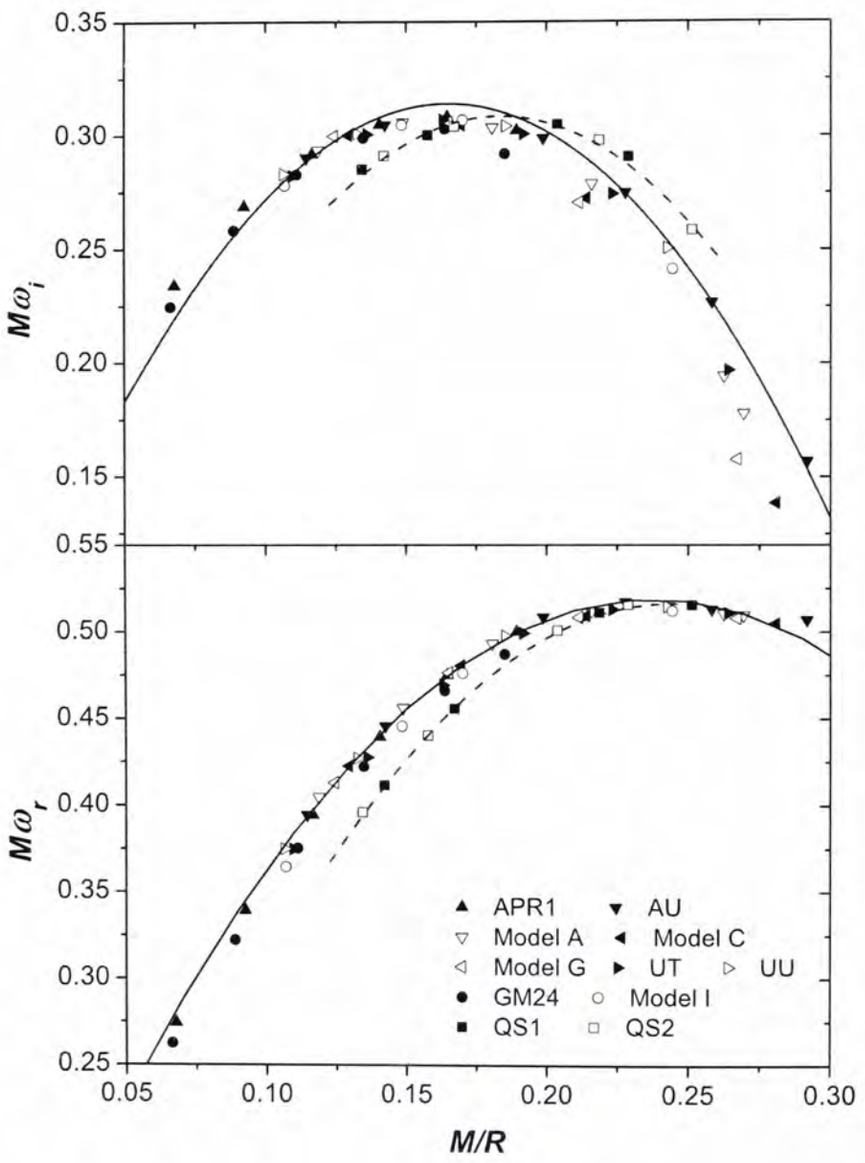

Figure 6.3: Same as Fig. 6.2 for the first w mode.

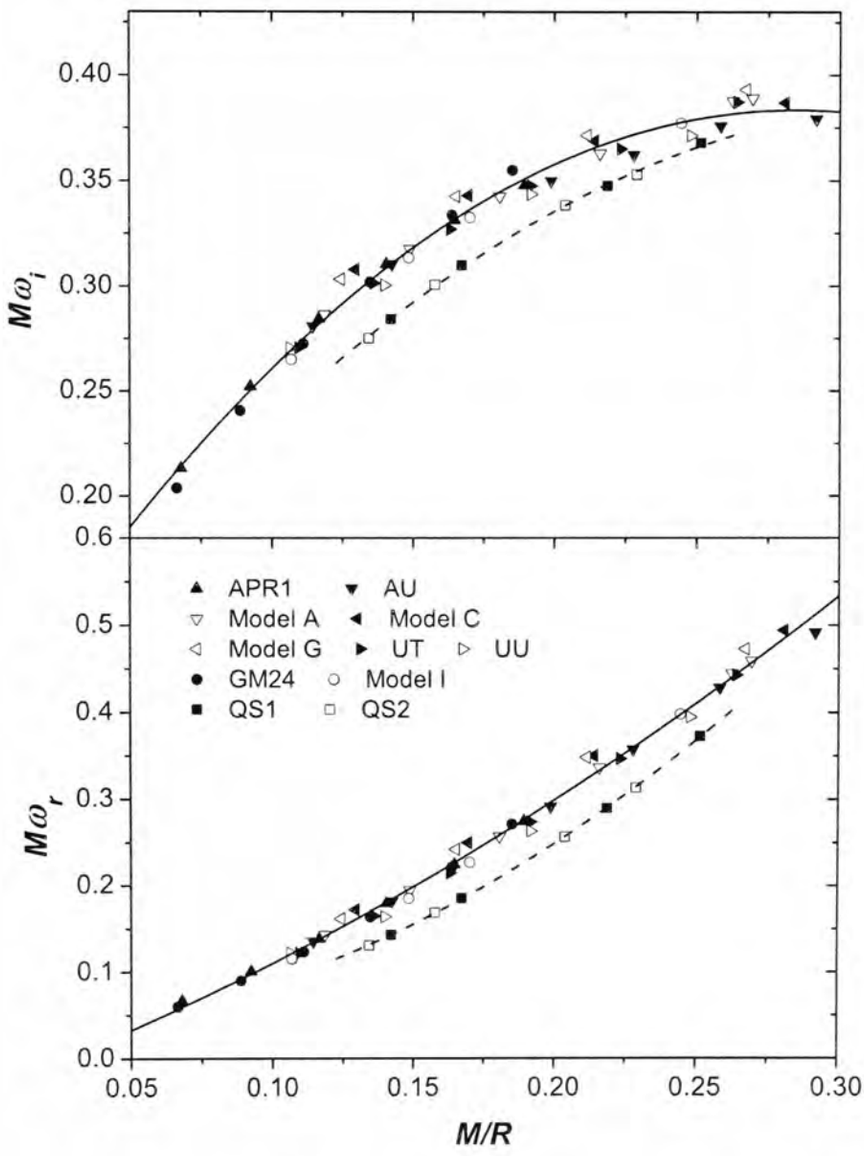

Figure 6.4: Same as Fig. 6.2 for the first w-II mode.

are based on different combinations of M and R, the best choice of independent variables on universality is hence debatable. However, as LD and Zerilli equations can be scaled to become dimensionless, a true universality is hence believed to be dimensionless. Then the compactness ratio is the only possible parameter to demonstrate the normalized QNM spectrum, if M and R are considered only.

6.3 Universality on moment of inertia

In this section, we examine the possibility to use the moment of inertia as a geometric parameter for constructing the universality of GW QNM spectra. In short, we replace the role of compactness M/R by another dimensionless factor $\eta \equiv \sqrt{M^3/I}$. The new factor is designed to mimic the role of compactness ratio in describing the stellar structure. Consider the moment of inertia can be viewed as mean-distance-square away from the center, i.e. $I \sim \langle mr^2 \rangle$. Therefore the quantity $\sqrt{I/M}$ is on the equal footing as radius, and $\sqrt{M^3/I}$ is an effective compactness.

Fundamental mode and spacetime modes are mainly determined by the matter distribution inside the star but not the low density profile near the surface. But radius R is sensitive to the EOS near the surface, which is apparently not a good variable to demonstrate the universality of QNM. As an illustration, consider the case of a typical neutron star with $R = 10$ km and $M = 2$ km. Due to some physical reasons, such as formation of crest, or numerical uncertainty, like choice of truncation pressure, on the surface, there is a 1 km error of the radius. The percentage error of compactness ratio is hence about 10%. However, the original moment of inertia is $I \sim 10^{-1}\bar{\rho}R^5$, where 10^{-1} is the typical order of inertia constant, $\bar{\rho} \sim 10^{14}$ g cm^{-3} is the mean density. The error of radius is equivalent to add a low density layer which contributes a moment of inertia $I_s \sim \rho_s R^4 \Delta R$, where typical surface

QNM	frequency	α	β	ξ
f mode	real	0.57	0.13	-0.0047
f mode	imaginary	1.2×10^{-4}	2.2×10^{-4}	-3.7×10^{-5}
w mode	real	-4.1	3.1	-0.085
w mode	imaginary	-5.9	3.1	-0.097
w-II mode	real	2.5	0.078	0.0081
w-II mode	imaginary	-1.8	1.6	0.022

Table 6.2: Parameters of quadratic fit to the universality of QNM frequencies against η, the functional form is referred to Eq. 6.8.

density $\rho_s \sim 10^{11}$ g cm^{-3}, $\Delta R \sim 1$ km is the width of the low density layer. Comparing I_s with I, the percentage error is about 10^{-3} only. According to our experience, f mode, spacetime modes frequencies and mass vary less than 1% for different numerical treatment near the surface, the moment of inertia seems to be a more appropriate independent variable.

We plot the mass-normalized f mode, first w mode, and the first w-II mode against the new variable η in Fig.s 6.5, 6.6, 6.7, and 6.8. The QNMs are calculated from 10 realistic EOS mentioned in the previous section. The configurations and mode frequencies of the stars are exactly the same as those plotted in Fig.s 6.2, 6.3, 6.4. To mimic the compactness case, universalities are fitted by quadratic functions of η,

$$M\omega = \alpha\eta^2 + \beta\eta + \xi \ , \tag{6.8}$$

which values of parameters α, β, ξ are shown in Table 6.2.

We analyze the figures one by one. Real and imaginary parts of f mode are plotted in Fig. 6.5, with quadratic-form universalities fitted. Comparing Fig. 6.5 with Fig. 6.2, we find that the quality of universality for η is apparently better. For the imaginary part, the distribution is more likely a cubic function on $M^3/I(\equiv \eta^2)$ instead of quadratic function of η. This reminds us the quadrupole radiation formula, and so we alternatively normalize the mode

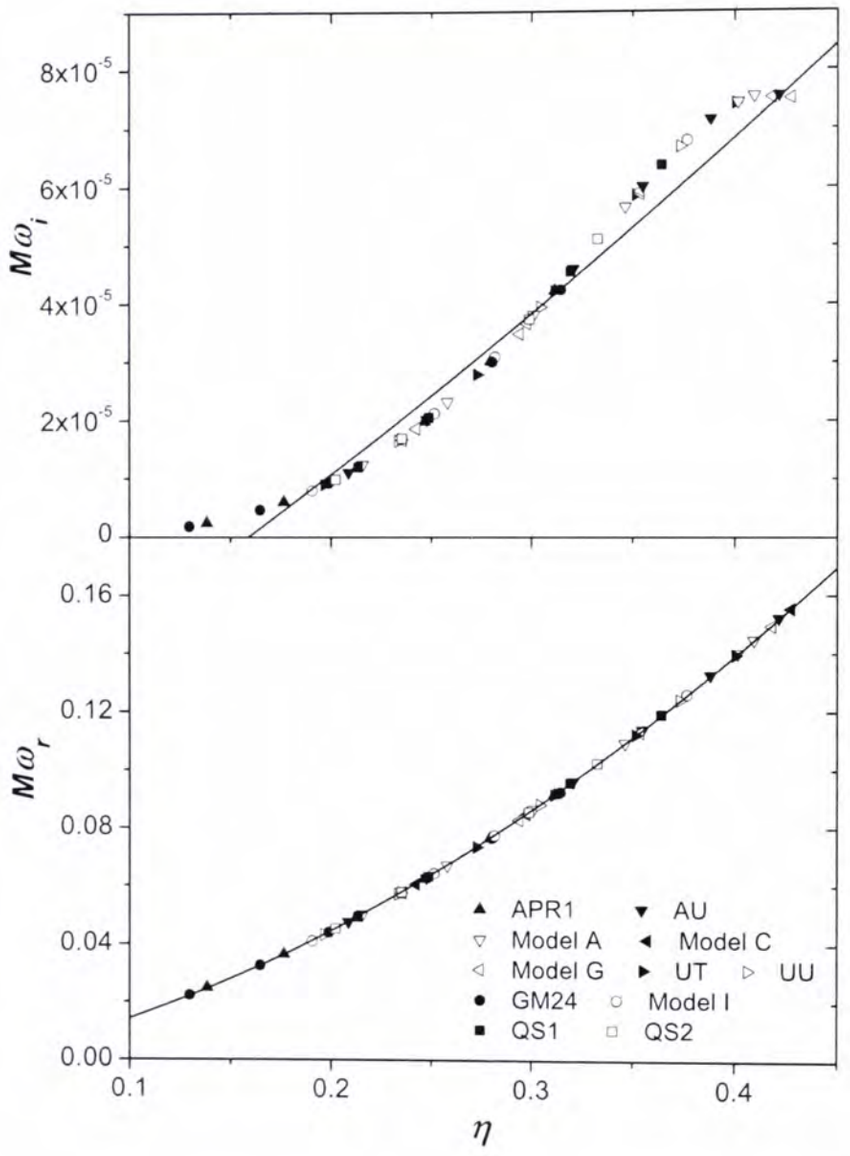

Figure 6.5: Normalized f mode is plotted against η. The lower panel shows the result of real frequency ω_r, and the upper panel shows the imaginary frequency ω_i. Solid line shows our quadratic universality fit, following Eq. 6.8 with parameters shown in Table 6.2.

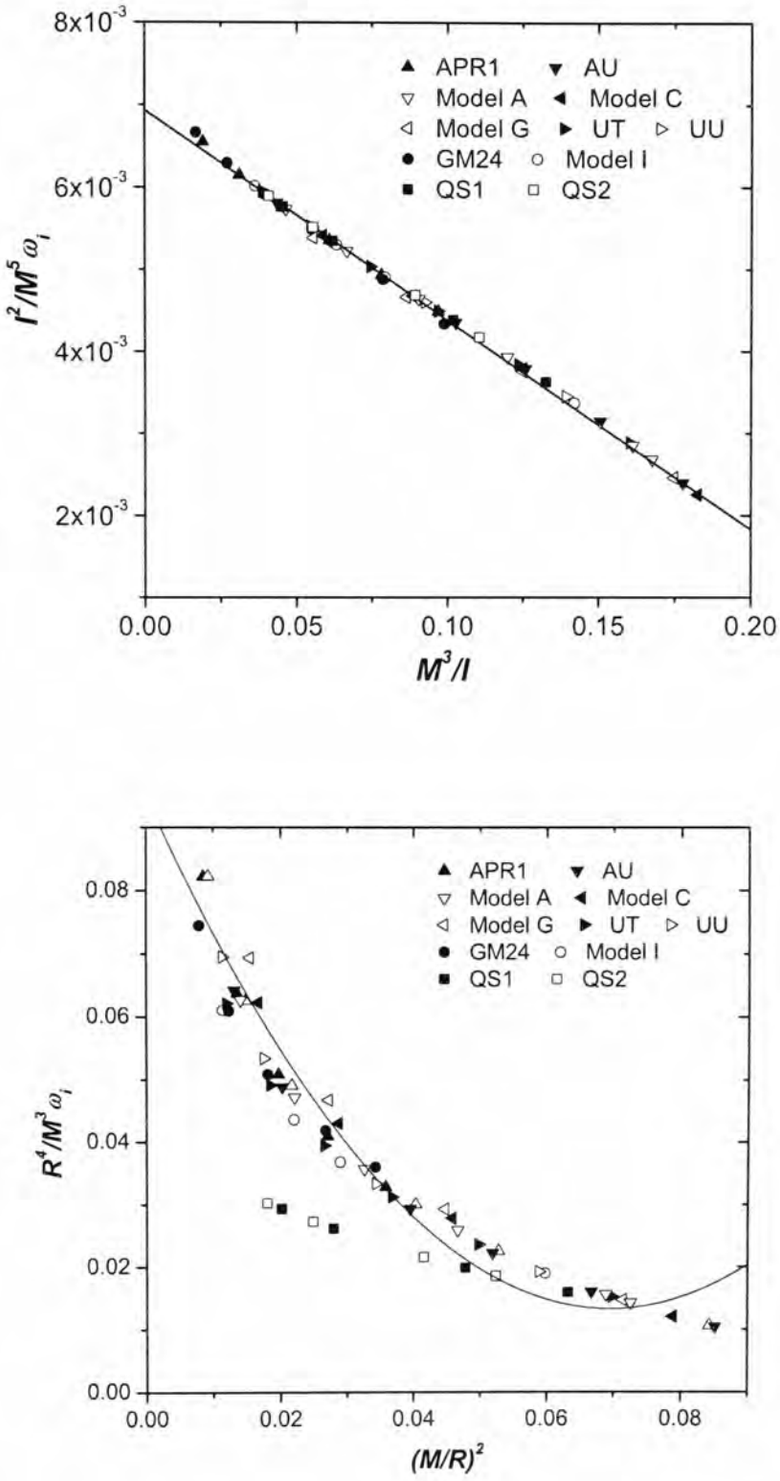

Figure 6.6: Upper panel shows the damping rate of f mode plotted against M^3/I. ω_i's are normalized by I^2/M^5, in order to mimic the quadrupole radiation formula. Solid line is the fitted universality given by Eq. 6.9. As a comparison on radius-related variables on equal footing, the modes are normalized by R^4/M^3 and plotted against $(M/R)^2$ in the lower panel. Results are obviously scattered. Besides, the solid line is the best quadratic fit, which does not describe the pattern well.

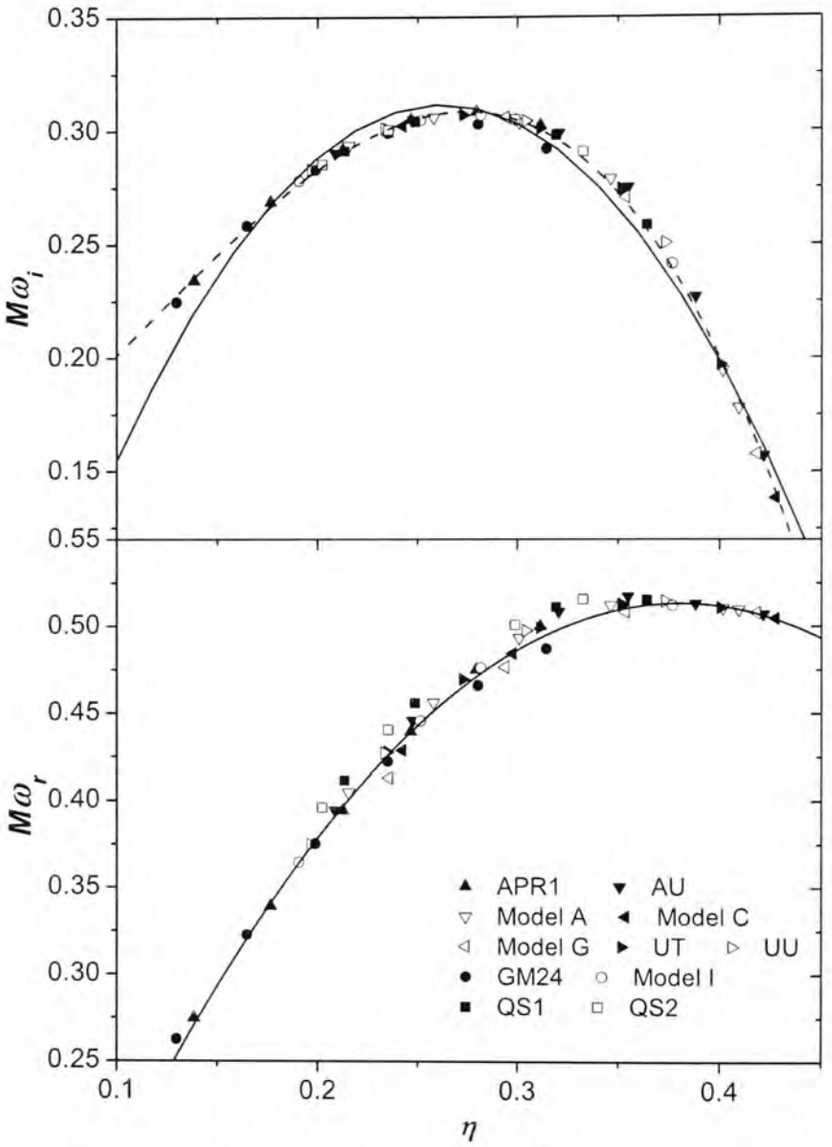

Figure 6.7: Distribution of normalized first w mode is plotted against η. The lower panel shows the results of real frequency ω_r, and the upper panel shows the imaginary frequency ω_i. Solid lines represent the quadratic function fitting the distribution of modes. The real frequencies are slightly scattered from the curve at $\eta \sim 0.3$, while imaginary part apparently follow a trend but it is not well described by the curve. We find a cubic function can improve the accuracy of the fitting, which is given by Eq. 6.10 and shown as the dashed line in the figure.

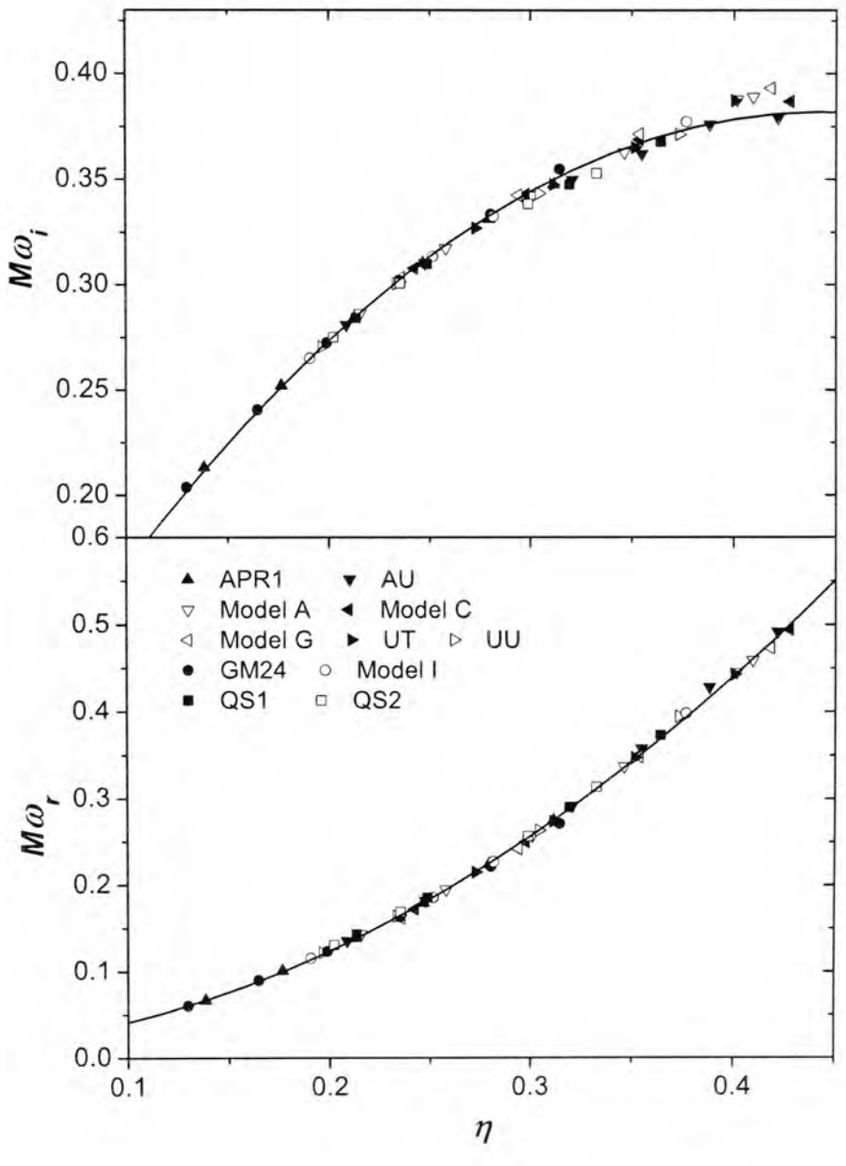

Figure 6.8: Normalized first w-II mode is plotted against η. The lower panel shows the ω_r, and the upper panel shows the ω_i.

frequencies by I^2/M^5 and fitted to a straight line as,

$$\frac{I^2}{M^5}\omega_i = 0.006938 - 0.02557\frac{M^3}{I} \ . \tag{6.9}$$

Our results are shown in Fig.6.6, we have checked that the data points of our representation are less scattered than the corresponding plot using compactness as geometric variable with R^4/M^3 as normalization (c.f. Fig. 2 of [5]). We conclude from our current data that the moment of inertia is a plausible geometric parameter the represent the universality of f mode.

For the first w-II mode, both real and imaginary parts are well fitted by quadratic functions on η as shown in Fig. 6.8. However, it is noted that the imaginary part begins to disperse when $\eta \gtrsim 0.3$, similar pattern is observed in the compactness plot Fig. 6.4 for $M/R \gtrsim 0.17$. The deviation enlarges when η (compactness) increases. Although the physical reason for this phenomenon is not exactly known, we believe the moment of inertia is an excellent geometrical factor to describe the universality of ω_r of w-II mode, while it is still good for ω_i for stars with low compactness.

Results of the first w mode is presented in Fig. 6.7. For the imaginary part, the moment of inertia demonstrates a universality as fit as compactness ratio in low compactness, but it further resolves the divergence in high compactness when comparing with Fig. 6.3. From the upper panel of Fig. 6.7, we use a cubic polynomial to represent the universal trend observed,

$$M\omega_i = 0.1252 + 0.5095\eta + 3.603\eta^2 - 11.001\eta^3 \ . \tag{6.10}$$

While quadratic function captures the main feature of the mode distribution, cubic polynomial show better agreement to less compact stars. Therefore we claim that the moment of inertia is a good choice of parameter for the ω_i of w mode. However, it does not work that good for the real part. Although w mode obviously follows an EOS independent trend in both plotting of compactness and η, the data points look more scattered in the plot of η when

comparing with Fig. 6.3. However, mode frequencies of QS become closer to the universality and lie on the ambiguous range of NS. Although the quality of the new universality is not improved, it is still fair to say that η can demonstrate a general pattern for real part of w mode regardless to the composition of compact stars.

Mode frequencies of QS are also plotted for other QNM. In the contrary to common belief that QS would give completely different GW spectra, Fig. 6.5, 6.7, 6.8 reveal f mode, w-II mode, and imaginary part of w mode lie nicely on the universal trends of neutron stars. This is a remarkable result that the universalities of NS and QS are unified when η is employed as the geometric factor. Recall the major difference between QS and NS is the density profile near stellar surface. Usual ordinary EOS give a thick low-density range near the outer boundary of TOV solution, in other words the density of EOS gradually vanishes when pressure approaches to zero. It is however not the case for QS, which the confinement of quarks would cause in a sudden drop of density near surface while the pressure drop is steady. This phenomenon causes a slowly varying energy density inside a QS, which deviates from the cases of NS that can be roughly described by the Tolman VII model [43]. We will elaborate this point in the next section, but our current observation suggests that the discrepancy of QS mode spectra originates from a wrong choice of description, which is closely related to the nature of the oscillation modes.

6.4 Origin of universality

In the previous section, we show that the quality of universality on QNM is improved dramatically when the moment of inertia replaces radius as the geometric factor. The universal curves do not only describe the QNM pattern of NS but also work fine for QS, which is promising. In this section, we are going to study the origin of universality based on analysis of stellar structure

and EOS. We start from the Tolman VII model, and extended the model to a commonly employed toy EOS, the polytropic model. The pattern of the moment of inertia and mode frequencies against compactness shift when stiffness of model is changed. The effects cancel each other to some extent and enhance the accuracy of universality as observed in previous section. We believe this is not a coincidence, but the phenomena is related to the pulsation mechanism of different oscillation modes.

6.4.1 Tolman VII model

As mentioned before, Andersson and Kokkotas [5] propose that the real part of f mode is roughly a function of mean density, while imaginary part is attributed to energy loss by quadrupole radiation. In spite of the physical sense, universality of f mode can still be noted if other combination of M and R are used as independent variables. Instead of considering dynamics of compact stars, Leung and Tsui [3] looked into the universality and individuality of QNM spectrum through perturbative analysis on the stellar structures. They proposed QNM spectra of all compact objects are roughly the same, because their matter profiles are well approximated by the Tolman VII model. For the QNM which are mainly determined by the matter distribution, mode frequencies can hence be approximated by that of Tolman VII model.

Tolman VII (TVII) model is one of the several analytically solvable solutions of TOV equation [20]. This model requires the energy density profile is a quadratic function as the normalized radius, i.e.

$$\rho(r) = \rho_0 \left[1 - \left(\frac{r}{R}\right)^2\right] \ , \tag{6.11}$$

where ρ_0 is the central density. With this density profile and the TOV equation, the mass distribution can be obtained by direct integration, pressure and metric factor ν can hence be analytically found. Analytical expression of the stellar profile is given in [3].

TVII model is particularly welcomed by theorists to act as a toy model for investigating phenomena of neutron stars. It is because the model possess an exactly known profile. Another reason is that the model gives a small density near the star surface which resembles the property of realistic stars. But the above properties are not enough to explain why TVII model demonstrates behavior similar to most stars constructed by realistic EOS. The applicability of this model has to be understood from the structure of TVII star, and also the thermodynamic relations implied by Eq. 6.11.

First of all, density profile of any hydrostatic spherically symmetric compact star can be expressed as a series of r/R,

$$\rho(r) = \rho_0 + \rho_2 \left(\frac{r}{R}\right)^2 + \rho_4 \left(\frac{r}{R}\right)^4 + \dots \,. \tag{6.12}$$

The odd terms are suppressed by the assumption of isotropicity. The zeroth order approximation is obviously a uniform density model, which fails to describe many dynamical properties of realistic stars. The next order correction is the Tolman VII model. It is noted that $\rho_2 = -\rho_0$ for this second order correction is implicitly required by the assumption of vanishing surface density. By the principle of perturbation theory, TVII model is hence a good approximation to realistic stars in view of its structure.

Profile of pressure and other quantities are hence the corresponding TOV solution consistent with the first order approximation to density profile. It is clarified that although pressure can be expressed as a closed form function of normalized radius, but the function is not a simple series, originated from the non-linearity of the TOV equation. According to our experience, TOV solution of realistic EOS indeed give a density profile close to the TVII model, while pressure profile is far from a quadratic function. However, this observation somewhat contradicts the perception that energy density plays a similar role as pressure in general relativity. One can always perform perturbation on pressure instead of density, which the first order correction is believed not

to be a good approximation. Perturbative approach itself is not enough to account for the well behavior of TVII stars.

We need some additional information to fix the uncertainties. We incorporate another commonly employed model, the polytropic EOS, which is presented as Eq. 6.1. Pressure and energy density are in general related by more than one parameters, such as temperature, chemical composition, etc. Under the assumption of adiabaticity, and conditions implied by the static background, pressure is a function of energy density only. Usual EOS of adiabatic gas is Eq. 6.1, which the γ is the crucial factor governing the response of matter under pressure variation. For ideal gases, γ is a rational fraction merely specified by the degree of freedom per gas molecules, whereas its value is influenced by nuclear interactions for realistic matter. Physicists conventionally refer EOS with large (small) γ as 'stiff' ('soft'). In general, γ varies with position inside a compact stars, because of EOS changes at different pressure and phase. Polytropic stars are hence approximations to realistic stars which are composed of a homogeneous EOS.

Our work here is to analyze TVII model in the context of polytropic EOS. For a compact star formed by any EOS, we are able to find out the local value of γ in analogy to Eq. 6.1, by the local pressure, energy density and their derivatives,

$$\gamma(r') = \frac{\rho(r')}{p(r')} \frac{dp}{d\rho}\Big|_{r=r'} . \tag{6.13}$$

Since γ is a function of radius, series expansion can be obtained as

$$\gamma(r) = \gamma_0 + \gamma_2 \left(\frac{r}{R}\right)^2 + \dots , \tag{6.14}$$

where γ_0 is the value of γ at star centre. Therefore polytropic model is the zeroth order approximation to any EOS, including the TVII model. Recall that any dimensionless parameter in TVII model can be expressed as a function of two dimensionless variables, the compactness ratio M/R and the normalized radial position r/R. Formulating the effective γ of TVII model by Eq. 6.13 and

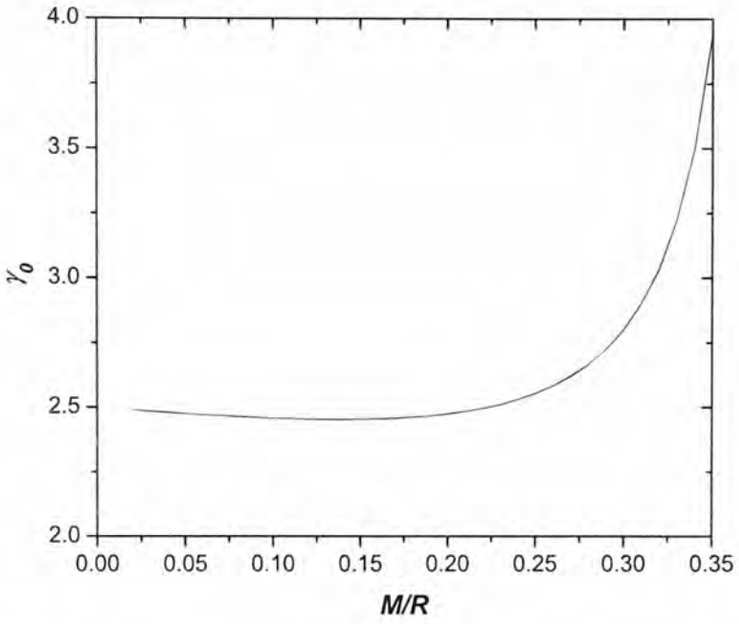

Figure 6.9: γ_0 is plotted against the compactness of TVII stars.

expand it as Eq. 6.14, one can see that all the expansion coefficients depend on compactness only. Since TVII model is an approximation near origin, the dominant factor of $\gamma(r)$ is the zeroth order coefficient γ_0.

We plot the variation of γ_0 against the compactness of TVII stars in Fig. 6.9. The value changes steadily within $\gamma_0 \sim 2.4 - 2.5$ when $M/R \lesssim 0.25$, which is the typical range of compactness ratio of NS. On the other hand, we consider the γ on TVII stars near the surface. If a neutron star possess a polytropic tail as the atmosphere, energy density profile near the surface varies as [9]

$$\rho(r) \sim (R - r)^{1/(\gamma-1)} \ . \tag{6.15}$$

For the density profile of TVII model,

$$\begin{aligned} \rho(r) \sim R^2 - r^2 &= 2R(R - r) - (R - r)^2 \\ &\sim (R - r) \text{ when } r \to R \ , \end{aligned} \tag{6.16}$$

which corresponds to the tail of a $\gamma = 2.0$ polytropic star. As $\gamma \sim 2.5$ at origin and $\gamma = 2.0$ near the surface, and the quantities varies smoothly as radius, it

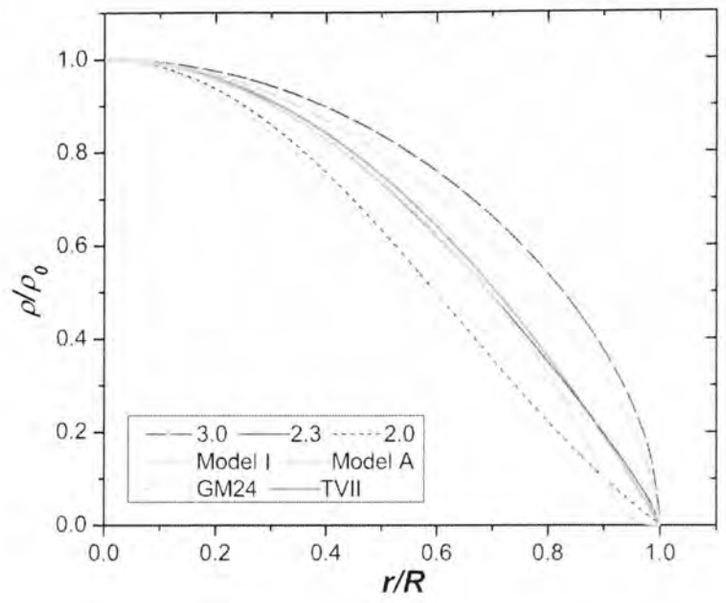

Figure 6.10: Density profiles, which is normalized by the central density ρ_0 and the radius R, is shown for 3 realistic stars (green lines), 3 polytropic stars (blue lines), and the Tolman VII model (red line). All the stars possess compactness ratio $M/R \sim 0.17$.

is anticipated that the behavior of TVII stars is similar to that of a polytropic star with γ between 2 and 2.5.

To further understand why TVII model is a good mock-up to realistic stars, we compare the normalized density profile of a TVII star with those of 3 realistic stars and 3 polytropic stars in Fig. 6.10. The 3 realistic EOS include GM24 as a well known soft EOS, Model I which is a stiff EOS, and Model A with moderate stiffness. The 3 polytropic stars are chosen with $\gamma = 2.0, 2.3, 3.0$, which cover typical stiffness of NS. From the plot, we find that the density profile of a polytropic star become more 'convex' as γ increases. The quadratic distribution of TVII model is surprisingly close to that of a $\gamma = 2.3$ polytropic star, it supports the analysis in the last paragraph that the effective γ of TVII model lies between 2 and 2.5.

Although the local value of γ of GM24 near origin is 1.6 while that of Model I is more than 3, profiles of realistic stars lie between $\gamma = 2.0$ and 3.0 polytropic stars. It is because most realistic EOS tend to soften at lower density,

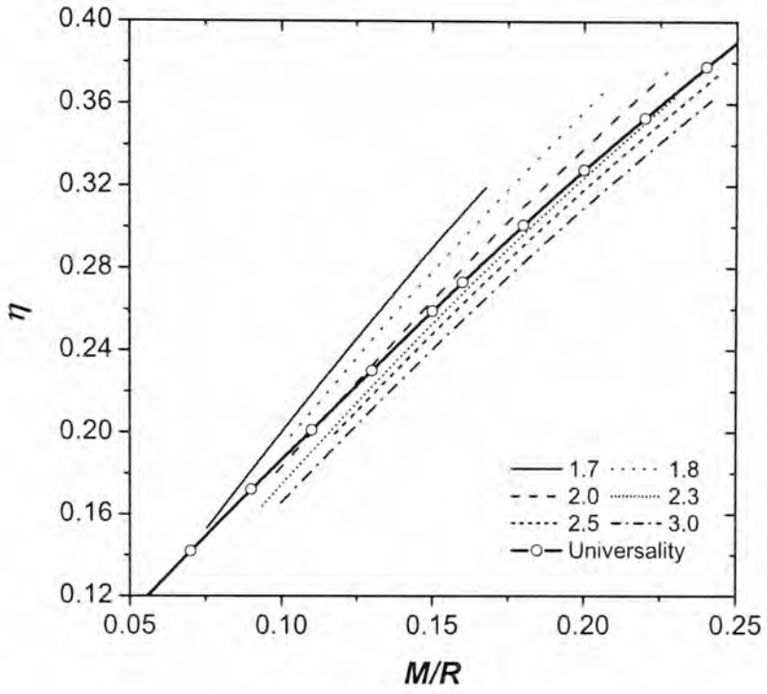

Figure 6.11: η of polytropic stars are plotted against compactness ratio. The range of γ ($1.7 \lesssim \gamma \lesssim 3.0$) captures effective γ of most realistic EOS. The universality curve, which is derived from formula of Haensel *et al.* [2], is also plotted for comparison. As γ increases, the pattern move towards high compactness region.

while GM24 becomes stiffer at low density region as composition of hyperon decreases. With reference to the density profiles, it is expected that the behavior of NS are bounded by 2.0 and 3.0 polytropic stars. Since TVII model looks similar to polytropic stars with effective $\gamma = 2.3$, it acts as an average to conventional realistic stars, and hence nicely demonstrates the universality.

6.4.2 Polytropic Model

In this subsection, we want to see how the moment of inertia and the QNM spectra would differ from universality for stars with density profile deviated from that of TVII model, a natural step is to consider polytropic stars with a broad range of γ.

We show the variation of η with respect to the compactness in Fig. 6.11. As mentioned before, the function η is considered because it is dimensionless, and plays an equal footing as M/R. If matter profile of stars are identical, we expect there is a linear relationship between the two quantities. However we have shown in Fig. 6.10 that, normalized density profile becomes more convex for larger γ. Consider stars with the same mass, radius of the one with smaller γ is longer than the one with larger γ, hence it is less compact. Meanwhile, this change of matter distribution also affects the moment of inertia, but the effect is relatively mild because the density is low in outer region. Therefore, the curve in Fig. 6.11 shifts towards high compactness region as γ increases.

Next, we want to investigate the trend of QNM spectra as γ alters. Without knowing precisely the physical origin of pulsation dynamics, we can only obtain empirical tendency by calculating f mode, w mode and w-II mode frequencies of polytropic stars, which are plotted as Fig. 6.12, 6.13 and 6.14. Results of f mode and w-II mode are similar, mode frequencies of both real and imaginary parts shift towards the higher compactness region as γ increases. Since η also changes in similar pattern in Fig. 6.11, influence of γ variation is suppressed if η is employed to describe these mode spectra. Empirically, this is the reason why universality is much improved if compactness is replaced by another geometric parameter. In physical sense, moment of inertia is a more appropriate geometric parameter to account for the oscillation of these modes, which is indirectly showing that f mode and w-II mode oscillations are characterized by the region of high density.

The imaginary part of w mode also shifts towards high compactness when γ increases, so it is anticipated that new variable η can produce a nice universality on η. The divergence of modes observed on the upper panel of Fig 6.3 is produced by the shift and the quadratic distribution of modes, in other words, a wrong choice of variable. Surprising results appear for ω_r of w mode. While it is believed spacetime modes are mainly determined by the matter distribution, w

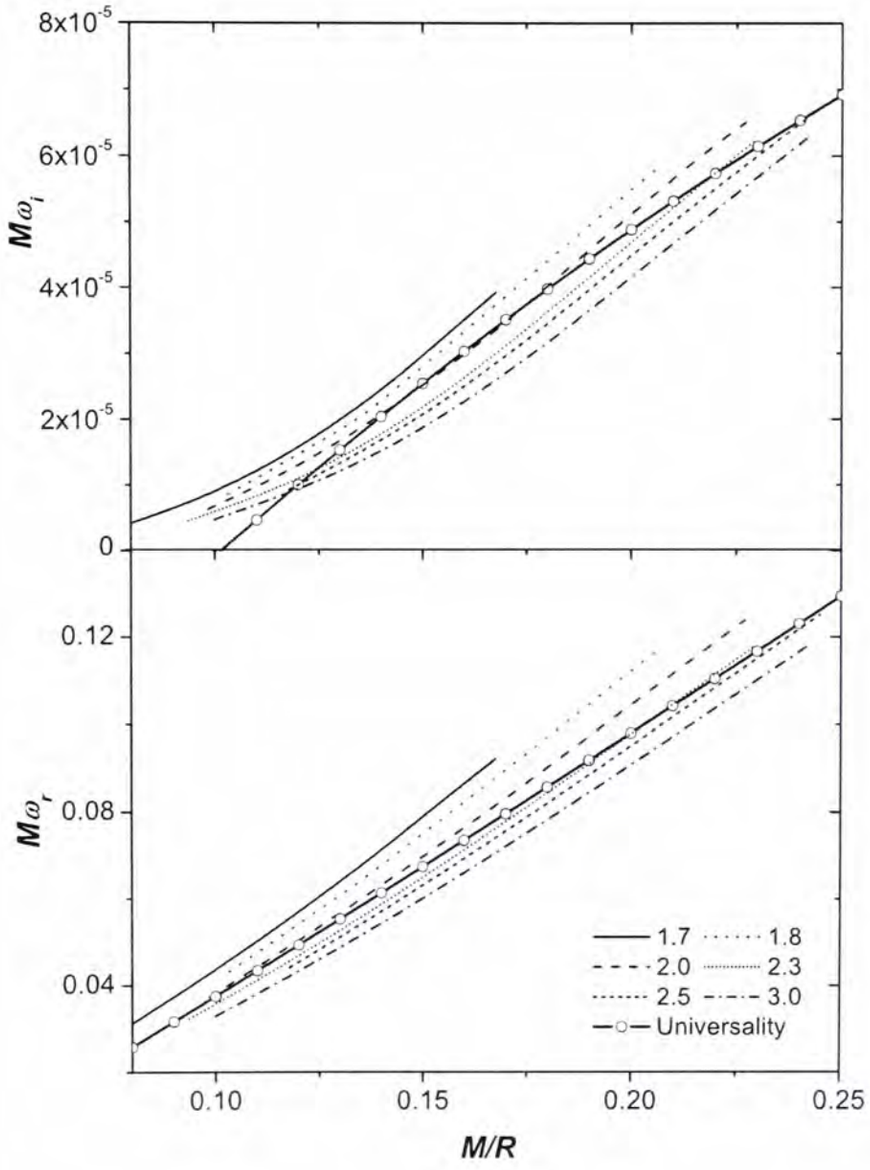

Figure 6.12: Normalized f mode frequencies of polytropic stars are plotted against compactness ratio. Universality curves (Eq. 6.7 with parameters in Table 6.1)are also plotted for comparison. Monotonic trend towards high compactness is noted when γ is increased for both real and imaginary parts.

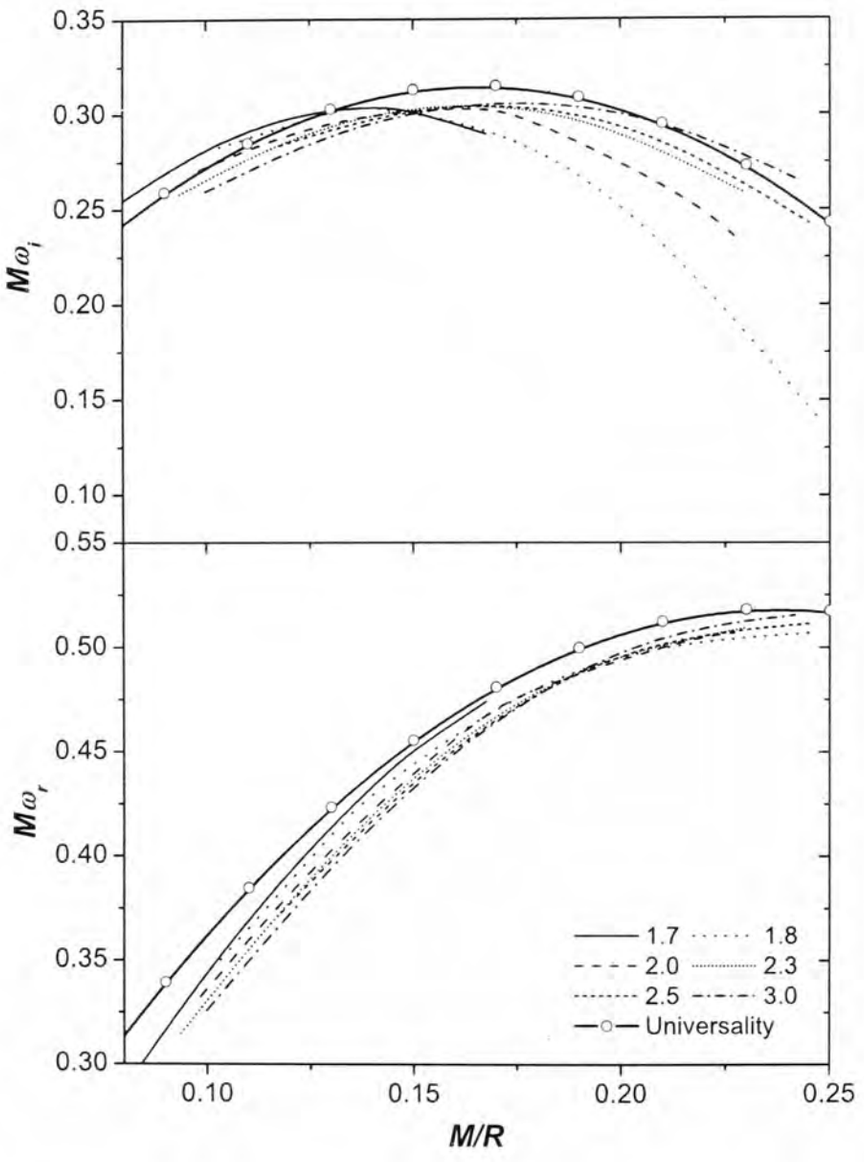

Figure 6.13: Same as Fig. 6.12 for the first w mode. When γ is increased, curve of imaginary part of shifts significantly. On the contrary, the real part is barely sensitive to the change of stiffness.

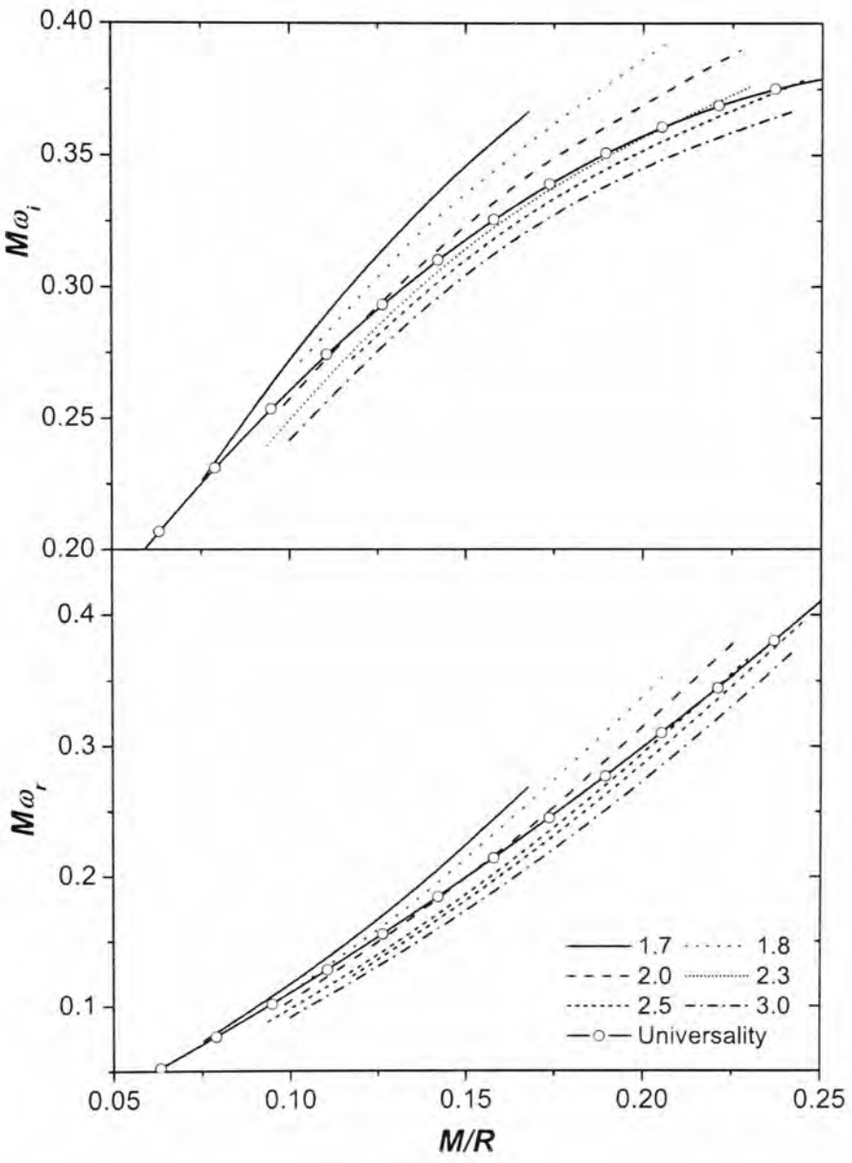

Figure 6.14: Same as Fig. 6.12 for the first w-II mode. Monotonic trend towards high compactness is noted when γ is increased for both real and imaginary parts.

mode real frequency roughly follows the same trend, in spite of the dramatically changed density profile of polytropic stars. Therefore, ω_r of w mode is the only case that η give worse pattern than the compactness. In fact, Andersson and Kokkotas [5] deduced from some toy models that w mode frequency is inversely proportional to the size of a star, which the size is apparently better accounted for by radius.

We postulate that if the trend we observe is not a coincidence of mode distribution, the failure of η on first w mode is because w mode is most sensitive to the redshift factor, which is a function of M/R in the Schwarzschild coordinate. However, there is still a puzzle that a compact star may possess a thick but low density atmosphere, which the radius becomes uncertain but w mode is not much affected. Furthermore, quadratic fitting of w mode real part on η in lower panel of Fig. 6.7 still captures essence of mode variation. We explain the failure by considering radius can be treated as a functional of the matter distribution, it can be approximated by a series of moments

$$R(m(r)) = \alpha_0 M + \alpha_2 \left\langle m(r) r^2 \right\rangle + \dots \ , \tag{6.17}$$

which the moment of inertia can be treated as the first order correction. For f mode, w-II mode, and imaginary part of w mode, the first order term is enough, but real part of w mode involves higher order corrections.

Finally, we use the analysis here to investigate the results of QS. A conventional analytic expression for quark matter EOS is the MIT bag model,

$$p = 3\rho + 4B + \hat{O} \ , \tag{6.18}$$

where $\hat{O}$ is the high order corrections due to temperature, quark masses, and interactions. The value of effective γ of MIT bag model is found to be enormous at most region inside QS, because of the non-vanishing bag constant B. (In this sense, incompressible star is a good approximation of QS, as effective $\gamma \to \infty$ for incompressible model.) Following the trends in Fig. 6.11-6.14, it is

anticipated that quantities of QS shift further towards the high compactness region, where the effects would eventually cancel each other and form nice relation between mode frequencies and η, except real part of w mode. It is indeed the case as we have shown in Fig. 6.5 - 6.8, hence explained why our new universality can describe pattern of QS well.

6.5 Application of universality

So far we have demonstrated that f mode, w-II mode and imaginary part of w mode exhibit nice universal dependence on η. The universality are nice in the sense that, (i) dispersion of modes on the plot are relatively mild when comparing with the compactness counterpart, (ii) the formula are constructed according to the results of NS, but they also fit QNM frequencies of QS. These properties are promising for extracting useful information from GW signals. They allow us to get more precise values of NS parameters, and also include QS into consideration.

We here present a simple application of the new universality formula, which is to infer mass, radius, and the moment of inertia if GW QNM is recognized. In the previous section, we have formulated five universalities for f mode, w-II mode and imaginary part of w mode, which are presented in Table 6.2. In the ideal case, we can pick two out of five formulae for the inference. It is possible that the inferred values can be more accurate if more than two universalities is employed, this require further investigation which is out of the scope of current investigation.

If we stick to the 'two equations for two unknown' formalism, selection of best combination of universalities is purely trial and error. We do not show our testing data but directly tell the best combination is ω_r of f mode plus ω_i of w mode, followed by the combination of both real and imaginary part of f mode. A simple intuition leading to our choices is to apparently compare the

exactness of universalities in Fig. 6.5, 6.6, 6.7 and 6.8. We directly exclude the imaginary part of w-II mode due to the scattering of mode with large η. The rest look accurate and we just present the best ones by experiment. One exception is the combination of ω_r of both f mode and w-II mode. Although both universalities look accurate, this combination usually produces values of mass with error larger than 10%. We believe it is not a matter of the choice of structure variable but a coincidence. We find the reason is related to the intrinsic distribution of mode frequencies, detailed analysis is given in Appendix E.

However, the detectability of QNM varies in reality, because of sensitive frequency range of detectors, energy content of each mode, and length of damping time, etc [42, 12]. The most plausible signal to be extracted by detectors in the foreseeable future is the f mode, followed by p mode and g mode. But the detection of all spacetime modes is pessimistic because of its fast damping rate and ineffective excitation. Since p mode and g mode do not show universality with respect to any geometric parameters of compact stars, it is most physically interested to investigate how stellar properties can be inferred from f mode signal.

Inference of stellar parameters from GW QNM is first discussed by Andersson and Kokkotas [5]. They incorporate two out of four universalities for real and imaginary part of f mode and w mode. Based on QNM of stars constructed by 12 different nuclear matter EOS, their formula for the f mode is given by,

$$\omega_r = 0.01635 + 0.7536\sqrt{\frac{M}{R^3}}\ ; \tag{6.19}$$

$$\omega_i = \frac{M^3}{R^4}\left[0.0862 - 0.2673\left(\frac{M}{R}\right)\right]\ . \tag{6.20}$$

Here we have converted their original equation into the unit system of km. Later, Benhar *et al.* [25] considers more recent proposals of EOS, including two QS models, to modify the universality of Andersson and Kokkotas and

give the following formula,

$$\omega_r = 0.01656 + 0.6916\sqrt{\frac{M}{R^3}} \; ; \tag{6.21}$$

$$\omega_i = \frac{M^3}{R^4}\left[0.087 - 0.271\left(\frac{M}{R}\right)\right] \; , \tag{6.22}$$

which all the parameters are in unit of km. (It is noted that our ω_r is defined as the angular frequency, which is 2π times ω_r in [5] and [25] that is ordinary frequency.)

To examine the applicability of f mode universality and demonstrate the high accuracy of our proposal, we compare results inferred by four sets of f mode universalities: 1. Eq. 6.19 and 6.20 proposed by Andersson and Kokkotas; 2. Eq. 6.21 and 6.22 proposed by Benhar *et al.*; 3. Eq. 6.7 formula proposed by Leung and Tsui [4] with parameters presented in Table 6.1; 4. Eq. 6.8 and 6.9 proposed in current thesis.

We pick the mode frequencies and stellar structure computed ourselves for the inference experiment. To be fair, we also consider the data calculated by Andersson and Kokkotas [5] for comparison, in order to eliminate possible inaccuracy of our numerical scheme of stellar profile construction and mode extraction, although we have checked that our code produces results with less than 1% deviation from theirs. In addition, we also conduct tests on QS, so as to verify if the inference scheme is applicable regardless of the composition of compact stars.

We assume only the f mode is detected, and its real frequency and damping time are extracted to high precision. By these two quantities, we can solve the simultaneous equations to obtain value of two stellar parameters from universalities. For the first three proposal, the inferred parameters are M and R because of their dependence in universality formulae, while the new proposal can provide value of M and I. For better comparison, we employ Eq. 6.6, the universal trend between specific moment of inertia and the compactness observed by Lattimer and Schutz [1], such that all four proposal can produce

EOS	M	M_A	R_A	I_A	M_B	R_B	I_B	M_L	R_L	I_L	M_I	R_I	I_I
AU	0.8	18	8.0	48	2.6	-2.2	4.1	8.1	0.16	16	-0.056	-2.6	-0.031
	1.0	11	6.8	29	-4.8	-3.6	-11	-4.7	-1.2	-6.9	-0.13	-0.67	-0.16
	1.6	-6.4	3.5	-6.6	-24	-8.6	-43	2.9	1.5	4.3	4.0	2.1	6.9
APR1	0.8	80	40	311	58	28	197	28	2.5	56	-0.066	-5.1	-0.23
	1.2	45	27	151	25	15	74	-4.5	-2.1	-6.5	-0.21	-1.6	-0.19
	1.6	34	22	108	8.6	8.6	28	-7.7	-1.9	-13	0.50	-0.11	0.78
EOS A	1.535	9.9	3.0	23	6.3	-3.5	6.3	15	0.89	28	0.40	-1.2	0.27
	1.328	-12	-3.9	-20	-26	-14	-48	-4.9	-1.9	-8.8	1.1	-0.46	1.8
EOS B	1.405	-8.7	-7.6	-18	-14	-14	-34	-41	-12	-61	-0.17	-3.5	0.54
	0.971	-15	-13	-31	-28	-22	-54	-7.7	-5.9	-12	1.4	-4.1	2.7
GM24	1.536	1.5	1.7	14	-16	-9.5	-28	-8.7	-6.3	-14	-2.2	-4.9	-2.6
	1.405	40	23	132	18	11	54	-6.6	-2.9	-10	2.5	-1.1	5.1
QS1	0.8	13	27	33	-1.9	15	-6.7	6.0	20	12	-0.096	18	-0.18
	1.4	0.68	16	7.3	-16	3.7	-31	-6.5	9.9	-11	0.93	12	1.3
QS2	1.0	23	34	66	6.1	21	15	-1.7	17	-1.9	-0.17	17	-0.3
	1.6	12	24	40	-9.4	9.2	-15	-3.8	9.7	-7.2	1.6	11	2.5

Table 6.3: Percentage error of compact star parameters inferred from f mode signal. Data of EOS AU and APR1 are calculated ourselves; EOS A, EOS B, GM24 are extracted from table of Andersson and Kokkotas [5]; QS1 and QS2 are QS computed ourselves. Unsubscripted M is the mass of a compact star in solar mass unit. Subscripted M, R, I denote percentage error of inferred mass, radius, and the moment of inertia, where the subscript denotes different universality proposal: A represents Andersson and Kokkotas; B represents Benhar *et al.*; L represents Leung and Tsui; I represents the proposal in current thesis.

values of M, R, and I. It is noted that we compute the moment of inertia for candidates of Andersson and Kokkotas by constructing their stellar profile according to the EOS and mass value provided in Table A of [5].

Our results are presented in Table 6.3. In general, our new universality produce more accurate results than all three previous proposals employing radius as a geometric parameter. Values of M and I are extraordinary precise in all three sets of data, error of most data are less than 1%, which is expected as they are fundamental variables in our universality. Error of radius inferred

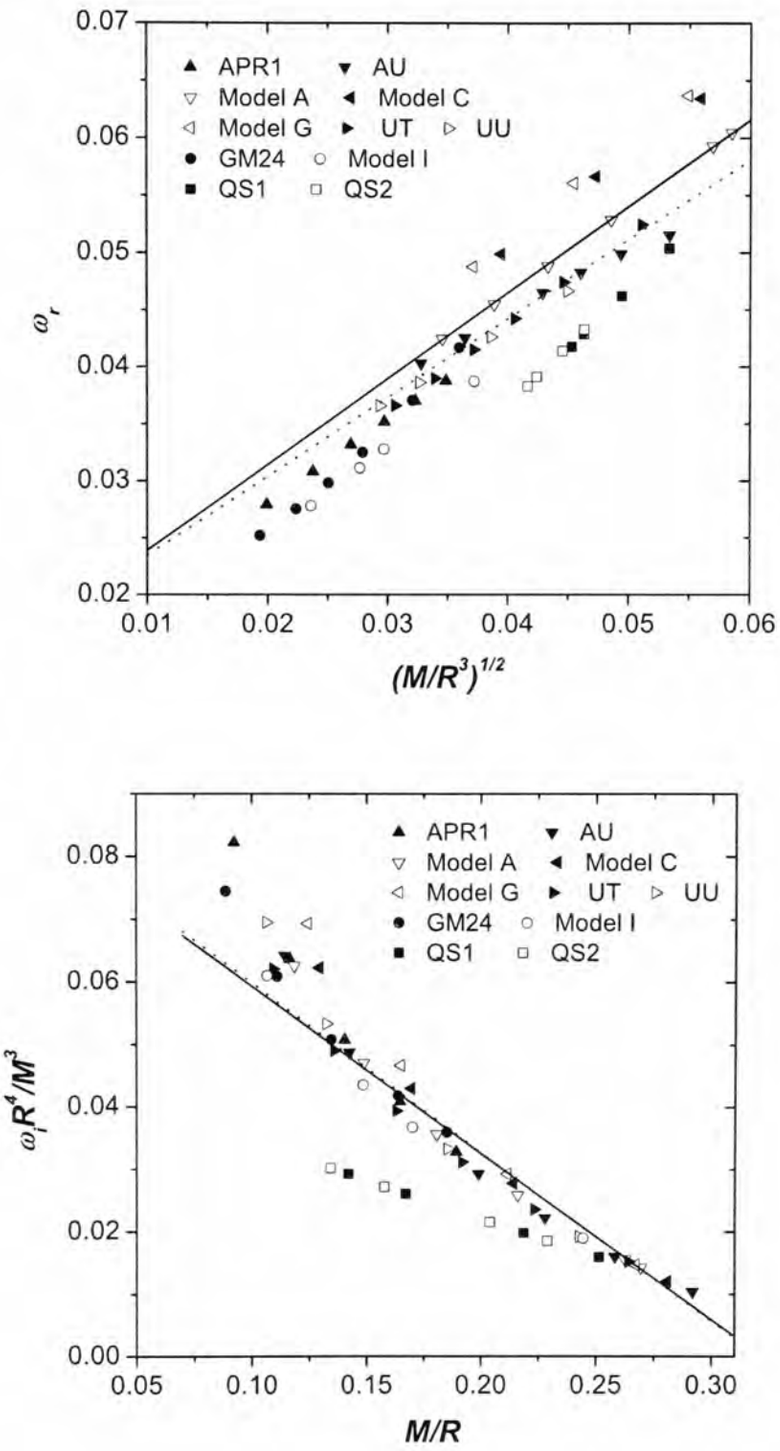

Figure 6.15: Pattern of f mode real part is plotted according to the proposal of Andersson and Kokkotas. Solid lines are universality proposed by Andersson and Kokkotas (Eq. 6.19 and 6.20), and dotted lines are universality proposed by Benhar *et al.* (Eq. 6.21 and 6.22).

is obviously larger in QS than NS, it is because Eq. 6.6 demonstrates pattern of NS, while QS follow another trend as Eq. 6.5.

For the proposal of Andersson and Kokkotas, and Benhar *et al.*, accuracy is not high, contain about 10% average error. Consider the mode distribution in Fig. 6.15, data points plotted according to their proposals are much scattered than in Fig. 6.2 and Fig. 6.5. We believe this is because their proposed functional form, a straight line function of the mean density M/R^3, is not an appropriate description to the pattern of f mode in spite of the physical implication. Their proposal cannot be transformed into a dimensionless form, which violates the principle of universality and breaks the symmetry between real and imaginary part of f mode, detail is presented in Appendix E.

The universality of Leung and Tsui can be expressed in a dimensionless form, hence its inferred results are more precise than Andersson and Kokkotas, and Benhar *et al.*. However its accuracy is worse than our new proposal, not only because the data points are more scattered against compactness than η, but their formula for imaginary part of f mode is also inappropriate. As shown in Fig. 6.2, the mode distribution is closer to a cubic function instead of the quadratic Eq. 6.7. We suggest an appropriate choice of normalization, such as using R^4/M^3 instead of M as suggested by Andersson and Kokkotas, would improve the accuracy of universality and inversion values.

We also compare the applicability of universality proposal by accounting for their accuracy. We consider the root-mean-square percentage error σ defined as

$$\sigma \equiv \sqrt{\frac{1}{N}\sum_{i}^{N}\left(1-\frac{\hat{y}_i}{y_i}\right)^2}\,, \tag{6.23}$$

where N is the population of QNM considered, y_i and $\hat{y}_i$ are respectively the exact and inferred values of of the i-th QNM. Similar to the previous test, we calculate σ of data presented in [5], our computed data for NS, and our computed values for QS. As shown in Table 6.4, our proposal is one order

frequency	proposal	σ_1	σ_2	σ_3
real	Andersson and Kokkotas [5]	0.099	0.10	0.2
real	Benhar *et al.* [25]	0.10	0.088	0.14
real	Leung and Tsui [4]	0.042	0.058	0.21
real	current thesis	0.0056	0.0037	0.0070
imaginary	Andersson and Kokkotas [5]	0.079	0.18	0.51
imaginary	Benhar *et al.* [25]	0.083	0.19	0.52
imaginary	Leung and Tsui [4]	0.061	2.2	0.55
imaginary	current thesis	0.021	0.015	0.011

Table 6.4: Root-mean-square percentage error σ of different proposals of f mode universality. The values of σ is calculated by (i) mode frequencies obtained by Andersson and Kokkotas (σ_1); (ii) mode frequencies computed ourselves (σ_2); (iii) mode frequencies of QS computed ourselves (σ_3).

more accurate for ω_r of f mode, while the error of imaginary part is reduced by several times. Furthermore, our universality is the only one that can precisely describe the pattern of QS. Therefore we claim our proposal can infer more precise values in general.

In addition, we present another method to get the value of R apart from employing universality of moment of inertia Eq. 6.6 to obtain from M and I. Recall that accuracy is not improved in our modified universality for real frequency for w mode. We find from work of Andersson and Kokkotas [5] that the mode distribution is more convergent when radius instead of mass is used as normalization. Following their approach, we plot the normalized frequencies in Fig. 6.16, and fit their distribution by a quadratic function

$$R\omega = 4.82 - 13.5\left(\frac{M}{R}\right) + 9.63\left(\frac{M}{R}\right)^2 . \tag{6.24}$$

It is reminded that employing M or R for normalization are qualitatively the same, one can always transform to another by multiplying the dimensionless compactness M/R. As shown in the figure, the universality best demonstrates mode frequencies of stars with high compactness, and exactness becomes worse but tolerable for $M/R \lesssim 0.18$. This indicates that real frequency of w mode

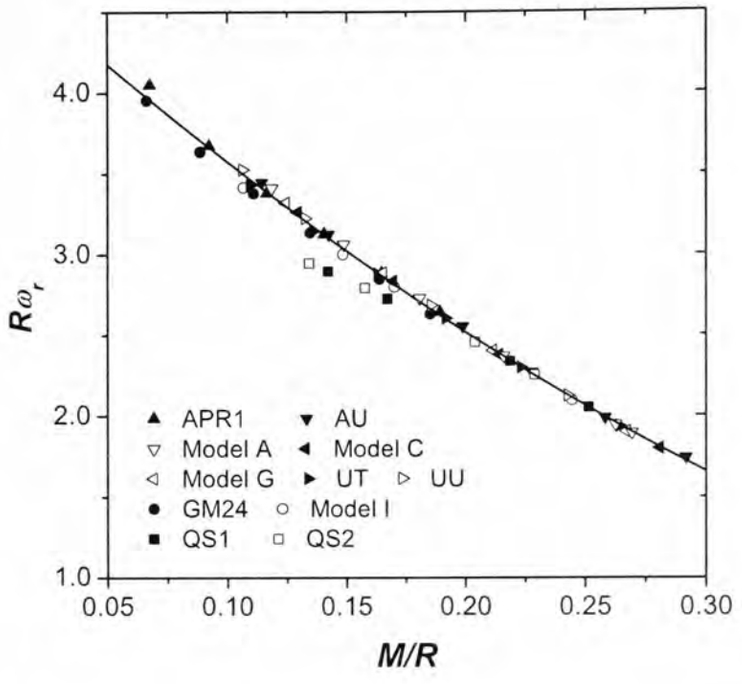

Figure 6.16: Real frequency of w mode is normalized by radius R and plotted against compactness ratio. Results of 10 ordinary EOS and 2 QS models show fair agreement with the quadratic fitted (solid line).

is a plausible source to determine the radius of a compact star.

As a summary, our new inference scheme based on universality in η is more efficient than previous proposal. It does not only give more precise values, but our formalism is also applicable for both NS and QS.

6.6 Summary

In this chapter, we have proposed a new presentation of universality of gravitational wave QNM spectrum for compact stars, which is to substitute radius by the moment of inertia as the geometric factor. Real and imaginary frequencies of f mode, first w mode and first w-II mode are computed for compact stars constructed by ten ordinary nuclear matter EOS and two quark matter models. When comparing the universality in compactness and the moment of

inertia, we find that mode frequencies of NS are less scattered in f mode, w-II mode and imaginary part of w mode, while the quality of w mode frequency is not much improved in our new formalism. The QNM of QS are also well described by the new universalities, which is conventionally believed to possess extraordinary behaviors.

The improvement is investigated by analyzing relationship between the matter distribution and the QNM spectra. We first review the case of the Tolman VII model, which is usually used as a role model to universality. It is found that the density profile of a TVII star is very close to a polytropic star with $\gamma = 2.3$. We realize that the effectiveness of TVII model is because $\gamma = 2.3$ is about the average stiffness of realistic EOS models. A survey on effect of stiffness is then conducted, by comparing the moment of inertia and QNM spectra of polytropic stars with a wide range of γ. When plotting against compactness, most quantities shift towards high compactness region as γ increases. Therefore, when moment of inertia is employed as the geometric parameter, influence of stiffness on QNM is suppressed due to cancellation. This is the empirical reason for the nice universalities observed. A more physical reason is that the moment of inertia is a quantity which better accounts for dynamics of mode oscillations of f modes and spacetime modes. Whereas radius is sensitive to low density regime of EOS and physics near surface of a star, the mode frequencies we considered in this section are dominated by global matter distribution of stars, which the dependence is similar to the moment of inertia. In fact, normalized QNM distribution demonstrate unified patterns on complex plane, e.g. Fig. E.1 and E.2, which is believed to be originated from physics underlying GW pulsation. It suggests that the dispersion of data points on universality against compactness, is merely a consequence of wrong choice of parameters.

After obtaining the more precise universality, we propose a simple application with the fitted formulae, which is to infer stellar parameters M, R and I

from GW signals detected. From the data presented in Table 6.3, we find that our new universalities yield more accurate results than previous proposals. In addition, parameters of QS can also be obtained under our new formalism, this would prompt investigation of quark matter in astrophysics.

This chapter in the current thesis is our first trial to analyze the relationship between QNM and the moment of inertia, there are more questions that maybe meaningful with this choice of geometric factor. In Section 6.5, we make use of 6 formulae to get 3 values, which the system is over-determining. Is it possible to gain more information from the extra mode frequencies, for example the internal structure just as the work in [10]? Besides, we only consider QNM which are mostly determined by matter distribution, what would be the distribution of p mode if they are plotted against η? Answering these interesting questions will be our next goal of endeavor.

Finally, we want to analyze the robustness of f mode and w mode against temperature by our new proposal of universality. As shown in Fig. 5.11, R changes for 10% upon cooling, while the variation of M and I are less than 2%. This is because temperature effect is significant in low density range only, while the behavior of nuclear matter are dominated by properties of elementary particles. As the mass of a compact star is dominated by matter in high density site, and the moment of inertia is determined by the distribution of dense matter, thus M and I are less sensitive to temperature than R. According to our proposal of universality, f mode and w mode distribute as functions of mass and the moment of inertia, it is hence expected that these modes are insensitive to temperature variations, which agrees with our conclusion in Chapter 5.

Chapter 7

Quark star properties and gravity mode oscillation

In Chapter 5, we show that g mode frequency is very sensitive to the temperature as well as the dynamic EOS. For both QS and NS, g mode drops linearly with temperature if beta equilibrium is held. On the other hand, mode frequency converges to a non-zero value if composition is preserved during the oscillation. These features cannot be explained by characteristics of the static stellar structure, which is nearly unchanged. This suggests that the pulsation mechanism of g mode is closely related to the local property of nuclear matter, that arouses our interest to investigate. However, the Shen EOS is derived from complicated calculations, which analytical study is not feasible. In order to understand the features, we focus on g mode of QS, of which the MIT bag model EOS can be expressed as series of approximations.

7.1 Introduction

In Section 4.3, we state that the restoring force of g mode oscillation is the buoyancy of nuclear matter, and claim that its frequency is specified by the sign of Schwarzschild discriminant. This issue is best illustrated in the context of the Newtonian theory of stellar pulsation, where the equation of motion is

presented as Eq. C.1 and C.2 in Appendix C. It is proposed that the stability of Newtonian normal mode is governed by the Brunt-Väisälä (BV) frequency, defined as

$$\omega_{BV}^2 = g^2(\frac{1}{c_0^2} - \frac{1}{c_s^2}) \ , \tag{7.1}$$

where $c_0^2 = dp/d\rho$ is the speed of sound according to the static EOS of stellar background [19, 44]; g is the classical gravity $g(r) = Gm(r)/r$. It is obvious that the sign of BV frequency square is identical to that of the Schwarzschild discriminant, because their sign-determining groups are the same as

$$\psi \equiv \frac{1}{c_0^2} - \frac{1}{c_s^2} \ . \tag{7.2}$$

By definition, it is a measure of the difference between the dynamic and the background speed of sound. Consider a fluid element experiences a perturbation in the radial direction, the Lagrangian pressure change Δp is the same as the pressure change of the background. However thermodynamic properties of the element change according to the dynamic EOS, while those of background follow the static EOS. Since density normally decreases radially outwards, the fluid element will be pulled back by gravity if the Lagrangian change of energy density $\Delta\rho$ (as a post-Newtonian analog to the mass density) of the fluid element is less than that of the background. Then the perturbation becomes stable and the fluid element oscillates by the restoring force of buoyancy.

Since g mode pulsation originates from the mechanism described above, it is proposed that the gravity normal mode frequency has the same order of magnitude as the average value of the BV frequency [19]. However, the Newtonian formalism is merely a simplification of the general relativistic formalism, and results of the linearized relativity may not necessarily follow the same trend. Extra verification is done to compare the mode frequencies obtained by both formalisms, and our work is presented in Appendix C. As shown in Fig. C.1, the g mode of QS computed by the Newtonian method are smaller than relativistic ones by about 10%, and the error is nearly unchanged with

temperature. This suggests that the g mode frequencies obtained by either linearized relativity or Newtonian formalism follow the same qualitative behavior against temperature. As a result, it is possible to deduce the behavior of relativistic g mode from the dependence of Newtonian BV frequency, which is our objective in this chapter.

7.2 g mode frequencies of quark stars

Recalling in Section 5, we have seen that β mode and Y_p mode frequencies of QS exhibit completely different behaviors against temperature. By analyzing the trend of g mode under each dynamic EOS, we are able to obtain some information about the quark matter EOS In particular, we are interested in two phenomena:

1. Temperature is definitely a factor affecting the stability of fluid motion. We find empirically in Fig.s 5.2, 5.1 and 5.8 that the β mode frequency of QS changes linearly with temperature around the range $\omega_r \approx 1$ Hz. But this result is obtained under the assumption that the temperature profile is relativistic isothermal. We are hence curious to know whether the linear relationship is caused by the magnitude of temperature, or it is solely a special phenomenon imposed by the relativistic isothermal profile. In addition, we want to see how temperature profile affects the g mode frequency.

2. Also shown in Fig.s 5.2, 5.1 and 5.8, Y_p mode is not sensitive to temperature, so we want to see what factor(s) instead determines the Y_p mode frequency. In Subsection 5.1.2, we have shown that Y_p mode frequency varies a lot if quark matter model with different m_s is employed. Therefore, we decide to investigate a more explicit dependence of Y_p mode on m_s, such that if this kind of GW signal is detected, it can provide us

some information on quark matter.

We should clarify that only one dynamic EOS is followed at a particular instance, therefore β mode and Y_p mode do not coexist. One factor determining the choice of dynamic EOS is that if the corresponding characteristic timescale is shorter than the period of stellar oscillation. For β mode to exist, it requires quark beta decay is fast enough to restore the beta equilibrium within a pulsation period. This criterion is invalid for f mode and w mode, because their oscillation frequencies are much higher than most theoretical expectations of quark beta decay timescale [19, 40]. Therefore most authors assume the preservation of chemical composition in QNM frequencies calculations (e.g. [12]). In fact, this issue is not particularly important for finding f mode and w mode because those modes are only sensitive to the matter distribution instead of dynamic property of composed matter, as we have described in Chapter 6. The situation is, however, completely different for g mode investigations. We roughly estimate the characteristic time of quark beta decay by considering its neutrino number flux $\dot{N}_T$ yielded [45]. We find that it can be shorter than the g mode oscillation period at high temperature. As suggested by Burrows [45],

$$\dot{N}_T = 5.4 \times 10^{30} T_9^6 \left(\frac{E_F}{500\ MeV} \right)^2 cm^{-3} s^{-1} \tag{7.3}$$

where E_F is the Fermi energy of quarks. Since each beta decay creates one neutrino, the average time of quark beta decay is estimated as $\tau \sim N/\dot{N}_T$. I put in typical data of quark matter in QS, where $N \sim 1$ fm^{-3}, $E_F \sim 300$ MeV, and g mode frequency of QS is about 100 Hz, we found that the beta decay time is faster than the oscillation period if $T \gtrsim 5$ MeV, but the relationship reverses at $T \lesssim 3$ MeV. This range of temperature for dynamic EOS change is consistent with the calculation conducted by Fu *et al.* [40]. As a result in Subsection 7.2.1, we consider β mode of QS with average temperature higher than 5 MeV; on the other hand, in Subsection 7.2.2 we consider the Y_p mode of zero temperature QS for consistence, and also simplicity.

7.2.1 Temperature profile and β mode frequency

In this subsection, we are interested in the dependence of β mode on temperature and temperature profile. As described in Chapter 3, we have to obtain the EOS in the form $\rho = \rho(p)$ by an additional information about temperature, usually given as a function of radius $T = T(r)$. In reality, temperature profile of newborn compact stars have to be generated by full general relativistic core collapse simulations. The resultant distributions are highly sensitive to the initial conditions, EOS employed, and the amount of physical effects incorporated. Universal pattern is difficult to be extracted from results of different simulation, only the magnitude of temperature can be roughly compared. In order to give a brief account for the temperature effect on g mode oscillation, we apply two simple temperature profiles on QS. One is the relativistic isothermal profile Eq. 5.1, which is particularly good for describing QS, as it is anticipated that the conductivity of QS is higher than that of ordinary neutron stars, even superconductivity may exist [46, 47]. For simplicity, we pick the other one as the purely isothermal profile,

$$T(r) = T_0 \ , \tag{7.4}$$

which is different from the previous model by a redshift factor.

In order to consider the effect of different temperature profile on the same star, all the stars investigated in this subsection have the same baryon number $N_{\text{baryon}} = 2.2 \times 10^{57}$ (corresponding to a pure neutron star with baryonic mass $\approx 1.84\ \mathrm{M}_\odot$), , in order to simulate different cooling stages of one QS. The EOS of the stars are the same, which is the MIT bag model described in Chapter 3, with strange quark mass $m_s = 150$ MeV and the bag constant $B = (154.5)^4\ \mathrm{MeV}^4$.

The β mode frequencies are tabulated as Table 7.1 for different temperatures and temperature profiles. We find that the frequency of the first β mode

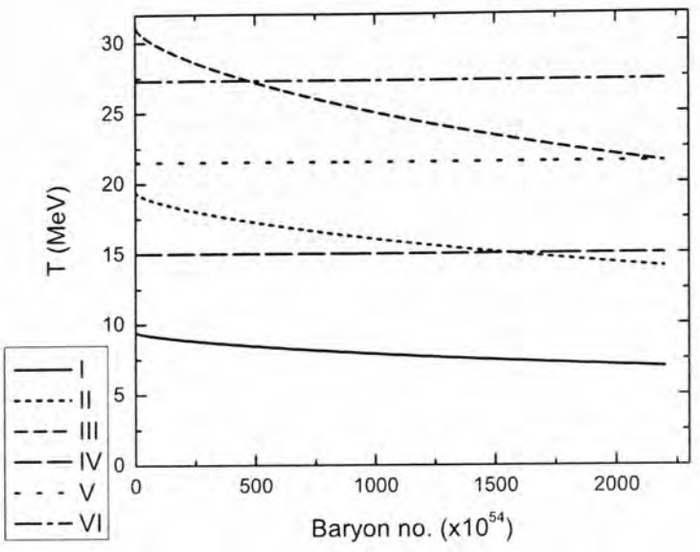

Figure 7.1: Temperature distribution against enclosed baryon number of the 6 stars described in Table 7.1. The total number of baryon is fixed as $N_{\text{baryon}} = 2.2 \times 10^{57}$.

Star	R (km)	M ($M_\odot$)	T_0 (MeV)	profile	ν_C (Hz)	ν_D (Hz)
I	9.478	1.553	5	relativistic	5.7	6.5
II	9.458	1.578	10	relativistic	11.6	13.3
III	9.356	1.624	15	relativistic	18.5	21.2
IV	9.461	1.575	15	constant	34.0	39.0
V	9.411	1.606	21.5	constant	50.1	57.5
VI	9.250	1.640	27.3	constant	67.5	77.8

Table 7.1: The frequency of the first β mode are listed for different temperatures. Notation 'relativistic' represents the QS with relativistic isothermal profile; while 'constant' represents QS with purely isothermal profile. All stellar configurations have the same baryon number $N_{\text{baryon}} = 2.2 \times 10^{57}$. Results calculated by the Newtonian formalism with the Cowling approximation (ν_C) and the linearized relativistic formalism (ν_D) are both presented, we find that the Newtonian approach usually gives values smaller than those produced by the linearized relativistic approach for about 15% .

is very sensitive to temperature profile. To account for this effect, we have constructed purely isothermal QS with $T_0 = 15, 21.5, 27.3$ MeV to compare with the relativistic isothermal cases with $T_0 = 15$ MeV (star III). The reasons of the values chosen are: for star IV, 15 MeV is chosen to check the heuristic relationship of the same characteristic temperature 15 MeV; for star V, 21.5 MeV gives the same surface temperature as star III; for star VI, 27.3 MeV is the average temperature inside star III.

From the temperature distribution plotted in Fig. 7.1, we can see that the average temperature of star IV and V are lower than star III, but their g mode frequencies are respectively 1 and 2 times larger than that of star III. Consider star III and VI have the same average temperature, but g mode frequency of star VI is about 3 times larger. These results tell us that temperature profile is a more significant effect on β mode frequency than the average temperature. The physical reason can be known from the relationship between the temperature profile and the BV frequency. In the Newtonian point of view, BV frequency measures the convective tendency of a fluid element. Convection takes place more easily, if temperature of a deeper region is hotter than the above. From Fig. 7.1, we see the relativistic isothermal stars (star I, II, III) are hotter near the stellar center, due to the redshift factor. Therefore, their convective stability is lower than that of the purely isothermal stars which have zero temperature gradient (stars IV, V, VI), and the β mode frequencies of relativistic isothermal stars are hence lower.

In addition, the linearity of β mode frequency on temperature exists in both temperature profiles. We examine this property by verifying the dependence of BV frequency through perturbation analysis. In Eq. 7.1, the square of BV frequency depends on g^2 and ψ. At a particular distance r from the centre, the term g^2 is determined by the stellar mass enclosed, which mainly depends on magnitude of energy density ρ of the enclosed matter. By Eq. B.1, the leading dependence of ρ is 4-th power of chemical potentials, and we will

show later that the magnitude of chemical potentials are hardly sensitive to temperature, therefore g^2 does not give any temperature dependence in the first approximation. So the magnitude of BV frequency mainly relies on ψ. After some manipulation of the total derivative of ρ, we get

$$\psi = \frac{d\rho}{dp} - \left(\frac{\partial\rho}{\partial p}\right)_s = \left(\frac{\partial\rho}{\partial s}\right)_p \frac{ds}{dp} , \tag{7.5}$$

which we express the energy density as an implicit function of the entropy per particle s and pressure; there is no other degree of freedom because the dynamic EOS is the same as the static EOS except the entropy preservation.

We first consider the term $\left(\frac{\partial\rho}{\partial s}\right)_p$. p and ρ in the massless MIT bag model is simply related by $\rho = 3p + 4B$, which causes a vanishing BV frequency. A non-zero strange quark mass would break this symmetry, introduces extra terms

$$A(\mu_s, T) \equiv \rho - 3p - 4B . \tag{7.6}$$

The expression of $A(\mu_s, T)$ is referred to Eq. B.3 in Appendix B, which is a function of μ_s and T but not other chemical potentials. The magnitude of μ_s is about 300 MeV, which is larger than m_s and $T \sim 10$ MeV, we conduct perturbation in quantities ms/μ_s and T/μ_s. The leading order expansion of $A(\mu_s, T)$ is

$$\rho - 3p - 4B = A(\mu_s, T) \approx \frac{3}{2\pi^2}\mu_s^2 m_s^2 + \frac{1}{2}m_s^2 T^2 . \tag{7.7}$$

Since p is held constant, $\left(\frac{\partial\rho}{\partial s}\right)_p$ effectively reduces to $\left(\frac{\partial A}{\partial s}\right)_p$.

Next, we consider the leading order expansion of the entropy per particle s. By definition, the entropy per particle of a fluid element is the fraction of the entropy density S and the total number density of particles (3 quarks plus electron, c.f. Eq. 3.10) N, i.e.

$$s = \frac{S}{N} ; \tag{7.8}$$

their expressions can be found in Appendix B. We stress that the conserved quantity of the adiabatic sound speed is the entropy per particle s instead of

the entropy density S, this issue is easily confused. Since both the expression of S and N involve the chemical potentials of all 4 particles, the relationship between them has to be obtained by constraints. The beta equilibrium relates μ_d, μ_s, and μ_e by Eq. 3.8. The relationship between μ_s and μ_u imposed by the charge neutrality is however complicated, so we employ the perturbation theory and obtain the leading order relation is

$$\mu_u \approx \mu_s \left(1 - \frac{1}{4}\left(\frac{m_s}{\mu_s}\right)^2\right) . \tag{7.9}$$

Incorporating the above equation, we can obtain the leading order expansions of S and N as

$$S \approx T\left(3\mu_s^2 - m_s^2 + \frac{14\pi^2}{9}T^2\right) , \tag{7.10}$$

$$N \approx \mu_s\left(\frac{3}{\pi^2}\mu_s^2 - \frac{9}{4\pi^2}m_s^2 + 3T^2\right) . \tag{7.11}$$

So the total derivatives of A and s can be expressed as

$$dA = \left(\frac{\partial A}{\partial \mu_s}\right)_T d\mu_s + \left(\frac{\partial A}{\partial T}\right)_{\mu_s} dT , \tag{7.12}$$

$$\begin{aligned} ds = \frac{1}{N^2}\Bigg\{ & \left[N\left(\frac{\partial S}{\partial \mu_s}\right)_T - S\left(\frac{\partial N}{\partial \mu_s}\right)_T\right] d\mu_s \\ & + \left[N\left(\frac{\partial S}{\partial T}\right)_{\mu_s} - S\left(\frac{\partial N}{\partial T}\right)_{\mu_s}\right] dT\Bigg\} , \end{aligned} \tag{7.13}$$

where

$$\left(\frac{\partial A}{\partial \mu_s}\right)_T \approx \frac{3}{\pi^2}\mu_s m_s^2 \quad ; \quad \left(\frac{\partial A}{\partial T}\right)_{\mu_s} \approx m_s^2 T ; \tag{7.14}$$

$$\left(\frac{\partial S}{\partial \mu_s}\right)_T \approx 6\mu_s T \quad ; \quad \left(\frac{\partial S}{\partial T}\right)_{\mu_s} \approx 3\mu_s^2 - m_s^2 ; \tag{7.15}$$

$$\left(\frac{\partial N}{\partial \mu_s}\right)_T \approx \frac{9}{\pi^2}\mu_s^2 - \frac{9}{4\pi^2}m_s^2 \quad ; \quad \left(\frac{\partial N}{\partial T}\right)_{\mu_s} \approx 6\mu_s T . \tag{7.16}$$

Consider only the first order terms, the constraint of constant pressure relates $d\mu$ and dT as,

$$dp = \left(\frac{\partial p}{\partial \mu_s}\right)_T d\mu_s + \left(\frac{\partial p}{\partial T}\right)_{\mu_s} dT = 0 , \tag{7.17}$$

where

$$\left(\frac{\partial p}{\partial \mu_s}\right)_T \approx \left(\frac{3}{\pi^2}\mu_s^2 - \frac{2}{\pi^2}m_s^2\right)\mu_s \; ; \; \left(\frac{\partial p}{\partial T}\right)_{\mu_s} \approx (3\mu_s^2 - m_s^2)T \; . \tag{7.18}$$

Combine the above equations will lead to

$$d\mu_s = -\frac{\pi^2(3\mu_s^2 - m_s^2)}{(3\mu_s^2 - 2m_s^2)}\frac{T}{\mu_s}dT \; . \tag{7.19}$$

It is noted that Eq. 7.19 also implies that a change of T only varies μ_s slightly, scaled by the term T/μ_s, therefore we can assume μ_s is constant to T at the leading order approximation. Now we can obtain the dependence of $\left(\frac{\partial A}{\partial s}\right)_p$. In the denominator,

$$\begin{aligned} ds &\approx \frac{1}{N^2}\Bigg\{\mu_s\left(\frac{3}{\pi^2}\mu_s^2 - \frac{9}{4\pi^2}m_s^2\right)\left(-6\frac{\pi^2(3\mu_s^2 - m_s^2)}{(3\mu_s^2 - 2m_s^2)}T^2 + (3\mu_s^2 - m_s^2)\right) \\ &\quad -T\left(3\mu_s^2 - m_s^2\right)\left(-9\left(\mu_s^2 - \frac{1}{4}m_s^2\right)\frac{(3\mu_s^2 - m_s^2)}{(3\mu_s^2 - 2m_s^2)}\frac{T}{\mu_s} + 6\mu_s T\right)\Bigg\}dT \\ &\approx \frac{1}{N^2}\mu_s\left(\frac{3}{\pi^2}\mu_s^2 - \frac{9}{4\pi^2}m_s^2\right)(3\mu_s^2 - m_s^2)dT \; , \end{aligned} \tag{7.20}$$

where we have neglected all terms equal to or higher order than $(T/\mu_s)^2$ and $(T/m_s)^2$; similarly in the numerator,

$$dA \approx \left(-3\frac{(3\mu_s^2 - m_s^2)}{(3\mu_s^2 - 2m_s^2)} + 1\right)m_s^2 T dT \; . \tag{7.21}$$

It is obvious that there is a T dependence in the numerator of $\left(\frac{\partial A}{\partial s}\right)_p$, while the denominator is dominated by powers of μ_s and hence insensitive to temperature. In sum, the term $\left(\frac{\partial \rho}{\partial s}\right)_p$ contributes a first order T dependence to ω_{BV}^2.

Similarly, we consider the contribution of ds/dp. By definition, the term is identical to $(ds/dr)/(dp/dr)$, which is actually a partial derivative $\left(\frac{\partial s}{\partial p}\right)_F$ subjected to the constraints F of the background, i.e. beta equilibrium, charge neutrality, and the temperature profile. Pressure gradient in the denominator is given by the TOV equation Eq. 2.9. We express Eq. 2.9 to the leading order

approximation

$$\frac{dp}{dr} \approx -\frac{1}{2}\left(\frac{3}{\pi^2}\mu_s^4 - \frac{5}{2\pi^2}\mu_s^2 m_s^2 + 6\mu_s^2 T^2\right)\frac{d\nu}{dr} \,. \tag{7.22}$$

On the other hand, the derivative of p can also be written in terms of μ_s and T,

$$\frac{dp}{dr} = \left(\frac{\partial p}{\partial \mu_s}\right)_T \frac{d\mu_s}{dr} + \left(\frac{\partial p}{\partial T}\right)_{\mu_s} \frac{dT}{dr} \,, \tag{7.23}$$

where the partial derivatives are the same as Eq. 7.18. The Eq.s 7.22 and 7.23 hence provide an relationship between $d\mu_s/dr$ and dT/dr, we express it up to the leading order,

$$\frac{d\mu_s}{dr} + \pi^2 \frac{T}{\mu_s}\frac{dT}{dr} \approx -\frac{1}{2}\mu_s \frac{d\nu}{dr} \,. \tag{7.24}$$

The numerator ds/dr is expanded as,

$$\begin{aligned} \frac{ds}{dr} &= \frac{1}{N^2}\Bigg\{ \left[N\left(\frac{\partial S}{\partial \mu_s}\right)_T - S\left(\frac{\partial N}{\partial \mu_s}\right)_T\right]\frac{d\mu_s}{dr} \\ &\quad + \left[N\left(\frac{\partial S}{\partial T}\right)_{\mu_s} - S\left(\frac{\partial N}{\partial T}\right)_{\mu_s}\right]\frac{dT}{dr}\Bigg\} \,, \end{aligned} \tag{7.25}$$

where the partial derivatives are given by Eq.s 7.15 and 7.16. Its leading order is hence

$$\begin{aligned} \frac{ds}{dr} &\approx \frac{1}{N^2}\Bigg\{ \left[\frac{18}{\pi^2}\mu_s^4 T - \frac{27}{\pi^2}\mu_s^4 T\right]\left(-\pi^2 \frac{T}{\mu_s}\frac{dT}{dr} - \frac{1}{2}\mu_s \frac{d\nu}{dr}\right) \\ &\quad + \left[\frac{9}{\pi^2}\mu_s^5 - 18\mu_s^3 T^2\right]\frac{dT}{dr}\Bigg\} \,. \end{aligned} \tag{7.26}$$

Here we can see the temperature profile plays a role in apart from the magnitude of temperature.

It is noted that $d\nu/dr$ is not sensitive to temperature. From Eq. 2.8, $d\nu/dr$ is a function of pressure and mass at the distance r, where mass is a functional of ρ by Eq. 2.7. By Eq.s B.2 and B.1, the leading order dependence of p and ρ are $\frac{3}{4\pi^2}\mu_s^4$ and $\frac{9}{4\pi^2}\mu_s^4$ respectively, so $d\nu/dr$ does not contribute temperature dependence at the leading order.

We check the behavior of the two terms in Eq. 7.26 one by one. For the first term,

$$\left[\frac{18}{\pi^2}\mu_s^4 T - \frac{27}{\pi^2}\mu_s^4 T\right]\left(-\pi^2\frac{T}{\mu_s}\frac{dT}{dr} - \frac{1}{2}\mu_s\frac{d\nu}{dr}\right) = \frac{9}{\pi^2}\mu_s^4 T\left(\pi^2\frac{T}{\mu_s}\frac{dT}{dr} + \frac{1}{2}\mu_s\frac{d\nu}{dr}\right) , \tag{7.27}$$

which is proportional to T. For the second term,

$$\left[\frac{9}{\pi^2}\mu_s^5 - 18\mu_s^3 T^2\right]\frac{dT}{dr} \approx \frac{9}{\pi^2}\mu_s^5\frac{dT}{dr} , \tag{7.28}$$

therefore the temperature dependence is solely determined by the behavior of temperature gradient. Suppose we have a temperature profile that varies homogeneously as temperature, i.e.

$$\frac{dT}{dr} \propto T , \tag{7.29}$$

the second term in Eq. 7.26 is proportional to T. Therefore, ds/dr is linearly proportional to temperature at the leading order. Recall Eq. 7.22 that the behavior of dp/dr is dominated by μ_s^4, so it hardly varies as temperature. As a result, ds/dp contributes a first order T dependence to the BV frequency, together with the contribution of $\left(\frac{\partial\rho}{\partial s}\right)_p$, we get $\omega_{BV} \propto T^2$, and hence explains the linearity of β mode on temperature. In addition, BV frequency square is proportional to m_s^2 due to the contribution of $\left(\frac{\partial A}{\partial s}\right)_p$ in Eq. 7.21. It is consistent with the fact that g mode is absent if strange quark mass is zero.

Finally, we stress that the temperature dependence of β mode we have shown is very depending on Eq. 7.29. So the frequency of a β mode will not exhibit a linear trend with temperature if there is inhomogeneous or dramatical change in the temperature profile. Consider the profile we have studied, for the relativistic isothermal profile,

$$\frac{dT}{dr} = T\left(-\frac{1}{2}\frac{d\nu}{dr}\right) \propto T , \tag{7.30}$$

so we can see the linearity of the mode frequencies. For the purely isothermal profile of which the temperature gradient is zero, the second term in Eq. 7.26

vanishes, so the first term governs the temperature dependence which also gives a first order of T. Therefore both of our temperature profile give β mode depends linearly with temperature. However, if the temperature profile changes, for example from relativistic isothermal to purely isothermal, then the linearity does not hold. It can be verified by data in Table 7.1 that the β mode frequency is higher for purely isothermal stars than relativistic isothermal stars, even though the average temperature of the purely isothermal one is lower.

7.2.2 Strange quark mass and Y_p mode frequency

At first glance, It is a little bit surprising that Y_p mode oscillation still exists in zero temperature. As entropy vanishes at zero temperature, stellar oscillation is implicitly adiabatic. By this fact, it is easily misunderstood that g mode oscillation does not present, because $(\partial\rho/\partial p)_s$ is believed to be the same as $d\rho/dp$ and BV frequency would vanish. In fact, the dynamic EOS deviates from the static EOS in other degrees of freedom apart from the entropy preservation. Consider the MIT bag model we use, all thermodynamic quantities are function of 5 variables μ_u, μ_d, μ_s, μ_e, T, which are related to each other by 4 constraints. Despite the isothermal condition and entropy preservation are coincident in zero temperature case, preservation of composition and beta equilibrium yield different values of chemical potentials, so g mode exists. In this subsection, we construct zero temperature QS with the same gravitational mass but composed by quark matter model with m_s. We try to obtain explicit m_s mode dependence of Y_p mode frequency, which should be useful to place some bounds on quark matter EOS if GW signal of a cold QS is detected.

We obtain the 1-st Y_p mode frequencies for 3 stars with $m_s = 70, 130, 150$ MeV. Bag constant is set to be $B^{1/4} = 154.5$ MeV. As stated before, we assume that the QS are cold such that temperature effect can be neglected, so we consider

m_s (MeV)	R (km)	ν_g (Hz)
0	10.048	0
70	9.886	22.3
130	9.548	83.0
150	9.401	115.0

Table 7.2: Frequencies of the first g mode ν_g of QS calculated by the linearized relativistic formalism. The QS are constructed by the zero temperature MIT bag model with different m_s. The three QS considered have the same gravitational mass $M = 1.6\ \mathrm{M}_\odot$.

the stars have zero temperature. The calculated results are presented in Table 7.2. It is observed that the 1-st g mode is highly dependent on strange quark mass. Within the typical range of strange quark mass $m_s \sim 70 - 130$ MeV, the frequency can differ by 4 times. Futher analyzing the data, it is not difficult to observe the dependence of Y_p mode frequency and m_s is roughly quadratic, i.e. $\nu_g \sim m_s^2$.

To explore the reason behind the quadratic relationship, we investigate the sign-determining group of BV frequency Eq. 7.1 in the zero temperature limit

$$\psi = \frac{1}{c_0^2} - \frac{1}{c_s^2} = \left(\frac{d\rho}{dp}\right)_\beta - \left(\frac{d\rho}{dp}\right)_{Y_p} . \tag{7.31}$$

Since temperature is zero, according to Eq. B.6 the entropy density of each fluid element is exactly zero in our model. So g mode oscillation is caused by the different constraint conditions between the static EOS, which follows beta equilibrium, and dynamic EOS, which chemical potential is preserved.

The zero temperature finite mass MIT bag model is obtained by setting $T = 0$ in Eq.s B.2 and B.1. It is noted that although our EOS is obtained by the Sommerfield expansion, the expressions are exact in the zero temperature limit [16]. We do not use explicit expressions of p and ρ because it is more

convenient to consider $A(\mu_s, T=0)$ in Eq. 7.6,

$$\begin{aligned} A(\mu_s, T=0) &= \frac{3}{\pi^2} m_s^2 \Big(\frac{1}{2}\mu_s \sqrt{\mu_s^2 - m_s^2} \\ &\quad - m_s^2 \log(\sqrt{\mu_s + m_s} + \sqrt{\mu_s - m_s}) + m_s^2 \log\sqrt{2m_s} \Big) \\ &\equiv m_s^2 G(\mu_s) \ , \end{aligned} \tag{7.32}$$

where we have extracted a m_s^2 and define a new function $G(\mu_s)$. Then Eq. 7.31 can be rewritten as

$$\psi = m_s^2 \left(\frac{dG}{d\mu_s}\right) \left[\left(\frac{\partial \mu_s}{\partial p}\right)_\beta - \left(\frac{\partial \mu_s}{\partial p}\right)_{Y_p} \right] = m_s^2 \left(\frac{dG}{d\mu_s}\right) \frac{\left(\frac{\partial p}{\partial \mu_s}\right)_{Y_p} - \left(\frac{\partial p}{\partial \mu_s}\right)_\beta}{\left(\frac{\partial p}{\partial \mu_s}\right)_{Y_p} \left(\frac{\partial p}{\partial \mu_s}\right)_\beta} \ , \tag{7.33}$$

where we have used the fact that G is a function of μ_s only.

Although the two partial derivatives in Eq. 7.33 depend on different EOS, they can be expressed in the same form

$$\frac{dp}{d\mu_s} = n_u \frac{d\mu_u}{d\mu_s} + n_d \frac{d\mu_d}{d\mu_s} + n_s + n_e \frac{d\mu_e}{d\mu_s} \ , \tag{7.34}$$

where we have used $n_i \equiv \partial p / \partial \mu_i$. The number densities are function of μ's only, so they are independent of constraint conditions. The constraint conditions only appear in the derivatives between μ's. For beta equilibrium, we have

$$\frac{d\mu_u}{d\mu_s} + \frac{d\mu_e}{d\mu_s} = 1 \ , \tag{7.35}$$

$$\frac{d\mu_d}{d\mu_s} = 1 \ , \tag{7.36}$$

$$\frac{dQ}{d\mu_s} = \frac{2}{3}\frac{dn_u}{d\mu_u}\frac{d\mu_u}{d\mu_s} - \frac{2}{3}\frac{dn_d}{d\mu_d}\frac{d\mu_d}{d\mu_s} - \frac{2}{3}\frac{dn_s}{d\mu_s} - \frac{dn_e}{d\mu_e}\frac{d\mu_e}{d\mu_s} = 0 \ ; \tag{7.37}$$

for chemical composition preservation, we have Eq. 7.37 and

$$\frac{d\mu_i}{d\mu_s} = \frac{n_i}{n_s} \frac{dn_s/d\mu_s}{dn_i/d\mu_i} \ , \tag{7.38}$$

for any particle species i. Eq. 7.38 can be derived by considering fraction of Eq. 3.9 for different i. For convenience, we rearrange Eq. 7.34 as

$$\frac{dp}{d\mu_s} = \tilde{A}\left(\frac{d\mu_u}{d\mu_s} + \frac{d\mu_e}{d\mu_s}\right) + \tilde{B}\left(\frac{2}{3}\frac{\partial n_u}{\partial \mu_u} - \frac{\partial n_e}{\mu_e}\frac{d\mu_e}{d\mu_s}\right) + n_d \frac{d\mu_d}{d\mu_s} + n_s \ , \tag{7.39}$$

where

$$\tilde{A} = \frac{\frac{2}{3}\frac{\partial n_u}{\partial \mu_u} n_e + \frac{\partial n_e}{\partial \mu_e} n_u}{\frac{2}{3}\frac{\partial n_u}{\partial \mu_u} + \frac{\partial n_e}{\partial \mu_e}} \ , \ \tilde{B} = \frac{n_u - n_e}{\frac{2}{3}\frac{\partial n_u}{\partial \mu_u} + \frac{\partial n_e}{\partial \mu_e}} \ . \tag{7.40}$$

It is noted that the coefficients $\tilde{A}$ and $\tilde{B}$ are determined by the static background but not the constraint conditions.

Since both constraint conditions involve the charge neutrality condition Eq. 7.37, the term associates with $\tilde{B}$ will be the same for both the static and dynamic EOS. Then the denominator in Eq. 7.33 will have 2 terms left

$$\begin{aligned} \left(\frac{\partial p}{\partial \mu_s}\right)_{Y_p} - \left(\frac{\partial p}{\partial \mu_s}\right)_{\beta} &= \tilde{A}\left\{\left(\frac{d\mu_u}{d\mu_s} + \frac{d\mu_e}{d\mu_s}\right)_{Y_p} - \left(\frac{d\mu_u}{d\mu_s} + \frac{d\mu_e}{d\mu_s}\right)_{\beta}\right\} \\ &\quad + n_d\left\{\left(\frac{d\mu_d}{d\mu_s}\right)_{Y_p} - \left(\frac{d\mu_d}{d\mu_s}\right)_{\beta}\right\} \ , \end{aligned} \tag{7.41}$$

where the beta equilibrium terms are both unity by Eq.s 7.35 and 7.36. For the composition preservation terms, we conduct the perturbation by treating m_s as the correction term. By Eq. 7.38, we have

$$\left(\frac{d\mu_d}{d\mu_s}\right)_{Y_p} \approx 1 + \left(\frac{m_s}{\mu_s}\right)^2 \tag{7.42}$$

$$\left(\frac{d\mu_u}{d\mu_s} + \frac{d\mu_e}{d\mu_s}\right)_{Y_p} \approx 1 + \left(\frac{m_s}{\mu_s}\right)^2 \ . \tag{7.43}$$

Therefore Eq. 7.41 becomes

$$\left(\frac{\partial p}{\partial \mu_s}\right)_{Y_p} - \left(\frac{\partial p}{\partial \mu_s}\right)_{\beta} \approx \left(\frac{m_s}{\mu_s}\right)^2 (\tilde{A} + n_d) \ . \tag{7.44}$$

Although Eq. 7.44 has a proportional factor of m_s^2, we have to verify two things before claiming its dependence is indeed m_s^2. The first one is to understand how μ_s changes with m_s. We consider a fluid element experiences a pressure p and follows the background constraints, by using Eq. 7.9, we get

$$d\mu_s = \frac{2}{3}\frac{m_s}{\mu_s} dm_s \ . \tag{7.45}$$

It means that the difference between μ_s of zero and finite strange quark mass model is suppressed by a first order term m_s/μ_s. Therefore we can treat μ_s does

not change with m_s at the leading order. Another thing we have to understand is how the term $(\tilde{A} + n_d)$ in Eq. 7.44 changes with m_s. Formal treatment requires tedious perturbation expansion, but since we are only interested in the least order contribution, we take an easier approach to consider the values of the quantities in the $m_s = 0$ limit, where

$$\mu_u = \mu_d = \mu_s \equiv \mu \quad ; \quad \mu_e = 0 \ , \tag{7.46}$$

$$n_u = n_d = n_s = \frac{\mu^3}{\pi^2} \quad ; \quad n_e = 0 \ . \tag{7.47}$$

Then $\tilde{A} \to 0$ and n_d possesses a μ^3 dependence which is insensitive to m_s. We conduct similar treatment on the remaining terms in Eq. 7.33,

$$\left(\frac{dp}{d\mu_s}\right)_{Y_p} = \left(\frac{dp}{d\mu_s}\right)_{\beta} = 3n_s \ , \tag{7.48}$$

$$\left(\frac{dG}{d\mu_s}\right) = \frac{3}{\pi^2}\mu_s \ . \tag{7.49}$$

Putting all these results into Eq. 7.33, we can get a m_s^4 dependence for ω_{BV}^2. Hence, our analysis verifies our numerical results that the BV frequency and the Y_p mode frequency vary quadratically with m_s.

7.3 Summary

In this chapter, relationships between QS g mode frequency and properties of quark matter are investigated. If the dynamic EOS preserves beta equilibrium, which is believed to be the case in high temperature regime $T \gtrsim 5$ MeV, β mode frequency is highly sensitive to the temperature profile. We verify that if the temperature profile changes homogeneously during cooling, g mode frequency will vary linearly with the average temperature of the QS. However, the mode frequency shifts significantly if the temperature profile dramatically alters. This can be understood from the Newtonian stellar pulsation theory that g mode is driven by the restoring force of convective stability, therefore

temperature gradient is a more important factor than magnitude of temperature. In addition, we show that β mode oscillation exists due to the non-zero value of m_s.

On the other hand, if the dynamic EOS preserves chemical composition, which is believed to be the case of a low temperature QS, i.e. $T \to 0$ MeV, Y_p mode frequency remains finite due to the difference of the static and the dynamic EOS. Based on our zero temperature MIT bag model employed, we find that the mode frequency is quadratically depending on the value of m_s. Therefore, if a g mode signal is detected from a cold QS, we can use the information to place some bounds on the quark matter EOS. As a summary, we arrange the order of nuclear matter effects on g mode frequency to be, dynamic EOS $>$ m_s $>$ temperature profile $>$ T.

Following the findings in this chapter, some characteristics of the QS g mode presented in Chapter 5 can be explained, but the applicability of these results may vary as cases in reality. One reason is that the MIT bag model we employed is the simplest quark matter model. Realistic quark matter EOS is more complicated, which may include quark species other than u, d, s, interactions between quarks [44], and the superconducting CFL phase [48]. Nevertheless, we believe our approach of analysis is still useful if other quark matter EOS is used, so we expect more complete and interesting behaviors on g mode will be deduced in the future.

Even though our works merely demonstrate results under simplified circumstances, all our mode frequencies computed by linearized relativistic formalism are much smaller than g mode of NS as shown in Chapter 5. This agrees with the argument of Fu *et al.* [19], who compute the QS g mode by the Newtonian formalism with the Cowling approximation. Although analytical explanation is not feasible due to the complexity of ordinary nuclear matter EOS, simple argument can be claimed according to the discussion in this chapter. We have shown that both β mode and Y_p mode exist in QS because the non-zero m_s

breaks the linear relationship between p and ρ (c.f. Eq. 5.2). The linear relationship emerges because quarks are modeled as ultra-relativistic ideal gases in the MIT bag model. But the nucleons in ordinary nuclear matter are not necessarily ultra-relativistic, due to the large nucleon mass and complicated nuclear interactions. As a result, the $p - \rho$ relationship of nuclear matter is fundamentally non-linear, such that g mode frequencies of NS are generally larger than those of QS.

Chapter 8

Gravitational radiation excitation by infalling shell

In the previous chapters, we have shown how gravity, fundamental and space-time modes vary as temperature. From the results, we deduce that there are three noticeable change of GW indicate cooling of compact stars: 1. sudden jump of mode frequencies induced by phase transition; 2. reduction of g mode frequency as the temperature decreases; 3. shift of g mode frequencies caused by possible change of dynamic EOS in different temperature range. However, these theoretical predictions of signal alternation are not necessarily noticeable in practice, because the recognizability of QNM depends on the quality of GW detectors, nature of each QNM, and most importantly, the energy content of each mode. In order to estimate the amount of energy contained in realistic GW emitted by hot compact stars, we consider a simple wave excitation mechanism, which is the asymmetric collapse of a matter shell.

8.1 Introduction

At the end of stellar evolution, supernova explosion is usually triggered as a redistribution of matter of the original star. Most of the exterior matter is propelled towards the deep space and form a nebula, leaving the core bare. The

massive remnant of core usually exists as a blackhole, compact star, or white dwarf according to the mass of the core and the explosion mechanism. The compact object greatly distorts the spacetime, imposes a strong gravitational field, causing part of the ejected masses to fall back. Since the explosion is not isotropic in general, distribution of falling matter can be asymmetric, causing a polar disturbance on the background spacetime. According to the theory of general relativity, such kind of disturbance will propagate away as GW, hence the asymmetric fall back of mass is a plausible excitation mechanism of gravitational radiation.

Complete analysis of this kind of gravitational radiation requires solving the whole set of Einstein equation, which is still a tough challenge to computational physics. However, the scenario can be linearized if we assume the fall back mass m_0 is much smaller than that of compact object M, i.e. $m_0 \ll M$. An important work in linearization of relativity is the work done by Zerilli [23], who considers polar perturbations on a spherical symmetric stationary background. It completes the previous work of Regge and Wheeler [35], who considered axial perturbations. Investigation of polar perturbation arouse much interest, because it would couple to fine structure of compact objects. Analytical tool of Zerilli is first employed by Davis *et al.* to investigate the GW emitted by an infall point particle [33]. They consider the particle with very little mass is falling radially at rest from infinity into a Schwarzschild blackhole. They found the this process would induce energy dissipation by gravitational radiation, which the peak of power spectrum is associated with QNM of the blackhole.

Since then, relationship between object infall and gravitational radiation is a hot topic of astronomical research; more complicated and realistic scenario is studied. For examples, Ruffini [49] extended the work of Davis *et al.* to consider a particle falling with finite initial velocity, which similar pattern is observed except the increased contribution in low frequency regime of power

spectrum. Lousto and Price [50] formulate the mathematical expression for a point mass falling from finite distance r_0 instead of infinity. By applying the Laplace transformation techniques, they find that multiple peaks are induced in the power spectrum in subsidiary to the peak in the infinite distance case. Nakamura and Sasaki [51] consider the case of a collapsing thin dust shell, the power spectrum is qualitatively the same as the case of a point particle except a phase factor depending on the geometry of the shell. Shapiro and Wasserman [52] investigate a generalized shell which includes thickness, and Haugan *et al.* [53] consider a dust ball as an approximation of a rigid uniform density star. Both works involve modification of the geometric phase factor.

While blackhole is one candidate of the supernova remnant, compact star is another possibility that consists of more property on various aspects of physics. According to the no hair theorem, a blackhole is believed an event horizon consisting of three properties only, charge, mass and angular momentum, regardless of the original nature of matter. However, neutron stars are supported by nuclear pressure in order to occupy a finite volume in space, hence their composition is closely related to the EOS of nuclear matter. Since the condition of high temperature and pressure inside a neutron star cannot be produced on the Earth in foreseeable future, physics of the superdense region is not known to date. A branch of astrophysicists attempt to study the nuclear EOS from gravitational wave emitted by neutron stars. Because polar oscillation modes of neutron stars are coupled with the fluid motion of the stars, theoretical work is conducted to investigate how pattern of QNM varies if different EOS model is employed [5]. In spite of the interesting findings, it is doubtful if realistic astronomical events can excite QNM that is energetic enough to be detected. Being one of the excitation mechanism, matter source moving around a neutron star is investigated through linerized general relativistic formalism. Work of Ferrari *et al.* [54] is one of the earliest attempt

, they consider the power spectrum of GW emitted when a test mass is approaching and then scattered by a NS. Unlike the scenarios of blackhole, sharp peaks are observed in power spectrum of polar GW, which correspond to fluid mode excitation of the NS. Besides, continuously orbiting mass can also cause resonant on the stellar oscillation modes, according to Gualtieri *et al.* [11].

While all of the above have assumed the infalling object are formed by dust, which does not involve hydrodynamics and self-gravity, more realistic situations are considered in recent investigation by the so-called 'hybrid' approach. The formalism incorporates an extended source, of which the matter distribution is a numerical solution of the full (non-linear) Einstein equation, but the spacetime perturbation and GW spectrum are calculated by linearized approach. By employing this method, a quadrupolar shell is considered by Nagar *et al.* [55] as a model to the scenario of matter accretion near a compact object. They find that the complicated source induces interference fringes caused by the geometric phase factor of the shell, which supports the analysis of Lousto and Price [50] using Laplace transformation. The approach is later extended by Ferrari *et al.* [56], which is able to combine a time-evoluting source with linearized formalism in frequency domain. Their scheme does not only produce results agree with previous works, but it is also possible to be generalized to case of a rotating blackhole. The hybrid approach is anticipated to produce more interesting results of gravitational wave in the future.

Although the hybrid approach is promising in simulating more realistic and complex matter source, relatively little attention is paid to the structure of neutron star as a supernova remnant. Most authors treated the neutron star is either uniform or composed of polytropic EOS, which are good models but do not cover all characteristics of realistic stars, particularly the finite temperature ones. Although those idealized model can also produce spacetime modes, p mode, and f mode pulsations, they fundamentally do not allow the g mode oscillation. As we have shown in Chapter 5 that g mode would provide

fruitful information about the temperature of compact stars, it is promising to check if a collapsing shell is an effective excitation mechanism for this kind of oscillation.

Apart from the g mode, the high temperature and density just after supernova explosion is also favorable for forming a QS. Various quark matter models agree that QS is more compact than NS, because its density is non-zero at the stellar surface. Therefore observations related to QS are quantitatively different from those of neutron stars, such as the moment of inertia [2] and the QNM spectra [4]. How about the power spectrum of GW excitation? It is the feature we want to investigate in this chapter.

The outline of this chapter is the following. We will spend a long Section 8.2 on detailing our numerical procedures. Although some publications have shown the mathematical expression for the polar oscillation within the scope of linearized general relativity, many of them involve typo and capability problems. We wish a set of self-consistent ingredients is gathered, which further investigation can be conducted easily following our steps. In the next section, we will present our results of computation. Power spectra of GW excited by a quadrupole shell falling at rest at spatial infinity are shown. While the spectra of QS and NS are qualitatively similar, their patterns are shifted. Similar phenomenon is observed for compact stars with the same composition but different temperature profile. We claim that this phenomenon is related to the nature of the peaks of power spectra. In Section 8.4, detectability of QNM is discussed by estimating the amount of energy included in each QNM. Waveform is also illustrated by inverse-Fourier transforming the scattering profile, which show that f mode is the most probably observed under this excitation mechanism. Since we consider hot compact stars in this thesis, the non-adiabatic effect of thermal conductivity is discussed in Section 8.5. Finally we verify the validity of our results by comparing them with GW computed by full general relativity simulation in Section 8.6.2. A summary is given in Section 8.7.

8.2 Formalism

In this chapter, we use the linearized general relativity formalism to solve the polar GW spectra excited by a matter shell radially falling from infinity. Although it is the simplest model to mimic the realistic GW excited by collapsing shell, heavy theoretical works have been done to obtain the first order perturbation. In the previous literatures, we find it is difficult to get a complete, error-free, and self-consistent set of equations to describe the whole process, several authors use their own notations and conduct perturbative analysis without showing the details. The inconsistency is possibly because the theory of general relativity contain freedoms allowing authors to choose their own coordinates and gauges for their convenience. The complicity of Einstein equation, which is a coupled tensor equation, is another source of error. We find that even the mostly cited publications contain typo in a few out of hundreds of mathematical expression. Unfortunately any small mistake in those expressions breaks intrinsic symmetries of some physical quantities, which significantly alters the results generated.

Following the discussion of the homogeneous Zerilli equation Eq. 4.9 in Chapter 4, we here retrieve the source term S_{lm} to describe the motion of an infalling shell. In order to provide guidelines for future works, source term of a general stress tensor is written, special conditions required by the infalling shell are added until necessary. Due to the complexity, I divide the whole situation into five parts. First, connection between the LD equation and the Zerilli function is re-examined. In Section 4.3, we provide the method suggested by LD in 1983 [9]. But their formalism leaves ambiguity, due to the distinct notation and modification of variables in their future work in 1985 [22]. In order to fix the normalization in order to compute the power spectrum by solving the inhomogeneous Zerilli equation Eq. 4.7, we pick the connection procedure of Fackerell [57] to compare the LD equation, the Zerilli equation,

and the source term we are going to consider. The following step is to construct the mathematical contribution of an infall shell in Zerilli formalism. We have compared the expressions of various authors and found that those written by Jhingan *et al.* [36] and Sago *et al.* [32] are the most accurate and easiest to follow. We employ their results to in all our calculation in this chapter. Since the dynamics of the shell is qualitatively the same as that of a test mass, our goal is to reproduce a source with the same functional form as that given by Davis [33]. Next, we present the findings of Nakamura and Sasaki [51], that the difference of power spectrum between a deformed dust shell and a point particle is merely a phase factor determined by the geometry of the shell. This section is ended by a brief discussion on Green's function method of constructing solution of the inhomogeneous Zerilli equation.

8.2.1 Connection between star and vacuum

In Chapter 4, we discuss the oscillatory equation inside the star and the vacuum background outside. Since both LD and Zerilli equation are obtained by linearizing the Einstein equation, there is a physical connection of the LD variables and the Zerilli function at the stellar surface. However, we find the connection formalism is artificially problematic, because of typo, and different selection of primary variables, expansion coefficients, Fourier transform components among different authors. Throughout this thesis, we employ the LD formalism inside the star and the Zerilli equation in vacuum. Lindblom and Detweiler do present a conversion from their metric variables to the Zerilli function in their 1983 paper [9], however it leaves uncertainties for our consideration of power spectrum due to two reasons: firstly, we use the LD equation proposed in 1985 [22], which the notations and primary variables are not the same as their 1983 paper; secondly, their main concern is to obtain the QNM, which permits an arbitrary wave amplitude, i.e. $Z = Ae^{-i\omega t}$ is an outgoing

solution for all A, but power spectrum is physically detectable quantity so the choice of normalization should be important. To solve the problems, we use the procedure of Fackerell [57] as the standard approach to compare the Zerilli function and LD variables.

Fackerell [57] follows the choices of the original Zerilli paper [23] to expand the metric perturbation as

$$h_{\mu\nu} = Y_{lm} e^{-i\omega t} \begin{pmatrix} f(r)H_0 & H_1 & 0 & 0 \\ \text{sym} & \frac{1}{f(r)} H_0 & 0 & 0 \\ 0 & 0 & r^2 K & 0 \\ 0 & 0 & 0 & r^2 K \sin^2\theta \end{pmatrix} , \tag{8.1}$$

where $f(r) = 1 - 2m/r = e^{-\lambda(r)}$ is the same as the metric factor e^{ν} on the stellar surface. We have expressed the above metric in terms of the spherical harmonics Y_{lm}, instead of the Legendre polynomial $P_l(\cos\theta)$ in the original paper. But we have checked with the corrected version of Zerilli's expression [32] that the $P_l(\cos\theta)$ of Fackerell is actually the spherical harmonics with zero magnetic quantum number m, i.e. $P_l(\cos\theta) = Y_{l0}(\Omega)$.

Comparing the same metric perturbation expressed by LD, Eq. 4.15, and Fackerell, Eq. 8.1, correlation of their symbols is obviously

$$\begin{pmatrix} H_0^F(-\omega) \\ H_1^F(-\omega) \\ K^F(-\omega) \end{pmatrix} = -r^l \begin{pmatrix} H_0^{LD}(\omega) \\ i\omega r H_1^{LD}(\omega) \\ K^{LD}(\omega) \end{pmatrix} , \tag{8.2}$$

where the subscript F and LD distinguish notations used by Fackerell and LD. According to Eq.s 8, 9, 13, 14 in [57], the connection of metric factor to the Zerilli function is

$$\begin{pmatrix} K^F(\omega) \\ H_1^F(\omega) \end{pmatrix} = \begin{pmatrix} g^F(\omega) & 1 \\ h^F(\omega) & k^F(\omega) \end{pmatrix} \begin{pmatrix} Z^F(\omega) \\ Z^F_{,r_*}(\omega) \end{pmatrix} , \tag{8.3}$$

where the connection factors are

$$g^F(\omega) = \frac{\lambda(\lambda+1)r^2+3\lambda mr+6m^2}{r^2(\lambda r+3m)} \tag{8.4}$$

$$h^F(\omega) = i\omega\frac{-\lambda r^2+3\lambda mr+3m^2}{(r-2m)(\lambda r+3m)} \tag{8.5}$$

$$k^F(\omega) = -i\omega\frac{r^2}{(r-2m)} \ . \tag{8.6}$$

We reserve the ω dependent notation for future analysis. On the other hand, LD give similar set of connection in their 1983 paper. We copy Eq. A27 in [9]

$$\begin{pmatrix} 0 & 1 \\ a^{LD} & b^{LD} \end{pmatrix}\begin{pmatrix} H_0^{1983} \\ K^{1983} \end{pmatrix} = \begin{pmatrix} g^{LD} & 1 \\ h^{LD} & k^{LD} \end{pmatrix}\begin{pmatrix} Z^{LD} \\ Z^{LD}_{,r_*} \end{pmatrix} \ , \tag{8.7}$$

where the subscript 1983 denotes symbols employed in their 1983 paper. It is stressed that the symbols are deviated in their 1985 paper. We do not quote functional form of a^{LD} and b^{LD}, because we find the L.H.S. of Eq. 8.7 actually transforms to simpler variables in LD 1985 notation [22]

$$\begin{pmatrix} 0 & 1 \\ a^{LD} & b^{LD} \end{pmatrix}\begin{pmatrix} H_0^{1983} \\ K^{1983} \end{pmatrix} = r^l\begin{pmatrix} K^{LD} \\ -rH_1^{LD} \end{pmatrix} \ , \tag{8.8}$$

where $r/R = 1$ on the surface. The connection coefficients provided by Lindblom and Detweiler are related to that of Fackerell as

$$g^F(-\omega) = g^{LD}(\omega) \tag{8.9}$$

$$\frac{-1}{i\omega}f^F(-\omega) = f^{LD}(\omega) \tag{8.10}$$

$$\frac{-1}{i\omega}k^F(-\omega) = k^{LD}(\omega) \ . \tag{8.11}$$

Now we have enough ingredients to connect the LD equation with the Zerilli equation. After some manipulations, we obtain

$$\begin{pmatrix} Z^{LD}(\omega) \\ Z^{LD}_{,r_*}(\omega) \end{pmatrix} = -\begin{pmatrix} Z^F(-\omega) \\ Z^F_{,r_*}(-\omega) \end{pmatrix} \ . \tag{8.12}$$

Incorporating this relation with Eq.s 8.7 and 8.8, Zerilli function can be constructed by LD variables, and the Zerilli equation is given by

$$(\frac{d^2}{dr_*^2} + \omega^2 - V)Z^{LD}(\omega)e^{i\omega t} = -S^F(-\omega)e^{i\omega t} \ , \tag{8.13}$$

where the term S^F is the source term formed by contracting the stress tensor [23]. In the sourceless case, the QNM for Eq. 8.13 is the frequency ω which gives $Z \sim e^{-i\omega r_*}$ at spatial infinity.

We end this subsection with several comments. The connection of the Zerilli function and the LD variables mentioned above has assumed the source term to be zero, i.e. $S_{lm} = 0$ in Eq. 4.7. If there is source, the connection is referred to Eq. A37 and A38 in [32]. But the sourceless connection is still useful in our case, because we will handle the source term by the Green's function method. Our treatment can find the amplitude of GW by integrating the source term with the sourceless solutions, therefore we convert values of the LD variables with the sourceless Zerilli function. We will show later that results of the Green's function do not depend on normalization. So does it mean our consideration here is meaningless? Technically, we think the detail of connection is still useful for the approach of directly integrating the Zerilli equation, but a more physical reason is that we clarify the LD equation is indeed connected to the Zerilli function, but not the Moncrief function (c.f. [58]). Eq. 4.7 is often referred to as the Zerlli-Moncrief equation, because both the Zerilli and Moncrief function follow the same differential equation. Despite the similarity, the functions represent different physics, but are related to each other by reconstructing some metric variables [36]. We have checked that the functional form of the source term of the Moncrief equation [58] is completely different from that of the Zerilli equation. One significant difference is that the Moncrief's source for an infalling particle diverges at spatial infinite, while Zerilli one remains finite. Since we aim to account for the power spectra using the quadrupole radiation formula of the Zerilli function, the above consideration ensures we are working

on the right track.

8.2.2 Matter source

In this section, I present the general procedure to construct the source term of the Zerilli equation generated by a point mass moving along a geodesic. For the case of a dust shell, or any distribution formed by dust particles, the source merely requires an integration of number density in spatial domain, in order to sum up the individual contributions of every dust particles. If the extended mass has an intricate distribution, or consists of hydrodynamics, such as those considered in hybrid approach, the formalism is still valid if the stress tensor is known. But the process is more complicated because there is are δ-functions in the dust particle source which simplifies several integration in calculations. Our approach in this section mainly follow the analysis of Jhingan and Tanaka in [36].

As mentioned before, Zerilli employed the RW gauge to simplify the metric perturbation, which is the left hand side of the linearized Einstein equation Eq. 4.1, and then contracted the metric perturbation to the Zerilli function obeying the Zerilli equation. Corresponding treatment is conducted on the stress tensor on the right hand side, and results in a single source term S_{lm}, which is a scalar function of r. Zerilli gives the expression relating S_{lm} to stress tensor expansion coefficients in [23], but it contains numerous typo that are later fixed by Sago *et al.* in [32]. We find the expression of Sago et al. is almost error-free, except the coefficient of $A^{(1)}$ in Eq. A42 should be $-4\pi\frac{\sqrt{2}}{\lambda r+3M}\frac{Mr}{\omega}$ instead of $-4\pi\sqrt{\frac{2}{\lambda r+3M}}\frac{Mr}{\omega}$. With this amendment, one can construct the correct source term by Eq.s A37-A44 and A47 in [32].

In practice, however, the expression of the original Zerilli source is complicated, quite a number of terms are redundant. Besides, it contains derivatives of various stress tensor coefficients, which imposes mathematical and numerical

difficulties. In order to facilitate manipulation of the Zerilli equation, Jhingan and Tanaka improved the original source term and give a simplified version as Eq. 2.29 in [36]. We denote their source term as S^{JT}, which the expression is

$$\begin{aligned} S^{JT} &= \frac{(r-2M)^2}{(\lambda r+3M)\sqrt{1+\lambda}}B^0_{,r} + \frac{(r-2M)(-12M^2+9Mr+r^2\lambda)}{r\sqrt{1+\lambda}(\lambda r+3M)^2}B^0 \\ &\quad -\sqrt{2}\lambda\frac{(r-2M)^2}{(\lambda r+3M)^2}A^1 + \omega\Big[-\frac{r^2}{(\lambda r+3M)}A^0 + \frac{(r-2M)^2}{(\lambda r+3M)}A \\ &\quad +\frac{(r-2M)^2}{(\lambda r+3M)\sqrt{1+\lambda}}B - \sqrt{2}\frac{(r-2M)}{\sqrt{\lambda(1+\lambda)}}F\Big] . \end{aligned} \tag{8.14}$$

We have corrected a typo on the coefficient of B, which should be $\omega\frac{(r-2M)^2}{(\lambda r+3M)\sqrt{1+\lambda}}$ instead of $\omega\frac{(r+2M)^2}{(\lambda r+3M)\sqrt{1+\lambda}}$ in Jhingan's paper. We try deriving Eq. 8.14 from the corrected expression, and find that they have the same functional form up to a constant multiplication factor, i.e. $\frac{8\pi}{\omega}S^{JT} = S_{lm}$. It is noted that a constraint Eq. 2.34 in [36] is used in the derivation, which eliminates the derivatives of A^1. We stress that the procedure up to this point is applicable to any matter distribution

We are now ready to calculate the source term of an infalling mass from its stress tensor. When a point particle with negligible volume is moving along a geodesic, the stress tensor is referred to as Eq. 4.4 with $i = 1$. We switch the integrating variable to the time-like parameter in Schwarzschild coordinate, t, and the stress tensor is transformed as,

$$\delta T^{\mu\nu} = m_0\frac{dt}{d\tau}\frac{dx^\mu}{dt}\frac{dx^\nu}{dt}\frac{\delta(r-r_0(t))\delta(\Omega-\Omega_0(t))}{r^2} . \tag{8.15}$$

Then the tensor is expanded by the complete set of tensor spherical harmonics as Eq. 4.5. The transformation can be done by multiplying the conjugate tensor spherical harmonics and take an integration. The result is effectively replacing the solid angle δ function by the conjugate of corresponding tensor harmonics. The angular functions are not only scalar spherical harmonics Y_{lm}, but also involve functions of their derivatives, conventionally denoted as W_{lm} and X_{lm}. Functional form of first few order of the angular pattern functions

are given on appendix D of [58]. Due to the complexity of the expansion coefficients, we do not show their explicit form in the current thesis, detail is referred to Table 1 of [32].

Now three of the four δ functions in Eq. 4.4 are removed, the last one gives the position of the particle at different time. Since we consider the Zerilli equation in the frequency domain, it is natural to perform a Fourier transform on the stress tensor. We take the notation employed by Zerilli

$$J(r,\omega) = \frac{1}{\sqrt{2\pi}} \int \tilde{J}(r,t) e^{i\omega t} dt \ , \tag{8.16}$$

for any time-depending function $\tilde{J}(r,t)$. It is important to verify the integrating constant of Fourier transform because it would affect the formula of radiation energy. We show the explicit form of the transformed coefficients as

$$A(r,\omega) = \frac{m_0}{\sqrt{2\pi}} \frac{dr}{d\tau} (r-2m)^{-2} Y^*_{lm}(\Omega(r)) e^{i\omega t(r)} \tag{8.17}$$

$$A^0(r,\omega) = \frac{m_0}{\sqrt{2\pi}} \frac{dt}{d\tau} (1-\frac{2m}{r})^2 \frac{1}{r^2} Y^*_{lm}(\Omega(r)) e^{i\omega t(r)} \tag{8.18}$$

$$A^1(r,\omega) = i\frac{m_0}{\sqrt{2\pi}} \sqrt{2} \frac{dt}{d\tau} \frac{dt}{dr} \frac{1}{r^2} Y^*_{lm}(\Omega(r)) e^{i\omega t(r)} \tag{8.19}$$

$$B^0(r,\omega) = i\frac{m_0}{\sqrt{2\pi}} \left[\frac{1}{2} l(l+1)\right]^{-\frac{1}{2}} \frac{dt}{d\tau} (1-\frac{2m}{r}) \frac{1}{r} \frac{dY^*_{lm}(\Omega(r))}{dr} e^{i\omega t(r)} \tag{8.20}$$

$$B(r,\omega) = \frac{m_0}{\sqrt{2\pi}} \left[\frac{1}{2} l(l+1)\right]^{-\frac{1}{2}} \frac{dr}{d\tau} (r-2m)^{-1} \frac{dY^*_{lm}(\Omega(r))}{dr} e^{i\omega t(r)} \tag{8.21}$$

$$G^0(r,\omega) = \frac{m_0}{\sqrt{2\pi}} \frac{1}{\sqrt{2}} \frac{dt}{d\tau} \frac{dt}{dr} \left[\left(\frac{d\theta}{dt}\right)^2 + \sin^2\theta \left(\frac{d\phi}{dt}\right)^2 \right] Y^*_{lm}(\Omega(r)) e^{i\omega t(r)} \tag{8.22}$$

$$F(r,\omega) = \frac{m_0}{\sqrt{2\pi}} \left[\frac{1}{2} l(l+1)(l-1)(l+2)\right]^{-\frac{1}{2}} \frac{dt}{d\tau} \frac{dt}{dr} \Big\{ \frac{d\phi}{dt} \frac{d\theta}{dt} X^*_{lm}(\Omega(r)) + \frac{1}{2} \Big[\left(\frac{d\theta}{dt}\right)^2 - \sin^2\theta \left(\frac{d\phi}{dt}\right)^2 \Big] W^*_{lm}(\Omega(r)) \Big\} e^{i\omega t(r)} \ . \tag{8.23}$$

A rule of thumb of the transformation is to write $(dt/dr)e^{i\omega t}$ whenever there is a δ-function in the time domain coefficients presented in Table 1 in [32]. Among the above expressions, the Schwarzschild variables, the proper time,

and derivatives with respect to any variables, are functions of the position r given by the equation of motion of the particle. In dealing with derivatives, they can be reduced to derivatives of r by appropriate employment of the chain rule.

8.2.3 Geodesic

The single particle source described in the previous subsection is generally valid for a particle moving along any trajectory, no matter it is a tiny companion orbiting around a compact object, or an accelerating rocket escaping from strong gravitational field. In this article, we consider the case of a radially infalling particle at rest from the spatial infinity. We assume the particle is moving under the gravitational field imposed by a spherically symmetric compact object at the origin, the geodesic equation in the Schwarzschild coordinate is

$$\frac{dt}{d\tau} = \frac{\tilde{E}}{1-2M/r} \tag{8.24}$$

$$\frac{dr}{d\tau} = -\sqrt{\tilde{E}^2 - \left(1-\frac{2M}{r}\right)\left(1+\frac{\tilde{L}^2}{r^2}\right)} \tag{8.25}$$

$$\frac{d\theta}{d\tau} = 0 \tag{8.26}$$

$$\frac{d\phi}{d\tau} = \frac{\tilde{L}}{r^2}\,, \tag{8.27}$$

where $\tilde{E}$ and $\tilde{L}$ are relativistic analog of the classical specific energy and angular momentum. Eq. 8.26 is an assumption we made to simplify the equations, there are two physical situation where this assumption holds, the first one is a radially falling object that we are considering, and the other is to confine the particle to move on an equatorial plane, i.e. $\theta = \pi/2$. For other type of motions, all geodesic equations have to be considered.

For the scenario we are considering, particle falls radially so there is no angular momentum, i.e. $\tilde{L} = 0$. Therefore Eq. 8.26 and 8.27 are both zero, the constancy of angular variables eliminates terms containing radial or time

derivatives of spherical harmonics $Y^*_{lm}(\Omega)$, i.e. B^0, B, G, F vanishes. Furthermore, the particle is at rest at infinity such that initial total energy is equal to the rest mass, i.e. $\tilde{E} = 1$. Putting the geodesic equations into stress tensor coefficients, we get the source term according to Eq. 8.14,

$$S_{lm} = \frac{\sqrt{2\pi}4m_0}{\lambda r + 3M}\left(1 - \frac{2M}{r}\right)\left[\sqrt{\frac{r}{2M}} - \frac{i2\lambda}{\omega(\lambda r + 3M)}\right] Y^*_{lm} e^{i\omega t(r)} \ . \quad (8.28)$$

This expression is equivalent to that computed by Davis et al. in [33], except a corrected typo of m_0 instead of M in the pre-factor. It is noted that Davis *et al.* assume the particle falls from pole, but this condition is not necessary to give the function Eq. 8.28, the condition of falling radially is enough. The Schwarzschild coordinate time $t(r)$ is the solution of the two remaining geodesic equations,

$$\begin{aligned} t(r) &= -\frac{4M}{3}\left(\frac{r}{2M}\right)^{3/2} - 4M\left(\frac{r}{2M}\right)^{1/2} \\ &\quad -2M \log\left(\frac{(r/2M)^{1/2} - 1}{(r/2M)^{1/2} + 1}\right) + \tilde{T}_0 \ , \end{aligned} \quad (8.29)$$

which $\tilde{T}_0$ is parameter determined by the initial time. We denote hereafter the source term in Eq. 8.28 as S^{one}.

I end this subsection with a comment on single particle source. In principle, the method presented above can construct the source term contributed by a particle moving along any trajectory, but it does not guarantee the term is well defined throughout the whole range of integration. We have once computed the source of a scattered particle, in reference to works of Ferrari *et al.* [54]. Our solution agrees with the authors' claim that the source diverges near the turning point of scattering. However, scattering of particle is not an extraordinary circumstance, which does not include exotic behavior. The divergence is soon verified to merely be a problem of coordinate chosen. In order to avoid the artificial singularity, Ferrrari *et al.* employ the Bardeen-Press-Teukolsky (BPT) approach in substitute of the RWZ approach in the problematic range. Transformation between the BPT and the RWZ formalism is shown in [59].

8.2.4 Source of infalling dust shell

In this chapter, we consider a thin dust shell falling radially. Since the dust shell is constructed by a collection of infalling particles, the source of shell is qualitatively the same as the single particle source, with a multiplication of a phase factor [51]. We illstrate this idea step by step. Suppose the shell is initially shaped as

$$r = r_0 g(\Omega) \ , \tag{8.30}$$

where $r_0 \to \infty$ such that every particles are well described by S^{one}. We define the spatial varying part of the geodesic time in Eq. 8.29 as $T(r)$,

$$t(r, \Omega) = T(r) + \tilde{T}_0(\Omega) \ . \tag{8.31}$$

An angular dependence is added to the geodesic time $t(r)$ because we are going to consider a collection of particles falling from every direction. Since all particles follow same set of geodesic equations, $T(r)$ describes time variation of every particles, only the initial time parameter $\tilde{T}_0$ is angular dependent. Since all particles of the shell start to fall at the same time, they have the same initial time t_0. We take the particle at the pole as reference and assume, without loss of generality, that $g(\theta = 0) = 1$, such that the initial time is $t_0 = T(r_0) + \tilde{T}_0(\theta = 0)$. For particles falling from other direction, the initial time is

$$t_0 = T(r_0 g(\Omega)) + \tilde{T}_0(\Omega) \ . \tag{8.32}$$

Therefore the geodesic time of any particle is

$$t(r, \Omega) = T(r) + T(r_0) - T(r_0 g(\Omega)) \ . \tag{8.33}$$

Consider the dust is initially distributed as $\sigma(\Omega)$. We compute the stress tensor of the shell as

$$\begin{aligned} T^{\mu\nu} &= \rho u^\mu u^\nu \\ &= \int \frac{\sigma(\Omega)}{r^2} \delta(r - R(\tau, \Omega)) \delta(t - T(\tau)) u^\mu u^\nu d\tau \ , \end{aligned} \tag{8.34}$$

which is simply a substitution $m_0\delta(\Omega) \to \sigma(\Omega)$ from the single particle case. By this analog, we can follow the same procedure in the previous subsections and construct the expansion coefficients. As we only consider a radially infalling shell, only A, A^0, A^1 remains. Functional form of the coefficients of the shell are the same as those of a single particle, except the transformation

$$m_0 Y^*_{lm} e^{i\omega t(r)} \to \int \sigma(\Omega) Y^*_{lm} e^{i\omega t(r,\Omega)} d\Omega \ . \tag{8.35}$$

Substituting Eq. 8.33 into the above equation, we can extract the single particle behavior as

$$\int \sigma(\Omega) Y^*_{lm} e^{i\omega t(r,\Omega)} d\Omega = f_{lm}(\omega) m_0 Y^*_{lm}(\theta = 0) e^{i\omega T(r,0)} \ , \tag{8.36}$$

where we define the phase factor f_{lm} as

$$f_{lm}(\omega) \ = \ \frac{1}{m_0 Y^*_{lm}(\theta = 0)} \int \sigma(\Omega) Y^*_{lm}(\Omega) e^{i\omega(T(r_0) - T(r_0 g(\Omega))} d\Omega \ , \tag{8.37}$$

which is a function of frequency only but not r. As a result, the Zerilli source of a radially falling shell only deviates from that of a single particle by a phase factor $f_{lm}(\omega)$. The resultant Zerilli function and power spectrum can be directly inferred from the single particle solution by some scaling.

8.2.5 Green's function

Now we have obtained the source term S_{lm}, the next step is to solve the inhomogeneous Zerilli equation Eq. 4.7 and obtain the GW power spectrum. As mentioned by Davis [33], there are two methods to find the wave amplitude, one is by integrating the inhomogeneous differential equation, another is to construct the Green's function by the homogeneous solution. In practice, direct integration consume more computational resources, because one has to tune the amplitude of the wave function at stellar surface, until a purely outgoing inhomogeneous solution is yielded at spatial infinity. For each value of ω,

several trial has to be made to obtain an approximate solution, which is not efficient.

We instead employ the Green's function approach, which the outgoing solution is fundamentally assumed for each procedure, and it only requires one integration for each ω. It is noted the we use the notation of Fourier transform of LD instead of Zerilli, such that the time dependence of Fourier component is $e^{i\omega t}$. Source term in this notation has to be obtained from Zerilli source S_{lm} by the transformation $\omega \to -\omega$. We hereafter denote S_{lm} as the source in LD notation. I directly quote the inhomogeneous solution $Z(r)$ constructed by the Green's function method,

$$Z(r) = \frac{1}{W(\omega)}\Big(Z_1(r)\int_{r_*}^{\infty} Z_2(r)S_{lm}(r)dr_* + Z_2(r)\int_{R_*}^{r_*} Z_1(r)S_{lm}(r)dr_*\Big) \ , \tag{8.38}$$

where R_* is the tortoise coordinate of the star radius; Z_1 is the homogeneous solution integrated from the stellar surface according to the solution of the LD equation, which may consist of both outgoing and ingoing components; Z_2 is a homogeneous outgoing solution at spatial infinity, i.e.

$$Z_2 = Z_0 e^{-i\omega r_*} \text{ as } r \to \infty \ , \tag{8.39}$$

with an arbitrary wave amplitude Z_0; $W(\omega)$ is the Wronskian of two solutions defined as

$$W(\omega) = Z_1 Z_{2,r_*} - Z_{1,r_*} Z_2 \ . \tag{8.40}$$

The Wronskian is independent of r because the Zerilli equation is a homogeneous Sturm-Liouville problem, it means that we can obtain the value of Wronskian at any position we like.

Since we assume the pulsating compact star is very far away from us, the wave amplitude we detect is that of the outgoing plane wave at spatial infinity, $r_* \to \infty$. Therefore the first term in Eq. 8.38 vanishes. After some

rearrangement, the wave function is

$$Z(r \to \infty) = \frac{e^{-i\omega r_*}}{Z_1(-i\omega)e^{-i\omega r_*} - Z_{1,r_*}e^{-i\omega r_*}} \int_{R_*}^{\infty} Z_1(r) S_{lm}(r) dr_* \ , \quad (8.41)$$

which the amplitude Z_0 can be eliminated. This expression is consistent with our quest of a purely outgoing wave at spatial infinity, behaving as $Z(r) = \hat{A}(\omega)e^{-i\omega r_*}$, which the wave amplitude $\hat{A}(\omega)$ is

$$\hat{A}(\omega) = \frac{-1}{e^{-i\omega r_*}(i\omega Z_1 + (1 - \frac{2M}{r})Z_{1,r})} \int_R^{\infty} \frac{Z_1(r) S_{lm}(r)}{1 - \frac{2M}{r}} dr \ . \quad (8.42)$$

We express the amplitude in terms of the integrating variable r we use in our numerical scheme, but not the tortoise coordinate r_*. The quantities are related by

$$r_* = r + 2M \ln \left| \frac{r}{2M} - 1 \right| \ . \quad (8.43)$$

In practice, we numerically integrate the Zerilli equation according to the boundary condition provided by the LD solution on the stellar surface, i.e. $r = R$, until a very far stopping position, $r \sim 10^4 R$. Consider the contribution of Z_1 in Eq. 8.42, it is easily verified that the wave amplitude $\hat{A}(\omega)$ is independent of the amplitude Z_1, hence the normalization in the LD equation is unimportant, which is a merit of the Green's function approach.

It is noted that the wave amplitude $\hat{A}(\omega)$ is complex in general, the GW waveform can be obtained by the inverse Fourier transform

$$Z(r_{\text{detector}}, t) = \frac{1}{\sqrt{2\pi}} \int \hat{A}(\omega) e^{i\omega t} d\omega \ . \quad (8.44)$$

On the other hand the power spectrum is calculated by the quadrupole radiation formula,

$$\frac{dE}{d\omega} = \frac{1}{32\pi} \frac{(l+2)!}{(l-2)!} \omega^2 |\hat{A}(\omega)|^2 \ , \quad (8.45)$$

which we copy from Davis' paper [33]. It is noted that the expression of the radiation formula depends on notation of Fourier transform, the form we are using is only applicable if Zerilli's transformation scheme is employed. Besides, we stress again that this radiation formula belongs to the Zerilli function but not the Moncrief function, although they satisfy the same differential equation.

8.3 Gravitational Wave excitation by collapsing shell

All the above computations only determine the source term S_{lm}, but affect neither the stellar structure nor the EOS of the compact star. In Chapter 3, we have stated that the structure of a compact star has to be fixed by equilibrium conditions and a temperature profile. We assume that the star is quasi-static during the whole process of shell collapse, implies that beta equilibrium and charge neutrality are sustained in the background. Determination of temperature distribution however requires considering various aspects of physics, including the cooling mechanism, neutrino transports, supernova mechanism [29]; stars with different composition can yield significantly different temperature profiles. Since there is not any concrete consensus on it, we are not going to investigate the variation of GW spectra caused by temperature change during a realistic stellar evolution. We instead focus our discussion on the temperature effect. To make the temperature effect becomes more significant, we do not employ the relativistic isothermal profile, but assume a temperature profile

$$T(r) = T_c \frac{p(r)}{p_c} + T_s \ , \tag{8.46}$$

where $p(r)$ and p_c are pressure at radial position r and the center respectively, T_c and T_s are parameters to be chosen to produce desired central and surface temperature. Eq. 8.46 is a falloff temperature profile from the center, which is to mimic the typical temperature distribution of a hot NS (such as Fig. 1 in [12]). As a direct comparison between the QS and the NS, the same same temperature profile Eq. 8.46 is assumed for both species.

Here we have all the ingredients to model the gravitational wave excited by a dust shell collapsing onto a hot compact star. The situation is most likely to happen just after a supernova explosion, which the remnant is still hot and exists as a compact star. Meanwhile, a portion of matter propelled

by explosion is not energetic enough to escape from the gravitational field and then falls back. Investigating such a scenario requires careful consideration on every procedures of the process, such as the explosion mechanism, evolution of proto-neutron stars, cooling of remnant, etc. As the first trial, we consider three simplified non-trivial cases for comparison. Firstly, we investigate the effect on power spectrum by the temperature difference inside a compact star. For simplicity, we employ the beta equilibrium throughout the whole stars, so we assume the lowest temperature, which is that on the stellar surface, to be 3 MeV [40]. We construct compact stars with various central temperature but the same surface temperature. The next interesting question is the effect of the surface temperature, so we compare stars with the same central temperature but different surface temperature. All the above investigation is conducted for both QS and NS, because the quark matter is believed to be favorable under high temperature and density environment. So quark stars is a possible form of hot supernova remnant, and we decide to compare the GW emitted from NS and QS.

We take the shell to be thin and spherical, such that w.l.o.g. $g(\Omega) = 1$ in Eq. 8.30. Under this setting, all the particles will fall at the same time, and the phase factor $f_{lm}(\omega)$ is frequency independent according to Eq. 8.37. However, this spherical shell is still possible to excite polar GW, due to the asymmetric angular distribution of the matter, i.e. angular distribution function $\sigma(\Omega)$ is not a constant. We further simplify the problem by assuming the integral of $\sigma(\Omega)$ in Eq. 8.37 is such that $m_0 f_{lm}(\omega) = 1$, our calculation then effectively reduces to the case of an infalling point particle with unity mass. In reality the factor $m_0 f_{lm}(\omega)$ is two to three orders smaller, but it only affects the spectrum by scaling, qualitative behavior of our result is not altered. It is noted that our assumption does not specify the angular distribution but only the normalization constant of integration, this means that our result is applicable to any spherical thin shell. Effect of the shape of the shell is discussed in

subsection 8.2.4, arbitrary shape merely contributes an oscillatory phase factor into the power spectrum we computed, which is neglected in this thesis for simplicity.

Suppose we have observed a star, the surface temperature is verified by considering the radiation spectrum or other measurements. As we cannot directly observe the temperature inside, but GW can carry information beneath, it is curious to see how the GW power spectrum changes as temperature gradient, and see what kind of information we can gather about the temperature from the GW. We consider compact stars with the same mass, $M = 1.4\ \mathrm{M}_\odot$, they have the same surface temperature, 3 MeV, but different central temperature, $8, 13, 23$ MeV, such that the temperature gap is $5, 10, 20$ MeV respectively. The thin shell is falling at rest from infinity, and absorbed by the star when it reaches the stellar surface. We place the detector at a far enough ($\sim 10000\ R$) position, such that the numerical integrated solution is very close to the wave function of a plane wave.

As shown in Fig. 8.1, general features of the power spectrum are nearly the same for NS with different central temperature but the same surface temperature. Five peaks are observed in the figure, including two sharp peaks and three broad peaks. The peaks are not significantly shifted among the three cases. In Fig. 8.2, the position of peaks are also very robust in the QS case, both the two sharp peaks and two broad peaks are nearly coincident for the three stars. Although it is not a physically interesting result, but it shows GW does not carry much information about the temperature profile.

We then consider two stars with the same gravitational mass $M = 1.4\ \mathrm{M}_\odot$ and central temperature 23 MeV but different surface temperature, $3, 5$ MeV. We contrast the power spectra of NS S203 and S185 in Fig. 8.3. Although the position of sharp peaks do not alter much, the broad peaks of the star with higher surface temperature shift towards lower frequency region. However, this phenomenon is not observed in the case of QS. As shown in Fig. 8.4, spectrum

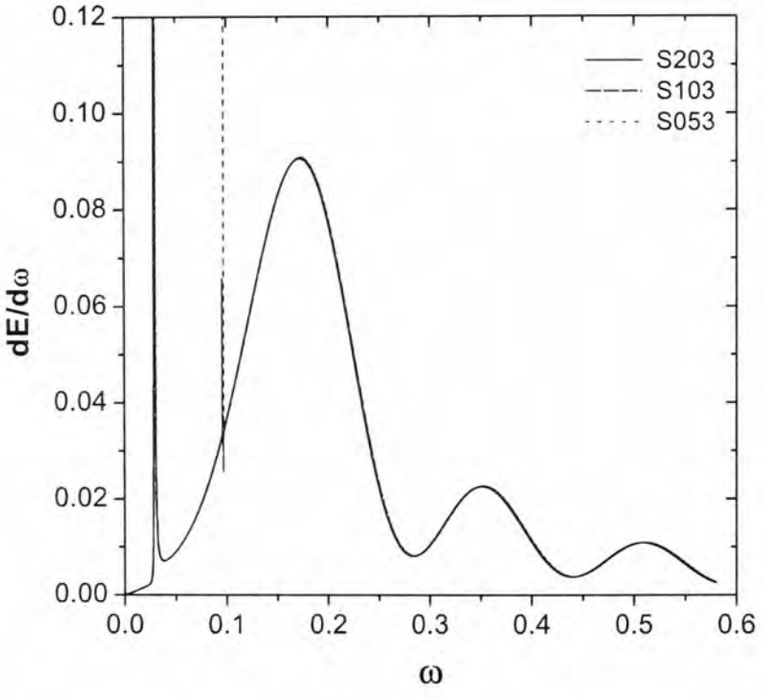

Figure 8.1: Power spectrum of GW excited by an infalling thin shell onto NS with the same surface temperature 3 MeV but different central temperature. Although the lines nearly coincide, but the figure actually shows the spectrum of three stars with central temperature $8, 13, 23$ MeV, denoted as stars S053, S103, S203 respectively.

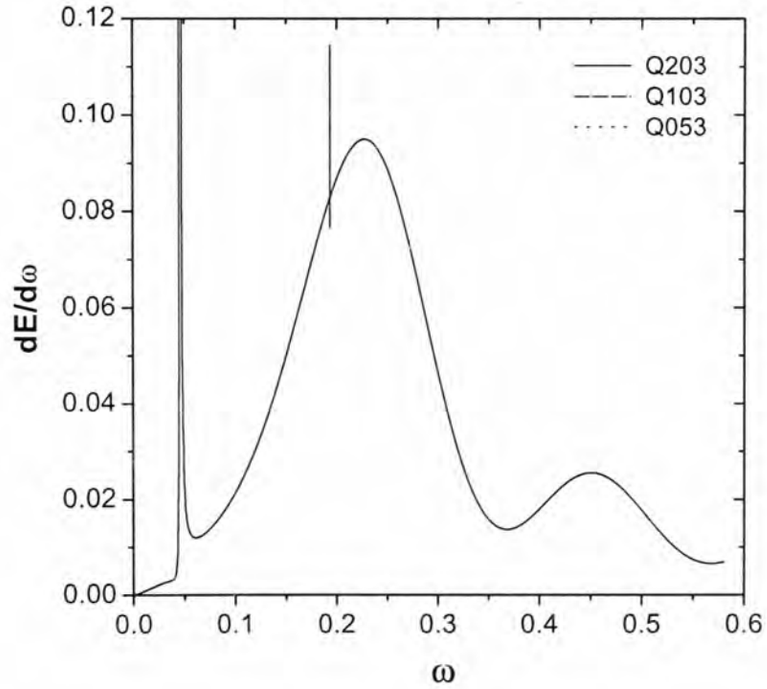

Figure 8.2: Same as Fig. 8.1 for QS. The lines nearly coincide, but the figure actually shows the spectrum of three QS with central temperature 8, 13, 23 MeV, denoted as stars Q053, Q103, Q203 respectively.

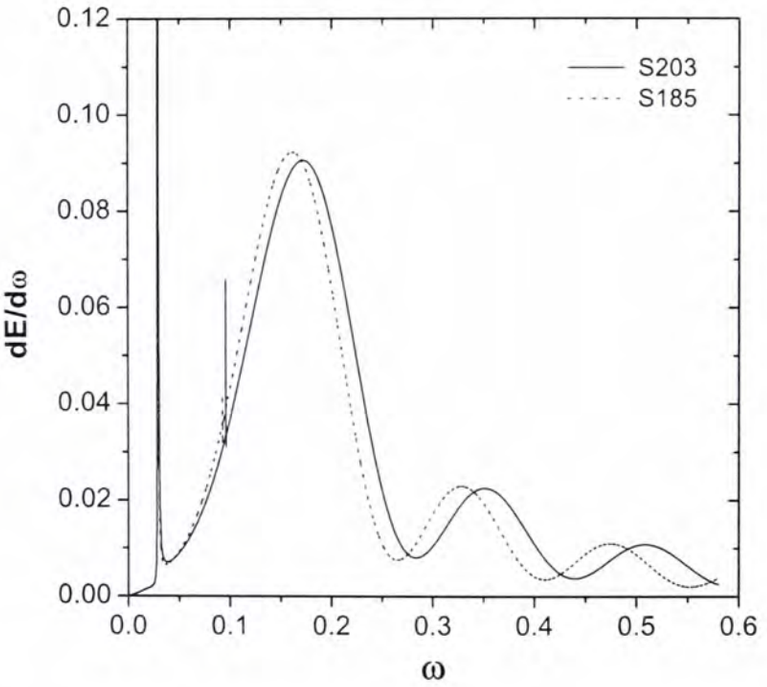

Figure 8.3: Power spectrum GW excited by an infalling thin shell onto NS with the same central temperature 23 MeV but different surface temperatures, 3, 5 MeV, denoted as stars S203 and S185 respectively.

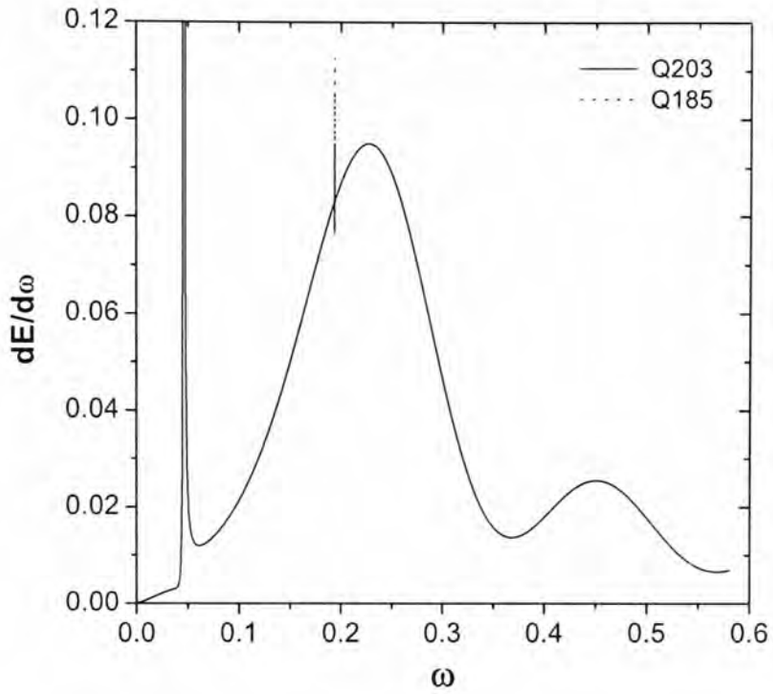

Figure 8.4: Same as Fig. 8.3 for QS. The QS with surface temperature 3(5) MeV is denoted as star Q203 (Q185).

of QS Q203 and Q185 coincide. Therefore we can say the effect of surface temperature on power spectrum depends on the nature of the compact star.

We finally compare the power spectra of an NS and a QS with the same temperature profile, presented in Fig. 8.5. The figure shows stars with different composition produce completely different different spectrum. Within the frequency range we plotted, there are three broad peaks for NS but only two for QS; both the peak position and underlying area are not similar for both stars. Besides, the positions of sharp peaks are also shifted, which differs from the previous cases that positions of sharp peaks sustain while temperature changes. These effects are, however, not surprising, because NS and QS are significantly different in stellar structure.

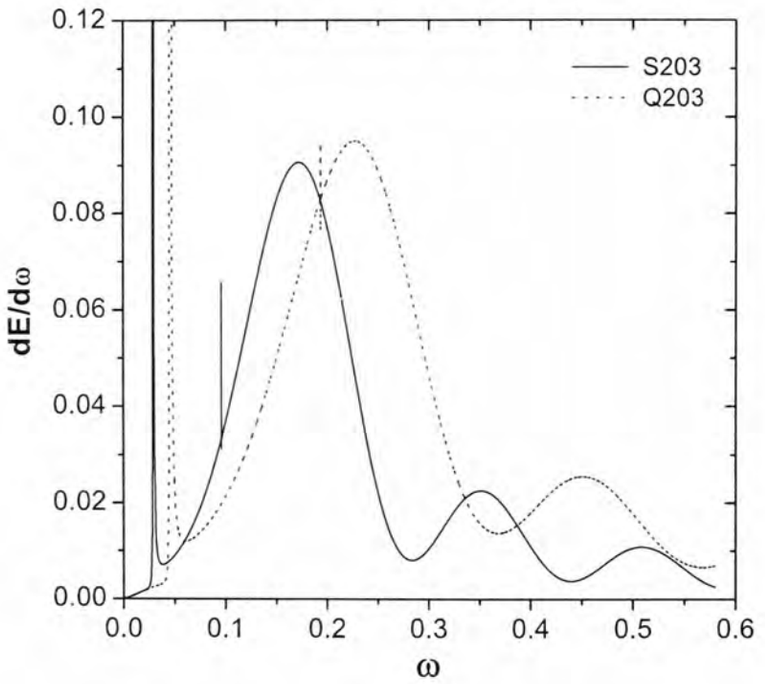

Figure 8.5: Power spectrum of GW excited by an infalling thin shell onto an NS and a QS with the same central temperature 23 MeV and the same surface temperature 3 MeV. Their notation S203 and Q203 are the same as in previous figures.

8.4 Features of radiation

In the previous section, we showed that the GW power spectrum is not sensitive to the temperature profile, and only slightly varies for neutron stars with different surface temperature. In the case of QS, the power spectrum is nearly independent of temperature. Therefore, we conclude from our tests that temperature is not a quantity that can be revealed from power spectrum of GW excited by shell collapse. The result is not interesting, we nevertheless investigate the features of a spectrum in details, in order to understand how robust the shape of a spectrum is.

8.4.1 Power spectrum

We pick the spectrum of star S203 in Fig. 8.1 (or 8.5) for analysis. Two notable features are observed in the spectrum, which are the sharp peaks and broad peaks. The sharp peaks are previously recognized by Ferrari *et al.* in their consideration of a point mass scattered by a NS [54]. They find that the sharp peaks are actually resonant excitation of fluid modes of the star, mainly f mode and p modes. So we computed the mode frequencies of S203 and other NS, and presented in Table 8.1. We see the f mode frequency of S203 is 0.293 km^{-1}, which matches the sharp peak at $\omega \sim 0.03$ km^{-1} in Fig. 8.1; the first p mode frequency is $\omega \sim 0.096$ km^{-1}, and there is a corresponding peak at about $\omega \sim 0.1$ km^{-1}. Therefore, our results agree with the argument of Ferrari *et al.*. We also find peaks in the power spectrum associated with higher order p modes, although their height and width are smaller than that of the f mode and the first p mode. Higher order p mode is barely observed in our graph merely due to the sparse resolution of the plotting. Similar analysis can also be conducted on QS, the f and p mode frequencies also nicely agree with the positions of the sharp excitation peaks.

After understanding the relationship between fluid mode frequencies and

Star	M ($M_\odot$)	R (km)	QNM	ω_r	ω_i
S203	1.4	14.6	f	0.0293	9.03×10^{-6}
			1-st p	0.0960	(4.88×10^{-7})
			1-st w-II	0.0842	0.149
			1-st w	0.210	0.146
			2-nd w	0.385	0.177
			3-rd w	0.550	0.197
S103	1.4	14.5	f	0.0297	9.26×10^{-6}
			1-st p	0.0970	(5.26×10^{-7})
			1-st w-II	0.0852	0.149
			1-st w	0.211	0.146
			2-nd w	0.386	0.177
			3-rd w	0.551	0.197
S053	1.4	14.5	f	0.0298	9.33×10^{-6}
			1-st p	0.0974	(5.37×10^{-7})
			1-st w-II	0.0855	0.149
			1-st w	0.211	0.147
			2-nd w	0.386	0.177
			3-rd w	0.552	0.198
S185	1.4	15.8	f	0.0291	8.91×10^{-6}
			1-st p	0.0927	(4.91×10^{-7})
			1-st w-II	0.0835	0.148
			1-st w	0.209	0.146
			2-nd w	0.383	0.177
			3-rd w	0.548	0.198

Table 8.1: QNM frequencies of NS S203, S103, S053, and S185. We only show the f-mode, the first w-II mode, the first three w mode, and the first p mode, which are possibly related to the features of the power spectrum within our frequency range. Only the first p mode is presented because the signal of the first mode is the strongest, and the behavior of higher order modes are similar to the first one. In addition, we find the imaginary part of g mode is too small to be excited, so we do not show frequency of g mode here. We add a bracket to the imaginary part of p mode because the value is not too confident due to the ambiguous treatment of the surface of a hot NS.

Star	M ($M_\odot$)	R (km)	QNM	ω_r	ω_i
Q203	1.4	9.46	f	0.0462	2.20×10^{-6}
			1-st p	0.194	2.25×10^{-7}
			1-st w-II	0.140	0.168
			1-st w	0.247	0.144
			2-nd w	0.458	0.178
Q103	1.4	9.46	f	0.0462	2.20×10^{-6}
			1-st p	0.194	2.30×10^{-7}
			1-st w-II	0.140	0.168
			1-st w	0.247	0.144
			2-nd w	0.458	0.178
Q053	1.4	9.46	f	0.0462	2.20×10^{-6}
			1-st p	0.193	2.32×10^{-7}
			1-st w-II	0.140	0.168
			1-st w	0.247	0.144
			2-nd w	0.458	0.178
Q185	1.4	9.46	f	0.0462	2.20×10^{-6}
			1-st p	0.194	2.25×10^{-7}
			1-st w-II	0.140	0.168
			1-st w	0.247	0.144
			2-nd w	0.458	0.178

Table 8.2: Same as Table 8.1 but for QS. We only present first two w mode because the third one exceeds our frequency range of consideration.

sharp peak positions, it is natural to refer the broad peaks as the excitation of space time modes of the star. Apart from this crude reason, the correlation sounds more convincing if the analysis of gravitational radiation of a Schwarzschild black hole is taken as an analog. In [33], Davis *et al.* regard the peaks of the GW power spectrum as 'a train' of blackhole QNM excitation. Since a black hole has no fluid mode, corresponding blackhole QNM for compact stars are the spacetime modes. However, we have two reasons to rule out this conjecture. Firstly, we consider the positions of broad peaks of S203 locate at $\omega \sim 0.17,\ 0.35,\ 0.51\ \mathrm{km}^{-1}$. If the conjecture is correct, then the second and the third peak are contributed by 2-nd and 3-rd w mode, while the first peak is the combination of the 1-st w mode and the 1-st w-II mode. But the frequencies of the high order peaks are about 10% lower than the w mode frequencies, and the contribution of w-II mode is not too convincing as the mode frequency locate near the foot of the 1-st peak. Another stronger reason is referred to the shift of spectrum for S203 and S185 in Fig 8.3. Frequencies of the broad peaks of S185 are 10% lower than that of S203, while the sharp peaks are nearly fixed. However, we have calculated that the spacetime modes of S185 and S203 are only deviated for not more than 1%. This mismatch in percentage peak shift puts the conjecture into high uncertainty.

If the broad peaks of power spectra are not excitation of the spacetime modes, then what is their physical origin? The comparison of S203 and S185 provides some hint to this issue. Due to the high contribution of the thermal electron pressure, surface of S185 expels outward and hence the radius of S185 is larger than S203 for about 10%. This percentage is close to the shift of broad peaks in the power spectrum. It suggests that the radius is one possibility of the cause. After some investigation, we find the broad peak frequencies ω_p actually locate at

$$\omega_p R_* \approx n\pi \ , \tag{8.47}$$

where n is any natural number, R_* is the tortoise coordinate of stellar surface

defined before, related to the stellar radius by Eq. 8.43.

Dependence of the tortoise coordinates is not surprising as the Zerilli equation is a wave equation in the tortoise instead of the Schwarzschild coordinates. Hence the existence of the broad peaks associate to the Zerilli function near the stellar surface, which is in fact the end point of the falling mass. We here give a hand-waving argument to the relationship Eq. 8.47 by considering the role of the Zerilli source. Because the test mass falls in the vacuum outside the star, the source term varies smoothly until reaching the radius and assumed absorbed by the star. When computing the wave amplitude by the Green's function method in Eq. 8.41, we have to integrate the some products of wave function from the stellar surface to infinity. Consider we multiply a step function onto the Zerilli source and mathematically extend the integral towards the negative infinity. The integration of the Green's function is effectively an inverse Fourier transform of the source term, because the Zerilli equation is a wave equation in a potential. After the transformation, the step function would introduce Fourier coefficients at harmonics of ωR_*, which is the cause of the broad peaks. Due to the complexity, the argument is not yet analyzed by detailed analytical calculation. Several interesting questions are remain unsolved. For example, why the position satisfying Eq. 8.47 are peaks but not troughs? Why the peaks located at $n\pi/R_*$ but not $2n\pi/R_*$ or other characteristics phase factor? How robust does Eq. 8.47 is for a general source term? Obtaining answers for these issues is our next goal of endeavor.

Despite the heuristic mathematical conjecture, we are quite confident the broad peaks are induced by the collision of the point particle on the stellar surface, instead of any QNM excitation. It can be more convincing to have a physical picture. When the particle is falling onto the star, GW is progressively excited with wide range of frequency. When it stops on the surface, considerable amount of the particle kinetic energy converts to GW with favorable frequency related to the position of the surface. The idea is in fact

more appreciable when the waveform is investigated in the next subsection. It is worthy to remark that similar broad peaks are observed by Nagar *et al.* in their simulation of quadrupolar shell accretion (Fig. 9 in [60]). They also claimed that the broad peaks do not match the spacetime mode frequencies, and regard the peaks are 'interference of gravitational field and motion of shell'. Although the broad peak in their figure does not satisfy the criteria Eq. 8.47, but we believe their peak shares the same as us in origin, because of similarity in position and width. The deviation from Eq. 8.47 is probably because their shell consists of hydrodynamics and disperses during falling. Therefore their Zerilli source is deviated from that of a point mass for at least a complicated phase factor Eq. 8.37, which shifts the peak position.

Therefore our interpretation on the features of the power spectrum is, the sharp peaks correspond to the excitation of fluid mode of the compact star, and the broad peaks are caused by the collision of the point particle onto the star. By this argument, the power spectra of various stars, Fig.s 8.1-8.5 can be explained. The spectra in Fig. 8.1 are nearly coincident, because both the radius and the fluid mode frequencies are differed by less than 2% for the three sample stars. It is because the thermodynamic properties deep inside the stars are dominated by the contribution of degenerate nuclear matter and the nuclear interactions, while temperature plays a relatively little role. Sharp peaks of S203 and S185 in Fig. 8.3 match well because their fluid mode frequencies are close, but their radii are deviated by about 10% and the broad peaks are thus shifted. Spectra of QS in Fig.s 8.2 and 8.4 are very close, because the first order correction of temperature in our quark star model scales at $T^2/\mu^2 \lesssim 0.01$, therefore the radius and QNM frequencies are little affected. Most notably difference in power spectrum is the effect of EOS, as shown in Fig. 8.5. It is expected because NS and QS are completely different in both the stellar structure and the property of local matter.

8.4.2 Wave function

Apart from the power spectrum, it is equally interesting to consider the gravitational waveform excited by a collapsing shell. The computation is simply taking the inverse Fourier transform as Eq. 8.44 on the wave amplitude spectrum $\hat{A}(\omega)$. We pick the initial conditions such that the particle falls from spatial infinity at time $t = -\infty$, and reaches the stellar surface $r_* = R_*$ at $t = 0$.

Since the power spectrum changes little for NS and QS with different central temperature, and QS with different surface temperature, it is expected the change of wave function in these cases are not more than an uninterested global phase shift. We concentrate our investigation on the corresponding cases of Fig.s 8.3 and 8.5.

We first discuss the features of waveform by that of S203 in Fig. 8.6 as an example. The waveform can mainly be separated into three parts: the gradual raise before $t - r_* = 0$, a sudden burst about $t = r_*$, and the periodic oscillation soon after the burst. The initial raise is the collective of gravitational wave induced by falling particle before reaching the stellar surface. Just as the case of an electromagnetic wave caused by an accelerating charge, an accelerating mass perturbs the background gravitational field and emits GW. Then the particle collides with the star and absorbed at $t = 0$. Part of the kinetic energy is released as GW and a burst is formed. Comparing the frequency and damping time of the burst, we find it corresponds to the broad peaks in the power spectrum. This finding agrees with our claim of broad peaks origin. In spite of the larger magnitude, the burst damps within the first tenth of milliseconds. After that, gravitational waveform is dominated by a periodic pattern, which is actually excitation of the f mode. The claim is verified by comparing the frequency and long term decay time of the pattern with the f mode frequencies.

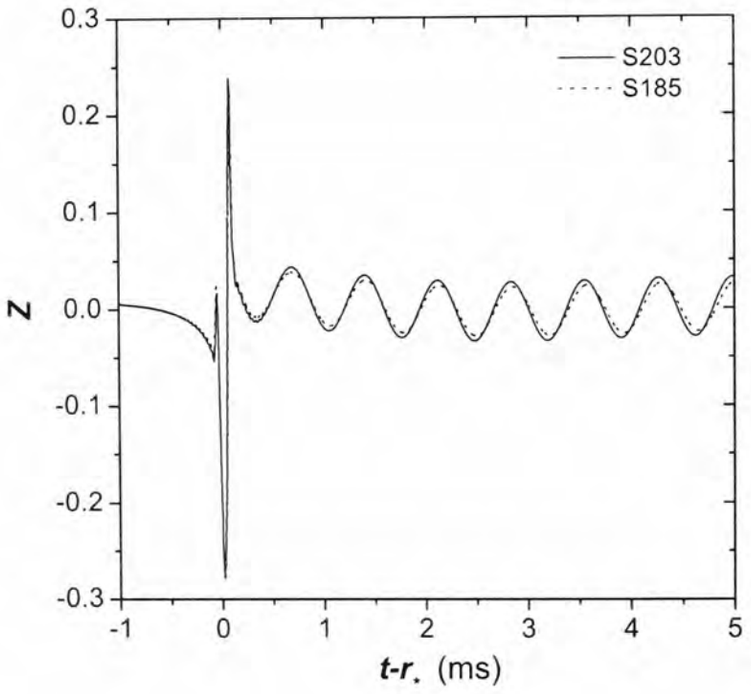

Figure 8.6: The gravitational waveform, which is excited by a shell falling from spatial infinity onto NS with different surface temperature, S203 and S185. The Zerilli function Z, which is presented in the unit system of km, is plotted against the retarded time $t - r_*$, in milliseconds. If the location of detector is fixed, the waveform is the time variation of the metric perturbation detected.

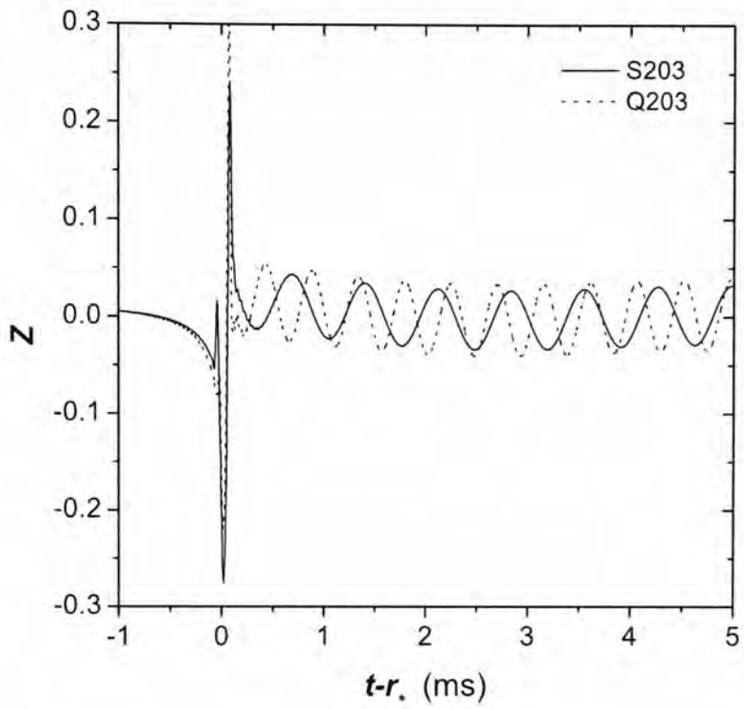

Figure 8.7: Same as Fig. 8.6 for the wave excited by shell falling onto NS S203 and QS Q203, which have the same temperature profile.

We use this interpretation to account for the difference in gravitational waveform in Fig.s 8.6 and 8.7. For the case of NS with different surface temperature, their waveforms are very close with slight phase difference. It is because the f mode of both stars are deviated by 1% only, the long term oscillating pattern are nearly identical. But their radius are different so that the stopping time of particle deviates by 10%, which slightly deform the shape of the burst and cause the phase lag of f mode GW. The difference between QS and NS is however much drastic, as illustrated in their power spectrum. Frequencies of both the burst and long term oscillation are higher for QS than NS. The reason is simply the deviation of f mode frequencies of both stars, as well as a smaller QS radius.

It is noted although sharp peaks of p mode is noticeable feature in the power spectrum, it is hard to recognize any signature of p mode in the waveform. The reason is the width of p mode excitation in the power spectrum is too

narrow, and the height of peak is far less than that of tjhef mode. In other words, the energy dissipated into p mode is far fewer than that of f mode, hence the waveform is dominated by the f mode feature. Detailed discussion of the excitation energy is given in next subsection.

8.4.3 Energy of excitation

In this subsection, we are going to consider the energy content of each mode or peak feature. The energy content of GW is interesting because it is closely related to the detectability of GW, and how well the signal can be recognized [42] [10]. In principle, we calculate the energy of each peak by integrating Eq. 8.45, which is to obtain the enclosed area of the spectrum. For the sharp peak of f mode, since we know it is a resonance between GW and fluid oscillation, we assume the shape of the peak obeys the standard Lorentzian distribution

$$\frac{dE}{d\omega} \approx \frac{2A}{\pi} \frac{\Gamma}{4(\omega - \omega_0)^2 + \Gamma^2} , \tag{8.48}$$

where ω_0 is the peak frequency; Γ is the width of the peak; A is the total area enclosed by the Lorentzian. For the broad peaks, since they are not resonant peaks, we do not fit them by the Lorentzian, but simply estimate the enclosed area by multiplying the full width at half maximum by the peak value. As the high order of broad peaks are far smaller than the first broad peak, i.e. less than 20%, and we are only interested in the order of magnitude instead of the precise values, we only calculate the energy content of the first broad peak.

We pick the power spectrum of S203 and Q203 in Fig. 8.5 to compare the relative magnitude of peaks of NS and QS. We calculate that the f mode peak of S203 contains 0.011 km of energy, and the first broad peak also contains about 0.011 km. If contribution of higher order peaks are added, about 40% of the energy is converted to the GW is distributed to the f mode. For Q203, energy content of the f mode is 0.016 km, while the first broad peak contains

0.014 km. If higher order peaks are included, the energy of the f mode is about 50% of the total GW energy.

From these results, we can see that the GW energy excited by a shell collapsing onto a QS is about 40% higher than that of an NS with the same mass. It is not surprising because the radii of the stars are different, such that the shell travels for a longer distance onto a QS, and hence gain more kinetic energy. A simple argument is to estimate the gravitational energy by a Newtonian formula, $E_G \sim M/R$, and so the extra energy gained by the shell in the QS case is about $(R_{NS}/R_{QS} - 1) \sim 50\%$, where $R_{NS} \sim 14.6\ km$ is the radius of S203; $R_{NS} \sim 9.46\ km$ is the radius of Q203.

We then compare the excitation of stars with different temperature profile. Since the stars with same surface temperature but different central temperature have nearly the same radius, and we have shown that their shape of broad peaks are nearly coincident in Fig.s 8.1 and 8.2, energy of excitation in the broad peaks are same for each type of star. We have also checked the excitation of f mode, the total energy contained in the mode is nearly identical for each type of star. Therefore, we can conclude that energy of excitation is barely affected by temperature gap between central and surface temperature, due to the similarity of stellar profile.

The effect of the surface temperature is quite different however. We find that both the broad peaks and sharp peaks of Q203 contain the same energies as those of Q185, it is because temperature is not an important factor to affect the structure of QS. In contrast, as seen in Fig. 8.3 that power spectra of NS S203 and S185 are shifted, the energy content of every features should be deviated. The enclosed area of the first broad peak of S185 is 0.010 km, which is 10% fewer than that of S203. It fits our expectation as the radius of S185 is about 10% longer than that of S203. However, the f mode peak of S185 only contains 0.0075 km, which is only 70% of that of S203. This magnitude of change exceeds all degree of difference of the extra gravitational energy gained

by the shell, the change of the f mode frequency. Consider the most notable feature of S185 is the 'long tail' sustained by thermal electrons near the surface, it should be the reason of the drastic decrease of the f mode energy. Recall that a QS can be viewed as a nearly incompressible model, and proportion of f mode energy is the greatest; S203 is most likely a typical neutron star; the long tail of S185 softens the overall stellar structure, and its f mode contains fewer energy. We believe the hardness of a compact star (or the value of effective γ) is a factor to determine the excitation energy of a QNM in addition to the mode frequencies, although it should be in the order of unity.

Sharp peaks corresponding to p modes deserve separate consideration. Unlike the f mode, the peak of a p mode is far weaker and it locates in a broad peak, so the signal of p mode interfere seriously with that of initial burst. As shown in Fig.s 8.8 and 8.9, the excitation spectrum of a p mode usually consists of a sharp peak and a sharp trough. It is hence difficult to extract the signal of p mode oscillation, because energy of excitation is estimated by directly integrating a range of spectrum and subtract the contribution of the broad peak. We first consider hot neutron stars with the same surface temperature. The first p mode of S053, S103 and S203 contain about 10^{-6} km. Their energy contents are close, and all of them are 10^4 smaller than that of the f mode. For the first p mode of S185, its energy is about half of that of S203, which is roughly the percentage decrease of the corresponding f mode energy of S185. On the other hand, the p mode energy of all QS are estimated at the range 10^{-8} km, which are 10^{-2} smaller than the p mode energy of a NS, and 10^{-6} to that of a QS f mode. In sum, shell collapse is not an efficient p mode excitation mechanism, because less than 0.01% of gravitational energy is distributed to it. The situation is worse by 2 order for QS, which the reason is suspected to be their nearly incompressible nature. Some GW detectors may employ the matched filtering technique to conduct narrow band detections [42]. If the sensitive range is finely tuned to include only the sharp peak but exclude the

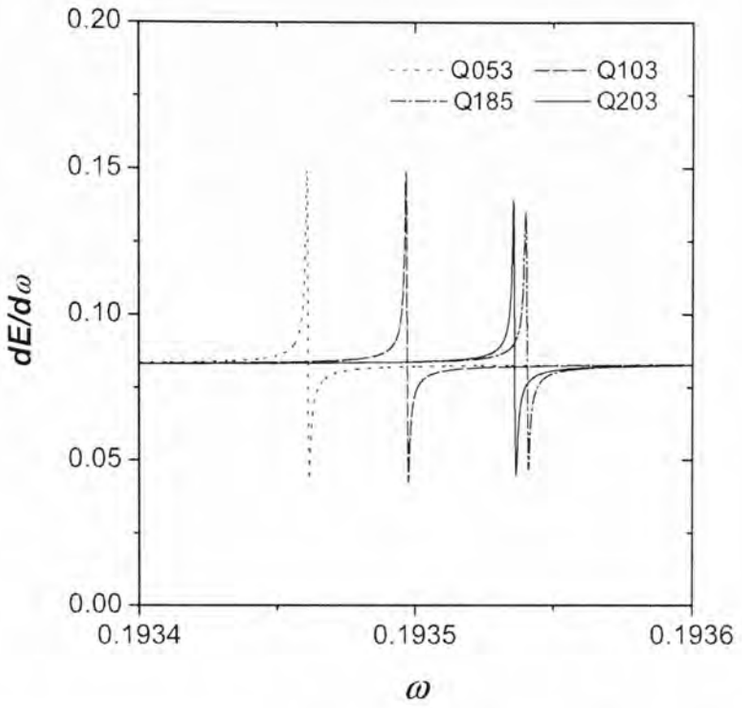

Figure 8.8: Power spectrum of GW excited by an infalling thin shell onto QS, zoomed in the vicinity of p mode frequency.

trough, detected energy of a QS mode can be 1 order larger, i.e. 10^{-7} km, while the energy content of the p mode peak is not much different from the total p mode energy for a NS.

As the conclusion to this section, we discuss the detectability and usefulness of each feature in the GW excited by the collapsing shell. GW energy induced by this way is mainly distributed to the initial burst and the f mode, only a little portion is channeled to the p mode. Exact distribution of energy can, however, be altered by the phase factor $f_{lm}(\omega)$, of which the shell is not thin and spherical in general. But the magnitude of the phase factor in all frequency range is the same order, it therefore does not affect the order of magnitude of each features. An illustration is to consider the case of a deformed sphere [51], the functional form of the phase factor is roughly $\sin a\omega/(a\omega)$ for some deformation coefficient a. It is therefore still confident that considerable amount of GW will be emitted through the f mode and the burst. Furthermore, although we get a nice empirical formula for the broad peak positions Eq. 8.47,

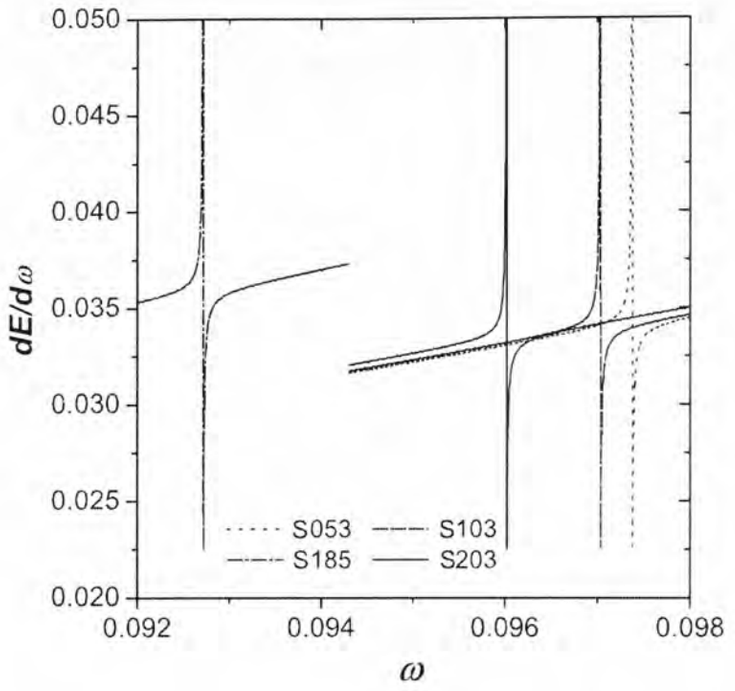

Figure 8.9: Same as Fig. 8.8 for NS.

it is no hope to obtain useful information from this burst. It is because the phase factor would greatly affect the broad peak positions as mentioned before, which blurs the physical importance of Eq. 8.47. The f mode peak position and width is however not much altered as the peak is sharp.

It seems more plausible to obtain information of a compact star from GW by the universality of f mode (c.f. Chapter 6), but the effectiveness still subjects to the signal-to-noise (S/N) ratio of the detected signals [42] [10]. Let the infalling shell is about 0.1 $M_\odot$, and the phase factor $f_{lm}(\omega)$ is about 0.1, energy contents calculated above are then reduced by an order of 10^{-4}. Energy contained in the f mode is about 10^{-6} $M_\odot c^2$, which is possible to be recognized by the Advanced LIGO to a S/N ratio higher than 10 [42]. Real frequency of the f mode can be recognized to a high precision, but the error of damping time is more than 10%. The accuracy is expected to be improved in the future generation of GW detectors. In addition, the energy contained in a p mode peak of an NS is about 10^{-10} $M_\odot c^2$ and 10^{-11} $M_\odot c^2$ for QS. This amount of energy is too low to achieve a remarkable S/N ratio, but considerable accurate p mode

can still be inferred due to effectiveness of modeled filtering [42]. Finally, we directly apply the consideration of the spacetime modes onto the broad peaks, as the peak frequency and width of a broad peak are the same order of magnitude as the real and imaginary part of spacetime modes. The burst contains 10^{-6} $M_{\odot}c^2$ in our configuration, but the required energy for a recognizable w mode is far higher than that of a f mode, which the S/N ratio is low even through detection of the Advanced LIGO. Recalling the peak position of the broad peaks are easily shifted by the shell geometry, and the detectability is low, details of initial burst is not physically interesting in reality.

Before moving to next section, we want to leave a few comments in supplement to the above investigations. Firstly, we do not present of results of g mode in detail. In fact, stable β mode does exist for our NS candidates but not the QS ones, while Y_p mode exists for both stars. However, the peak width of both kinds of g mode are too narrow, which is the same order as the damping frequency of g mode, i.e. smaller than 10^{-9} km^{-1} for NS and 10^{-16} km^{-1} for QS. Also, g mode signals are weakly excited, which its contribution to the waveform and power spectrum is not observed at our numerical resolution of frequency. From these observations, we claim that in spite of its sensitivity to temperature, g mode is not effectively excited by a collapsing shell. Alternatively, it is suggested that orbiting companion could excite considerable strong g mode [61], but it is out of the scope of this thesis.

As a further discussion of the effect of the dynamic EOS, we have calculated but not show here the power spectrum of S203 and Q203 if composition is preserved instead of holding beta equilibrium. As the radius of a star is unchanged, the position and shape of the broad peaks are exactly identical to its beta equilibrium counterpart. The position and width of a f mode peak is identical up to 6 sig. fig., agreeing with our pervious argument that f mode frequency mostly depend on the mass and the moment of inertia of the star.

Star	M ($M_\odot$)	R (km)	condition	ω_r	ω_i
S203	1.4	14.6	β	0.0960	(4.88×10^{-7})
			Y_p	0.101	(4.85×10^{-7})
Q203	1.4	9.46	β	0.194	2.25×10^{-7}
			Y_p	0.194	2.25×10^{-7}

Table 8.3: Frequencies of p mode of S203 and Q203 satisfying different dynamic EOS. The notation β represents beta equilibrium, and Y_p represents preservation of chemical composition.

Most significant deviation happens in the g mode and p mode, which the importance of g mode is very little in our scenario of GW excitation, and the p mode is not intensely excited. Therefore the overall feature of the power spectrum and the waveform are not significantly affected by the dynamic EOS. If we focus on the p mode excitation, we find that its frequency of an NS is shifted by 5% but the change of damping time is smaller than 1%; while both real and imaginary part of a QS p mode is the same up to 3 sig. fig.. The energy content of a p mode is the same order for both dynamic EOS, which is 10^{-6} km for an NS and 10^{-8} km for a QS. Therefore, all our investigation before is qualitatively true regardless for both dynamic EOS.

8.5 Non-adiabatic oscillation

In the previous sections, we investigate the oscillation of hot compact stars following the formalism of Lindblom and Detweiler [22], which has implicitly assumed the oscillation is adiabatic. Therefore the finite temperature we have added only affect the EOS (both static and dynamic) and hence the profiles of physical quantities only, but not the dynamical process during the pulsation. For most compact stars formed by ordinary nuclear matter that do not exhibit super-conductivity, adiabaticity is a good description to the dynamical properties. However, recent proposal suggests that quark matter in a QS may

exist in the form of color-flavor-locked phase (CFL) [48], in which massless bosons can be excited to provide super-conductivity [47] [46]. In order to have a deeper understanding of high temperature compact star oscillation, we include thermal conductivity as an non-adiabatic effect and consider its effect on QNM and power spectrum.

8.5.1 Mathematical Background

Recalling the formalism of linearized general relativity for gravitational wave investigation, the problem is divided into three parts: the stellar structure and the EOS, the coupling between matter and spacetime perturbation inside compact stars, the vacuum perturbation and the source term caused by the motion of mass outside the stars (c.f. Fig. 1.1). We use the TOV equation to construct the static background, which solely requires the star is hydrostatic equilibrium. In our consideration, we assume the hot compact star to be quasi-static, which pulsation timescale is shorter than any characteristics time of stellar structure changes. This assumption is not altered by conductivity, if there is no background heat flow, i.e. all the non-adiabatic effects are first order correction to an adiabatic background. So the TOV equation is still applicable to the non-adiabatic case. Outside the compact stars, we employ the RWZ formalism to describe the perturbation of spacetime. As all matter locate within the radius, there is no heat current flowing outside the boundary of star, therefore we can continue to use the Zerilli equation discussed above.

The only section that non-adiabatic effect may contribute, is the dynamics of the perturbation of matter, which is previously described by the LD equation. To date, the linearized theory of non-adiabatic pulsation is not well developed, due to its complexity in formulating the dynamics in general relativity, and poor understanding on realistic EOS of matter with non-zero temperature. A first attempt is made by Gualtieri *et al.* to include the effect

of heat conductivity and thermal dissipation [62].

Following similar treatment as we state in Section 8.2, Gualtieri *et al.* starts by linearizing the Einstein equation. Since the metric is not related to the temperature, perturbation of Einstein tensor is the same as before. One the other side, consider the stress tensor of a fluid element with the contribution of heat flux is

$$T_{\mu\nu} = (p+\rho)u_\mu u_\nu + p g_{\mu\nu} + u_\mu q_\nu + q_\mu u_\nu \ , \tag{8.49}$$

where the 4-heat-current q_μ is a conserved quantity, satisfying

$$u_\mu q^\mu = 0 \ , \tag{8.50}$$

in our case that there is no heat generating and absorption mechanism inside the star. The first order perturbation of the stress tensor Eq. 8.49 is expressed as

$$\begin{aligned} \delta T_{\mu\nu} &= (\delta p + \delta\rho)u^{(0)}_\mu u^{(0)}_\nu + (p_0+\rho_0)(\delta u_\mu u^{(0)}_\nu + u^{(0)}_\mu \delta u_\nu) \\ &\quad + \delta p g^{(0)}_{\mu\nu} + p_0 \delta g_{\mu\nu} + (\delta q_\mu u^{(0)}_\nu + u^{(0)}_\mu \delta q_\nu) \end{aligned} \tag{8.51}$$

where δ denotes the Eulerian change of the corresponding quantities. Similar to other thermodynamic quantities, the heat current perturbation is expanded in spherical harmonics and Fourier components as,

$$\delta q_t = 0 \tag{8.52}$$

$$\delta q_r = \kappa e^{-\nu/2} Q_{1lm} r^{l-1} Y^{lm} e^{i\omega t} \tag{8.53}$$

$$\delta q_\theta = \kappa e^{-\nu/2} Q_{2lm} r^{l} \partial_\theta Y^{lm} e^{i\omega t} \tag{8.54}$$

$$\delta q_\phi = \kappa e^{-\nu/2} Q_{2lm} r^{l} \partial_\phi Y^{lm} e^{i\omega t} \tag{8.55}$$

where the thermal conductivity κ is a property of matter. The system can be simplified by viewing the system in a reference frame that consider the total energy instead of the mass, of the matter is at rest [62] (which is referred to

as the 'centre of energy frame' hereafter). Then the velocity of a fluid element is re-defined as

$$\delta\hat{u}_\mu \equiv \delta u_\mu + \frac{\delta q_\mu}{p_0+\rho_0} \ , \tag{8.56}$$

and the metric tensor is transformed to

$$\delta T_{\mu\nu} = (\delta p+\delta\rho)u^{(0)}_\mu u^{(0)}_\nu + (p_0+\rho_0)(\delta\hat{u}_\mu u^{(0)}_\nu + u^{(0)}_\mu \delta\hat{u}_\nu) + \delta p g^{(0)}_{\mu\nu} + p_0\delta g_{\mu\nu} \ , \tag{8.57}$$

which generalizes the perturbed stress tensor in adiabatic case. Therefore the non-adiabatic oscillation equations preserve the structure of the LD equation. In this reference frame, other dynamical variables are re-defined as

$$\hat{W}_{lm} = W_{lm} + e^{-\lambda(r)/2}\frac{\kappa}{i\omega}\frac{Q_{1lm}}{p_0+\rho_0} \tag{8.58}$$

$$\hat{V}_{lm} = V_{lm} - \frac{\kappa}{i\omega}\frac{Q_{2lm}}{p_0+\rho_0} \tag{8.59}$$

$$\hat{X}_{lm} = X_{lm} - e^{\nu(r)/2-\lambda(r)}\frac{\kappa p_0'}{i\omega}\frac{Q_{1lm}}{p_0+\rho_0} \ . \tag{8.60}$$

Additional perturbed thermodynamic quantities have to be considered, including the perturbation of energy density ρ and the entropy per particle s

$$\triangle\rho = \sum_{\omega,l,m} -e^{-\nu/2}r^l E_{lm}Y_{lm}e^{i\omega t} \tag{8.61}$$

$$\triangle s = \sum_{\omega,l,m} -e^{-\nu/2}r^l \Sigma_{lm}Y_{lm}e^{i\omega t} \ . \tag{8.62}$$

Expressing them in the centre of energy frame, we have

$$\hat{E}_{lm} = E_{lm} - e^{\nu(r)/2-\lambda(r)}\frac{\kappa\rho_0'}{i\omega}\frac{Q_{1lm}}{p_0+\rho_0} \ , \tag{8.63}$$

and

$$\hat{E}_{lm} = c_s^{-2}\hat{X}_{lm} + nT\alpha_1\hat{\Sigma}_{lm} \ , \tag{8.64}$$

which is derived from the thermodynamic relation

$$d\rho = c_s^2 dp + nT\alpha_1 ds \ , \tag{8.65}$$

where α_1 is defined as

$$\alpha_1 \equiv \frac{1}{nT}\left(\frac{\partial\rho}{\partial s}\right)_p \ . \tag{8.66}$$

It is noted that choosing a new reference frame does not change the choice of coordinates or gauge, it is only a mathematical trick of factorization, so the metric perturbations H_0, H_1, K do not alter.

In general, non-adiabatic effects highly depend on temperature gradient inside the star, but the temperature profile varies greatly at different evolution stages, and it is sensitive to the initial conditions given by supernova explosion. As a simple physically meaningful approximation, Gualtieri et al. focus the investigation on relativistic isothermal stars [62] following Eq. 5.1.

Incorporating the dissipative effect described by the relativistic theory of irreversible thermodynamics, perturbation of heat current is connected to the dynamic equations and form a sixth order differential equation system in analog to the LD equation

$$
\begin{aligned}
H_1' &= -\frac{1}{r}\left[l+1+\frac{2Me^{\lambda}}{r}+4\pi r^2 e^{\lambda}(p-\rho)\right]H_1 \\
&\quad +\frac{1}{r}e^{\lambda}\left[H_0+K-16\pi(p+\rho)\hat{V}\right] && (8.67)\\
K' &= \frac{1}{r}H_0+\frac{1}{2r}l(l+1)H_1-\left[\frac{l+1}{r}-\frac{\nu'}{2}\right]K-\frac{8\pi(p+\rho)e^{\lambda/2}}{r}\hat{W} && (8.68)\\
\hat{W}' &= -\frac{l+1}{r}\hat{W}+re^{\lambda/2}\Big[\frac{e^{-\nu/2}}{(p+\rho)}\hat{E}-\frac{l(l+1)}{r^2}\hat{V}+\frac{1}{2}H_0+K\Big] && (8.69)\\
\hat{X}' &= -\frac{l}{r}X+(\rho+p)e^{\nu/2}\Big\{\frac{1}{2}(\frac{1}{r}-\frac{\nu'}{2})H_0+\frac{1}{2}\left[r\omega^2e^{-\nu}+\frac{l(l+1)}{2r}\right]H_1 \\
&\quad +\frac{1}{2}(\frac{3}{2}\nu'-\frac{1}{r})K-\frac{l(l+1)}{2r^2}\nu'\hat{V} \\
&\quad -\frac{1}{r}\Big[4\pi(p+\rho)e^{\lambda/2}+\omega^2e^{\lambda/2-\nu}-\frac{1}{2}r^2\frac{d}{dr}(\frac{e^{-\lambda/2}\nu'}{r^2})\Big]\hat{W}\Big\}\ , && (8.70)\\
Q_1' &= nT\frac{i\omega e^{\lambda-\nu/2}}{\kappa}\hat{\Sigma}+e^{\lambda}\frac{l(l+1)}{r}Q_2 \\
&\quad -\left(\frac{l+1}{r}+\frac{\nu'-\lambda'}{2}+\frac{\kappa'}{\kappa}-\frac{nTs'}{p+\rho}\right)Q_1\ , && (8.71)\\
Q_2' &= -\frac{l}{r}Q_2+\frac{1}{r}Q_1-nT\alpha_1p'\frac{C_p}{(p+\rho)}Q_2\ , && (8.72)
\end{aligned}
$$

where the definition of H_0 and $\hat{V}$ are the same as the LD formalism, with the replacement of hatted coordinates; entropy perturbation is connected with

others by

$$\hat{\Sigma} = C_p \left[\frac{Q_2}{T} + \frac{\alpha_1}{p+\rho} \hat{X} \right] \; ; \tag{8.73}$$

C_p is the specific heat capacity at constant pressure defined by the thermodynamic relation

$$C_p = T \left(\frac{\partial s}{\partial T} \right)_p \; . \tag{8.74}$$

The first four equations, Eq.s 8.67-8.70, are analog of the LD equation; the additional two, Eq.s 8.71-8.72, describe the profile of heat current perturbations. The deviations are: quantities are considered in the centre of energy frame (hatted coordinates) instead of the centre of mass frame , which is mathematically unimportant to the solution and QNM as the structure of equations is not altered; substitution of term $c_s^2 X$ in Eq. 4.13 by $\hat{E}$ in Eq. 8.69, which is the crucial point contributed by the non-adiabatic effect. According to Eq. 8.64, $\hat{E}$ reduces to $c_s^2 X$ in the adiabatic case where entropy is preserved, i.e. $\Sigma = 0$ (equivalently $\hat{\Sigma} = 0$ as the centre of energy frame reduces to the centre of mass frame at the adiabatic case). It is consistent that the new set of equations reduce to the LD equation without the entropy variation. In other words, the strength of non-adiabatic effect is determined by $\hat{\Sigma}$. Magnitude of $\hat{\Sigma}$ can be briefly accounted for in Eq. 8.71, it locates with a coefficient containing the inverse of conductivity. If the value of conductivity is low, it would intrinsically suppress the magnitude of Σ, which agrees with expectation that the adiabatic assumption is valid if conductivity is low.

Because the metric perturbations are same as those in the LD equation, the connection between the new set of equations and the Zerilli function is exactly the same as before by Eq.s 8.7 and 8.8.

8.5.2 Numerical results

Because the equations of Gualtieri *et al.* [62] require relativistic isothermality, we construct an isothermal QS, following the same MIT bag model as before,

with a surface temperature 20 MeV. The new sets of equation require additional thermodynamic properties for computation, while most of them can be calculated by derivatives of the analytical grand potential, the conductivity is determined by the heat transfer mechanism which is considered separately. In order to maximize the non-adiabatic effect for observation, we employ the greatest conductivity proposed, which is the superconductivity of CFL QS [46]. They assume massless bosons are excited in the CFL phase and travel freely within the star, and hence conduct heat. After some unit conversion, the conductivity κ_{CFL} is given by

$$\kappa_{CFL} = 1.74 \times 10^{47} T_{\mathrm{MeV}}^3 R_{\mathrm{km}} \ \mathrm{km}^{-2} \ , \tag{8.75}$$

where T_{MeV} is the value of temperature in MeV, R_{km} is the radius of the QS in km. Although we are not using the EOS of CFL quark matter, we want to employ its conductivity due to two reasons. Firstly, we want to probe the upper bound of non-adiabatic effect, so we use the greatest conductivity proposed, though the existence of CFL superconductivity in such a high temperature is doubtful. Secondly, the mathematical structure of CFL EOS follows that of the MIT bag model, their difference is the relationship determining the chemical potential of quark species. This would slightly alter the buck properties of the EOS, but do not cause dramatically qualitative change in the matter behavior, i.e. precise values of quantities, like pressure and entropy, will be difference in both quark matter model, but the overall structure of the QS does not change much.

We compare the power spectrum without or with non-adiabatic effect in Fig. 8.10. Both spectra belong to the same star, but their dynamics are described by the LD equation and the non-adiabatic oscillation equation respectively. Broad peaks are not altered because the radius does not depend on the dynamics. Position of the sharp peaks do not vary much, which agrees with

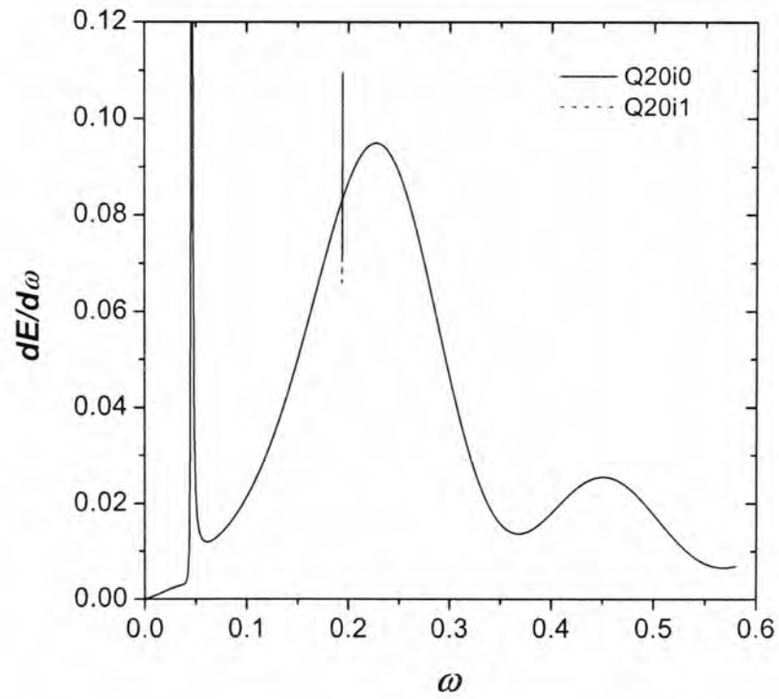

Figure 8.10: Power spectrum of GW excited by an infalling thin shell onto a relativistic isothermal QS with surface temperature 20 MeV. The dotted line shows the effect if conductivity is included into the calculation. The notation Q20i0 and Q20i1 respectively correspond to the situations that conductivity is zero or finite.

Star	M ($M_\odot$)	R (km)	QNM	ω_r	ω_i
Q20i0	1.4	9.47	f	0.0461	2.19×10^{-6}
			1-st p	0.194	2.24×10^{-7}
			1-st w-II	0.140	0.168
			1-st w	0.247	0.144
			2-nd w	0.458	0.178
Q20i1	1.4	9.47	f	0.0461	2.19×10^{-6}
			1-st p	0.194	5.66×10^{-7}
			1-st w-II	0.140	0.168
			1-st w	0.247	0.144
			2-nd w	0.458	0.178

Table 8.4: QNM frequencies of an relativistic isothermal QS oscillating with or without the non-adiabatic effect. We show that the f mode, the first w-II mode, the first two w mode, and first p mode as before. The imaginary part of the non-adiabatic p mode is not found by conventional mode extraction method, detail is shown in Appendix G.

the claim of Gualtieri *et al.* [62] that non-adiabatic effect on the real frequencies of f mode and p mode is minor. We calculate the mode frequencies in Table 8.4. Both the real and imaginary part of f mode, which is closely related to the pattern of power spectrum, are not affected by the non-adiabatic effect up to 3 sig. fig.. We have checked that the difference emerges at the 7 sig. fig.. Real frequency of the first p mode is also not much changed, the greatest influence of conductivity is on the imaginary part of p mode, which damps about two times faster in the non-adiabatic case. This could be understood by the pulsation characteristics of p mode, that the pressure perturbation is large. Change of pressure causes heat variation due to some thermodynamic relations, heat dissipative effect is thus active and acts as a mechanism to loss mode energy in addition to the GW.

As a result, the general feature of a power spectrum is not affected by the non-adiabatic effect, there is only minor difference corresponding to the sharp peaks of p mode. Since the imaginary part changes more vigorously than the real part, we expect that the sharp peak locates very close to the adiabatic p

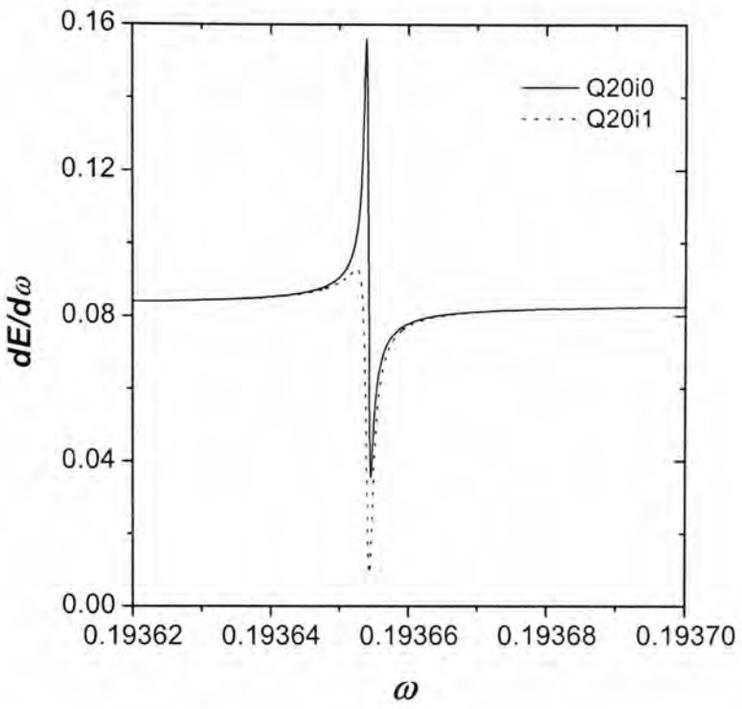

Figure 8.11: Same as Fig. 8.10 but zoomed in the vicinity of p mode frequency.

mode but the width is varied. We plot in Fig. 8.11 the power spectrum in the vicinity of p mode frequency, it is clear that the p mode peak is significantly damped by the non-adiabatic effect. The whole energy content of the feature, the sharp peak and the trough, contains a net energy for 10^{-8} km in the adiabatic case, but the thermal dissipation draws out 10^{-7} energy. As shown in Fig. 8.11, the non-adiabatic effect nearly cuts the whole sharp peaks and deepens the trough, which turns out to be a net loss of energy. It is not too surprising, however, that a resonant at p mode frequency causes vigorous fluid motion inside the QS, which facilitates energy depleting in heat and reduces the energy channeled into GW.

Lastly, we have computed the scattering and power spectrum in the vicinity of g mode. As discussed before, the g mode of a QS caused by adiabatic oscillation is hardly excited, and its theoretical damping time is extraordinary long. When non-adiabatic effect is added, the damping time is significantly

shorter because the thermal dissipation is a more efficient energy depletion mechanism than the GW [62]. In the scattering profile, we found the signal of g mode disappeared in the non-adiabatic case. It is probably because the damping time is much faster, the QNM locates far from the real axis in the complex plane, and hence reduces the contribution to the spectrum. Although a larger imaginary part usually causes a wider excitation peak, however no obvious peak is observed in the power spectrum. The energy should be lost by resonant damping just the p mode case.

8.6 General relativistic simulation

In the previous sections, we consider the collapsing shell excited GW by making at least two assumptions. First, the perturbation is small that does not alter the background; secondly, the infalling shell is thin and formed by dust. Based on them, we obtain the power spectrum and the waveform, possessing some interesting features presented before. We want to ask if these features are realistic and detectable, or they are merely caused by over-simplifying the problem in the linear approximation regime. Therefore, we try to verify our results by comparing them with the data generated by, the state-of-the-act, 3-dimensional full general relativistic numerical simulation.

8.6.1 Technical briefing

Our simulation employs the code Cactus, which can numerically solve the full set of non-linear Einstein equation without making any assumptions [63, 64]. All the hydrodynamics of the star and the falling matter can be included, as well as their gravitational interaction. It is noted that we use the notations and units of Cactus in this section, which all quantities are expressed in solar mass $M_\odot = 1.477$ km, and the isotropic coordinates is employed instead of the Schwarzschild coordinates. The radial distance of both coordinate systems are

related by

$$r_{Sch} = r_{iso}\left(1 + \frac{M}{2r_{iso}}\right)^2 . \tag{8.76}$$

As before, the scenario we consider is the time just after supernova explosion, matter of the original star is either expelled to the deep space, or collapses into a remnant as a hot compact star. A portion of the expelled matter do not have enough energy to escape from the gravity of the remnant. They would attract each other, form a shell and fall back to the center. Since there is no universality of the shell matter distribution, we follow the approach of [55] to formulate the collapse of an artificial shell in order to investigate the features of GW excitation. The shell is thin (but the width is finite) and the density distribution is given by

$$\rho = \rho_0 e^{-\kappa(r-r_0)^2} \sin^2\theta , \tag{8.77}$$

where in this section the ρ is the rest mass density instead of the total energy density before; κ is the factor controlling the width of the shell, we choose a value that gives a full width of half maximum $w = 0.5$; ρ_0 is the maximum density determined by the total rest mass and the position of the shell.

For simplicity, we consider the remnant is a polytropic star with background EOS

$$p = k\rho^\Gamma , \tag{8.78}$$

where we choose $k = 1000$ and $\Gamma = 2.0$. We pick the initial central density of the star to be 1.28×10^{-3} which yields a star with gravitational mass $M \approx 1.4$ and radius $R \approx 8.13$. Matter of the shell is distributed according to Eq. 8.77 and follow the same EOS as the star. It is noted that the initial configuration, which is essentially a polytropic TOV star surrounded by an artificial polytropic shell, is not a solution of the Einstein equation. The configuration is rectified by intrinsic initial value problem solver in Cactus, which is inevitably slightly varied.

Our system is placed in a cube with 225 grids in both x, y, z directions. Separation of each grid is 0.2, which implicitly places the boundary at $x, y, z = \pm 22.5 \approx 2.8\ R$. Evolution time step is chosen as 0.08. Upon evolution, the Cactus code updates the configuration by solving the whole set of coupled differential equations in the Einstein equation. The evolutionary EOS is the ideal fluid EOS instead of the polytropic model in the background, which the functional form is given by

$$p = (\Gamma - 1)\rho\epsilon\ , \tag{8.79}$$

where ϵ is the internal energy per rest mass of a fluid element. The quantities ρ and ϵ evolve according to a relativistic version of the Euler equation and corresponding conservation laws. This EOS includes heating effect during the shell collapse.

In order to conduct the simulation in high enough resolution within finite computational time, we can only place the boundary such close to the star surface. Gravitational perturbation does not, however, propagates as waveform, because the radiation zone of GW is far beyond the boundary we choose. Instead of recording the gauge invariant GW, we pick the wave extraction method employed by Shibata and Sekiguchi [65, 66]. They consider the GW is related to the oscillation of stellar matter by the quadrupole formula, Eq. 18 in [65], and extract the waveform by computing derivatives of the quadrupole moment of the star, Eq. 21 in [65]. Since this method mainly requires data inside the star, GW can be extracted from our simulation without the needs to impose a large grid as far as the wave zone. However, the definition of the quadrupole moment is not gauge invariant, which depends on the choice of coordinates in general. Waveform computed in this way is merely the GW observed in a specific gauge and coordinate system, which is not exactly the gauge invariant GW. Besides, quadrupole moment does not measure the oscillation of spacetime metric, which intrinsically exclude spacetime modes excitation.

However, according to a few test run conducted by Shibata and Sekiguchi, both the gauge invariant wave and the quadrupole wave are close in frequency and magnitude. Moreover, w mode is believed to be weakly excited in our scenario. Therefore we still apply their approach for simplicity.

8.6.2 Numerical results

The major difference between the linear approximation and full GR simulation, is that Einstein equation is non-linear in nature, therefore the assumption of linearity is not valid if the perturbation is large. In the linear regime, qualitative behavior of our results do not alter if a larger falling mass is considered, the GW power spectrum and waveform are simply scaled by a constant. However, shell with different masses cause significantly different distortion on the background system. For examples, the shell would deform the background star, gravity of the shell elements also affect each other during the collapse, these are all ignored in the linear approximation.

To account for the effect of shell mass, we conduct two runs with the same background star but shells with total rest mass $m_0 = 0.1$ and 0.01 (where I define the m_0 to be the volume integral of the rest mass density under a flat background). Although it may not be the true definition of rest mass, the actual value is unimportant for us because we are looking for features of the pulsation instead of calculating the wave precisely. In fact, the 'rest mass' we defined should be the same order as the physical one, it would not much affect the wave behavior and our qualitative analysis. Position of the peak density is placed at 1.5 times of the initial stellar radius, i.e. $r_0 \approx 12.2$.

The waveform is shown in Fig. 8.12. In order to account for the non-linear effect, we normalized the wave by the rest mass of the shell. If the linear assumption is still valid, waves shown on up and down panels should be identical, but here is obviously not the case. From the figure, we find that the

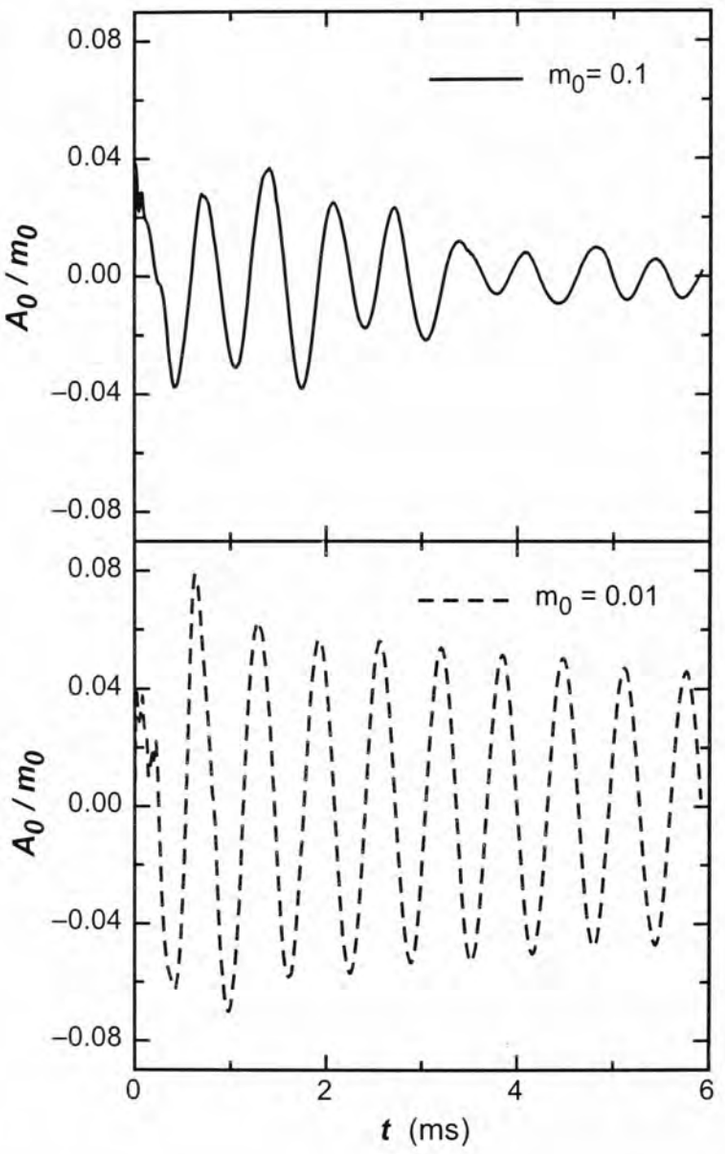

Figure 8.12: Quadrupole wave obtained through full general relativistic 3D simulation. Above (below) panel shows wave induced by a shell with $m_0 = 0.1$ ($m_0 = 0.01$). The wave is normalized by m_0, and plotted against time in milliseconds. The wave amplitude is exactly zero for $t < 0$ by definition.

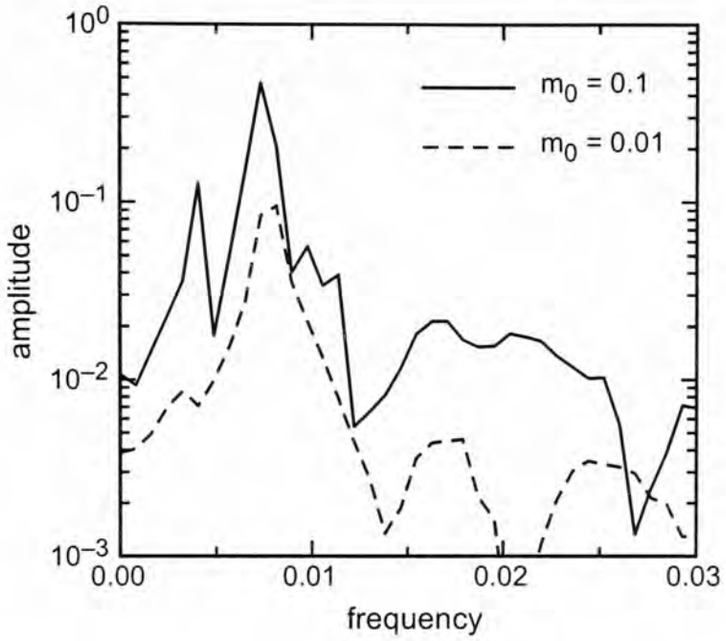

Figure 8.13: Fourier transform of the quadrupole wave in Fig. 8.12. The amplitude spectrum is shown in log scale of $M_\odot$ unit, while the unit of frequency is $M_\odot^{-1}$.

normalized wave amplitude in $m_0 = 0.01$ case is about two times larger than the $m_0 = 0.1$ case. It suggests that a shell with smaller mass is more efficient to excite GW, in the context of ratio of energy channeled into it. Furthermore, the wave in the $m_0 = 0.01$ case shows a nearly monotonic pattern, while beat-like interference pattern is observed for the $m_0 = 0.1$ case.

To study this issue in details, we conduct Fourier transform on the quadrupole wave and present the results in Fig. 8.13. Mainly two major sharp peaks are observed, whose frequencies are about 0.004 (first peak) and 0.0075 (second peak) for both configurations. The second peak of the $m_0 = 0.1$ case is higher than that of the $m_0 = 0.01$ case, but for less than 1 order. It is consistent with the analysis of normalized wave amplitude regarding the high excitation efficiency of less massive shell. The height of the first peaks are however deviated by more than an order, so that interference effect is less serious in the $m_0 = 0.01$ case and the wave looks more monotonic.

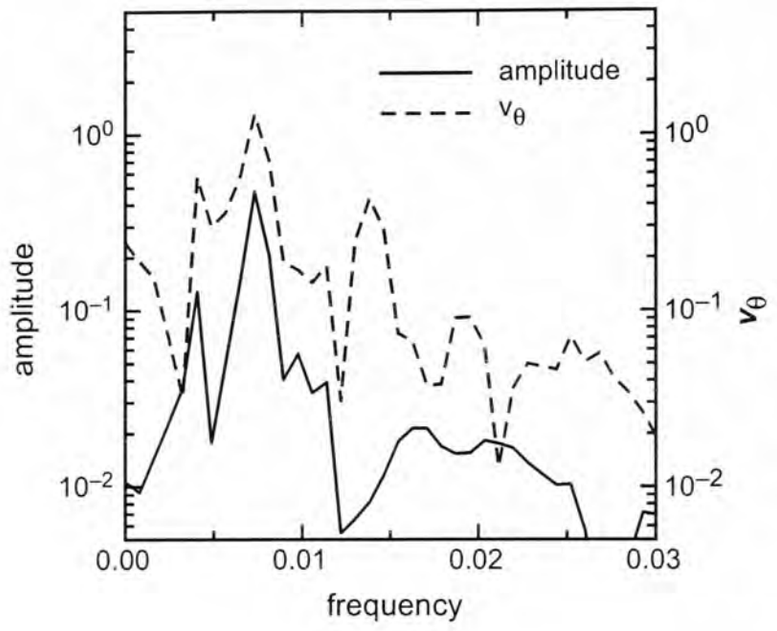

Figure 8.14: The dashed line shows the Fourier transform of v_θ at diagonal position $5M_\odot$ away from the stellar centre for the case $m_0 = 0.1$. For comparison, we show the Fourier transform of the quadrupole wave in solid lines.

In order to verify whether these peaks indeed correspond to fluid mode oscillation, instead of numerical errors, we check if they couple with the fluid motion at those frequencies. The $m_0 = 0.1$ case is picked for considertaion. We plot in Fig. 8.14 the Fourier transform of the fluid velocity along the θ direction, v_θ, at diagonal position $5M_\odot$ away from stellar centre. The reason why we choose v_θ is because the velocity along the radial direction is dominated by the radial oscillation of the star. Although the radial oscillation does not generate GW, its amplitude is too large that screen the polar oscillation mode.

As shown in Fig. 8.14, there are peaks of v_θ corresponding to the 0.004 and 0.0075 peaks in the wave amplitude spectrum, therefore the peaks are seemingly physically meaningful features. The next question is to identify what the peaks are. We identify the peaks by employing the universality of the f mode suggested by Leung and Tsui obtained by the linearized formalism [4], Eq. 6.7 with parameters shown in Table 6.1. It is noted that the equation

is dimensionless, therefore all numerical parameters are independent of units. In the $m_0 = 0.1$ case, the total mass of the polytropic star after the shell has been combined with the remnant is $M \approx 1.5$. The value of mass is not definite, it is because the system has not reached an equilibrium, the total energy and the matter distribution are still fluctuating until the end of our simulation. Since the radius is not well defined for a vigorously pulsating star, we pick the corresponding radius for a $M \approx 1.5$ polytropic star, $R \approx 7.5$, which the value is 9.1 after transforming to the Schwarzschild coordinate system used in obtaining the universality. The fundamental mode frequency generated by the universality is 0.0081, which is close to and less than 10% deviated from the second peak located at 0.0076 in our simulation. Consider the universality is empirically obtained by consideration in the linear regime, and the compactness of our polytropic star is not so well defined, also the spectral resolution of our Fourier transform of simulated waveform is not too high to obtain a precise peak value, we believe the result of universality already shows that the second peak corresponds to the f mode of the star.

If the second peak is the f mode peak, then the first peak is postulated to be the g mode peak. It is because only g mode is the only fluid mode with a frequency smaller than that of f mode for a non-rotating star. Since g mode is highly sensitive to the EOS, there is no universality proposed. It is well known that the restoring force of g mode is buoyancy of the fluid element, which is usually caused by chemical or temperature gradient. In other words, there is no g mode if the EOS obeyed by the background is the same as that of the oscillating elements, such that pressure is always a single-valued function of density. So we can verify our conjecture by removing the heating mechanism in our simulation. We do this by switching the evolutionary EOS from the ideal fluid to the polytropic EOS, such that ϵ is a monotonic function of ρ throughout the evolution.

We pick the $m_0 = 0.1$ case for consideration, because it possess the strongest

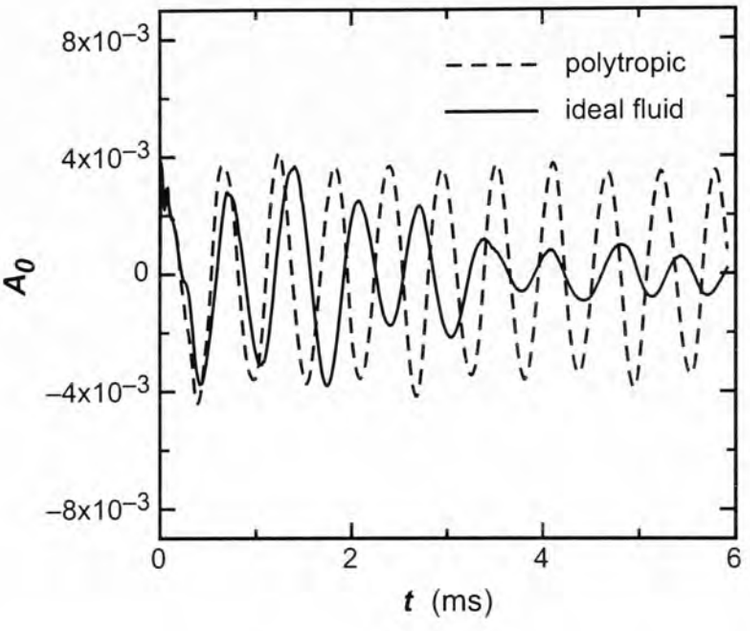

Figure 8.15: Quadrupole wave induced by a collapsing shell, which the evolutionary EOS is the ideal fluid EOS (solid line) and the polytropic EOS (dashed line). The solid line is the same as the upper panel of Fig. 8.12 up to a normalization. The waves are not normalized, and plotted against time in milliseconds.

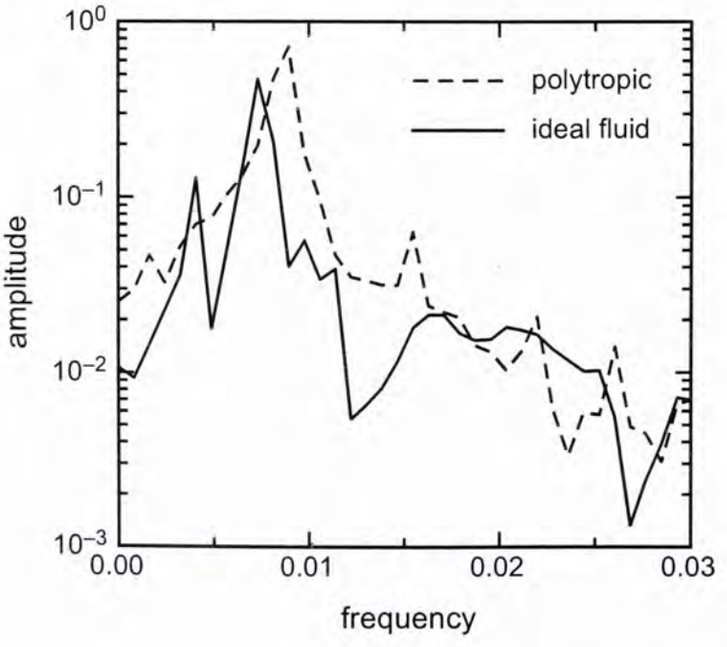

Figure 8.16: Fourier transform of the quadrupole wave in Fig. 8.15. The amplitude spectrum is shown in log scale of $M_\odot$ unit, while the unit of frequency is $M_\odot^{-1}$.

first peak as shown in Fig. 8.13. All initial configuration is the same as before, i.e. the initial stars are identical and the shell is placed at the same position with the same mass. However, as we have mentioned that the initial configuration is not necessarily a solution of the Einstein equation, the true initial condition of our configuration requires rectification that incorporates the evolutionary EOS. The rectified initial configuration is different for ideal fluid and polytropic case, i.e. their matter distribution are slightly deviated. But this deviation is minor, and does not affect our conclusion to be drawn.

We show their waveform in Fig. 8.15 and the Fourier spectrum in Fig. 8.16. Wave amplitude of both setup are close initially, but wave of the ideal fluid case soon produces beat-like interference pattern, while the wave of polytropic case is pretty monotonic. Consider the Fourier spectrum, several sharp peaks are noticed in the polytropic case, among which the highest locates at frequency ≈ 0.0084. This peak can be verified as the f mode peak by the universality employed before (The star has an equilibrium mass $M \approx 1.55$, corresponding radius is $R \approx 8.8$ in Schwarzschild coordinate, and the inferred f mode frequency ≈ 0.0085). It is noted that the mass at equilibrium is slightly larger than that in the ideal fluid case due to the initial configuration rectification. After locating the f mode, we see that there is no sharp peak with frequency than the f mode, i.e. there is no peak corresponding to the 0.004 peak in the ideal fluid case. There is a small hill at frequency ≈ 0.002, but we believe it is merely noise but not a QNM peak. We claim this because the hill is not strong, about 2 order weaker than f mode and even weaker than the peak at frequency ≈ 0.015, and it is given by the third data point in the Fourier spectrum, which the result at this frequency range is not accurate. It is worthy to note that the high frequency peaks in the polytropic case is thought to be p mode excitations. However similar peaks are hardly recognized in the ideal fluid case, and since there is no universality for p mode, verification of those peaks requires more future works.

Since the first peak is observed in the ideal fluid case, where heating mechanism presents; but missing in the polytropic case, where is fluid motion is adiabatic, it further evidences that the first peak is a g mode excitation. The result is quite surprising, because analysis in the linear regime shows that g mode is very difficult to be excited, as little energy is channeled into this mode and the width is very narrow. However, both the strength and the width of the g mode peak observed in our full GR simulation is comparable to those of the f mode. The g mode wave thus significantly affects the overall GW waveform. The linearized formalism fails to produce a strong g mode may be because it assumes the background to be static and not affected by the infalling mass. In reality, a massive shell can, however, cause vigorous disturbance to the compact star, effects include dragging of the stellar matter, as well as heating due to rapid pressure change by the radial pulsation. It suggests that g mode GW may commonly exist in realistic scenarios. Since g mode is closely related to the EOS, and its low frequency lies on the more sensitive range of GW detectors, our finding can lead to more interesting experimental and numerical results in the future.

We finally compare the waveform obtained from linear and full GR approach. Signal of f mode obviously dominates the late time behavior in both calculations. However, apart from the significance of g mode, two other features are different between both approaches, which are the rise of wave amplitude before the shell reaches star surface, and the burst when the shell collides with the star. We consider them one by one. Firstly, the initial rise in linearized approach is the perturbation of background metric induced by the accelerating particle. Since the mass of the falling particle is small by definition, and the star is assumed to be static, the magnitude of gravitational perturbation induced is hence weak. In the full GR case, main portion of shell matter falls onto star roughly at $t \approx 0.1$ ms. As shown in Fig. 8.12, for example, the wave amplitude at this time range is comparable to the late time

mode pulsation, which is much larger than that of the linearized approach. This is because the shell in full GR simulation imposes great distortion to the matter inside the star; it causes a drastic change of quadrupole moment and hence yields quadrupole wave. Secondly, the burst observed in the linearized approach originates from the sudden energy release when the particle's falling motion is stopped by the star. This feature is however absent in the full GR simulation. It is because the shell in the linearized approach is assumed to be thin, so that all energy is concentrated in a small spatial region, and release all in the meantime it reaches star radius. On the contrary, matter shell in the full GR simulation occupies a finite Gaussian width, and its internal pressure spreads the matter distribution during evolution. Since the shell matter steadily merges with the star, energy of the shell is gradually released during the whole process. Therefore there is no strong burst in the full GR simulation. This phenomenon can also be explained by a non-trivial phase factor in Eq. 8.37 corresponding to a thick and deformed shell. The factor shifts and disperses the broad peaks in power spectrum even in the linearized approach, which reduces the strength of the burst.

8.7 Summary

In this chapter, we compute the power spectrum and the waveform of GW induced by an infalling dust shell onto hot compact stars. Regge-Wheeler-Zerilli formalism of the linearized theory of general relativity is employed. We find that the power spectrum involves regularly located broad peaks, as well as sharp peaks with particular frequencies. It is verified that the broad peaks correspond to the sudden release of energy when the shell collides with the compact star, therefore the peak position is only related to the stellar radius. On the other hand, the sharp peaks are excitation of QNM of the compact star. The f mode is the most significantly excited, followed by p modes, while

g mode and spacetime modes are hardly excited. Moreover, the GW waveform is dominated by the f mode oscillation and the initial burst of energy release, other features are barely observed.

This scenario is most likely to happen one minute after the supernova explosion, which the remnant could exist as a compact star, and a portion of less energetic expelled matter falls back to the central compact object. Since temperature of a new born compact star is as high as 10^{11} K range, thermal effect becomes a non-trivial factor on the stellar properties in addition to the EOS. It is interesting to know how temperature affects gravitational emission, therefore we construct three cases for comparison. Firstly, we consider compact stars with the same surface temperature observed, but the temperature profile is different beneath. The power spectrum is however not much altered, it is because the EOS in high density region is dominated by the properties of nuclear matter, while the contribution of temperature is relatively little. Then we compare two stars with the same central temperature but different surface temperature. Sharp peaks shift due to the change of mode frequencies. The broad peaks of the hotter one shift towards lower frequency because of the extended radius, it is because the electron contribution becomes significant in low density region, such that the high temperature largely increases electron pressure and expels the radius. Furthermore, it is believed that quark matter can be a stable form of matter under extremely high temperature and density. We thus compare the GW power spectrum and waveform excited by a hot QS to that of a hot NS. Because QS is more compact, temperature barely affects its structure and the f mode frequency. Therefore the power spectrum of QS is even less sensitive to temperature than that of NS. Nevertheless, features of the GW emitted by NS and quark stars are dissimilar, because their structure are completely different.

If quark stars is considered, it is more appropriate to consider non-adiabatic stellar oscillation, as quark matter may exist in CFL phase which permits

superconductivity and facilitates thermal transport. We find that the GW power spectrum is nearly insensitive to the non-adibatic effect, because the f mode frequency and the radius of QS are not affected. Most significant deviation appears at the p mode peak, where thermal dissipation significantly withdraws energy from the oscillation, causing a trough in power spectrum. This phenomenon is, however, not easily noticeable in realistic detection, unless very precise matched-filtering technique is employed.

Our aim of this chapter is to verify if shell collapse can excite GW energetic enough for detection. We find that f mode consists of about half of the GW energy. For a typical example of a deformed shell 0.01 solar mass, energy contained in the f mode is $\sim 10^{-6}$ $M_{\odot}c^2$, which is possible to be recognized by advanced GW detectors with reasonable precision on the frequency. Another half of the energy is given to the initial burst. In spite of the rich energy content, it does not contain any physically meaningful information. A little portion, about 4 order less than the f mode energy, is carried by p modes. The signal is weak but marginally extractable, due to the high signal-to-noise ratio of p mode detection scheme. We attempt to look for the g mode, but its width is too narrow and the signal is not strong to be recognized in the power spectrum. It is reminded that all mode excitation energies we have computed in this chapter should be treated as the upper limits of realistic scenarios. It is because the energy of a collapsing shell will also dissipate in various physical mechanisms, such as nuclear reactions ignited by the collision between the shell and the compact star, and the radiation loss due to heat up of matter. Therefore, not all kinetic energy of the shell is channeled to the GW, and the detection of those weakly excited modes are even more pessimistic in reality.

We also conduct several runs of full general relativistic simulation, in order to verify the validity of our results generated by linearized formalism. Although the f mode is still a dominant feature in the simulated quadrupole wave, it is surprising that the strength of g mode excitation is comparable to that of f

mode. It is because the full GR simulation includes heating effect, as well as interaction between the shell and star, which both effects facilitate g mode pulsating mechanism. On the contrary to the conclusion drawn from results of linearized formalism that g mode is unimportant, full GR simulation suggests g mode could be more common than expected, which could provide fruitful information about the EOS and temperature of compact stars.

All in all, we believe shell collapse is effective to excite the f mode, as supported by both linearized and full GR approaches. Excitation of other modes is however doubtful. Although sharp, but weak, signals of p mode is noticed in the results of linearized formalism, and there are peaks suspected to be p mode excitations in the full GR simulation of polytropic star, there is no corresponding peaks observed in the full GR simulation of ideal fluid star. The exact reason is unknown, but we guess that the suppression of p mode should be due to the limited time evolution allowed in our simulation. Since the damping time of p mode is as long as 1s, our truncation essentially reduces the contribution of p mode, therefore the detection of p mode is still optimistic. On the other hand, g mode is not observed in the results of the linearized approach, but its signal is significant in full GR simulation. Considering the simulation captures more physical process than the linearized formalism, and various physical phenomena are recently proposed to be possible g mode induction mechanism during supernova explosion (e.g. [67]), detection of g mode is hence encouraging. Spacetime w modes are QNM that are least possible to be excited. No clear signal is noticed in the power spectrum computed by linearized formalism. However, this argument cannot be verified by the full GR simulation, as the spacetime modes GW is not included in the quadrupole wave. But even if spacetime modes contain as much energy as the f mode, we believe they are still scarcely detected because their short damping time greatly reduces their detectability by current generation of GW detectors.

Chapter 9

Conclusion and remarks

The aim of this thesis is to extend the investigation of the gravitational radiation induced by stellar oscillation, from the regime of zero temperature compact stars to hotter newly born ones. We want to verify if temperature would affect the features of GW, so as to provide theoretical guidelines on what kind of information of a hot compact star could be obtained from GW detections.

Firstly, the QNM spectra of hot compact stars are computed under the formalism of linearized theory of general relativity. We consider the hot compact stars may exist in two possible forms, NS and QS. By imposing the relativistic isothermal temperature profile, quasi-static compact stars are constructed and set to oscillate. Spacetime modes and fluid modes are investigated for stars with different surface temperature. We find that the f mode and w mode frequencies are barely sensitive to the temperature, but g mode frequency shifts dramatically for both kinds of star. In addition, we try to investigate the cooling process of a hot supernova remnant by considering compact stars with the same baryonic mass but varing temperature. When temperature decreases, the f mode and w mode frequencies vary for a few percent while the g mode frequency can be reduced by an order. If phase transition from QS to NS happen after the temperature passes the critical temperature of quark matter, a shift of GW mode frequencies for not less than 10% can be observed, which can

be a plausible way to probe high density matter properties via astronomical observations.

In order to understand the thermal insensitivity of the f mode and w mode, we propose a modified version of universality between these mode frequencies and the geometric parameters of a compact star. We find that the moment of inertia demonstrates more robust universal pattern on the QNM spectra, than the suggestions in previous literature that incorporate radius as a dependent factor. It is also surprisingly found that the QNM spectra of QS lie on the same pattern under the new representation, although QS are previously believed to exhibit behaviors different from NS. These empirical relations suggest the reason of the thermal insensitivity is that, temperature plays a little role in determining the stellar structure when comparing with other properties of nuclear matter. As a by-product of these nice universalities, we are able to construct an accurate scheme to infer the mass, the moment of inertia, and the radius of a compact star if GW signal is detected.

On the other hand, the pulsation mechanism of g mode is examined by studying the correlation between mode frequencies and the properties of quark matter in a QS. We found that the dynamic EOS is the most important factor, which can alter the mode frequency for an order. If the chemical composition is preserved, g mode is mainly determined by the value of strange quark mass, while the temperature effect is relatively weak. However, the mode frequency is an order smaller if beta equilibrium is held. The β mode frequency changes significantly if the temperature profile varies. But if the functional form of the profile is preserved, β mode frequency drops linearly as the average temperature decreases.

Lastly, we want to estimate if these properties of QNM can be recognized in realistic GW detection, so we consider the scenario that gravitational radiation is induced by a shell falling onto a hot compact star. We find that the GW power spectrum excited contains sharp peaks and broad peaks, which

correspond to QNM excitations, as well as energy released when the shell collides with the star. Half of the GW energy is channeled to the f mode, and another half is contained by a burst due to the collision. The energy content of a p mode is 4 order less than that of the f mode, while the spacetime modes and g modes are barely excited. According this finding, the cooling of compact stars cannot be observed from collapse-inducing GW unless a phase transition occurs and causes a jump of f mode frequency.

All the results mentioned above are computed by the linearized theory of general relativity. We verify their validity by comparing them with the data generated by full general relativity simulations. From the quadrupole wave calculated, we find that the f mode is still the dominant wave signal excited by a collapsing shell. However, a suspicious excitation of gravity mode is observed, whose energy content is comparable to that of f mode, and the signal considerably interferes the f mode waveform. Further tests reveal that the magnitude of g mode excitation is more significant if the collapsing shell is more massive, and if heating mechanism is incorporated. It suggests that the g mode is excited by the heating of stellar matter due to the non-linear pull of the shell's gravity. Consider this intriguing phenomenon is observed in our simple setup, it indicates that the excitation of g mode would be more common than expected in reality.

After all, we discover several unsolved problems that deserve further investigation in the future. Firstly, we do not calculate the p mode frequencies of hot compact stars, because an appropriate description of the surface of hot compact stars is not known yet. During our investigation, we have tried fitting the surface profile with a polytropic model, but the result is desperate since the effective γ is less than 1 when the density is low, which produces a long tail which extends to infinity. Other suggestions include fitting the EOS with some other analytic functions, employing physical models (such as ideal Fermi gas) for the low density region, or choosing other temperature profile

or equilibrium conditions near the surface, which their applicability require further verifications. But these works are worthy, because we have shown in Chapter 8 that the p mode is also sensitive to temperature, and its excitation is marginally recognizable. We expect a gradual change of p mode frequency would be observed if the star is cooling.

Besides, we only employ one finite temperature nuclear matter EOS, the Shen EOS [27, 28], in this thesis. It is intriguing to know if our observed features also exist for other EOS. Apart from the standard Lattimer and Swesty EOS [26], Ishizuka *et al* propose a modified version of the Shen EOS with the contribution of hyperons [68]. We guess the f mode and w mode are also insensitive to temperature, while the behaviors of p mode and g mode may be different.

Furthermore, the significant g mode excitation in our full general relativity simulation may provide many interesting aspects. It is because the g mode is highly sensitive to the detailed properties of nuclear matter, which is the major concern of nuclear physicists. Since the g mode frequency of QS is one order less than that of NS (c.f. Chapter 5 or [19]), originated from the phenomenon of quark confinement, the g mode GW signal is hence a possible signature to identify QS. However, the validity of our analysis on quadrupole wave requires verification, it will be more convincing if our result agrees with simulation calculating gauge invariant GW.

Finally, I would like to make a few comments on the development of GW astronomy in future. On the theoretical side, mathematical work becomes increasingly difficult due to the complexity of GR, as well as more and more physics incorporated. Full numerical simulation will dominate due to the progressively advance of computational equipment. One of the most promising technology is the development of General Purpose computing on Graphics Processing Units (GPGPU). It is anticipated that the architecture of GPU is favorable for scientific computation, some trial Cactus simulations running on

GPGPU is 2 order more effective than traditional CPU. I believe this would lead to a revolution in computational relativity within a few years. On the experimental side, realistic gravitational wave is far more noisy than the results of theorists, because the current generation GW detectors are not too sensitive, the background surrounding pulsating compact objects is dirty, and QNM frequencies change due to stellar rotation and the presence of multiple superfluid, etc. Before GW becomes a reliable source of astronomical information, countless problems have to solved by collaboration between theorists and experimentalists, I believe the situation will be ever more challenging but interesting for the scientists of this field in the future.

Appendix A

Unit conversions

In this thesis, we employ two different unit systems in the macroscopic and the microscopic region. In the macroscopic region, where stellar oscillation is calculated, we set the gravitational constant G, the speed of light c, and the Boltzmann constant k_B are unity, i.e. $G = c = k_B = 1$. Then all macroscopic quantities, such as the stellar mass and radius, are measured in some powers of km. In the microscopic region, where the EOS is calculated, we set the reduced Planck constant $\hbar$, and the speed of light c, and the Boltzmann constant k_B are unity, i.e. $\hbar = c = k_B = 1$. Then all microscopic quantities, such as the energy density ρ and pressure p, are measured in some powers of MeV.

All physical quantities can be scaled to our unit system by multiplying a certain combination of fundamental constants. We show the values of scaling constants in Table A.1. The conversion between macroscopic and microscopic quantities is also shown in the same table.

Macroscopic quantity	Unit conversion	Scaling constant
Frequency ω	$\mathrm{s}^{-1} \rightarrow \mathrm{km}^{-1}$	$c^{-1} = 3.3356 \times 10^{-6}\mathrm{s\ km}^{-1}$
Pressure p	$\mathrm{kg\ m}^{-1}\mathrm{s}^{-2} \rightarrow \mathrm{km}^{-2}$	$Gc^{-4} = 8.2599 \times 10^{-39}\mathrm{kg}^{-1}\mathrm{m\ s}^{2}\mathrm{km}^{-2}$
Energy density ρ	$\mathrm{kg\ m}^{-1}\mathrm{s}^{-2} \rightarrow \mathrm{km}^{-2}$	$Gc^{-4} = 8.2599 \times 10^{-39}\mathrm{kg}^{-1}\mathrm{m\ s}^{2}\mathrm{km}^{-2}$
Distance r	$\mathrm{m} \rightarrow \mathrm{km}$	$1 = 10^{-3}\mathrm{m}^{-1}\mathrm{km}$
Mass m	$\mathrm{kg} \rightarrow \mathrm{km}$	$Gc^{-2} = 7.4236 \times 10^{-31}\mathrm{kg}^{-1}\mathrm{km}$
Number density n	$\mathrm{m}^{-3} \rightarrow \mathrm{km}^{-3}$	$1 = 10^{9}\mathrm{m}^{3}\mathrm{km}^{-3}$
Mass density	$\mathrm{kg\ m}^{-3} \rightarrow \mathrm{km}^{-2}$	$Gc^{-2} = 7.4236 \times 10^{-22}\mathrm{kg}^{-1}\mathrm{m}^{3}\mathrm{km}^{-2}$
Temperature T	$\mathrm{K} \rightarrow \mathrm{km}$	$k_B Gc^{-4} = 1.1404 \times 10^{-70}\mathrm{K}^{-1}\mathrm{km}$
Microscopic quantity		
Distance	$\mathrm{fm} \rightarrow \mathrm{MeV}^{-1}$	$\hbar^{-1}c^{-1} = 5.0677 \times 10^{-3}\mathrm{fm}^{-1}\mathrm{MeV}$
Temperature T	$\mathrm{K} \rightarrow \mathrm{MeV}$	$k_B = 8.617 \times 10^{-11}\mathrm{K}^{-1}\mathrm{MeV}$
ρ and p	$\mathrm{MeV\ fm}^{-3} \rightarrow \mathrm{MeV}^{4}$	$\hbar^{3}c^{3} = 7.6837 \times 10^{6}\mathrm{MeV}^{-1}\mathrm{fm}^{3}\mathrm{MeV}^{4}$
Number density n	$\mathrm{fm}^{-3} \rightarrow \mathrm{MeV}^{3}$	$\hbar^{3}c^{3} = 7.6837 \times 10^{6}\mathrm{fm}^{3}\mathrm{MeV}^{3}$
Converting quantity		
ρ and p	$\mathrm{MeV\ fm}^{-3} \rightarrow \mathrm{km}^{-2}$	$Gc^{-4} = 1.3234 \times 10^{-6}\mathrm{MeV}^{-1}\mathrm{fm}^{3}\mathrm{km}^{-2}$
ρ and p	$\mathrm{MeV}^{4} \rightarrow \mathrm{km}^{-2}$	$(\hbar c)^{-3}Gc^{-4} = 1.7223 \times 10^{-13}\mathrm{MeV}^{-4}\mathrm{km}^{-2}$
Number density n	$\mathrm{MeV}^{3} \rightarrow \mathrm{km}^{-3}$	$(\hbar c)^{-3} = 1.3014 \times 10^{47}\mathrm{MeV}^{-3}\mathrm{km}^{-3}$

Table A.1: Unit conversion table.

Appendix B

Series expansion of quark star EOS

In Section 3, we present the quark matter EOS employed in this thesis, which is the finite temperature MIT bag model with non-zero strange quark mass [16]. In practical calculations, the formulae Eq.s 3.3-3.5 are expanded by the standard Sommerfield expansion. Since the largest parameter is the chemical potential μ of quarks ($\sim$ 300 MeV), the thermodynamic quantities are expanded in series of strange quark mass m_s ($\sim$ 100 MeV) and temperature T ($\sim$ 10 MeV).

In this section, we show the expression of energy density and pressure up to the 2-nd order correction in the Sommerfield expansion,

$$\begin{aligned}
\rho &= \sum_f^{u,d} \frac{3}{\pi^2}\left(\frac{\mu_f^4}{4}+\frac{\pi^2}{2}\mu_f^2T^2+\frac{7\pi^4}{60}T^4\right)+\frac{1}{\pi^2}\left(\frac{\mu_e^4}{4}+\frac{\pi^2}{2}\mu_e^2T^2+\frac{7\pi^4}{60}T^4\right) \\
&+\frac{3}{\pi^2}\left(\frac{1}{8}\Big(\mu_s(2\mu_s^2-m_s^2)\sqrt{\mu_s^2-m_s^2}-2m_s^4\log(\sqrt{\mu_s+m_s}+\sqrt{\mu_s-m_s})\right. \\
&\left.+2m_s^4\log\sqrt{2m_s}\Big)+\frac{\pi^2}{6}T^2(3\mu_s^2-2m_s^2)\frac{\mu_s}{\sqrt{\mu_s^2-m_s^2}}\right. \\
&\left.+\frac{7\pi^4}{120}T^4\frac{(2\mu_s^4-5m_s^2\mu_s^2+4m_s^4)}{(\mu_s^2-m_s^2)^2}\frac{\mu_s}{\sqrt{\mu_s^2-m_s^2}}\right)+B\ , \qquad \text{(B.1)}
\end{aligned}$$

$$
\begin{aligned}
p &= \sum_f^{u,d} \frac{1}{\pi^2}\left(\frac{\mu_f^4}{4}+\frac{\pi^2}{2}\mu_f^2T^2+\frac{7\pi^4}{60}T^4\right)+\frac{1}{3\pi^2}\left(\frac{\mu_e^4}{4}+\frac{\pi^2}{2}\mu_e^2T^2+\frac{7\pi^4}{60}T^4\right) \\
&+\frac{1}{\pi^2}\left(\frac{1}{8}\Big(\sqrt{\mu_s^2-m_s^2}\mu_s(2\mu_s^2-5m_s^2)+6m_s^4\log(\sqrt{\mu_s+m_s}+\sqrt{\mu_s-m_s})\right. \\
&-6m_s^4\log\sqrt{2m_s}\Big)+\frac{\pi^2}{2}T^2\mu_s^2\sqrt{\mu_s^2-m_s^2} \\
&\left.+\frac{7\pi^4}{120}T^4\frac{\mu_s(2\mu_s^2-3m_s^2)}{(\mu_s^2-m_s^2)^{3/2}}\right)-B\ . \qquad \text{(B.2)}
\end{aligned}
$$

From the above expressions, we can obtain the expression for $A(\mu_s,T)$ in Eq. 7.6,

$$
\begin{aligned}
A(\mu_s,T) &= \frac{3}{\pi^2}m_s^2\Big(\frac{1}{2}\mu_s\sqrt{\mu_s^2-m_s^2}-m_s^2\log(\sqrt{\mu_s+m_s}+\sqrt{\mu_s-m_s}) \\
&+m_s^2\log\sqrt{2m_s}+\frac{\pi^2}{6}T^2\frac{\mu_s}{\sqrt{\mu_s^2-m_s^2}}+\frac{7\pi^4}{120}T^2\frac{m_s^2\mu_s}{(\mu_s^2-m_s^2)^{5/2}}\Big) \qquad \text{(B.3)}
\end{aligned}
$$

which reduces to Eq. 5.2 in the zero-strange-quark-mass limit. In addition, the above expressions can be further expanded to become series of $(T/\mu_s)^2$ and $(m_s/\mu_s)^2$. The accuracy is hence the same order as the term $(m_s/\mu_s)^4$ (provided that $m_s > T$).

The grand potential density of the system Ω is related to the pressure by,

$$p = -\Omega\ , \qquad \text{(B.4)}$$

which satisfies the thermodynamic relation

$$d\Omega = -SdT-\sum_i n_i d\mu_i\ , \qquad \text{(B.5)}$$

where S is the entropy density and T is temperature; n_i and μ_i are number density and chemical potential of the i-th particle species respectively. Hence thermodynamic quantities, such as S, n_i and c_s^2, can be obtained by partially differentiating Eq. B.2 [16]. For examples,

$$
\begin{aligned}
S=\left(\frac{\partial p}{\partial T}\right)_{\mu_i} &= \left(\mu_u^2+\mu_d^2+\frac{1}{3}\mu_e^2+\mu_s^2\sqrt{\mu_s^2-m_s^2}\right)T \\
&+\left(\frac{49\pi^2}{45}+\frac{7\pi^2}{30}\frac{\mu_s(2\mu_s^2-3m_s^2)}{(\mu_s^2-m_s^2)^{3/2}}\right)T^3\ , \qquad \text{(B.6)}
\end{aligned}
$$

and

$$n_u = \frac{\partial p}{\partial \mu_u} = \frac{1}{\pi^2}\left(\mu_u^3 + \pi^2 \mu_u T^2\right) \ , \tag{B.7}$$

$$n_d = \frac{\partial p}{\partial \mu_d} = \frac{1}{\pi^2}\left(\mu_d^3 + \pi^2 \mu_d T^2\right) \ , \tag{B.8}$$

$$n_s = \frac{\partial p}{\partial \mu_s} = \frac{1}{\pi^2}\left((\mu_s^2 - m_s^2)^{3/2} + \pi^2 \frac{(2\mu_s^2 - m_s^2)T^2}{2\sqrt{\mu_s^2 - m_s^2}} + \frac{7\pi^4 m_s^4 T^4}{40(\mu_s^2 - m_s^2)^{5/2}}\right) , \tag{B.9}$$

$$n_e = \frac{\partial p}{\partial \mu_e} = \frac{1}{3\pi^2}\left(\mu_e^3 + \pi^2 \mu_e T^2\right) \ . \tag{B.10}$$

Appendix C

Accuracy of simplified mode extraction scheme

In Chapter 5, we calculate the frequencies of QNM by employing the approach of LD and Zerilli under the framework of linearized general relativity. This formalism is believed to be the most accurate calculation of mode frequencies next to the wave extraction from full numerical simulations of stellar dynamical process. In this method, however, complicated matter and spacetime perturbation equations have to be solved, which are 4^{th} and 2^{nd} order differential equation respectively. The complexity is not only a challenge to numerical manipulation, but also imposes difficulty in extracting physics beneath. As a result, authors attempt methods to simplify the mode extraction process, which the most commonly perceived approaches include the Newtonian oscillation scheme and the Cowling approximation.

Since GR is a modification of the Newtonian theory of dynamics, some GR phenomenon consist of classical counterparts, although their precise properties are slightly different. Due to the simplicity, theoretical investigation of stellar pulsation starts from the Newtonian regime, by considering the normal mode oscillation of a compact star. Later works in linearized GR verified that there is a classical normal mode in correspondence to each fluid QNM of compact star. In fact, fluid modes are classified according to the pulsation mechanism

of their Newtonian counterpart.

On the other hand, not all kinds of fluid mode would strongly couple with the gravitational field. By bearing in mind that GW can be excited, it is not a conflict to neglect the metric perturbation in order to neglect the the fluctuation of gravity, which is the idea of the Cowling approximation [69]. Previous works show that the Cowling approximation can produce accurate results for high order p modes and g modes [69], it is because these kinds of modes are mainly driven by the oscillation of fluid elements.

In this section, we are going to test the accuracy of mode frequencies obtained by employing both simplifications. For better comparison, we employ the matter profile generated by the TOV equation in the Newtonian formalism. Since oscillation energy do not lose by gravitational radiation in the Newtonian theory, classical mode does not consist of an imaginary part. Real frequency is the eigenvalue of the matter perturbation equation [19, 44]

$$\frac{d}{dr}(r^2\xi_r) = \frac{g}{c_s^2}(r^2\xi_r) + \left[\frac{l(l+1)}{\omega^2} - \frac{r^2}{c_s^2}\right](\frac{\delta p}{\rho}) \tag{C.1}$$

$$\frac{d}{dr}(\frac{\delta p}{\rho}) = \frac{\omega^2 - \omega_{BV}^2}{r^2}(r^2\xi_r) + \frac{\omega_{BV}^2}{g}(\frac{\delta p}{\rho}) \ , \tag{C.2}$$

where ρ is the background energy density, δp is the Eulerian change of pressure, ξ_r is the Eulerian change of radial displacement, g is the classical gravity $g(r) = Gm(r)/r$; ω_{BV} is the Brunt-Väisälä (BV) frequency defined in Eq. 7.1. The Sturm-Liouville type problem is set up by two boundary conditions, which are the regularity at the stellar centre and vanishing pressure on the surface.

As shown in Fig. C.1, g mode frequencies computed by the simplified formalism are accurate, which the deviations are about 10%. Mode frequencies of $M = 1.0$ M_{sun} is roughly 20% more accurate than those of $M = 1.4$ M_{sun} star. It is an expected result as the major difference between both formalism is the treatment of gravity, error of simplified scheme hence reduces in the situation with a weaker gravitational field. It is worthy to note that Fu *et al.* employed the same simplified formalism to estimate the g mode frequencies of newly

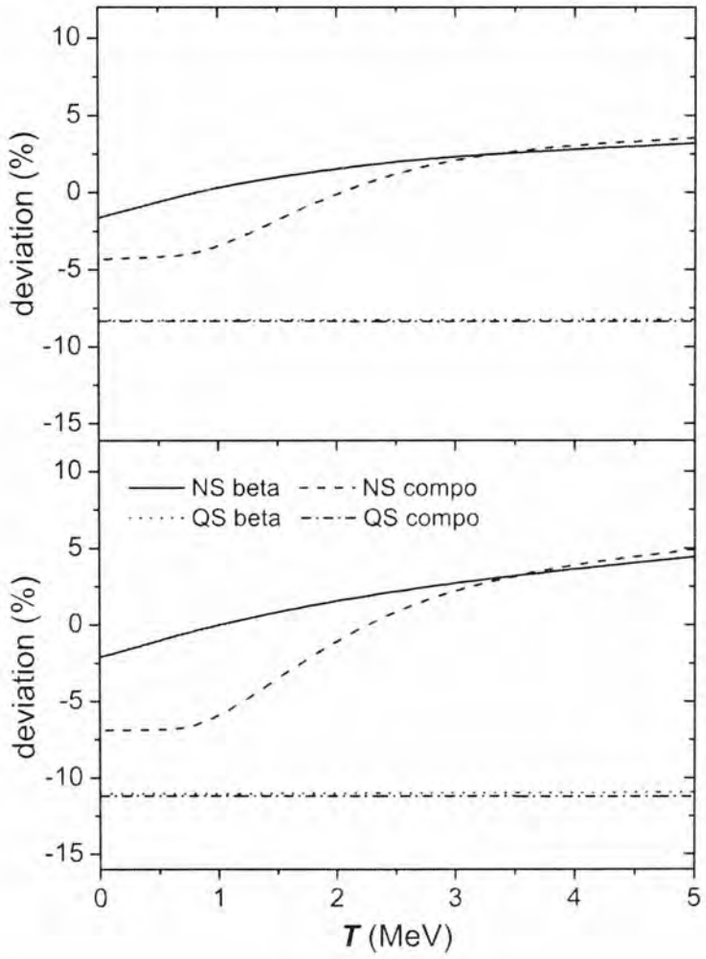

Figure C.1: Percentage error of g mode frequencies computed by the Newtonian formalism with the Cowling approximation, when comparing to value obtained by the linearized general relativistic formalism. The upper (lower) panel shows results of compact stars with $M = 1.0$ $\mathrm{M_{sun}}$ ($M = 1.4$ $\mathrm{M_{sun}}$).

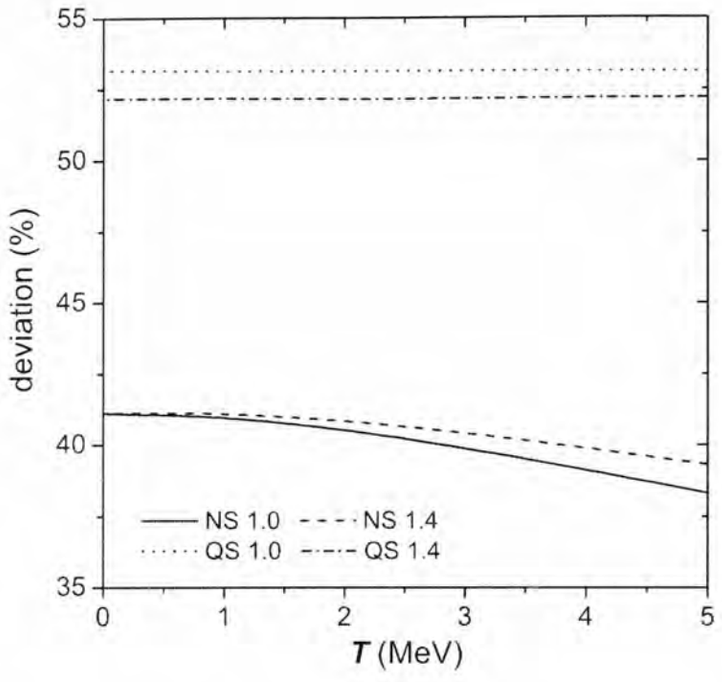

Figure C.2: Percentage error of f mode frequencies computed by the Newtonian formalism with the Cowling approximation, when comparing to value obtained by the linearized general relativistic formalism. The oscillations are calculated by assuming chemical composition is preserved, because the dynamic EOS only affects the results for less than 0.1%.

born compact stars [19]. They claim that g mode is a plausible signature for distinguishing hot NS and QS, as the normal mode frequencies of NS are 1 order faster than those of QS. Our results in this appendix show the argument of Fu *et al.* remains convincing in relativistic scenario.

In addition, we also show the deviation of f mode value computed by both methods in Fig. C.2. Quality of f mode calculation is much worse than that of g mode, values computed by the simplified formalism is about 50% higher. It is noticed that the percentage error is not reduced for less massive stars, this suggests that the failure is not originated from the Newtonian gravity but the inappropriate application of the Cowling approximation. When considering the eigenfunction of the f mode oscillation, the scaled magnitude of the metric perturbation is comparable to the perturbation of fluid motion [39], which

means that the oscillation is mainly driven by gravity. Suppression of space-time oscillation by the Cowling approximation seriously alters the pulsation mechanism of the f mode, it hence produces significantly deviated values.

Appendix D

Computation of moment of inertia

We discuss in this section about the method of computing the moment of inertia of a slowly rotating hydrostatic star. In classical physics, the moment of inertia I is related to the angular momentum J by a linear relationship

$$J = I\Omega \ , \tag{D.1}$$

which the moment of inertia can be uniquely determined by the matter distribution. But this definition is not always valid for a rotating relativistic star. Firstly, a compact star is not a large piece of solid, it is expected that a star would rotate as sliced layers, in other words the angular velocity is not a constant of radial distance from the centre. Secondly, the background configuration of the star is governed by the TOV equation, but the set of equations only describes hydrostatic but not rotating stars. In general, the moment of inertia is not well defined for compact stars, even though angular momentum is a gauge invariant physical quantity. However, Eq. D.1 remains a good approximation if the rotation is slow, then the TOV equation is still a nice description of the matter profile, and the slices of matter are rotating with roughly the same angular speed.

Our computation of the linearized relativistic moment of inertia follows

the formalism mentioned in [16]. As stated in Section 6.2, the crucial quantity involved in the moment of inertia is the function $\bar{\omega}$. Define a metric junction j

$$j(r) = e^{-(\nu(r)+\lambda(r))/2} \ , \tag{D.2}$$

then Eq. 6.3 is simplified as

$$\frac{d^2\bar{\omega}}{dr^2} + \left(\frac{1}{j}\frac{dj}{dr} + \frac{4}{r}\right)\frac{d\bar{\omega}}{dr} + \frac{4}{r}\frac{1}{j}\frac{dj}{dr}\bar{\omega} = 0 \ , \tag{D.3}$$

where $j(r)$ can be calculated by the the background TOV configuration.

Unique solution of Eq. D.3 has to be obtained by specifying two boundary conditions. The first condition is the regularity of quantities at the origin, the first derivative of $\bar{\omega}$ is required to vanish, i.e. $(d\bar{\omega}/dr)_{r=0} = 0$. Another boundary condition is on the surface, which is parametrized by J

$$J = \frac{1}{6}R^4\left(\frac{d\bar{\omega}}{dr}\right)_{r=R} \ ; \ \Omega - \frac{2J}{R^3} = \bar{\omega}(R) \ . \tag{D.4}$$

It is remarked that the solution of $\bar{\omega}$ depends on Ω, but the moment of inertia does not. Consider we multiply Eq. D.3 by an arbitrary constant A and define a new variable $\tilde{\omega} = A\bar{\omega}$, the equation and the boundary condition at the origin are not altered. The only changes happen on the surface, both relations in Eq. D.4 are multiplied by A. By Eq. D.1, the scaling of the surface boundary condition can be viewed as choosing another Ω to vary the J, but leaves the moment of inertia unchanged. In practice, an arbitrary value of $\omega(0)$ can be taken for integration, which is equivalent to choose an arbitrary Ω to determine the unique value of I. The uncertainty of normalization can be removed by considering the ratio of $\bar{\omega}$ and its derivative

$$\frac{(d\bar{\omega}/dr)_{r=R}}{\bar{\omega}(R)} = \frac{6I}{R^4 - 2IR} \ , \tag{D.5}$$

which is a function of the moment of inertia.

Appendix E

Comment of exactness of inference scheme

In [5], Andersson and Kokkotas suggest that if GW QNM is extracted, mass and radius of the neutron star can be obtained from the empirical universality formulae. In their paper, they have compared which combinations of universalities can produce the most accurate value of M and R. Neglecting the p mode which is sensitive to factors other than the stellar structure, they find that combinations of real and imaginary part of f mode and w-mode can give precise values of mass and radius.

E.1 Precision of the mass inferred

They test the accuracy of their scheme by applying it on several polytropic stars. According to their results presented, the values of mass are usually precisely obtained with less than 2% error; while the value for radius obtained is relatively poor, with a typical deviation for about 10%. The most accurate combinations of universalities are any two from the imaginary part of f mode, the real part, and the imaginary part of the first w mode, whereas results worsen if the unviersality of the f mode real part is incorporated. We believe it is because the universality formulae for those 3 modes (Eq. 8, 10, 11 in [5])

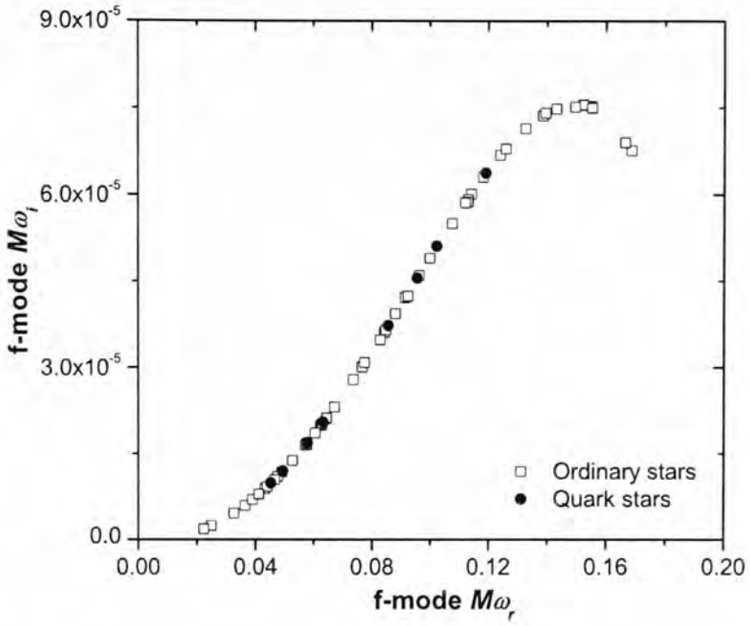

Figure E.1: Real frequencies of f mode are plotted against the imaginary frequencies. The blank squares are data points of NS constructed by ten realistic EOS, while the data of QS of two quark matter models are plotted as filled dots for comparison. All the EOS are referred to Chapter 6.

can be scaled to become dimensionless, i.e. $M\omega = f(M/R)$ for function f. However an intrinsic mass factor is incorporated in the universality of f mode real part. Our argument can be illustrated by the plot of the normalized f mode real frequency against its imaginary part in Fig. E.1. We can see from the complex plane that the normalized frequencies distribute on a single contour, even though their universality with respect to the compactness are not too fit. It strongly suggests that f mode frequency should follow a trend required by some unknown physical reasons. Therefore an addition of mass factor into the universality formula inevitably induces individuality, and reduces the accuracy if the universality is applied in the inference scheme.

From the figures in their paper, it is perceived that the combination of the f mode imaginary part and the w mode real part give the best estimations of mass and radius, because their universalities are well fitted to the mode

frequencies generated (Fig. 2 and 5 in [5]). However, the imaginary frequencies of f mode span about 20% around the fitting curve (Fig.6 in [5]), it is surprising that this universality formula can also produce good results.

Why a poor universality can yield a good inference scheme? To answer this question, we construct the complex plot of normalized w mode in Fig. E.2. Similar to the f mode, normalized w mode also distribute on a simple contour. Consider the details of inference scheme. We have two dimensionless universality formulae, $M\omega_1 = f_1(M/R)$ and $M\omega_2 = f_2(M/R)$, and the GW QNM frequencies detected, ω_1 and ω_2. This forms a system of two algebraic equations with two unknowns (the most obvious choice is $M, M/R$. Although it is not unique, the accuracy of inferred values is not affected by the selection of variables). One routine to solve the equation is the following. Firstly, the value of mass is fixed by the fraction of observed frequencies, i.e.

$$\frac{\omega_2}{\omega_1} = \frac{M\omega_2}{M\omega_1} = \frac{f_2(M/R)}{f_1(M/R)} \,. \tag{E.1}$$

It is noted that although the fraction $\frac{f_2(M/R)}{f_1(M/R)}$ is a function of compactness, it actually describes the pattern of normalized mode frequency $M\omega$. In other words, the two universality formulae can be viewed as a parametrized equation of $M\omega_r$ and $M\omega_i$. Then the value of mass is put into one of the universalities and get the corresponding value of compactness, it is then obvious to obtain the radius by mass and compactness. Pictorially, it is equivalent to find the intersection between two lines: (i) a line describing the normalized mode distribution on a complex plane given by the universalities, (ii) a straight line passing through the origin with the slope $= \omega_2/\omega_1$. Therefore, the value of mass is actually not determined by universality formula with respect to compactness, instead it is fixed by the contour of normalized mode on complex plane. No matter how poor the universality is, and whatever the choice of geometric factor is, the value of mass can be accurately obtained if the combined function by the two universalities can produce a fit contour on the complex

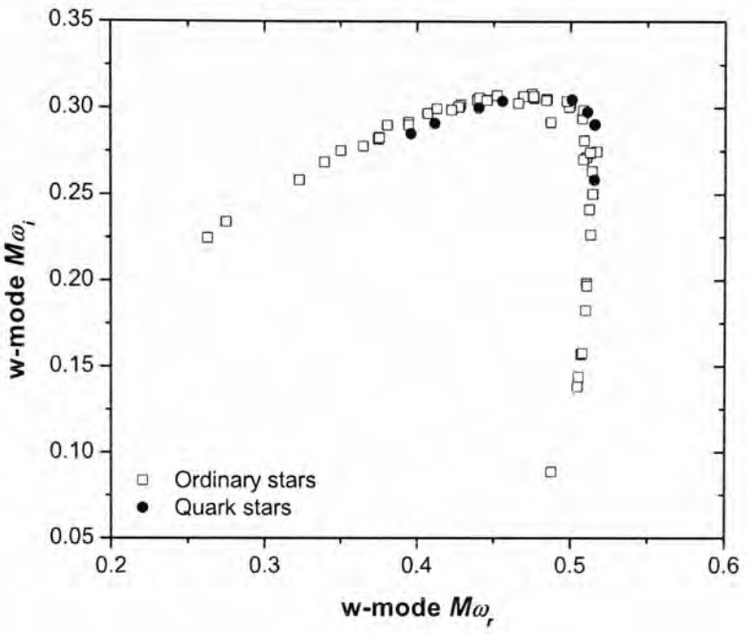

Figure E.2: Same as Fig. E.1 for real part and imagiary part of w-mode.

plane. Nevertheless, accuracy of another inferred value is determined by the preciseness of the universalities. It is noted that the above analysis does not limit to real and imaginary part of the f mode, but it is applicable to any combinations of mode frequencies, either real or imaginary part.

Lastly, we discuss the ability to infer parameters of QS. In Chapter 6, our new proposal of universalities incorporating the moment of inertia can find precise mass and the moment of inertia for QS if GW QNM are recognized, because our formulae more precisely demonstrate the universal trend of mode frequencies. However, we have discussed poor universality description may also give good results. Despite the inability to represent data points of quark stars, the universalities with respect to compactness may be useful in finding the mass of QS. Therefore, we also plot the data points of QS in Fig. E.1 and E.2. We see that the mode frequencies of QS also distribute on the contour of NS, hence mass of QS can also be precisely inferred. We believe the concurrency between the QS QNM pattern and that of NS is not a coincidence, it should

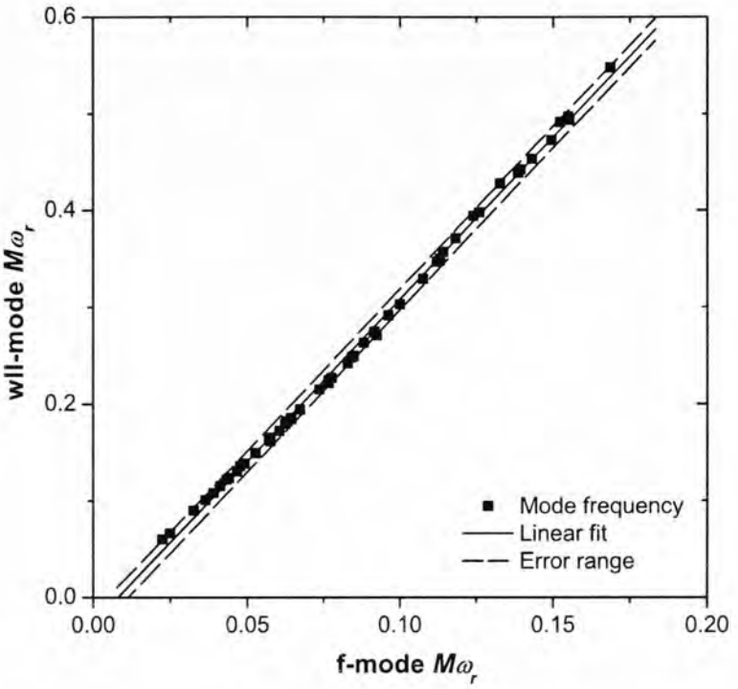

Figure E.3: Distribution of the normalized f mode real frequency with respect to the w-II mode real frequency. The pattern is fitted by a straight solid line. We also present the error range of the fitting as dashed lines.

be originated from the dynamics of the pulsation mode, which is an interesting research topic in the future.

E.2 Accuracy of universality combinations

In Chapter 6, we have mentioned that the combination of the first w-II mode real part and the f mode real part do not form a good inference scheme, in spite of the apparent accuracy of their universality. This unexpected result is originated from the relationship between the first w-II mode and the first f mode when normalized by mass.

We plot the normalized mode distribution of the real part of f mode against the real part of the first w-II mode in Fig. E.3. The frequencies are about linear to each other, so we use a straight line to fit the data points. We find the slope

is positive and the x-intersection is very close to the origin, which is the cause of large error on the inference scheme.

As we have stated, the first step of the scheme is to fix the mass by finding the intersection between the mode distribution pattern described by universalities, and a straight line characterized by experimentally detected values. Let the straight line is $y = Sx$ and pattern is represented by $y = Ax + B$. Solution of the equation is $x = B/(S - A)$, and the relative error is given by

$$\frac{\delta x}{x} = \sqrt{\left(\frac{\delta B}{B}\right)^2 + \left(\frac{\delta S^2 + \delta A^2}{(S-A)^2}\right)}\,, \tag{E.2}$$

where δS is experimental error of frequency detection, δA and δB are the fitting errors caused by dispersion of modes. If the x-intersection is close to origin, which is mathematically equivalent to a small B, the first term in Eq. E.2 and hence the relative error will be large. Furthermore, S must be positive because the mode frequencies are positive. The second term in Eq. E.2 is larger if the mode distribution gives a positive slope A. As a result, the failure of producing precise results from the combination of the f mode real part and the first w-II mode real part is related to the distribution of mode frequencies. It is merely a coincidence which is not related to the choice of dependent variable. Our argument is shown schematically in Fig. E.4.

In general, the relative pattern of mode frequencies may not be a straight line, such as those shown in Fig. E.1 and E.2. Mode distribution possess tangentially positive or negative in different frequencies. Therefore, a particular combination of universality do not always infer accurate values. Since different region of mode pattern corresponds to stars with different compactness, our analysis here can help deciding which inferred value is more accurate, if significantly deviated values are obtained from different combination of universalities.

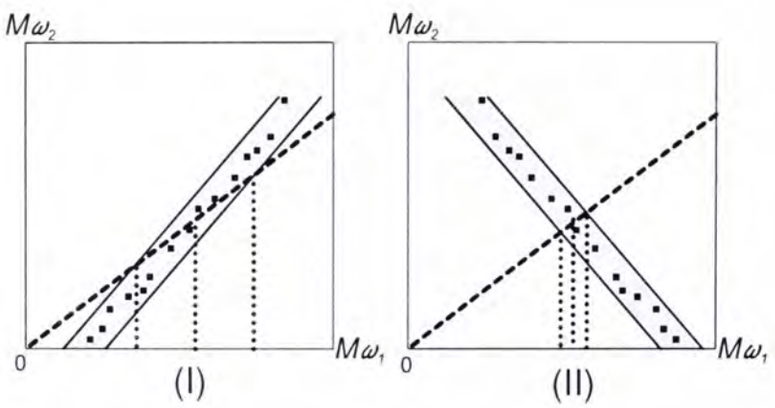

Figure E.4: The panel I (II) shows a sample which the mode distribution follows a positive (negative) sloped straight line. Some sample mode frequencies are plotted as squares; the solid lines are bounds of error range of the linear fitting; the grey area is the error range; the dashed line is the ratio of the detected frequencies. The three vertical dotted lines show the exact inferred value and its error bounds.

Appendix F

Calculation of sound speed

Pressure and energy density are usually provided as primary quantities in the EOS, either in the form of EOS table or algebraic expressions, so these quantities can be easily employed in calculation by interpolation or algebraic manipulation. However, the sound speed is usually not given as a primary quantity, obtaining it requires taking a differentiation on existing data of pressure with respect to energy density under certain set of constraints. The operation is both mathematically and computationally difficult to handle. If the EOS is in analytic form, such as the MIT bag model, the sound speed has to be expressed in a long and complicated mathematical form. The situation is even more though for tabulated EOS, the constraints of sound speed may require differentiating multi-variable-interpolated values, which usually causes numerical instability. We here present a simple and systematic method to compute the sound speed under any constraint. Because all the calculations only involve exact or numerical derivatives of primary variables that can be obtained easily, this formalism is also useful to compute quantities involving derivatives of thermodynamic quantities, such as the specific heat capacity.

Consider the general constraint F

$$d\vec{F} = \vec{0} \,, \tag{F.1}$$

where $\vec{F}$ is an array of equations. The total derivative can be expanded as a

linear combination of derivatives of primary variables x_i

$$d\vec{F} = \begin{pmatrix} \partial_1 F_1 & \cdots & \partial_n F_1 \\ \vdots & & \vdots \\ \partial_1 F_k & \cdots & \partial_n F_k \end{pmatrix} \begin{pmatrix} dx_1 \\ \vdots \\ dx_n \end{pmatrix} = \vec{0} \,. \tag{F.2}$$

The number of constraints should be less than the number of independent variables by 1, otherwise the EOS is either over-determined or incomplete. I insert the total derivative of pressure into the matrix equation Eq. F.2 and get

$$\begin{pmatrix} \partial_1 p & \cdots & \partial_n p \\ \partial_1 F_1 & \cdots & \partial_n F_1 \\ \vdots & & \vdots \\ \partial_1 F_{n-1} & \cdots & \partial_n F_{n-1} \end{pmatrix} \begin{pmatrix} dx_1 \\ \vdots \\ \vdots \\ dx_n \end{pmatrix} = \begin{pmatrix} dp \\ 0 \\ \vdots \\ 0 \end{pmatrix} . \tag{F.3}$$

I denote the square matrix on the left hand side as δF. By inverting δF, we can get the relationship between differentiate of pressure and those of primary variables. In a more physical tone, we know how much the primary variables changes when there is an infinitesimal pressure variation. By considering the total derivative of energy density $d\rho$ and incorporating it into Eq. F.3, we get

$$d\rho = \begin{pmatrix} \partial_1 \rho & \cdots & \cdots & \partial_n \rho \end{pmatrix} (\delta F)^{-1} \begin{pmatrix} dp \\ 0 \\ \vdots \\ 0 \end{pmatrix} . \tag{F.4}$$

Therefore, the speed of sound under the constraint F can be obtained as

$$c_F^{-2} = \left(\frac{\partial p}{\partial \rho}\right)_F^{-1} = \left[\begin{pmatrix} \partial_1 \rho & \cdots & \cdots & \partial_n \rho \end{pmatrix} (\delta F)^{-1}) \right]_1 , \tag{F.5}$$

where the notation $[(\cdots)]_1$ represents the first element in the array.

Appendix G

Mode extraction of non-adiabatic oscillation

Finding QNM frequencies is not an easy task even the linearized GR formalism is employed. It is because the LD equation and the Zerilli equation are complicated for manipulation, as well as the divergent nature of eigenfunction at spatial infinity due to the non-zero imaginary part of QNM. For the mode with a relatively small imaginary part, i.e. $\omega_i << \omega_r$, such as the f mode, p mode, and g mode, mode frequencies can be extracted by analyzing the scattering cross section, as suggested by Ferrari *et al.* [70, 71]. This method only requires integrating the whole set of equations in the real frequency domain, such that the wave function remains well defined at spatial infinity. In spite of the past success, we find the formalism suggested by Ferrari *et al.* is valid only if there is no internal dissipation during oscillation. For non-adiabatic oscillations, modification is required to obtain the true value of damping rate.

Since the original derivation of Ferrari *et al.* involves tedious mathematical derivation, we instead present their formalism in the context of quantum scattering theory. Since we are working in frequency domain, the whole system is assumed to oscillate at a single frequency ω. The principle of scattering method is to look for resonance peak of wave amplitude within a range of real ω. Since the frequency is real, both the LD equation and the Zerilli equation

are real, therefore the solution is an exactly real function. The Zerilli function at spatial infinity can hence be expressed as a linear combination of sinusoidal functions

$$Z(\omega_r) = \alpha \cos \omega_r r - \beta \sin \omega_r r \tag{G.1}$$

for some real coefficients α, β. It can be transformed to

$$Z(\omega_r) = \sqrt{\alpha^2 + \beta^2} e^{-i\delta} (e^{i\omega_r r} + e^{2i\delta} e^{i\omega_r r}), \tag{G.2}$$

where we pick $e^{i\omega_r r}$ as the incoming solution. δ is the phase shift of scattering, defined as

$$e^{2i\delta} = \frac{\alpha - i\beta}{\alpha + i\beta} \ . \tag{G.3}$$

On the other hand, scattering theory tells that if the scattering is elastic, the phase factor is

$$e^{2i\delta} = \eta(\omega_r) = \frac{(\omega_r - \omega_0) - i\Gamma}{(\omega_r - \omega_0) + i\Gamma} e^{i\phi} \tag{G.4}$$

where ω_0 is the resonant frequency; Γ is the damping rate due to energy loss; ϕ is the background phase. The physical meaning of the parameters actually define a QNM as $\omega = \omega_0 + i\Gamma$. Compare both expressions, we are able to write

$$\alpha + i\beta = f(\omega_r)((\omega_r - \omega_0) + i\Gamma) \tag{G.5}$$

$$\alpha - i\beta = f(\omega_r)((\omega_r - \omega_0) - i\Gamma) e^{i\phi} \ , \tag{G.6}$$

for some complex factor $f(\omega_r)$ contributed by other QNM, and the choice of normalization, etc. After some manipulations, the scattering amplitude is found to be

$$\alpha^2 + \beta^2 = 4|f(\omega_r)|^2((\omega_r - \omega_0)^2 + \Gamma^2) \ . \tag{G.7}$$

If the imaginary part of QNM is small, the factor $f(\omega_r)$ varies smoothly and slowly at the vicinity of ω_0, therefore QNM can be obtained by fitting the scattering profile with a quadratic function

$$\alpha^2 + \beta^2 \sim (\omega_r - \omega_0)^2 + \Gamma^2 \ . \tag{G.8}$$

However, the above method is not accurate when there is energy dissipating mechanism other than the GW. Analysis before Eq. G.3 is still true, as it only assumes the whole system is oscillating in a single real frequency, although α and β may not be both real. Modification is however needed afterwards because the scattering is no longer elastic. Eq. G.4 is modified as

$$e^{2i\delta} = \eta(\omega_r) = \frac{(\omega_r - \omega_0) - i\Gamma_1 + i\Gamma_2}{(\omega_r - \omega_0) + i\Gamma_1 + i\Gamma_2} e^{i\phi} \ , \tag{G.9}$$

where Γ_1 is the rate of energy lost by wave, Γ_2 is rate of energy lost by other dissipation mechanism [72]. It is noted that the norm of this inelastic $\eta(\omega_r)$ is no longer unity, so the phase δ is not real in general. By definition, the QNM frequency is

$$\omega = \omega_0 + i(\Gamma_1 + \Gamma_2) \ , \tag{G.10}$$

which the imaginary part is a direct sum of both dissipation rates. On the other hand, if we strictly follow the approach of Ferrari *et al.*, Eq. G.8 becomes

$$\alpha^2 + \beta^2 \sim (\omega_r - \omega_0)^2 + \Gamma_1^2 + \Gamma_2^2 \ , \tag{G.11}$$

hence the extracted value becomes

$$\omega_0 + i\sqrt{\Gamma_1^2 + \Gamma_2^2} \ , \tag{G.12}$$

which obviously disagrees with the correct value except in the elastic case, i.e. $\Gamma_2 = 0$.

In fact, QNM frequency can be extracted more readily by considering the phase factor η. The factor can be obtained from the Zerilli function and its derivative at spatial infinity

$$\eta = \frac{i\omega_r Z - Z'}{i\omega_r Z + Z'}. \tag{G.13}$$

The norm square of the inelastic phase factor is noted as

$$\begin{aligned} |\eta|^2 &= \frac{(\omega - \omega_0)^2 + (\Gamma_1 - \Gamma_2)^2}{(\omega - \omega_0)^2 + (\Gamma_1 + \Gamma_2)^2} \\ &= 1 - \frac{4\Gamma_1\Gamma_2}{(\omega - \omega_0)^2 + (\Gamma_1 - \Gamma_2)^2} \ , \end{aligned} \tag{G.14}$$

which is a standard Lorentzian function. Consequently, QNM can be extracted by finding the Lorentzian parameters from $|\eta|^2$.

This method is only applicable in the non-adibatic case, because $|\eta|^2 = 1$ in elastic scattering. However QNM frequencies can be extracted by fitting either real or imaginary part of η

$$Re(\eta) = \frac{(\omega_r - \omega_0)^2 - \Gamma^2}{(\omega_r - \omega_0)^2 + \Gamma^2} \cos\phi + \frac{2\Gamma}{(\omega_r - \omega_0)^2 + \Gamma^2} \sin\phi \tag{G.15}$$

$$Im(\eta) = \frac{(\omega_r - \omega_0)^2 - \Gamma^2}{(\omega_r - \omega_0)^2 + \Gamma^2} \sin\phi - \frac{2\Gamma}{(\omega_r - \omega_0)^2 + \Gamma^2} \cos\phi \ . \tag{G.16}$$

Although none of them is a standard function, this method is sometimes more accurate than the scattering method of Ferrari *et al.* for QNM with a small imaginary part. In the method of Ferrari *et al.*, the imaginary part is obtained by finding the minimum position of a trough. If the frequency resolution of scattering profile is not fine enough, the minimum point has to be determined by interpolation. Then the small damping rate is obtained by interpolating data points with much higher magnitudes, so the percentage error of extracted value is large. However, η is considered in our method, which is at the order of unity. Therefore the fitting of parameters can be more precise and the mode frequency obtained is more accurate.

Bibliography

[1] J. M. Lattimer and B. F. Schutz, Astrophysical Journal **629**, 979 (2005).

[2] M. Bejger and P. Haensel, Astronomy and Astrophysics **396**, 917 (2002).

[3] L. Tsui and P. Leung, Astrophysical Journal **631**, 495 (2005).

[4] L. K. Tsui and P. T. Leung, Monthly Notices of the Royal Astronomical Society **357**, 1029 (2005).

[5] N. Andersson and K. D. Kokkotas, Monthly Notices of the Royal Astronomical Society **299**, 1059 (1998).

[6] R. A. Hulse and J. H. Taylor, Astrophysical Journal **195**, L51 (1975).

[7] S. A. Hughes, Annals of Physics **303**, 142 (2003).

[8] K. S. Thorne and A. Campolattaro, Astrophysical Journal **149**, 591 (1967).

[9] L. Lindblom and S. L. Detweiler, Astrophysical Journal Supplement Series **53**, 73 (1983).

[10] L. K. Tsui, P. T. Leung, and J. Wu, Physical Review D **74**, 124025 (2006).

[11] G. Miniutti, J. A. Pons, E. Berti, L. Gualtieri, and V. Ferrari, Monthly Notice of the Royal Astronomical Society **338**, 389 (2003).

[12] V. Ferrari, G. Miniutti, and J. Pons, Monthly Notice of the Royal Astronomical Society **342**, 629 (2003).

[13] E. Witten, Physical Review D **30**, 272 (1984).

[14] K. A. Olive, Science **251**, 1194 (1991).

[15] O. G. Benvenuto and G. Lugones, Monthly Notices of the Royal Astronomical Society **304**, 25 (1999).

[16] N. K. Glendenning, *Compact Stars: Nuclear Physics, Particle Physics, and General Relativity*, Springer, 2000.

[17] J. M. Lattimer and M. Prakash, Science **304**, 536 (2004).

[18] K. W. Wong and M. C. Chu, Physical Review D **70**, 063004 (2004).

[19] W. J. Fu, H. Q. Wei, and Y. X. Liu, Physical Review Letters **101**, 181102 (2008).

[20] R. C. Tolman, Physical Review **55**, 364 (1939).

[21] J. R. Oppenheimer and G. M. Volkoff, Physical Review **55**, 374 (1939).

[22] S. Detweiler and L. Lindblom, Astrophysical Journal **292**, 12 (1985).

[23] F. J. Zerilli, Physical Review D **2**, 2141 (1970).

[24] W. Baade and F. Zwicky, Physical Review **46**, 76 (1934).

[25] O. Benhar, V. Ferrari, and L. Gualtieri, Physical Review D **70**, 124015 (2004).

[26] J. M. Lattimer and F. D. Swesty, Nuclear Physics, Section A **535**, 331 (1991).

[27] H. Shen, H. Toki, K. Oyamatsu, and K. Sumiyoshi, Nuclear Physics, Section A **637**, 435 (1998).

[28] H. Shen, H. Toki, K. Oyamatsu, and K. Sumiyoshi, Progress of Theoretical Physics **100**, 1013 (1998).

[29] J. A. Pons, S. Reddy, M. Prakash, J. M. Lattimer, and J. A. Miralles, Astrophysical Journal **513**, 780 (1999).

[30] A. Reisenegger and P. Goldreich, Astrophysical Journal **395**, 240 (1992).

[31] C. W. Misner, K. S. Thorne, and J. A. Wheeler, *Gravitation*, W. H. Freeman, 1973.

[32] N. Sago, H. Nakano, and M. Sasaki, Physical Review D **67**, 104017 (2003).

[33] M. Davis, R. Ruffini, W. H. Press, and R. H. Price, Physical Review Letters **27**, 1466 (1971).

[34] H. P. Nollert, Classical and Quantum Gravity **16**, R159 (1999).

[35] T. Regge and J. A. Wheeler, Physical Review **108**, 1063 (1957).

[36] S. Jhingan and T. Tanaka, Physical Review D **67**, 104018 (2003).

[37] C. W. Yip, Oscillations of compact stars, Master's thesis, The Chinese University of Hong Kong, 1998.

[38] K. D. Kokkotas and B. G. Schmidt, Living Reviews in Relativity **2** (1999).

[39] J. Wu and P. T. Leung, Monthly Notices of the Royal Astronomical Society **381**, 151 (2007).

[40] W. J. Fu, G. H. Wang, and Y. X. Liu, Astrophysical Journal **678**, 1517 (2008).

[41] A. Burrows, E. Livne, L. Dessart, C. D. Ott, and J. Murphy, Astrophysical Journal **640**, 878 (2006).

[42] K. D. Kokkotas, T. A. Apostolatos, and N. Andersson, Monthly Notices of the Royal Astronomical Society **320**, 307 (2001).

[43] J. Lattimer and M. Prakash, Astrophysical Journal **550**, 426 (2001).

[44] J. P. Cox, *Theory of Stellar Pulsation*, Princeton University Press, 1980.

[45] A. Burrows, Physical Review Letters **44**, 1640 (1980).

[46] I. A. Shovkovy and P. J. Ellis, Physical Review C **67**, 048801 (2003).

[47] I. A. Shovkovy and P. J. Ellis, Physical Review C **66**, 015802 (2002).

[48] M. Alford and S. Reddy, Physical Review D **67**, 074024 (2003).

[49] R. Ruffini, Physical Review D **7**, 972 (1973).

[50] C. O. Lousto and R. H. Price, Physical Review D **55**, 2124 (1997).

[51] T. Nakamura and M. Sasaki, Physics Letters B **106**, 69 (1981).

[52] S. L. Shapiro and I. Wasserman, Astrophysical Journal **260**, 838 (1982).

[53] M. P. Haugan, S. L. Shapiro, and I. Wasserman, Astrophysical Journal **257**, 283 (1982).

[54] V. Ferrari, L. Gualtieri, and A. Borrelli, Physical Review D **59**, 124020 (1999).

[55] A. Nagar, J. A. Font, O. Zanotti, and R. D. Pietri, Physical Review D **72**, 024007 (2005).

[56] V. Ferrari, L. Gualtieri, and L. Rezzolla, Physical Review D **73**, 124028 (2006).

[57] E. Fackerell, Astrophysical Journal **166**, 197 (1971).

[58] A. Nagar and L. Rezzolla, Classical and Quantum Gravity **22**, 167 (2005).

[59] T. Nakamura, K. Oohara, and Y. Kojima, Progress of Theoretical Physics. Supplement , 1 (1987).

[60] A. Nagar, G. Díaz, J. A. Pons, and J. A. Font, Physical Review D **69**, 124028 (2004).

[61] L. Gualtieri, E. Berti, J. A. Pons, G. Miniutti, and V. Ferrari, Physical Review D **64**, 104007 (2001).

[62] L. Gualtieri, J. A. Pons, and G. Miniutti, Physical Review D **70**, 084009 (2004).

[63] J. A. Font, M. Miller, W. M. Suen, and M. Tobias, Physical Review D **61**, 44011 (2000).

[64] J. A. Font et al., Physical Review D **65**, 084024 (2002).

[65] M. Shibata and Y. Sekiguchi, Physical Review D **68**, 104020 (2003).

[66] M. Shibata and Y. Sekiguchi, Physical Review D **71**, 024014 (2005).

[67] C. D. Ott, A. Burrows, L. Dessart, and E. Livne, Physical Review Letters **96**, 201102 (2006).

[68] C. Ishizuka, A. Ohnishi, K. Tsubakihara, K. Sumiyoshi, and S. Yamada, Journal of Physics G: Nuclear and Particle Physics **35**, 085201 (2008).

[69] L. Lindblom and R. J. Splinter, Astrophysical Journal **348**, 198 (1990).

[70] V. Ferrari, Philosophical Transactions: Physical Sciences and Engineering **340**, 423 (1992).

[71] V. Ferrari and M. Germano, Proceedings of the Royal Society of London, Series A: Mathematical and Physical Sciences **444**, 389 (1994).

[72] K. Gottfried and T. M. Yan, *Quantum Mechanics: Fundamentals: Fundamentals V. 1*, Springer, 2003.